Journal of Engineering

ISSN 1726-4073

A Scientific Refereed Journal
Published by College of
Engineering University of
Baghdad

January
2013

Number 1

Volume 19

ISSN 1726-4073

مجلة الهندسة

مجلة علمية محكمة تصدرها
كلية الهندسة ـ جامعة بغداد

كانون الثاني
2013

العدد 1
المجلد 19

ENGINEERING

College of Engineering Baghdad University Baghdad

List of Contents

English Section: Page

Numerical Prediction of Bond-Slip Behavior in Simple Pull-Out Concrete Specimens

Dr.Ala'a Hussein Alwan Al-Zuhairi
Lecturer, University of Baghdad
College of Engineering-Civil Department
Email: alaalwn@yahoo.com

Wjdan Dhaif Sahi Al-Fatlawi
Ass. Lectuer, Ministry of Municipalities and Public Works-Sewerage Directorate-Design Department
Email: wjdan_civil@yahoo.com

ABSTRACT

In this study the simple pullout concrete cylinder specimen reinforced by a single steel bar was analyzed for bond-slip behavior. Three-dimension nonlinear finite element model using ANSYS program was employed to study the behavior of bond between concrete and plain steel reinforcement. The ANSYS model includes eight-noded isoperimetric brick element (SOLID65) to model the concrete cylinder while the steel reinforcing bar was modeled as a truss member (LINK8). Interface element (CONTAC52) was used in this analysis to model the bond between concrete and steel bar. Material nonlinearity due to cracking and/or crushing of concrete, and yielding of the steel reinforcing bar were taken into consideration during the analysis. The accuracy of this model is investigated by comparing the finite element numerical behavior with that predicted from experimental results of three pullout specimens. Good agreement between the finite element solution and experimental results was obtained.

Key words: bond-slip relationship, plain bar, FEM, ANSYS program, pull-out test.

التخمين العددي لتصرف علاقة الربط-الأنزلاق في نموذج سحب خرساني بسيط

د.علاء حسين علوان الزهيري
مدرس

وجدان ضايف ساهي الفتلاوي
مدرس مساعد

الخلاصة

في هذة الدراسة تم تحليل نموذج سحب خرساني اسطواني بسيط مسلح بسيخ حديد املس منفرد في مركـز الاسـطوانة بواسـطة طريقة التحليل اللاخطي للعناصرالمحددة ثلاثية الابعاد باستعمال برنامج نظام التحليل الحاسوبي ANSYS لدراسة تصرف الـربط بين الخرسانة وحديد التسليح الاملس. اذ تم استعمال عناصر طابوقية ثلاثية الأبعاد ذات ثمان عقد نـوع Isoperimetric تـسمى (Solid65) لتمثيل خرسانة الاسطوانة بينما تم تمثيل حديد التسليح باستعمال العنصر المحوري(Link8). اما المنطقه البينيه(منطقة التماس بين الخرسانة والحديد) فقد تم تمثيلها باستعمال عنصر التداخل (Contac52) والذي يربط العناصر الطابوقيـة والعناصـر المحورية لتمثيل سلوك الربط بين الخرسانة وحديد التسليح مع الأخذ بنظرالاعتبار التصرف أللاخطي لكلا المادتين، والذي يـشمل تشقق و/أوتهشم الخرسانة وخضوع حديد التسليح. لقد تمت مقارنة نتائج التحليل العددي مع النتائج العملية لثلاث نمـاذج سـحب نموذجية للتحقق من دقة التمثيل اذ تم الحصول على تقارب وتوافق بدرجة جيدة بين نتائج التحليل العددي والنتائج العملية.

الكلمات الرئيسية: علاقة الربط- الأنزلاق، قضيب أملس، طريقة العناصر المحددة، برنامج ANSYS، فحص السحب

1. INTRODUCTION

The ability of using of reinforced concrete as a structural material is derived from the combination of concrete which is strong in compression with reinforcing steel that is strong and ductile in tension. Maintaining composite action requires transfer of load between the concrete and steel. This load transfer is referred to as bond. Bond stress is defined as the shear stress acting on the surface between the bar and concrete in the direction of the bar. It governs some phenomena in reinforced concrete such as cracking and tension-stiffening during the loading stage till failure. Bond can be activated under various actions like pure tension, pull-out, push-in …etc. Selection of any one of these loading methods depends on many variables such as characteristics of reinforcing bar, concrete physical properties, and member geometry.

The idealization of bond in finite element method (FEM) allows considering several phenomena: plasticity, contact, cracking …etc.). This is may be the reason why FEM has been applied to bond modeling by several researchers starting by the pioneer work of Ngo and Scordelis, 1967 to the most recent advancements (Bamonte et al, 2003, Sezen and Mohle, 2003, Jendele and Cervenka, 2006, and Khalfallh and Ouchenane, 2007).

In this paper, the finite element method is used to investigate bond behavior of pull-out cylinder reinforced with a plain steel bar. The analysis is made utilizing the computer program ANSYS 9.0.

2. THE DETAILS OF TEST SPECIMEN:

The pull-out cylinder specimen (150×300mm) shown in Fig.(1) was used in this study. The bonded length (L) was taken equal to 12times the bar diameter. It was assumed that the slip is constant along the bonded length (L) of the steel bar. Consequently, the bond stress (u) is uniform. Hence, the bond stress can be calculated from equilibrium condition as follows:

$$A_b \times f_s = L \times \pi \times \phi_b \times u$$

$$\pi \times \frac{\phi_b^2}{4} \times f_s = L \times \pi \times \phi_b \times u \qquad (1)$$

$$u = \frac{\phi_b}{4L} \times f_s$$

Where,

u = average bond stress.
L = bonded length.
ϕ_b = steel bar diameter.
A_b = cross section area of steel bar.
f_s = tensile stress in steel.
Since L was taken as equal to $12\phi_b$, therefore:

$$u = \frac{f_s}{48} \qquad (2)$$

Three specimens were tested experimentally by varying the diameter of the steel plain bar as (10, 12, and 16)mm. The results of the test were used in the comparison that made with the results of the finite element analysis.

3. FINITE ELEMENT MODEL:

3.1 Element Types

The solid brick element, SOLID65, was used to model the concrete in ANSYS program. The solid element has eight nodes with three degrees of freedom at each node, translations in the nodal x, y, and z directions. The element is capable of plastic deformation, and cracking in three orthogonal directions. The two-noded LINK8 bar (truss) element was used to model the steel reinforcement. At each node, the degrees of freedom are identical to those for the SOLID65. The element is also capable of plastic deformation. Point to point contact element (CONTAC 52) was used to model bond-slip of reinforcement bar in the present study. The element joins two surfaces that may maintain or break physical contact and may slide relative to each other. Also, it is capable of supporting only compression in the direction normal to the interface between the two surfaces and Coulomb shear-friction in the tangential direction. The 3-D point-to-point contact element has three degrees of freedom at each node in the element coordinate system. The orientation of the interface is defined by the node locations.

3.2 Material Properties

Concrete: SOLID65 elements are capable of predicting the nonlinear behavior of concrete materials using smeared crack approach Willam and Warnke, 1975. The smeared crack approach has been adopted widely in the last decades. Concrete is a quasi-brittle material and has very different behaviors in compression and tension. The stress-

strain relation for concrete in compression was described by multilinear elastic model as shown in Fig. (2). Based on the compressive strength of concrete, the stress-strain relationship was obtained using the following equation (MacGregor, 1992)**:**

$$f = \frac{E_c \varepsilon}{1 + \left(\frac{\varepsilon}{\varepsilon_o}\right)^2} \quad (3)$$

Where,

f = stress at any strain ε, MPa.

ε = strain at stress f.

ε_o = strain at the ultimate compressive strength f_c', $\varepsilon_o = \frac{2 f_c'}{E_c}$.

E_c = concrete elastic modulus

$E_c = 4700\sqrt{f_c'}$ MPa (ACI 318 Code).

The failure surface of the concrete proposed by Willam and Warnke, 1975, is adopted in this study.

Steel Reinforcement: a multilinear isotropic hardening with von- Mises yield criterion model is used to define the material properties of steel bar. The tensile stress-strain response of steel based on the test data shown in Fig. (3) is used in the present analysis by picking the values in data table of ANSYS 9.0 program.

Bond- Slip Model: The interface element (CONTAC 52) is capable of supporting only compressive forces in the direction normal to the interface surface and shear (Coulomb friction) in the tangential direction. The interface element (CONTAC 52) may have one of three conditions:closed and stuck, closed and sliding, or open. The force-deflection relationships for the interface element (CONTAC 52) can be separated into normal and tangential (sliding) directions as shown in Fig.(4).

The element (CONTAC 52) is defined by two stiffnesses: normal stiffness (k_n) and tangential stiffness (k_s). The normal stiffness (k_n) is calculated from the following equation (Fardis and Buyukozturk, 1980).

$$k_n = \frac{d}{0.7}\left[\pi E_s K_f^3 \left(\frac{f_c'}{27.4}\right)^6\right]^{1/4} \text{(MPa/mm)} \quad (6)$$

where:

E_s= Elastic Modulus for steel bar.

K_f= is the foundation modulus, depending on the tensile stress in the reinforcement as:

$$K_f = 820 - 1.17 f_s \quad \text{N/mm}^3 \quad (7)$$

where, f_s is the tensile stress in the reinforcement (MPa).

The tangential (sticking) stiffness (k_s) is found by multiplying the friction by normal stiffness.

The input data for the concrete, steel reinforcement, and interface element are summarized in Table (1).

Table (1): Materials properties of the pull-out specimens

Material type	Parameter	Values for		
		Case1	Case2	Case3
Concrete	Compressive strength, f_c' (MPa)	31.0		
	Tensile strength, $f_t = 0.1 f_c'$ (MPa) (Chen, 1982)	3.1		
	Young modulus, E_c (MPa)	26187.6		
	Poisson's Ratio, ν (assumed)	0.15		
Reinforcing steel	Actual diameter (mm)	10.85	12.60	15.75
	Yield stress, f_s (MPa)	369.4	378.6	300.9
	Young modulus, E_s (MPa)	210083.1	210136.3	206859.0
	Poisson's Ratio, ν (assumed)	0.3		
	Bonded length = $12d_b$ (mm)	130	150	190
Interface (contact)	Coefficient of Friction μ (assumed)	0.3		

3.3 Finite Element Modeling

The specimen is a concrete cylinder of 150mm diameter, and 300mm length, with single concentric plain bar. Contact elements (interface elements) are alternatively used at the interface between the concrete and the steel bar. To obtain good results from the concrete element (Solid 65) is arranged in a rectangular mesh i.e., the mesh is set-up such that square or rectangular elements are created. The meshing of reinforcing bar has corresponded to the meshing of concrete volume. The boundary conditions for the geometric model are applied by fixing the nodes at the top surface of cylinder in three directions except the nodes adjacent to the steel bar and the nodes of unbounded length fixed in two directions (x and y). The finite element model of the cylinder specimen is shown in Figs. (5) and (6).

4. RESULTS AND DISCUSSION:

Bond-slip relations have been established from the finite element analysis and compared with the experimental results as shown in Fig. (7) for three cases of verification. All curves have mostly the same trend.

The bond-slip curves are obtained for plain bars of 10mm, 12mm and16mm diameter during the loading stage only. No slip greater than that shown in these curves could be obtained because after this stage the bar is pulled continuously out of the concrete cylinder.

These figures clarify that bond stress is composed of two components. At initial stages of loading the main parts of the bond are generated from chemical adhesion between the concrete and steel reinforcement. Typical values of bond stress ranging from (0.03 to 0.9) MPa. The generation of this component of bond stress is not accompanied by a significant slip between the reinforcing steel and the surrounding concrete. As the applied tensile force increases, the second component of the bond will start due to friction developement. The role of the chemical bond is more pronounced in the smooth bars and its effect decreases or diminishes as the reinforcing bar diameter increases.

Table(2) shows experimental and nummerically calculated loads that measured and predicted at bond failure. It is observed that the mimum force required overcoming the bond strength mobilized between reinforcing bar and surrounding concrete is increased with increasing of bar diameter. However, this trend is obosite when the tensile stress in bar material (steel) is considered. between results predicted from finite element analysis and those obtained experimentally may be attributed to sophisticated method in determining of the normal stiffness of the interfce (contact) element. Fig.(8) shows the average bond-slip relationships for different diameters of steel bars embeded in concrete cylinder specimens of the compressive strength. It is cleared that the bond stress decreases with increasing of bar diameter

Table (2): Experimental and predicted bond failure loads for three cases

Test case	Nominal size of steel bar (mm)	Actual diameter of steel bar (mm)	Expermental results			F.E. analysis results			Error, E (%) $E=\frac{F.E-Exper}{Exper}\times 100$
			Max. force (kN)	Max. stress in steel (MPa)	Average bond stress (MPa)	Max. force (kN)	Max. stress in steel (MPa)	Average bond stress (MPa)	
1	10	10.85	16.156	174.8	3.64	17.000	183.9	3.83	5.2
2	12	12.60	18.722	150.2	3.13	20.500	164.5	3.43	9.4
3	16	15.75	26.430	135.7	2.83	27.000	138.7	2.89	2.2

.

5. FAILURE MODE

The pull-out failure is observed in both experimental tests and finite element analysis. No cracking of the concrete is indicated in any of test specimens as shown in Fig. (9). On the other hand, no yielding was occurred in steel bar. Fig.(10) shows the pull bar and deformation of interface elements which connects the concrete and steel reinforcement.

6. CONCLUSIONS

1. The trend of bond-slip realation was found inpependent of bar diameter.
2. The use of interface (contact) element through analytical study helps the numerical solution to exhibit a good agreement with experimental results.
3. The differences (errors) between the results predicted by FEA and those obtained experimentally is attributed to the difficulty of determining the normal stiffness of the interface element
4. For both experimental and Nummerical analyses, bond strength increases by decreasing the diameter of steel bar embeded in concrete cylinder specimens of the same compressive strength.
5. Chemical adhesion decreases with the increase of embedded bar diameter. This resistance is observed at the early stage of loading when the pullout force is applied without any slippage of the reinforcing bar.
6. The pull-out failure is the predominant type of failure observed in specimens. Neither cracking of concrete nor yielding of steel bars was indicated.

REFERENCES:

ANSYS Theoretical Manual, Version 11.0.

Bamonte, P., Coreonelli, D., and Gambarova, P.G., “Smooth Anchored Bars in NSC and HPC: A Study on Size Effect”, Journal of advanced concrete technology, Vol. 1, No.1 January 2003, pp.42-53.

Chen, W. F., “Plasticity in Reinforced Concrete” McGraw-Hill Book Company, Inc., New York, pp.474, 1982.

Fardis, M., and Buyukozturk, M.,“Shear Stiffness of Concrete by Finite Elements”ASCE Proceedings, Journal of Structure Division, Vol. 106, No.St6, June 1980, PP.1311-1327.

Hong, S. and Park, S. "Uniaxial Bond Stress-Slip Relationship of Reinforcing Bars in Concrete", 2012, Advances in Materials Science and Engineering, Vol. 2012 Article ID 328570, 12 pages, Hindawi Publishing Corporation.

Jendele, L.,and Cervenka, J., **“**Finite Element Modeling of Reinforcement With Bond”, Computer and structures Journal 84 ,August 2006, pp. 1780-1791.

Khalfallah, S., and Ouchenane, M., “Prediction of Bond Between Steel and Concrete by Numerical Analysis”, The Open Civil Engineering Journal, University of Jijel, Algeria, 2008, Vol.2, pp. 1-8.

Khalfallah, S., and Ouchenane, M., **“**A Numerical Simulation of Bond for Pull-out Tests the Direct Problem”, Asian Journal of Civil Engineering (Building and Housing), Vol.8, No.5, 2007, pp. 491-505.

MacGregor, J.G., "Reinforced Concrete Mechanics and Design", Prentice-Hall, Inc.,Englewood Cliffs, NJ, 1992

Ngo, D. and Scordelis, A. C., "Finite Element Analysis of Reinforced Concrete Beams**",** ACI Journal, Vol. 64, No. 3, March1967, pp. 152- 163.

Sezen, H., and Moehle, J.P., **"**Bond-Slip Behavior of Reinforced Concrete Members", The Earth Engineering Research Centers Program of the National Science Foundation at the University of California, Berkeley, 2003.(Internet)

Willam,K., and Warnke, E., **"**Constitutive Model for the Triaxial Behavior of Concrete**"**, Proceedings, International Association for Bridge and Structural Engineering, Vol.19, ISMES, pp.174, Bergamo, Italy, 1975.

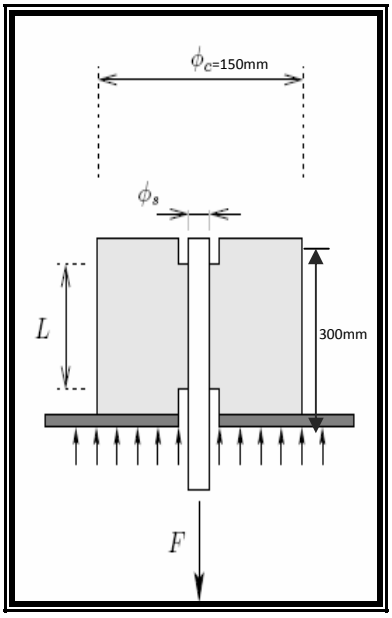

Fig. (1): Pull-out specimen

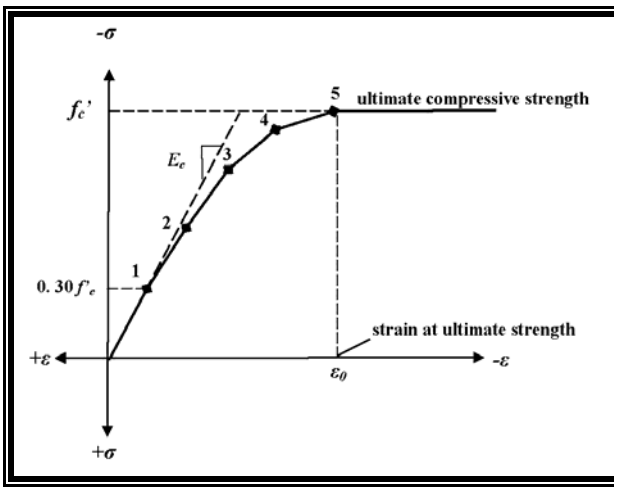

(a): Stress-Strain curve of concrete

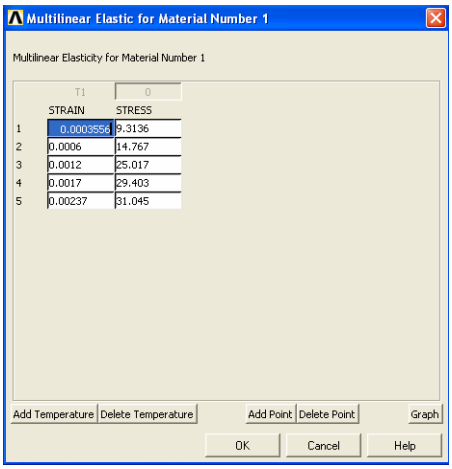

(b): Data table for stress-strain curve of concrete

Fig. (2): The adopted stress-strain curve of concrete in ANSYS 9.0 program

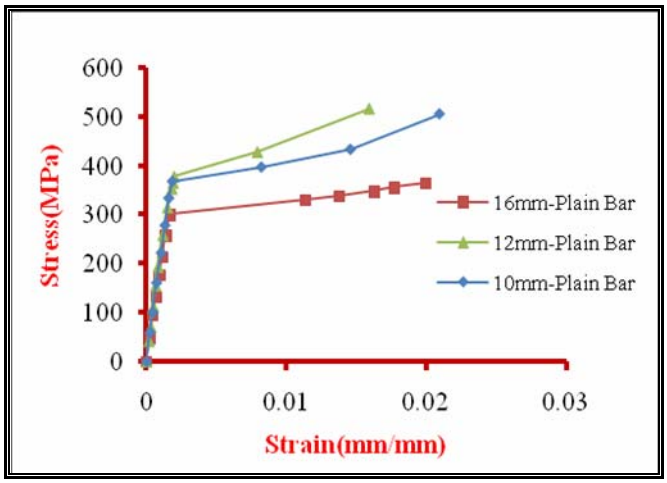

Fig. (3): Stress-strain diagrams for tested reinforcing steel bars

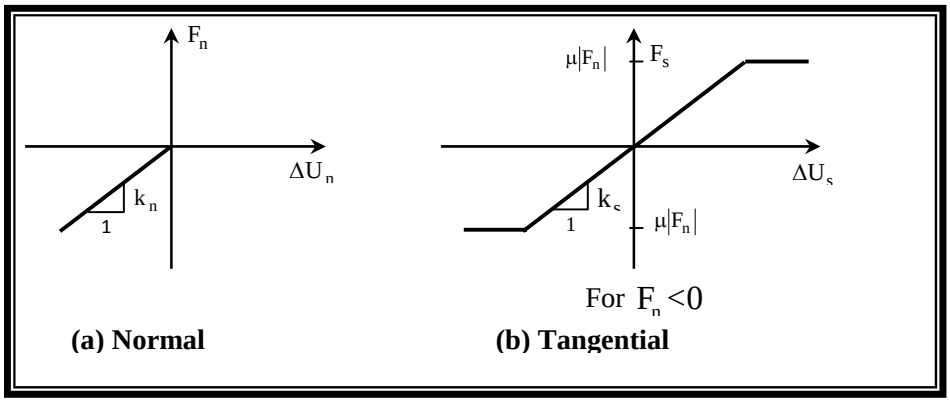

Fig. (4): Interface force-deflection relationship ANSYS

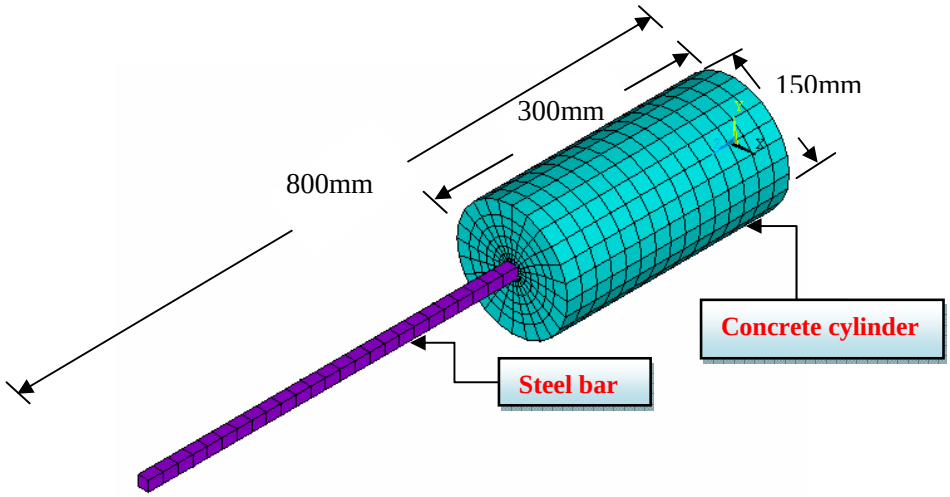

(a) 16mm diameter

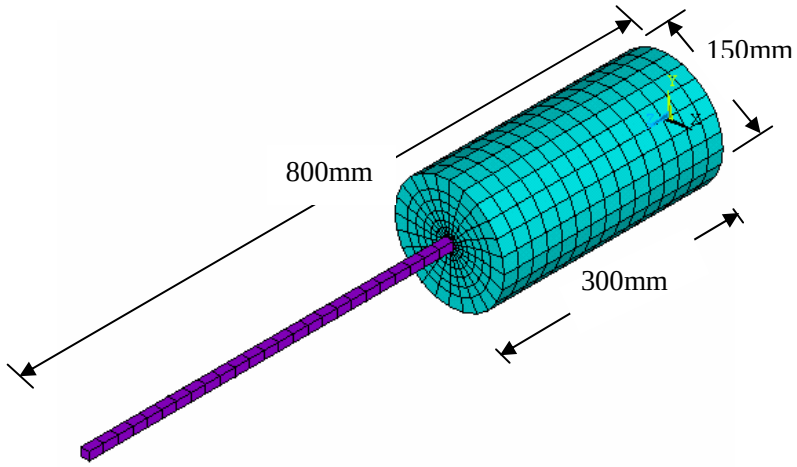

(b) 12mm diameter

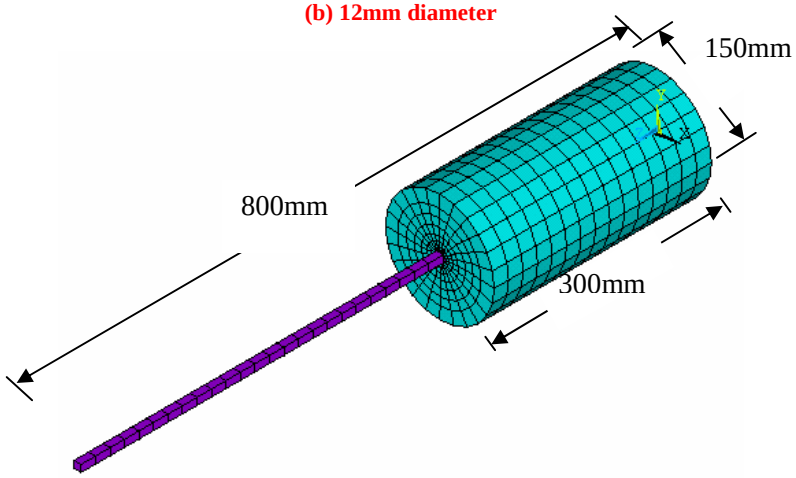

(c) 10mm diameter

Fig. (5): Finite element mesh of pull-out specimens created using ANSYS 9.0 program

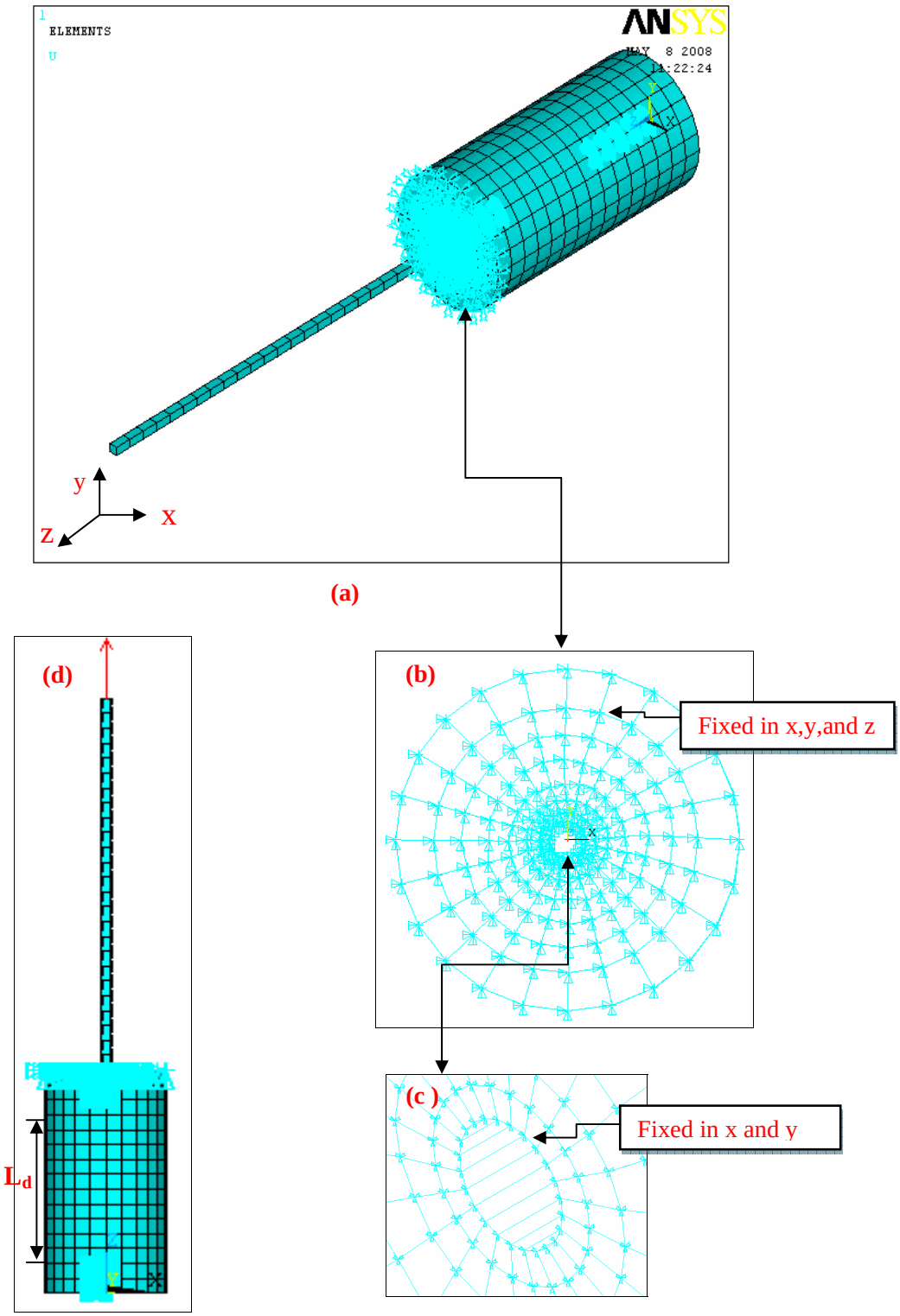

Fig.(6) :Applying boundary condition and force
(a, b, and c) Applying boundary conditions
(d) Applying development length and force

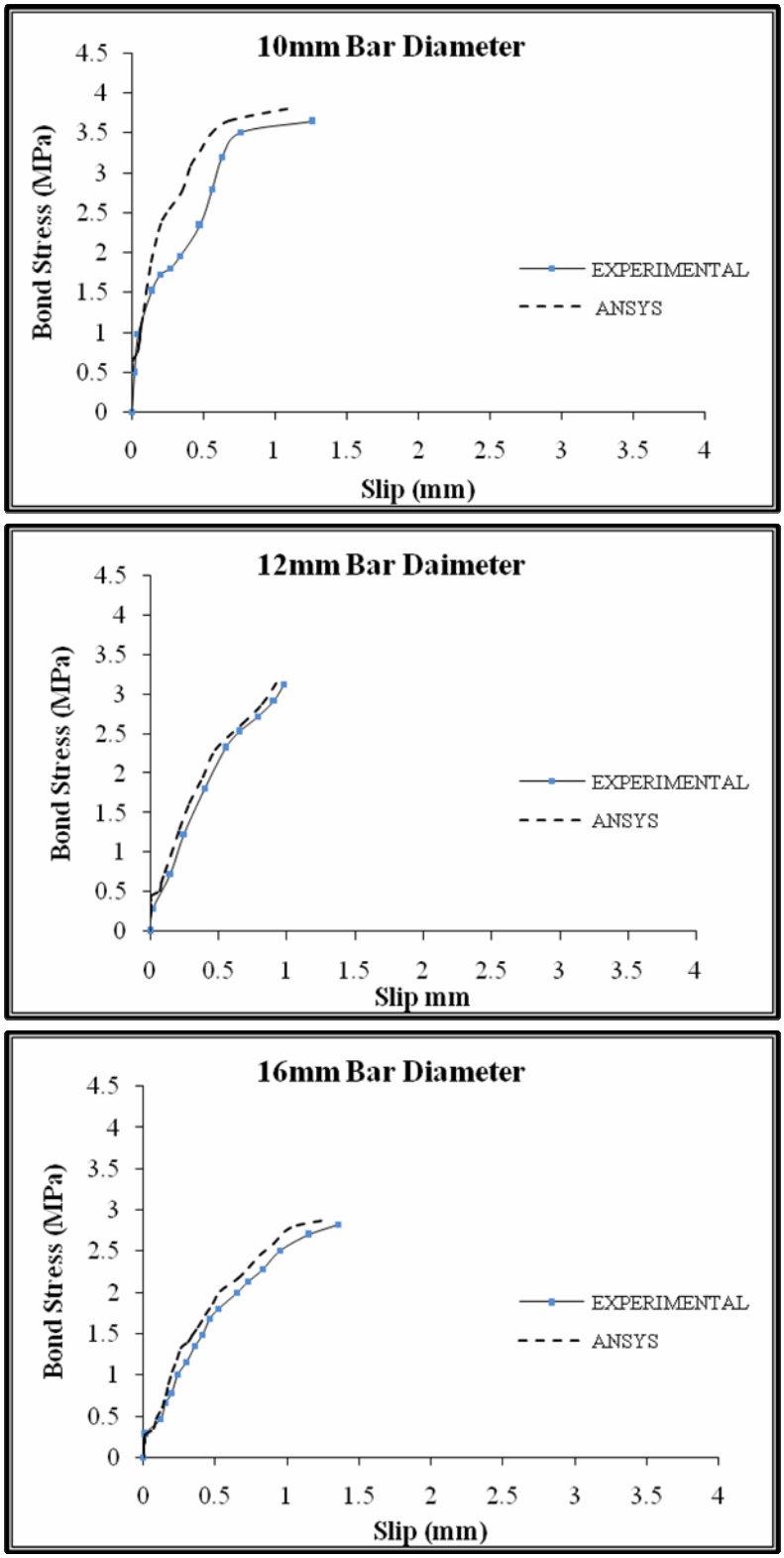

Fig. (7): Bond-slip relationships of concrete compressive strength 31.045MPa and for different steel bar diameters

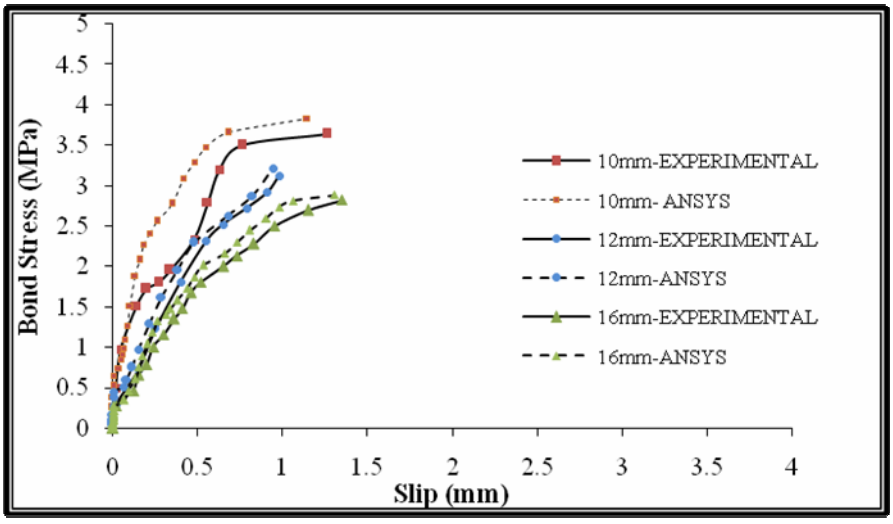

Fig. (8): Bond stress-slip relationship for compressive strength 31.045MPa with different diameters

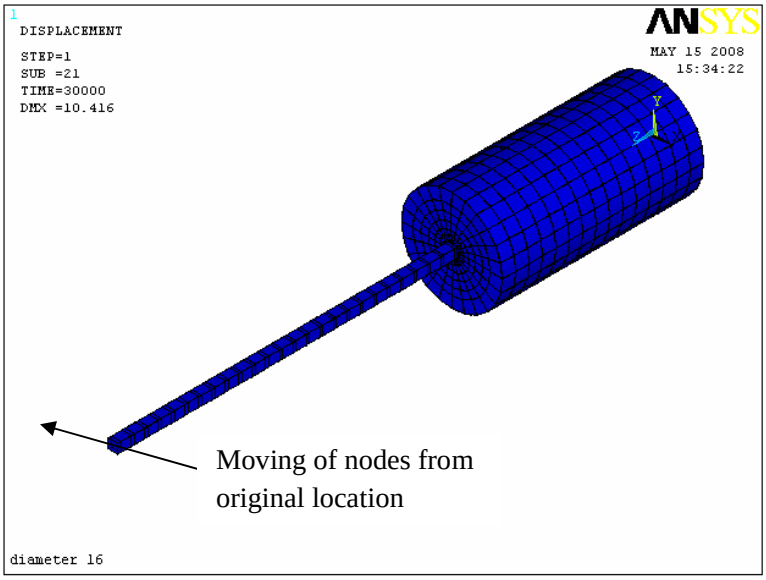

Fig. (9): The deformed and un-deformed shape of the model.

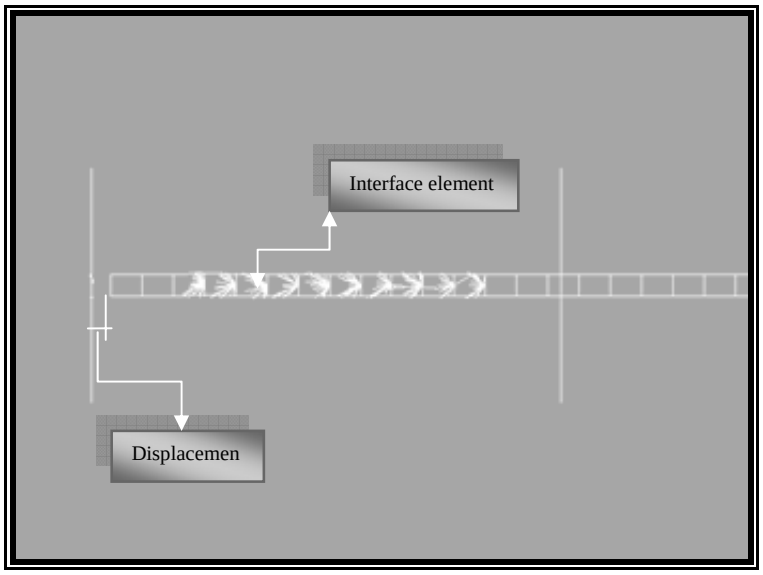

Side view (a)

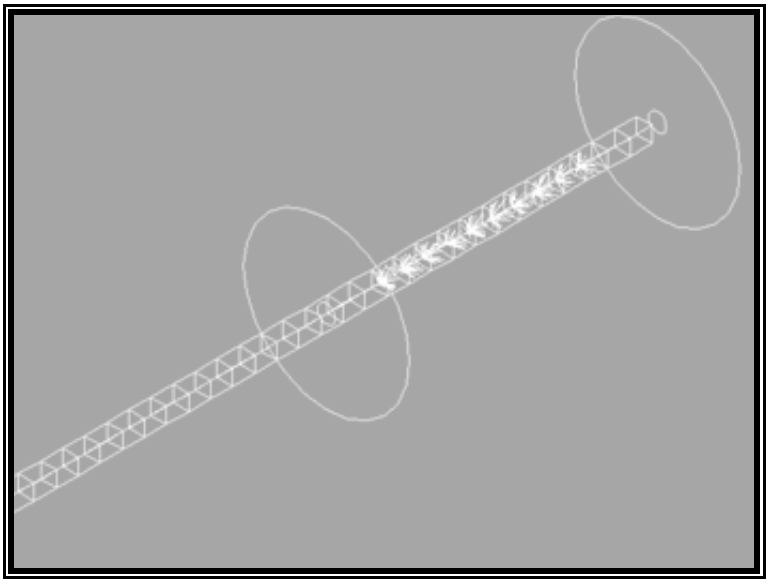

(b) Iso view

Fig. (10): Pull steel bar and deformation of interface elements.

Effect of Petroleum Products on Steel Fiber Reinforced Concrete

Asst.Prof.Dr. Nada Mahdi Fawzi and Sara Alaa Abed AL-Ameer

Department of Civil Engineering, University of Baghdad

ABSTRACT

This Investigation aims to study the effect of adding Steel fibers with different volume fractions V_f (o.5, 0.75, and 1% by volume of concrete) with aspect ratio 100 on mechanical properties of concrete, and also finding the influence of petroleum products (Kerosene and Diesel) on mechanical properties of Steel Fiber Reinforced Concrete (SFRC).

The experimental work consists of two groups: group one consists of specimens (cubes and prisms) plain and concrete reinforced with steel fiber exposed to continuous curing with water. Group two consists of specimens (cubes and prisms) plain and concrete reinforced with steel fiber exposed to kerosene and diesel after curing them in water for 28 days before exposure.

The results of all tests refer that the specimens (plain and reinforced concrete with steel fiber with different volume fraction) exposed to kerosene were better than the specimens (plain and reinforced concrete with steel fiber with different volume fraction) exposed to diesel.

Key words: Steel Fibers, Kerosene, Diesel, Reinforced concrete

تأثير المشتقات النفطيه على الخرسانه المسلحه بالالياف الحديديه

الخلاصه

الهدف من هذا البحث هو دراسه تاثير اضافه الياف الحديد بنسبه مختلفه (0.5، 0.75، و 1% من حجم الخرسانه) دو نسبه باعيه 100 على الخواص الميكانيكيه للخرسانه، وكذلك أيجاد تأثير المشتقات النفطيه (النفط الابيض وزيت الكاز) على الخواص الميكانيكيه للخرسانه المسلحه بالالياف الحديديه.

العمل المختبري مكون من مجموعتين : المجموعه الاولى تتضمن نمادج (مكعبات ومواشير) من الخرسانه الاعتياديه والمسلحه بالالياف الحديد معرضه الى الانضاج المستمر للماء. اما المجموعه الثانيه تتضمن نمادج (مكعبات ومواشير) من الخرسانه الاعتياديه والمسلحه بالالياف الحديد معرضه الى النفط الابيض او زيت الكاز بعد انضاجها بالماء لمده 28 يوم قبل التعرض.

أشارت جميع نتائج الفحوصات أن النمادج (الغير مسلحه والمسلحه بالياف الحديد بنسب مختلفه) المعرضه للنفط الابيض كانت افضل من نتائج النمادج (الغير مسلحه والمسلحه بالياف الحديد بنسب مختلفه) المعرضه لزيت الكاز

INTRODUCTION

The long life of many reinforced concrete structures which have been exposed to aggressive environment for years shows that concrete has a significant durability in these environments .This has encouraged the tremendous developments in the use of large concrete structures, reinforced or pre-stressed, for the production, storage and transportation of oil products, to overcome the shortage in steel materials in some parts of the world. A Reinforced concrete tanks are used instead of steel tanks for petroleum products storage. Change from steel to concrete for storage purpose was due to low cost of repair, maintenance, and construction. In addition, concrete offers considerable resistance to fire and explosive during war times.

Steel tanks and pipes have traditionally been used for storage and transportation of petroleum products around the world. However, in many countries especially those which do not have steel industry, storage in these structures could occur. In addition, the high costs of construction and maintenance, the need for larger capacities and safety requirements for steel tanks have urged the people concerned to look for new alternatives of constructional materials. Concrete oil-storage tanks have been tried for at least seventy years and would have many advantages if adequate impermeability could be assured without the use of expensive impermeable liners. The critical storage and cost of steel during the Second World War expanded progressively the use of concrete for the construction of oil tanks. Before 1914, many concrete tanks were built in the USA for storage of heavy oils and during the Second World War the USA navy built concrete tanks for fuel oil Storage **(Spamer 1944)&(Shepard 1944)**.

The main problems that restrict the successful use of concrete to store fuel oil are: the leakage of oils especially the lighter products (that having specific gravity 0.875 at temperature 15C) through the pore structure, shrinkage cracks and joints **(Lea 2004)**.

However the serviceability of reinforced concrete storage containers necessitates control of cracking and impermeability. Generally, concrete materials suffer from the inherent characteristics of low tensile strength and

Tendency to cracks under tensile stresses produced by external loads, shrinkage, creep, or thermal gradients. In most cases, long term loading extends the magnitude of cracks in both plain and reinforced concrete **(Abdul- Ahad et al., 2000)**.

The advantages of using reinforced concrete tanks as follows: **(Concrete Storage Structure 1983)**

- The availability and low cost of raw materials results in economic construction costs.
- A remarkable durability in almost all types of environments resulting in significant reduction in maintenance and maintenance cost accordingly.
- Good fire and earthquake resistance, thermal, impact and explosion properties.
- Suitability for underground and under sea storage.
- Constructional flexibility in different shapes and capacities according to the shape of mould lubricated.
- Owing to their dead weights they have the capability of forming buoyant or fixed structures.

The disadvantages of used reinforced concrete tanks as follows: **(Matti 1976) & (Faiyadth 1985)**

- Capability of light petroleum products to penetrate concrete.
- The unavoidable cracking due to shrinkage and thermal movement
- Possibility of fracturing by different settlements.
- Deterioration of the bond between steel and concrete in addition to deterioration in concrete itself if saturated by oils.

RESEARCH SIGNIFICANCE

Concrete is the most commonly used material in construction industry. There are a number of reasons for this such as high strength, ease of

production, low cost, good compatibility with other materials, especially with steel, durability under aggressive conditions. Ordinary concrete includes cracks with large width and has low tensile or flexure strength, but when Steel Fibers added to concrete can improve its properties like compressive strength, flexural strength, impact resistance, ability to control cracks and products cracks with small width, and also improve the toughness. The essential objective from this research to study the mechanical properties of steel fiber reinforced concrete when exposed to kerosene and diesel.

STEEL FIBER REINFORCED CONCRETE

Although concrete is a widely used construction material, it has major disadvantages such as a low tensile strength and low strength to weight ratio, and it is liable to cracking **(Cement& Concrete Institute 2010).**

Fiber reinforced concrete (FRC) is Portland cement concrete reinforced with randomly distributed fibers. In FRC, of small fibers are dispersed and distributed randomly in the concrete during mixing, and thus improve concrete properties in all directions. Fibers help to improve the post peak ductility performance, pre-crack tensile strength, fatigue strength, impact strength and eliminate temperature and shrinkage cracks **(Nemati 2010).**

The brittle nature of plain concrete cannot be neglected and an approach to make concrete a ductile material is necessary. In this regard, steel is no doubt a useful reinforcement material for concrete whether it is in the form of a SF or a reinforcing bar. The addition of SF to concrete can improve the tensile strength and ductility, but it will also reduce the workability **(Chang et al., 2009)**

The addition of SF in the concrete mix allows the development of tensile stresses along the entire cracked depth of a section. These stresses can provide the required ultimate bending strength. SF provides also other properties that improve the structural behavior under service loads, for instance **(ACI 544(1996))**

- Crack width reduction
- More uniform distribution of cracks
- Improvement of structural behavior under cyclic loads
- Increase in structural ductility
- Improve impact & abrasion resistance

The use of *SFRC* in building construction has increased continuously due to its better mechanical properties, mainly, the energy absorption capacity. The energy dissipated to pull out the fibers from the cracked concrete is much higher than the Energy dissipated to crack the concrete matrix. Therefore, the energy absorption capacity is the main material property benefited by fiber reinforcement **(Barros and Cruze (1998)).**

PROPERTIES OF STEEL FIBER REINFORCED CONCRETE

1. Compressive Strength

Fibers do little to enhance the static compressive strength of concrete, with increases in strength ranging from essentially nil to perhaps 25%. Even in members which contain conventional reinforcement in addition to the steel fibers. The fibers have little effect on compressive strength. However, the fibers do substantially increase the post-cracking ductility, or energy absorption of the material (Neves et and Fernades (2006)).

2. Direct Tension

In direct tension, the improvement in strength is significant, with increases of the order of 30 to 40 % reported for the addition of 1.5% by volume of fibers in mortar or concrete (ACI 544 1R-96).

3. Flexural Strength

Increases in the flexural strength of SFRC are substantially greater than in tension or compression because ductile behavior of the SFRC on the tension side of a beam alters the normally elastic distribution of stress and strain over the member depth. The altered stress distribution is essentially plastic in the tension zone and elastic in the compression zone, resulting in a shift of the neutral axis toward the compression zone strength concrete. The main reason for the discrepancy in fiber cement

composite is that the post- cracking stress-strain curve on the tensile side of the fiber cement or fiber concrete beam is very different from that in compression (Snyder and Lankard (1972)).

EFFECT OF CRUDE OIL OR ITS PRODUCTS ON PROPERTIES OF PLAIN AND REINFORCED CONCRETE

Meissner et al. (**1944**) have studied the influence of high octane gasoline on mechanical properties of mortar cubes (50 mm) soaked for 180 days. He has investigated that small reduction in compressive strength and no effect in tensile strength for the specimens.

Al – Saraj (**1995**) has studied the mechanical properties of concrete exposed to gas oil and aircraft engine fuel for soaking period of water – cured specimens, he found:

1. The compressive strength of concrete exposed to gasoline and fuel decreased by about 6.8 – 16.3% and 9.2 – 19.3% respectively.
2. The splitting tensile strength was also decreased about 7.3 – 16.8% and 10 – 20.5% for gasoline and fuel exposure respectively
3. The flexural strength was reduced by about 7.3 – 16.8%, and 10 – 20.5% for gasoline and fuel exposure respectively.
4. Modulus of elasticity is reduced by about 17.4-21.9% and 20.5-26.3% for gas oil and fuel, respectively.

Mohammed (**1997**) has investigated that in the field the effectiveness of cured oil on concrete under loadings (30, 40, 50, and 70% from ultimate load) on short and long term loadings. He concluded that:

1. High compressive strength reduction takes place due to higher amount of the oil absorbed relative to its low viscosity reaching 12.52% after 2month soaking.
2. Splitting tensile strength is also reduced due to oil penetration, at lower rate as compared with the compressive strength.
3. Modules of rupture increases due to oil absorption reaching 4% while for loaded specimen, further increase takes place reaching 6 – 8% compared with initial oven dried specimen.
4. The rate of crude oil absorption is high at early stage of soaking and increases slowly with time, and increase moderately at 70% compressive stress / strength ratio.

Rashed (**1998**) has studied the effect of petroleum products (kerosene and gas oil) on steel fiber reinforced concrete. He concluded that:

1. The compressive strength was reduced by about 19 and 20.8% for kerosene and gas oil exposure respectively.
2. The splitting – tensile strength was also reduced by about 18 and 18.3% for kerosene and gas oil exposure respectively.
3. The modulus of rupture of steel fiber concrete exposed to kerosene and gas oil was reduced after 30 days of exposure.

Blaszczynski (**2002**) has investigated that the durability analysis of concrete exposed to a crude oil products environment shows that significant reduction in compressive strength and its bond to reinforcement can occur.

EXPERIMENTAL WORK

Materials

Cement

The cement used is an Ordinary Portland Cement taken from one stocked quantity and supplied from (Taslooja) factory; it is used in casting all specimens throughout the experimental work. It stored in laboratory by plastic containers were used to enclose the cement in order to minimize the effect of humidity throughout the experimental work.

The physical and chemical properties of the cement are shown in Tables (1) and (2) respectively, with the estimated cement

compounds based on Bogue's equations given in (ASTM C 150-00). This cement complied with the (Iraqi specification No.5/1984).

Fine aggregate (Sand)

Al-Akhaidhur well-graded natural sand used of 4.75-mm maximum size was used for concrete mixes of this investigation. Table (3) shows the sieve analysis of this aggregate and Table (4) which represented the properties of the used sand. The grading is lied in (Zone No. 1) and conformed to the limits of Iraqi specification No. 45/1984.

Coarse Aggregate (Gravel)

The Coarse Aggregate used in this research is crushed washed aggregate brought from Al-Nibaii area of maximum size 10mm. **Table (5)** shows the sieve analysis of this aggregate and **Table (6)** which presented the properties of coarse aggregate. It conforms to the **Iraqi specification I.S.O.45/1984**.

Water

Water is used in this research for mixing and curing. It is ordinary potable water for Baghdad City.

Steel Fiber

High tensile steel fibers crimped type was used in this research with 0.5, 0.75 and 1% by volume of concrete (V_f =0.5, 0.75 and 1%). Table (7) shows the properties of the used steel fibers as given by the manufacture.

Petroleum Products

Kerosene and Diesel

Kerosene and diesel product from AL-Daura refinery was used. Tables (8) and (9) show the chemical analysis of the Kerosene and diesel used in this study.

Mix Design and Mixture

In this research, there are two groups of concrete mixes according to the type of exposure. Group one consists of two series have tested with compressive strength, air dry density, and flexural strength (modulus of rupture) exposed to continuous curing with water tested at age (30, 60, 90 and 120) days. Group two consists of two series have tested with compressive strength, air dry density, and flexural strength (modulus of rupture) exposed to kerosene or diesel (after curing them in water for 28 days before exposure) tested at age (60, 90 and 120) days. All the concrete mixes are designed according to **(ACI 211)** by the volume method with the target strength (30 MPa) at 28 days and the mix proportions of the concrete are given in **Table (9)**. All the concrete in this research had the same volumetric proportion of fine and coarse aggregate, and the amount of water (mix water) is kept the same in these concrete mixes, resulting in a constant W/C of (0.54) for all mixes.

Results and Discussion

Compressive strength

The result of compressive strength of concrete mixes (reference and reinforced concrete with different volume fraction of steel fiber (0.5, 0.75 and 1% by volume of concrete)) are shown in **Tables from (10) to (12)** and plotted in **Figure from (1) to (3)**.

The test results present that the compressive strength of reference concrete is increased as the time of continuous curing in water increase , this is due to continuous hydration of cement paste, then, increases the bond between cement paste and aggregate **(Shetty 2000) and (Neville 2010)**.

From the test results, it can be seen that the concrete mixes reinforced with SF is increased continuously with the time of curing in water was increase. The maximum increase was 48% when using 1% SF at 120 days as a compared at 30 days of curing.

From test results it can be seen that the compressive strength of the cubes (reference and reinforced with SF V_f (0.5, 0.75, and 1%)) mixes exposed to kerosene or diesel, at 60 days the compressive strength of them is greater than the compressive strength of the cubes (reference and reinforced with SF V_f (0.5, 0.75, and 1%)) cured in water. This is due to the pores inside the concrete which was still partially filled with water and leads to further hydration that delay the deterioration of concrete **(AL-Harby 1998)**. But at 120 days of exposure to kerosene or

diesel, the compressive strength of concrete cubes (with and without SF) is decrease. The decreased in compressive strength for plain and for steel fiber reinforced concrete exposed to kerosene or diesel may be attributed to the weakening in the bond strength between cement paste and aggregate and between concrete matrix and fibers with the time of exposure. **(AL-Harby 1998) and (Francis et al., 2010)**.

Density

The result of density of concrete mixes (reference and reinforced concrete with different volume fraction of steel fiber (0.5, 0.75 and 1% by volume of concrete) are shown in **Tables from (13) to (15)** and plotted in **Figure from (4) to (6)**.

From test results it can be notice that: The specimens cured in water show an increase in density as the time of curing period increased too, this is due to continuous hydration of cement, and this is in complete comply with other researches like **(Shetty 2000)**

The density of the cubes exposed to kerosene or diesel at age 60 days (after curing them in water for 28 days) is higher than the density of those cubes curing in water for the same ages. The maximum increased when used SF 1% with rates 0.65% and 0.35% for kerosene and diesel respectively. This is due to the inside pores which were partially filled with water and let to continuous hydration of cement.

At 120 days from exposure to kerosene or diesel, the density of the specimens (with and without SF) is decreased. This happens because the harmful effect of petroleum products on the bond between aggregate and cement paste and between the SF and matrix, so this led to increase porosity and decrease the strength and density **(Matii 1976) and (AL-Harby 1998)**.
The increase or decrease in density for the reinforced cubes exposed to kerosene or diesel is higher than the density for plain concrete.

FLEXURAL STRENGTH (MODULUS OF RUPTURE)

The result of Flexural strength of concrete mixes (reference and reinforced concrete with different volume fraction of steel fiber (0.5, 0.75 and 1% by volume of concrete) are shown in Tables from (16) to (18) and plotted in Figure from (7) to (9).

The test results show that, the flexural strength is increased as the curing period with water or exposed to kerosene or diesel is increase. The largest increase happens at 120 days of curing are 32.6%, 46.8%, 54% and 57.5% for plain and reinforced concrete using SF with V_f (0.5, 0.75 and 1%) curing with water respectively.

The results show that, the flexural strength of the specimens (with and without SF) exposed to kerosene or diesel increase with the time of exposure and the maximum increase at 120 days of exposure with rates 12%, 32%, 33% and 36% and 19%, 33%, 35% and 37% for plain and reinforced concrete with SF with V_f (0.5, 0.75 and 1%) exposed to kerosene and diesel respectively. The increase in flexural strength of concrete specimens exposed to kerosene and diesel are due to closing and autogenously healing of crack and flaws in concrete due to possible volume change by effect of products. **(Matti 1976)**.

The test results also show that, the Flexural strength of specimens reinforced with SF is greater than the flexural strength of plain concrete specimens, this behavior is due to the increase in crack resistance of the composite and ability of fibers to resist forces after the concrete matrix has cracked. **(Salih et al., 2005).**

CONCLUSIONS

1. The maximum increase percentage in compressive strength for specimens reinforced with SF with V_f (0.5, 0.75, and 1%) and continuously cured in water at 120 days was 9.1, 11.9 and 18.9 respectively as compared with plain concrete.
2. The decreasing or increasing in compressive Strength for specimens reinforced with SF and exposed to kerosene or diesel is better than the plain concrete exposed to same conditions. The percentage increases in compressive strength 3.8, 6.5, and 9.3 and 8, 10.9 and 16.5% at 60 and 120 days for 0.5, 0.75, and 1% Steel Fiber content by concrete volume respectively as compared with plain concrete exposed to kerosene and the

percentage increases in compressive strength 3.9, 5.3 and 8.4% and 6.5, 10.4 and 15% at 60 and 120 days for 0.5, 0.75, and 1% Steel Fiber content by concrete volume respectively as compared to plain concrete exposed to diesel.

3. The density of reinforced specimens cured in water is increased as the percentage of SF increase and the maximum increase was 4.9% when SF 1% is used.
4. The density of the specimens exposed to kerosene or diesel at age 60 days (after curing them in water for 28 days) is higher than the density of those specimens cured in water for the same ages. The maximum increase when used SF 1% is used with rates 0.65% and 0.35% for kerosene and diesel respectively.
5. At 120 days from exposure to kerosene or diesel, the density of the specimens (with and without SF) is decreased.
6. The flexural strength of the prisms cured in water was increased as the curing period increased. The maximum increasing happen at 120 days of curing are 32.6%, 46.8%, 54% and 57.5% for plain and reinforced concrete using SF with V_f 0.5, 0.75 and 1% cured with water respectively.
7. The flexural strength of the prisms (with and without SF) exposed to kerosene or diesel increased with the time of exposure and the maximum increase was at 120 days of exposure with rates 12%, 32%, 33% and 36% and 19%, 33%, 35% and 37% for plain and reinforced concrete using SF with V_f (0.5, 0.75 and 1%) exposed to kerosene and diesel respectively.
8. Flexural strength of prisms reinforced with SF is greater than the flexural strength of plain concrete prisms cured in water or exposure to kerosene or diesel. The maximum increasing percentage in flexural strength was when used 1% SF at 120 days. The rates were 41.8%, 55.6% and 48.5% for water, kerosene and diesel respectively.

REFERENCE

- "**Concrete Storages Structures**", VSL International LTD, Berne / Switzerland**,** May 1983, pp.1-2.
- Abdul-Ahad, R.B. and Mohammed, A.A. "**Compressive and Tensile strength of Concrete Loaded and Soaked in Crude Oil**", Engineering Journal of the University of Qatar, Vol. 13, 2000, pp. 123-140.
- Abed AL-Ameer, S.A,"**Effect of Petroleum products on Steel Fiber Reinforced Concrete**", Ms.c. Thesis, university of Baghdad, December, 2010.
- ACI Committee 211.4R-91 "**Guide for Selection Proportions for High-Strength Concrete with Portland Cement and Fly Ash**", Reported by ACI Committee 211, Reapproved 1998, ACI Manual of Concrete Practice, 2009, pp 2-9.
- ACI Committee 544, 1R-96 "**Report on Fiber Reinforced Concrete**", Reported by ACI committee 544, Reapproved 2002, ACI Manual of Concrete Practice, 2009, pp.9-12.
- AL – Saraj, K.I., "**Strength Characteristics of Plain Concrete Exposed to Oil**". Ms.c. Thesis, Military College of engineering Baghdad, October 1995, pp. 84
- Barros, J.A.O. and Cruze, J.S. "**Fracture Energy of Steel Fiber Reinforced Concrete**", University of Minho, Department of Civil engineering-School of engineer, 1998, pp. 1-19.
- Blaszczynski, T. and Scigallo, J., "**Assessment of ultimate bearing capacity of RC sections affected by mineral oil**", Archives of Civil and Mechanical Engineering, Polish Academy of Science, Wroclaw; 2002, 41 – 56.
- Cement and Concrete Institute "**Fiber Reinforced Concrete**", Published by Cement & Concrete, Midrand. 2010, <http://www.cnci.org.za>

- Chang, C.C., Tsai, C.T., Li, L.S. and Hwang, C.L. "**Durability Design and Application of Steel Fiber Reinforced Concrete in Taiwan**", the Arabian Journal for Science and Engineering, Volume 34, Number 1B, April 2009, pp. 57-79.
- Faiyadth, F.I., "**Bond characteristics of oil saturated concrete**", The Interanational Journal of cement and light weight concrete, Vol.7, No.2, May 1985, pp. 115 – 131.
- Francis, R.A, Mattioli, A. and Smith, S. "**Relining of Potable Water Tanks for Strength and Corrosion Resistance**", Technical paper from the Internet, Corrosion and preventation 2010, pp. 1-9.
- Lea. F.M. **The Chemistry of Concrete**. London, Arnold, 2004, pp.338.
- Matti. M.A. "**Some Properties and Permeability of Concrete in Direct Contact with Crude Oil**" Ph. D. Thesis, University of Sheffield, 1976.
- Meissner, H. and Pearson, J. Discussion of the paper " **Tests of Gasoline – Resistance Coatings**", ACI., Proc. Vol. 15, No. 6, June 1944, pp. 292.
- Mohammed, A.A., "**Properties of Crude Oil Soaked Concrete Exposed to Loading**" Ms.c. Thesis, University of technology, April 1997, pp.94.
- Nemati, K.M. "**Progress in Concrete Technology, Fiber Reinforced Concrete FRC**", University of Washington, Spring Quarter, 2010
- Neves, R.D. and Fernades de Alameida J.C. "**Compressive Behavior of Steel Fiber Reinforced Concrete**", Structural Concrete Journal, No.1, 2006.
- Neville, A.M. and Brooks, J.J. **Properties of Concrete**, Second Edition, England, 2010, pp.317, 403.
- Rashed, L. "**Behavior of Fiber Reinforced Concrete Exposed to Oil**" M.Sc. Thesis, University of technology Baghdad, 1998.
- Salih, S.A., Rejeb, S.K. and Najem, K. B. "**The Effect of Steel Fibers on Mechanical properties of High Performance Concrete**", Al-Rafidain Engineering, Vol.13, No.4, 2005, pp. 26-44.
- Shepard, E. R., "**Concrete Tanks for Military Use**", ACI Journal, proc. Vol. 15, N0. 5, April 1944, pp. 429-439.
- Shetty, M.S. **Concrete Technology**, India, 2000, pp.526-531.
- Snyder, M. J. and Lankard, D. R., " **Factors Affecting the Flexural Strength of Steel Fibrous Concrete**", ACI journal, Vol. 69, No. 1, January 1972, p.p 96- 100
- Spamer, A. M., "**Navy Installations of Protective Linings for Prestressed Concrete Tanks Containing Liquid Fuels**", ACI. Journal, Proc. Vol. 15, No. 5, April 1944, pp. 417-428.
- المواصفات العراقيه، المواصفه القياسيه رقم 5 "**السمنت البورتلاندي**"، الجهاز المركزي للتقييس والسيطره النوعيه، بغداد، 1984 .
- المواصفات العراقيه، المواصفه القياسيه رقم 45 "**ركام المصادر الطبيعيه المستعمل في الخرسانه وفي البناء**"، الجهاز المركزي للتقييس والسيطره النوعيه، بغداد، 1984 .
- الحربي، موفق جاسم **"تأثير المشتقات النفطيه على المنشأت"**، المركز القومي للمختبرات الانشائيه ، مديريه البحوث والشوؤن الفنيه، بغداد، تموز 1998.

Table (1) Physical Properties of Cement

Physical properties	Test result	Limits of Iraqi spec. No. 5/1984
Fineness (Blaine Specific surface (m^2/kg))	290	≥ 230
Time of Setting (Vicat test) Initial Set (hrs : min) Final Set (hrs : min)	1 : 48 4 :27	0 : 45 (min) 10 : 00 (max)
Compressive Strength (MPa) 3 Days 7 Days	20.6 31.8	15.00 (min) 23.00 (max)

Table (2) Chemical Analysis and Composition of Cement

Compound composition	Percentage by weight	I.O.S.5: 1984: limits
CaO	58.98	--------
SiO_2	19.74	--------
Al_2O_3	3.72	--------
Fe_2O_3	3.54	--------
SO_3	2.73	Max.2.8%
MgO	3.78	Max. 5%
Na_2O	0.22	--------
K_2O	0.67	--------
Loss On Ignition (L.O.I)	3.46	Max.4%
L.S.F	0.92	(0.66-1.02)
Insoluble Residue (I.R)	0.74	Max.1.5%
Bogue Potential Compound Composition, %		
C_3S	52.26	---------
C_2S	17.17	---------
C_3A	3.87	---------
C_4AF	10.77	---------

Table (3) Grading Analysis of Fine Aggregate.

Sieve size (mm)	Accumulated percentage passing (%)	Limit of Iraqi specification

		No. 45/1984 (Zone 1)
9.50	100	100
4.75	90	90 – 100
2.63	71	60 – 95
1.18	51	30 – 70
0.60	30	15 – 34
0.30	9	5 – 20
0.15	1.2	0 – 10

Table (4) Properties Fine Aggregate

Property	Results	Iraqi specification limits I.O.S 5/1984
Grading Zone	First	------
Fineness Modulus	2.56	------
Apparent Specific Gravity	2.58	------
Bulk Density(Kg/m^3)	1670	-----
Absorption %	3	------
Sulfate Content (SO_3) %	0.21	≤ 0.5

Table (5) Grading Analysis of Coarse Aggregates.

Sieve size mm	percentage passing (%)	Limit of Iraqi specification No. 45/1984
37.5	100	100
20	100	95-100
10	42	30-60
4.57	2.1	0-10

Table (6) Properties of Coarse Aggregate

Property	Results	Iraqi specification limits I.O.S.5/1984
Apparent Specific gravity	2.6	……..
Absorption	0.68%	……
Sulfate content (SO_3)	0.05%	Max. 0.1%
Finer than sieve No.200 (75 μm)	2.2%	Max. 3%
Bulk Density (kg/m^3)	1600	……

Table (7) Properties of used Steel Fibers.

Property	Specification
Density	7860 kg/m^3
Ultimate strength	1500 MPa
Modulus of elasticity	2 *10^5 MPa
Poisson's ratio	0.28
Length	50 mm
Diameter	0.5 mm
Aspect ratio	100

Table (8) Properties of Kerosene and Diesel

Oil Inspection Data	Kerosene Results	Diesel Results
Moisture content% by volume	0%	0%
Sulfur content% by weight	0.31%	0.8%
pH	7.6	6.3
Specific gravity (gm/cm^3) at:		
20C°	0.784	0.829
25C°	0.708	0.825
30C°	0.777	0.821
35C°	0.774	0.817
40C°	0.770	0.813

Viscosity (centipoises) at:		
20C°	1.185	4.635
25C°	1.092	3.960
30C°	1.019	3.570
35C°	0.935	3.257
40C°	0.855	2.943

Table (9) The mix proportion of concrete according to ACI (211-91).

The materials	The mix proportion Kg/m^3
Water	228
Cement	422
Coarse aggregate	768
Fine aggregate	807

Table (10) Results of Compressive Strength (MPa) of Concrete Mixes cured in Water.

No.	Mixes	Age (Days)			
		30	60	90	120
1	Ref.	35.9	42.5	44.52	49.51
2	Mix.0.5	37.93	45.75	48.12	54.02
3	Mix.0.75	39.3	46.85	49.5	55.41
4	Mix.1	39.7	47.6	52.15	58.78

Table (11) Results of Compressive Strength (MPa) of Concrete Mixes exposed to Kerosene.

No.	Mixes	Age (Days)		
		60	90	120
1	Ref.	39	42	41
2	Mix.0.5	40.5	45	42.12
3	Mix.0.75	41.53	45.98	43.25
4	Mix.1	42.62	47.12	46.17

Table (12) Results of Compressive Strength (MPa) of Concrete Mixes exposed to Diesel.

No.	Mixes	Age (Days)		
		60	90	120
1	Ref.	38.45	41.43	38.87
2	Mix.0.5	39.95	43.95	40.98
3	Mix.0.75	40.5	44.85	42.5
4	Mix.1	42.65	46.25	43.76

Table (13) Results of density (kg/m^3) for concrete specimens cured in water.

No.	Mixes	Age (Days)			
		30	60	90	120
1	Ref.	2375	2417	2438	2453
2	Mix.0.5	2390	2458	2477	2519
3	Mix.0.75	2418	2471	2497	2540
4	Mix.1	2429	2495	2530	2574

Table (14) Results of density (kg/m^3) for concrete specimens exposed to kerosene.

No.	Mixes	Age (Days)		
		60	90	120
1	Ref.	2395	2412	2402
2	Mix.0.5	2420	2448	2437
3	Mix.0.75	2433	2468	2454
4	Mix.1	2445	2485	2478

Table (15) Results of density (kg/m^3) for concrete specimens exposed to diesel.

No.	Mixes	Age (Days)		
		60	90	120
1	Ref.	2389	2406	2396
2	Mix.0.5	2417	2443	2430
3	Mix.0.75	2426	2463	2440
4	Mix.1	2435	2479	2463

Table (16) Results of Flexural Strength (MPa) of Concrete Specimens Cured in Water.

No.	Mixes	Age (Days)			
		30	60	90	120
1	Ref.	2.94	3.44	3.45	3.9
2	Mix.0.5	3.35	4.21	4.5	4.92
3	Mix.0.75	3.5	4.45	4.72	5.4
4	Mix.1	3.65	4.6	4.98	5.72

Table (17) Results of Flexural Strength (MPa) of Concrete Specimens Exposed to Kerosene.

No.	Mixes	Age (Days)		
		60	90	120
1	Ref.	3.21	3.55	3.6
2	Mix.0.5	3.5	4.45	4.65
3	Mix.0.75	3.88	4.62	5.1
4	Mix.1	4.2	4.82	5.65

Table (18) Results of Flexural Strength (MPa) of Concrete Specimens Exposed to Diesel.

No.	Mixes	Age (Days)		
		60	90	120
1	Ref.	2.98	3.48	3.57
2	Mix.0.5	3.46	4.39	4.61
3	Mix.0.75	3.6	4.57	4.85
4	Mix.1	3.85	4.75	5.3

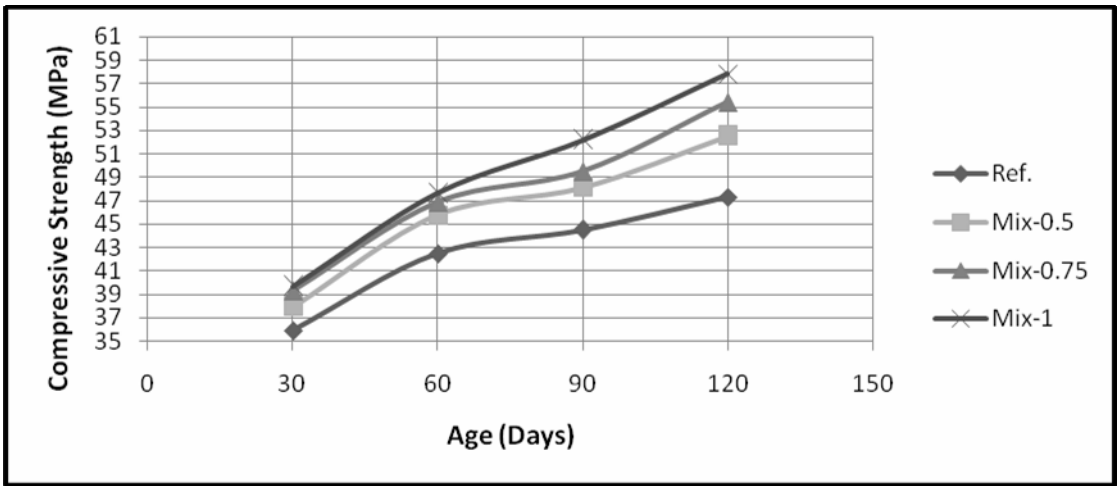

Figure (1) Effect of Steel fiber content on compressive strength of concrete cured in water.

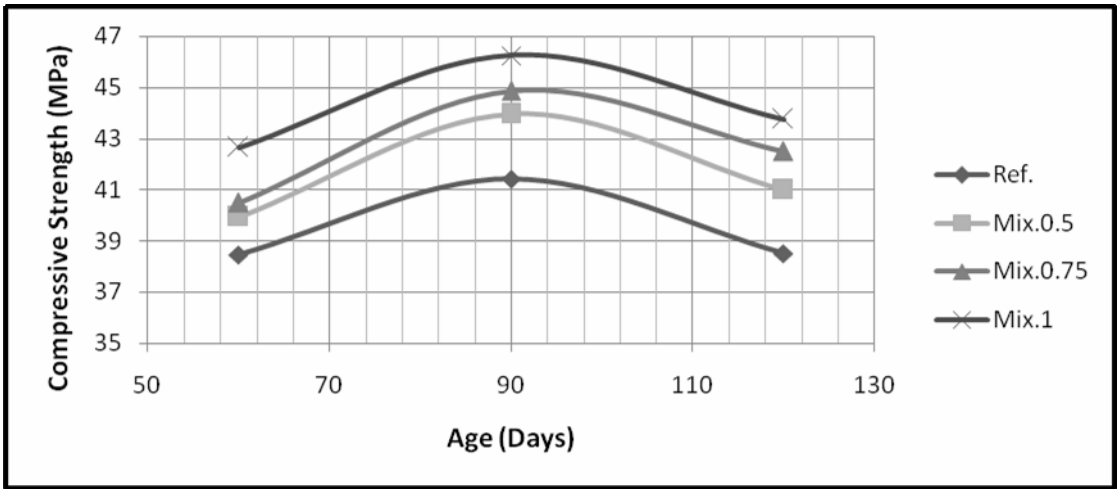

Figure (2) Effect of Steel fiber content on compressive strength of concrete exposed to Kerosene.

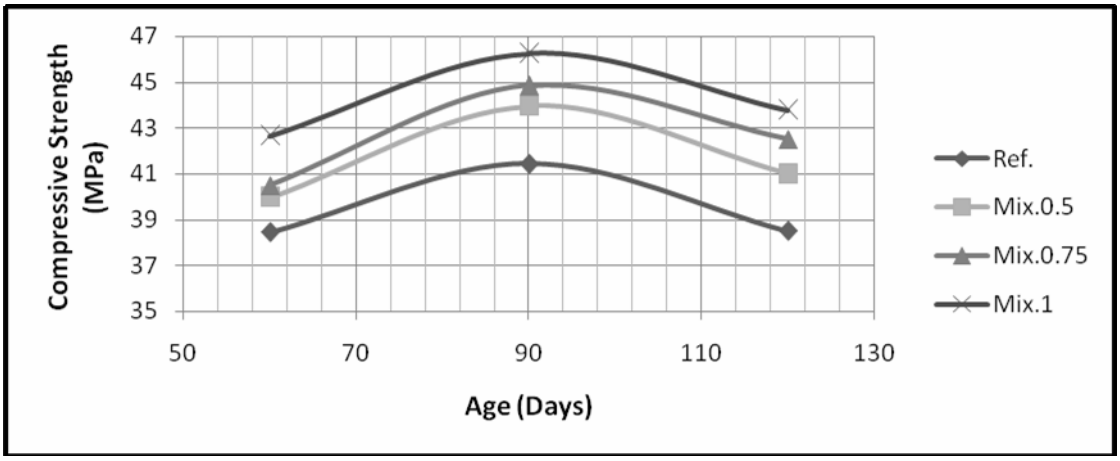

Figure (3) Effect of Steel fiber content on compressive strength of concrete exposed to Diesel.

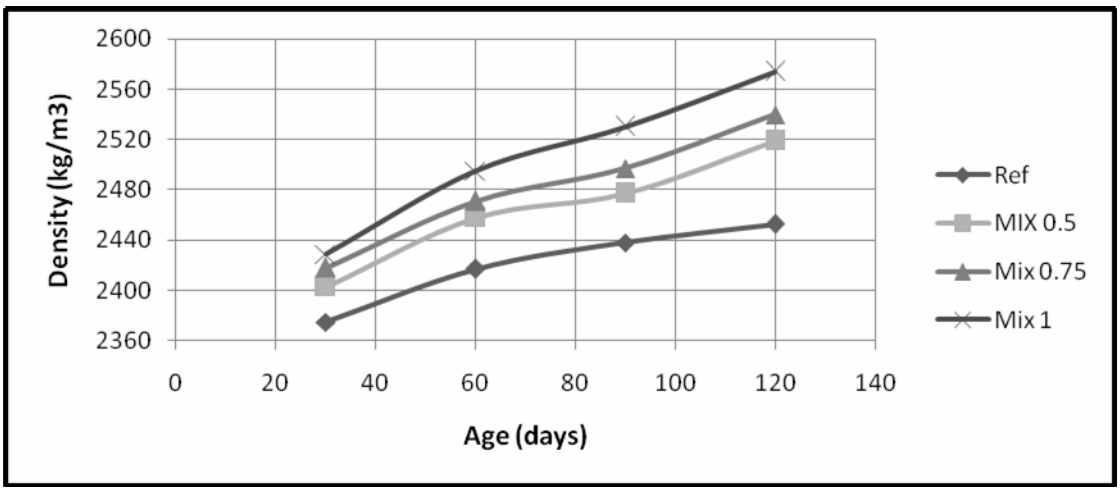

Figure (4) Effect of Steel fiber on density of concrete cured in water.

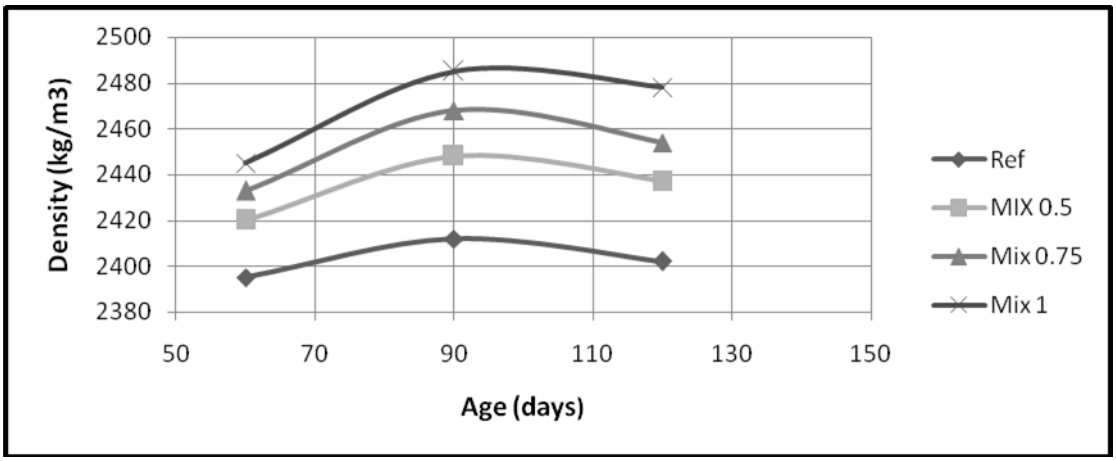

Figure (5) Effect of Steel fiber on density of concrete exposed to Kerosene.

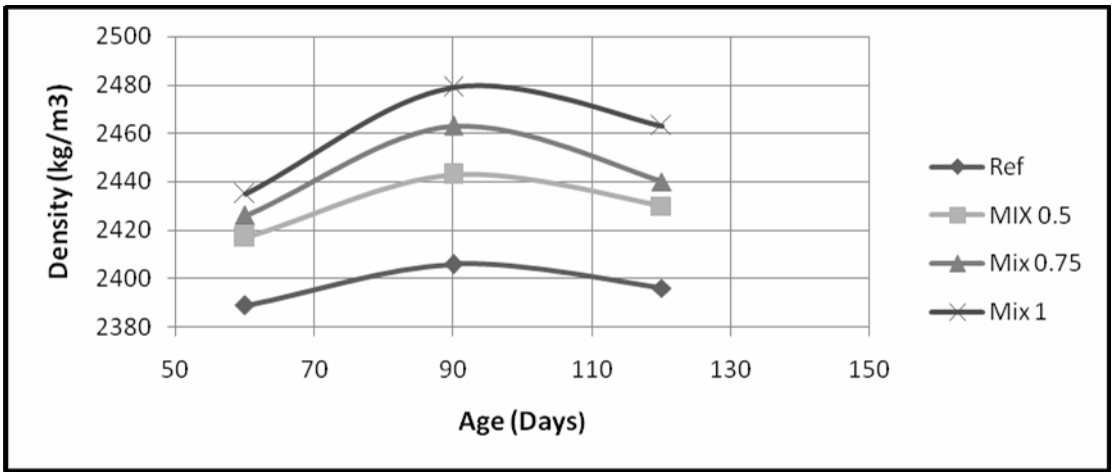

Figure (6) Effect of Steel fiber on density of concrete exposed to Diesel.

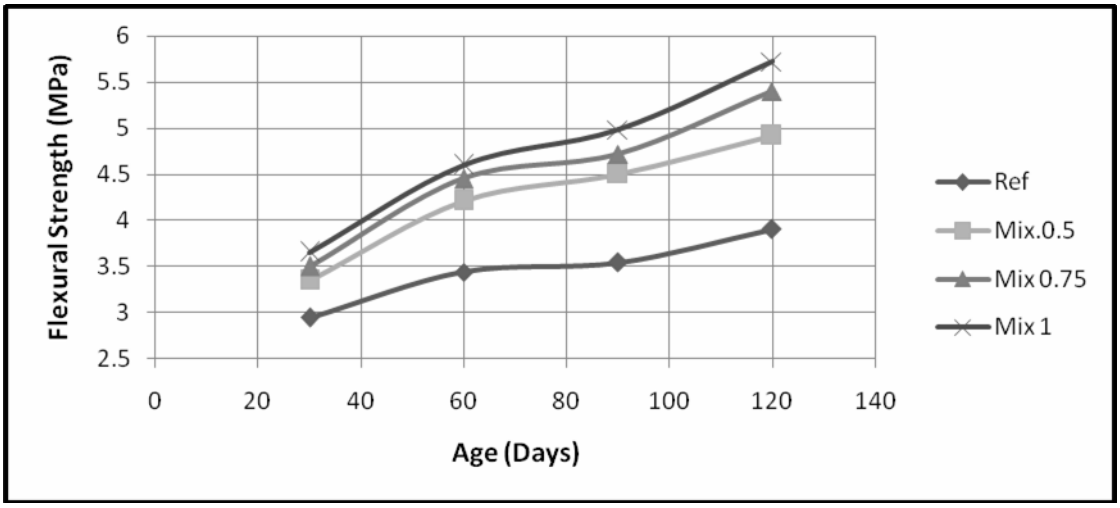

Figure (7) Effect of Steel fiber contents on Flexural Strength of concrete cured in water.

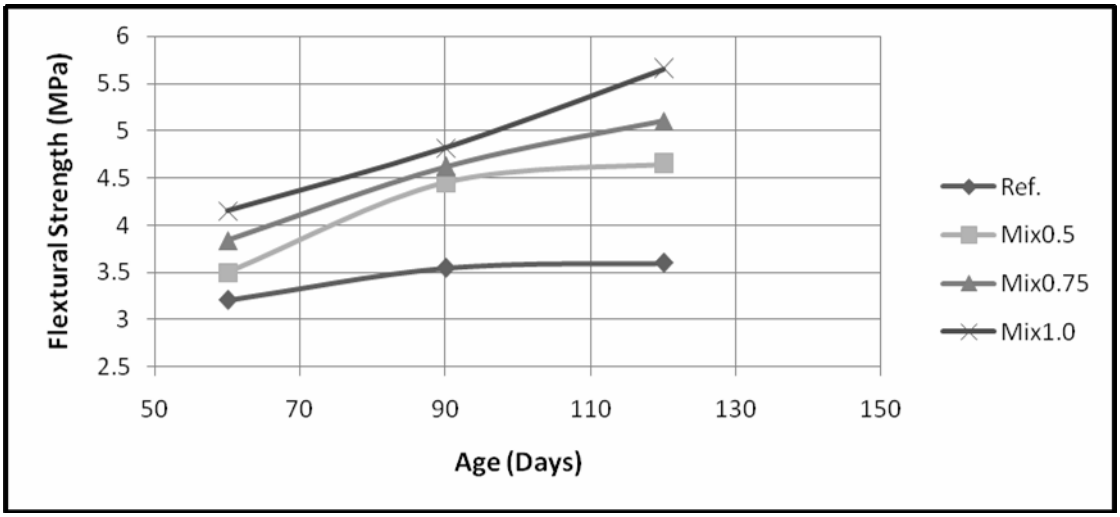

Figure (8) Effect of Steel fiber on Flexural Strength of concrete exposed to kerosene.

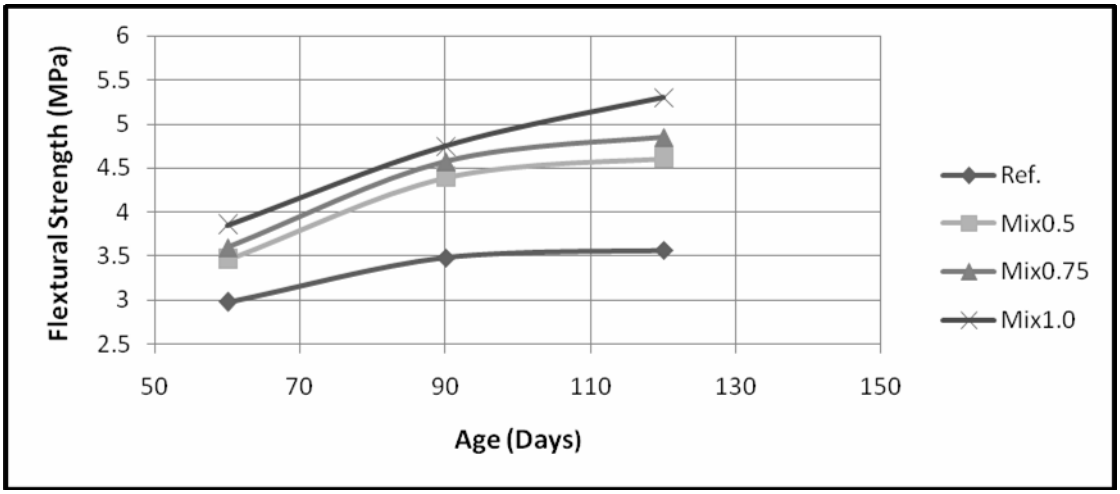

Figure (9) Effect of Steel fiber on Flexural Strength of concrete exposed to Diesel.

Effect of the Iranian Seperation Dikes on the Water Salinity Patterns Within Al Huweizah Marsh

Dr.Mahmoud Saleh Mahdi Al Khafaji
mahsal@hotmail.com
Building and Construction Eng. Dept., University of Technology/Baghdad-Iraq

ABSTRACT
Al Huweizah Marsh is considered as the largest marsh at the southern part of Iraq. About one third of the marsh is located within the Iranian territory. Iran began to construct earth dikes along the Iraqi-Iranian international borders to separate the Iranian part of the marsh.
The electrical conductivity, EC, value was adopted to be the indicator for the water salinity within the marsh. A steady two-dimensional water quality routing model was implemented by using the RMA2 and RMA4 softwares within the SMS computer package to estimate the distribution of the EC values within the marsh seasonally during the wet, moderate and dry water years. The EC distribution Patterns were estimated considering the expected two cases of the marsh future hydrological and geometrical conditions of the marsh, Case 1: without existence of the earth dikes and Case2: with the existence of the earth dikes.
The estimated distribution patterns of EC values showed that the construction of the earth dikes, Case2, deteriorate the water salinity within most of the Iraqi part of the marsh during the four seasons of the wet, moderate and dry water years. During the wet and moderate years, the EC values are greater than the maximum allowable limits within most of the Iraqi part of the marsh except small portions near the outfall of the Iraqi feeders of the marsh and the lower portion of the southern part of the marsh during winter of the moderate years. While during the four seasons of the dry years, the marsh water is stagnant and the EC values are much greater than the maximum allowable limits.

Key Words: Separation dikes, water quality, distribution patterns, SMS, RMA, Al Huweizah.

تأثير السدة الايرانية الفاصلة على انماط توزيع ملوحة المياه في هور الحويزة

الخلاصة
يعتبر هور الحويزة اكبر الاهوار في جنوب العراق. ما يقارب ثلث من مساحة هور الحويزة يقع ضمن الاراضي الايرانية. بدأ الجانب الايراني بأنشاء سداد ترابية على طول الحدود الدولية العراقية-الايرانية لفصل جزء الهور الواقع ضمن الاراضي الايرانية. تم اعتماد قيمة التوصيلية الكهربائية كمؤشر لنوعية المياه داخل الهور. تم اعداد نموذج للجريان الثابت ثنائي البعد لإستتباع ملوحة المياه بإستخدام البرامج RMA4, RMA2 ضمن الحقيبة البرمجية SMS لإيجاد انماط توزيع قيم التوصيلية الكهربائية داخل الهور فصلياً خلال السنوات الفيضانية والمعتدلة والجافة لحالتي الهور المتوقعة مستقبلاً من الناحية الهيدرولوجية وتغير حدود الهور، الحالة الاولي: بدون وجود السداد الترابية والحالة الثانية: مع وجود السداد الترابية.
بينت انماط توزيع قيم التوصيلية الكهربائية التي تم ايجادها إن إنشاء السداد الترابية (الحالة الثانية) يؤدي الى تدهور نوعية مياه الهور في معظم مساحة الجزء العراقي من الهور خلال الفصول الاربعة للسنوات الفيضانية والمعتدله والجافة. خلال السنوات الفيضانية والمعتدلة تكون قيم التوصيلية الكهربائية اكبر من الحد الاعلى للقيم المسموح بها في معظم مساحة الجزء العراقي من الهور ماعدا أجزاء صغيرة بالقرب من مصبات المغذيات العراقية في الهور وفي القسم السفلي من الجزء الجنوبي من الهور خلال فصل الشتاء في السنوات المعتدلة. في حين تكون مياه الهور راكدة وقيم التوصيلية الكهربائية اكبر بكثير من الحد الاعلى للقيم المسموح بها في كل مساحة الهور خلال الفصول الاربعة في السنوات الجافة.

INTRODUCTION

Al Huweizah Marsh, **Fig. 1,** is considered as the largest marsh at the southern part of Iraq. It is located at the east side of Tigris River at Maissan and Al Basrah Governorates. The eastern part of this marsh (about one third of the total area) is located beyond the Iranian borders.

The main water resources of Al Huweizah Marsh, **Fig. 1**, can be classified into two types depending on the existence of water control structures. The first, controlled feeders, are Al Msharah, and Al Ka'hla Rivers which are sharing the same intake located north of Al Amarah Barrage on Tigris River and controlled by head regulators located upstream of each river. The second, uncontrolled feeders are Al Karkheh River and AsSanna'f Marsh, which are feed by AtTeeb, Dwayreach, Kmait Rivers, the surface runoff of AShama'ashir area and the drain water of Sa'ad River irrigation project.

The main discharge outlets of Al Huweizah Marsh are Al Kassara and AsSwaib Rivers.

Al Kassara River water is discharged to Tigris River through two sets of pipes. These pipes will be replaced by a control structure with a design discharge of 125m^3/sec. AsSwaib River flows from the southern part of Al Huweizah Marsh and directly outfalls in Shat Al Arab River with an average flow of 600 m^3/sec. A control structure with a design discharge of 200m^3/sec has been designed to control the outflow of this river into Shat Al Arab River (Ministry of Water Resources, el. at 2007).

Agricultural and industrial projects are constructed and developed along the two sides of Al Karkheh River within the Iranian territories. The river was dammed and finally earth dikes were proposed to construct along the Iraq- Iran boundary to separate the Iranian part of the marsh. This will affect the ecological system of the marsh because the ecology of Al Huweizah Marsh is closely related to the inflowing freshwater resources from Al Karkheh River.

The Iranian border dike (presently under construction) crosses through the marsh and bisects the existing marsh into two parts, thus Al Azim Marsh (in Iran) is functioning as a single isolated marsh. The presuming dike elevation is 6m a.m.s.l. (UNEP and IRAN, 2004). The reduced flowing water from Al Karkheh River into the marsh, using of Al Karkheh River water for irrigation of the nearby areas and the drainage of extra water into the marsh will deteriorate the water quality of the marsh.

Hyder A. Al Thamiry, 2009, developed a hydrological routing model to evaluate the hydrological effect of constructing this proposed dike on the Iraqi part of Al Huweizah Marsh during wet, moderate and dry water years.

This research aims to evaluate the effect of the proposed Iranian separation dike on the water quality distribution of Al Huweizah Marsh based on the results of the hydrological routing model that was developed by Hyder, 2009. A steady two-dimensional hydraulic model was implemented using the SMS software to evaluate this effect.

TOPOGRAPHY OF THE MARSH

A Digital Elevation Model (DEM) of the whole marsh area and of the Iraqi part of the marsh, **Fig. 2**, was developed using the topographical survey carried out for the Iraqi part of Al Huweizah Marsh using the ultra sound device, Ministry of Water Resources-CRIM, 2007, the topographical map of the Iranian part of the marsh which was presented by UNEP (UNEP and IRAN, 2004) and with the combined support of various maps and satellite images.

HYDROLOGICAL STATE OF THE MARSH

According to the expected hydrological and geometrical future condition of the marsh the hydrological state of the marsh can be classified into two cases:

Case1: The expected future condition of the marsh with the existence of the outlet control structures (Al Kassarah and AsSwaib) and without existence of the dikes, the marsh area will be considered as one unit, and the proposed outlet control structures.

Case2: The expected future condition of the marsh with the existence of the presumed dike and outlet control structures. Assuming the marsh will be bisected into Iraqi and Iranian parts.

A schematic diagram for the hydrological interference between the Iraqi Part and the functional and degraded Iranian part of the marsh is shown in **Fig. 3**.

Based on the results of the hydrological routing (Hyder, 2009) the seasonal inflow discharges of the marsh feeders and the water surface elevation within the marsh for the wet,

moderate and dry water year were estimated for the two cases and listed in T**able 1**.

WATER QUALITY OF THE MARSH

The water quality within Al Huweizah Marsh varies with time depending on the source of water and whether the water passes urban areas. Except the dissolved Oxygen, DO, the electrical conductivity, EC (or TDS), all other contaminants are about within the acceptable limits for drinking water standards. The maximum recorded EC at Al Msharah River, AzZubair River, Um AtToos River, Al Husa'chi River, Al Kassara River, and AsSwaib River stations is slightly higher than the acceptable limit. While the maximum recorded Ec at AsSanna'f Marsh outfall , AtTeeb River, Dwayreach River, Kmait River, and Sa'ad Drain let stations was 9000 µS/cm and to be higher than the acceptable limit in most of the measurements (Ministry of Water Resources-CRIM, 2007).

Available information on Karkheh River water quality was restricted to total dissolved solids (TDS), pH, Electrical conductivity (EC), anions and cations for the main stations UNEP and IRAN, 2004. The electrical conductivity (EC) of the water was adopted to be the indicator of the water salinity. This parameter is adopted because it gives indication about the concentration of TDS and because of the availability of recorded data concerning this contaminant.

The distribution patterns of EC within the marsh area are studied according to the recorded data of the Iraqi feeders and the available data of Al Karkheh River. The water quality of Tigris River was adopted for the Iraqi feeders of the marsh. The available averaged values for the EC of Al Karkheh River at the Marsh inlet will be adopted for wet, Moderate and dry years.

Since there is no predicted data of any contaminant within the two Iranian part of the marsh, the functional and degraded Iranian marshes, the EC of Kmait Flood Escape station (E: 705094, N: 3539729) was adopted to simulate the future EC of these marshes. The main points of similarity between the selected station and the marshes are:

- Kmait flood escape is like a blind drain since the inflow into this escape is from Sa'ad irrigation project and during Moderate and dry years no water will be spilled into Al Huweizah marsh through AsSanna'f Marsh. This behavior is similar to that of the Functional and Degraded Iranian marshes.
- The evaporation and precipitation are approximately equal to that of the Iranian side of the marsh.

The maximum recorded value of EC in Kmait flood escape was adopted to be the EC value of the functional and degraded Iranian marshes during the Moderate water year while the average of the EC values was used for the wet year. Since the results of the hydrological routing, Hyder A. Al Thamiry, show that after construction of the proposed separation dike there will be no flow from the Iranian part of the marsh to the Iraqi part of the marsh during the dry year. The adopted values of EC for wet, Moderate and dry water years of each feeder for the two cases are listed in **Table 2**.

STEADY TWO –DIMENSIONAL WATER QUALITY MODEL

A steady two-dimensional water quality model has been implemented by using the RMA4 model within the SMS computer package (Brigham Young University-USA, 2009) to simulate the water quality distribution within the marsh.

It is a finite element water quality transport numerical model in which the depth concentration distribution is assumed uniform. It computes concentrations for up to 6 constituents, either conservative or non-conservative, within the one-and/or two-dimensional computational mesh domain. The water quality model, RMA4, is designed to simulate the depth-average advection-diffusion process in an aquatic environment.

The RMA4 model requires an RMA2 model within the same package which is a two-dimensional depth averaged finite element hydrodynamic numerical model to be implemented first. It computes water surface elevations and horizontal velocity components for sub critical, free surface two-dimensional flow fields.

The results of the RMA2 model, water depth, water surface and velocity pattern, will be the input data for the finite element water quality transport numerical model, RMA4 model.

RMA2 MODEL

RMA2 model computes a finite element solution of the Reynolds form of the Navier-Stokes equations for turbulent flow. Friction is calculated with the Manning's or Chezy equation, and eddy viscosity coefficients are used to define turbulence characteristics.

According to the considered two cases of the marsh future condition, **Fig. 2**, a triangular finite element mesh of the whole marsh has been developed over an area approximately 1800 km^2, where the area of the Iraqi part is about 1300 km^2. These meshes are built using an "adaptive tessellation" technique.

The developed Digital Elevation Model (DEM), **Fig. 2,** of the whole marsh area and the Iraqi part of the marsh was used to be the topographical data that are required to develop these models. These data were sampled onto the computational nodes of the mesh using inverse weighted interpolation scheme. Slope adjustments were necessary at some locations such as the banks of the main canals inside the marsh. This modification helps model solution stability. The eddy viscosity must be assigned to allow the model to solve the equations. As typical for all finite element models, the eddy viscosity affects stability and turbulent fluid characteristics. During the model preparation, a solution was prepared for a range of eddy viscosities to investigate the model's sensitivity. Ultimately, two different techniques were adopted in the definition of the eddy viscosity number. The first specifies directly an eddy viscosity value and the second let the model automatically compute an appropriate value via the "automatic Peclet number". The Peclet number is defined by the following equation:

$$Peclet = \frac{\rho u\, dx}{E} \qquad (1)$$

Where ρ is the fluid density, u is the average element velocity, dx is the length of the element in the stream wise direction and E is the eddy viscosity.

Both definitions of the eddy viscosity were used within the model and the model was let to decide the more appropriate method to be used. Wetting and drying parameters had to be specified as part of the geometry. The complete definition of the model geometry requires friction factors to be assigned at each mesh element. The friction factors of the soil were divided into four values corresponding to the four soil zones which were classified according to the water depth and the existence of plants within the marsh area using the available satellite images and site visits, these values are listed in T**able 3** and shown in **Fig. 4**. It is to be noticed that the friction factor for water depth less than 2 m is listed in this table. When the water depth within the marsh is deeper the factor will be adopted as 0.07 for all soils (Brigham Young University-USA, 2009).

RMA2 MODEL BOUNDARY CONDITIONS

As previously mentioned, there are two hydraulic models; the first is of the whole marsh area and the second for the Iraqi part. The downstream boundary conditions for both models are the same which are Al Kassara and AsSwaib Rivers while the difference in the upstream boundary conditions is the feeding water that flow into the marsh from Al Karkheh River. The reason of this difference is the existence of the proposed separation Iranian dike that will prevent the incoming water from Al Karkheh River to flow into the Iraqi part, when the water levels within the Iranian part is lower that 6 m.a.s.l. The water will spill over this dike when the water level exceeds 6 m.a.s.l.

Al Huweizah Marsh has five inlets, as shown in **Fig. 5**:

- Al Karkheh River, within the Iranian borders, which is divided into three tributaries when joining Al Huweizah Marsh, was treated as a one source point. This feeder will be replaced by a line source along the Iraq-Iran border that represents the inflow into Iraqi part of the marsh from Functional and Degraded Iranian.
- AsSanna'f Marsh and Al Msharah River outfall were treated as a one source point since Al Msharah River flows into AsSanna'f Marsh before AsSanna'f Marsh outfall at Al Huweizah Marsh.
- Um AtToos River outlet.
- Al Husa'chi River outlet.
- AzZubair River outlet.

The marsh has two outlets as shown in **Fig. 5**:

- Al Kassara River
- Al AsSwaib River.

The upstream boundary conditions are constant inflow from each feeder for the two cases

while the down stream boundary condition is the water surface elevations at the marsh outlets for the two cases. Results of Hyder, 2009 hydrological routing study, T**able 1**, were adopted to be the boundary conditions for the RMA2 model of the two cases.

RMA4 MODEL

Geometric data of the RMA2 model and results of applying this model for the two cases, Case 1 and Case 2, seasonally for the wet, moderate and dry water years were the data base of the RMA4 (a finite element water quality transport numerical model in which the depth concentration distribution is assumed uniform).

DIFFUSION COEFFICIENT

In the RMA4 model the diffusion coefficient (D) can be specified either manually based on the previous studies or automatically using Peclet number. In this research the diffusion coefficient was specified automatically by using Peclet number.

The model automatically adjusts D after each time step, based upon a provided Peclet number, depending upon the element size and calculated velocity within each element. The Peclet methodology is very similar to that of RMA2. The Peclet number is a dimensionless parameter. However, for RMA4, the Peclet number (P) takes the form (Brigham Young University-USA, 2009).

$$P = \frac{udx}{D} \qquad (2)$$

hence

$$D = \frac{E}{\rho} \qquad (3)$$

Where

P : Peclet number (unit less)

ρ : Fluid density (kg/m^3)

u : average elemental velocity calculated at the guess points (m/sec)

E : Eddy Viscosity for RMA2

D: diffusion coefficient for RMA4 (m^2/sec)

dx=length of element (m)

RMA4 MODEL BOUNDARY CONDITIONS

As has been previously mentioned, there are two hydraulic models and two water quality models; the first couple of models are of the whole marsh area and the second are of the Iraqi part of the marsh.

The upstream boundary conditions are the EC values (electrical conductivity) of the inflow water from each feeder**, Table 2**.

No Downstream boundary conditions are needed since the diffusion coefficient is auto-calculating and the results were compared with that of seasonal observation in Moderate year.

RESULTS

Results of applying the RMA4 model for the EC during the four seasons, Autumn, Winter, Spring and Summer for the Wet, Moderate, and Dry water years for **Case1** and **Case 2**, are shown in **Figs. 6** to **17,** these figures show the seasonal variations in the distribution of the EC within the marsh and the effect of constructing the presuming dike on the values and distribution of this contaminant. These results give a good explanation for the effect of constructing the presuming dike on the water quality of the marsh.

These results show that construction of the presuming dike causes the following:

1- Wet water year:

a. Autumn: The value of EC will increase within the Iraqi part of the marsh. The value of EC will be greater than the maximum acceptable limits of the international specification for drinking and agricultural uses (WHO, 2008 and FAW, 1994) 2500µs/cm, in the Southern zone of the marsh. This is due to ceasing of the flow from Al Karkheh River.

b. Winter: The value of EC will increase within the Iraqi part of the marsh due to ceasing of the flow from Al Karkheh River, but the increase of inflow discharge of the Iraqi feeders reduces this effect. The value of EC will increase to greater than 2500µs/cm in the lower part of the Southern zone of the marsh.

c. Spring: In this season the inflow from the Functional and Degraded parts of the marsh start to flow into the Iraqi part of the marsh this causes increase in the value of EC within the Iraqi part of the marsh especially in the

Eastern zone of this part where EC will be greater than 2500µs/cm. Furthermore; existence of Ajerda dike, **Fig. 5**, obstructing the flow into the southern zone of the marsh and impounding the bad quality water above this dike.

d. Summer: In this season the inflow from the degraded part of the marsh will stop while that of the Functional part will be continued and the inflow from the Iraqi feeders of the marsh will decrease. So, the value of EC will increase especially in the northern zone of the Iraqi part of the marsh where EC will be greater than 2500µs/cm.

2- Moderate water year:

a. Autumn: Ceasing of Al Karkheh River flow into the marsh in this season causes increase in the EC value within most of the marsh area, EC>2500µs/cm, except a small zone near the outfalls of the Iraqi feeders of the marsh.

b. Winter: The value of EC will increase within the Iraqi part of the marsh due to ceasing of the inflow from Al Karkheh River, but the increase of inflow discharge of the Iraqi feeders reduces this effect. The value of EC will increase to 2000µs/cm in the lower part of the Southern zone of the marsh. This value is within the acceptable limit.

c. Spring: In this season the drainage water from the Iranian agricultural areas start to inflow from the Functional part of the marsh into the Iraqi part of the marsh. This causes increase in the EC value within most of the marsh area, EC>2500µs/cm, except a small area near the outfalls of the Iraqi feeders of the marsh and a small area in the southern zone of the marsh. Furthermore; existence of Ajerda dike, **Fig. 7**, obstructing the flow into the southern zone of the marsh and impounding the bad quality water above this dike and this increases the EC value to greater than 6500 µs/cm in the middle zone of the marsh.

d. Summer: In this season the inflow from the Functional part of the marsh decreases and its effect extends as a strip along the dike and near Ajerda dike where EC>2500 µs/cm.

3- Dry water year:

a. Autumn: In this season, ceasing of Al Karkheh River flow into the marsh and decreasing the flow from the Iraqi feeders cause decrease in the water depth of the marsh and then the flow within the marsh will stop. The EC value will be greater than 3200 µs/cm within most of the marsh area.

b. Winter: Ceasing of Al Karkheh River inflow into the marsh in this season causes increase in the EC value, EC>3200 µs/cm within the whole marsh area.

c. Spring: Although there is a difference in the water depth within the marsh area during Winter and Spring, but the values of EC in this season are similar to that of Winter. This is because the marsh is fed completely from the Iraqi feeders

d. Summer: In this season the inflow from the Iraqi feeders will decrease and there is no flow from Al Karkheh River So, the value of EC will increase to more than 4500 µs/cm within the whole marsh area.

CONCLUSIONS

Al Karkheh River is one of the most important feeding sources of the marsh. Constructing the presuming dike decreases the marsh area and the inflow discharges that are vital to conserve expediential water depth within the marsh and to insure suitable flow within the marsh with suitable water quality distribution patterns.

Constructing the Iranian separation dike and discharge the drainage water of the nearby agricultural project into the Iranian part of the marsh and then into the Iraqi part of the marsh during the wet years deteriorates the water quality of the marsh. The EC will be greater than the maximum acceptable limits within most of the marsh area during the four seasons of the wet and moderate year.

During winter in the moderate years, the increase of inflow discharges of the Iraq feeders reducing this effect. Therefore, the value of EC in the lower part of the Southern zone of the marsh will be within the acceptable limit. During the dry years, cease of Al Karkheh River inflow into the marsh synchronous with the decrease of inflow discharge from the Iraqi feeders. This causes decrease in the water surface elevation and marsh area and ceases the flow within the marsh. The marsh water will be stagnant and the EC values will be much greater than the maximum allowable limits.

To prevent the deterioration of the ecological system of the Iraqi part of the marsh, the inflow discharge into the marsh from the controlled Iraqi feeders, Al Msharah and Al Ka'hla, must be

increased to preserve the concentrations of water contaminants within the acceptable limits and to prevent any losses from the area of the Iraqi part of the marsh, the chocking in water flow due to Ajerda dike must be removed, hydrological and water quality monitoring stations must be constructed within the marsh and on all the feeders and outlets of the marsh and the pollution sources which affect the marsh ecological system must be studied.

REFERENCES

Brigham Young University, USA, 2009, "SMS Manual, Environmental Modeling Research Laboratory".

FAO: Ayres, R. S. and D. W. Westcot. 1994. Water Quality for Agriculture. FAO Irrigation and Drainage Paper 29 Rev 1.

Hayder A. Al Thamiry, 2009 "Hydrological Damage of Iranian Separation Dike on the Iraqi Part of Al Huweizah Marsh". The 6th Engineering Conference/ College of Engineering/ Baghdad University (5-7 April 2009) Vol. V, P112-126, April 2009.

Ministry Of Water Resources, Ministry Of Environment, Municipalities And Public Works Iraq And Italian Ministry For The Environment, Land And Sea, 2007, " The New Eden Project - Master Plan For Integrated Water Resources Management In The Marshlands Area"; Outlet Of The Huweizah Marsh Along The Kassara River, technical Report; Baghdad, Iraq.

Ministry of Water Resources-CRIM, 2007. "Study the Rehabilitation of Al Huweizah Marsh Ecological System" Vol.1 to Vol.7.

UNEP and Iran, 2004." Azadegan Environmental Baseline Studies". Ch 4; Administration of Iran.

WHO, 2008, Guidelines for Drinking-water Quality, third edition, Volume 1, Recommendations.

Table 1. Seasonal inflow (m^3/sec) from the marsh feeders and water surface elevation within the marsh for Case 1 and 2. (after Hayder A. Al thamiry, 2009).

Case	Season	Discharge (m^3/sec)												Marsh water surface Elevation (m.a.m.s.l)		
		AsSamaf			AzZubair			UmAt Toos			AlHusa'chi			Al Karkheh		
		Wet	Moderate	Dry	Wet	Moderate	Dry	Wet	Moderate	Dry	Wet	Moderate	Dry	Wet	Moderate	Dry
Case 1	Autumn	25	12	5	20	8	2	33	13	3	48	18	5	98	97	57	Wet	4.5	3.8	3.5
	Winter	123	70	14	30	18	2	49	31	3	69	44	5	615	263	80	Moderate	6.3	4.9	3.7
	Spring	33	20	11	30	10	1	49	17	2	69	23	3	635	227	70	Dry	8.6	5.6	3.9
	Summer	20	11	5	15	7	2	25	11	3	35	16	4	90	41	5		6.9	4.3	2.7
Case 2	Autumn	25	12	5	20	8	2	33	13	3	48	18	5	Functional: Wet 0	Degraded: Wet 0	Degraded: Dry 0		4.3	3.1	2.8
	Winter	123	70	14	30	18	2	49	31	3	69	44	5	Functional: Moderate 7	Degraded: Wet 0	Degraded: Moderate 0		4.8	3.8	3.0
	Spring	33	20	11	30	10	1	49	17	2	69	23	3	Functional: Dry 0	Degraded: Wet 67	Degraded: Moderate 0		7.2	4.9	3.2
	Summer	20	11	5	15	7	2	25	11	3	35	16	4	154	5	0		5.9	3.7	2.6

Table 2: Seasonal Electrical Conductivity (Ec (µS/cm)) values of Al Huweizah Marsh feeders (after CRIM, 2007, MoWRS, 2007, and UNEP and IRAN, 2004).

Dry year							
Feeder	AsSanna'f	AzZubair	Um AtToos	Husa'chi	Kassara	AsSwaib	Al Karkheh River (averaged values)
Autumn	3342	3342	3342	3342	Estimated from the model		2279
Winter	4018	4018	4018	4018			1160
Spring	4477	4477	4477	4477			961
Summer	3422	3422	3422	3422			1730
Wet year							
Autumn	1410	1410	1410	1410	Estimated from the model		2279
Winter	1933	1933	1933	1933			1160
Spring	1410	1410	1410	1410			961
Summer	1442	1442	1442	1442			1730
Moderate year							
Autumn	1545	1536	1264	1599	1741	2583	2279
Winter	1162	1144	1135	1176	1376	2343	1160
Spring	1219	1204	1200	1227	1596	2455	961
Summer	1280	1286	1287	1300	1675	2600	1730
The minimum, maximum and average values of the conductivity (Ec) values for Kmait flood Escape are 5320, 8600 and 6960 µS/cm, respectively.							

Table 3: Friction factor for different soil zone (Brigham Young University-USA, 2009).

Soil Zone	Friction factor
1	0.030
2	0.070
3	0.040
4	0.045

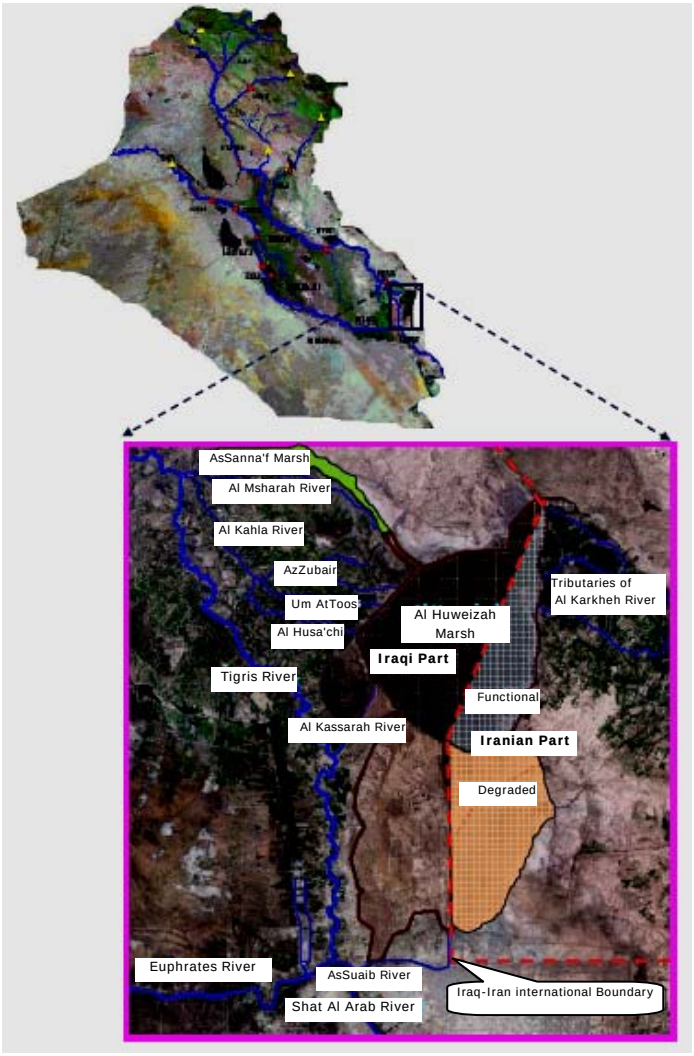

Fig. 1 : Location and Physiography of Al Huweizah Marsh.

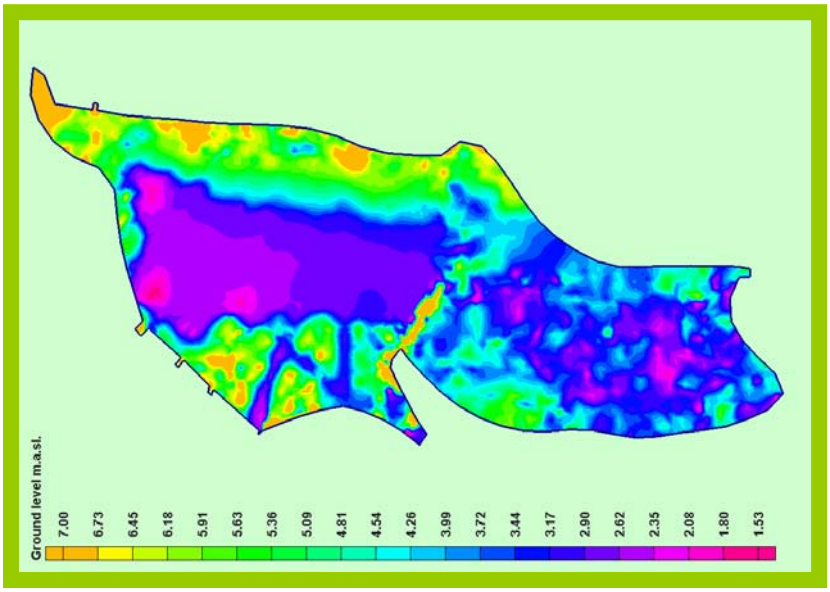

Fig. 2. DEM of the marsh

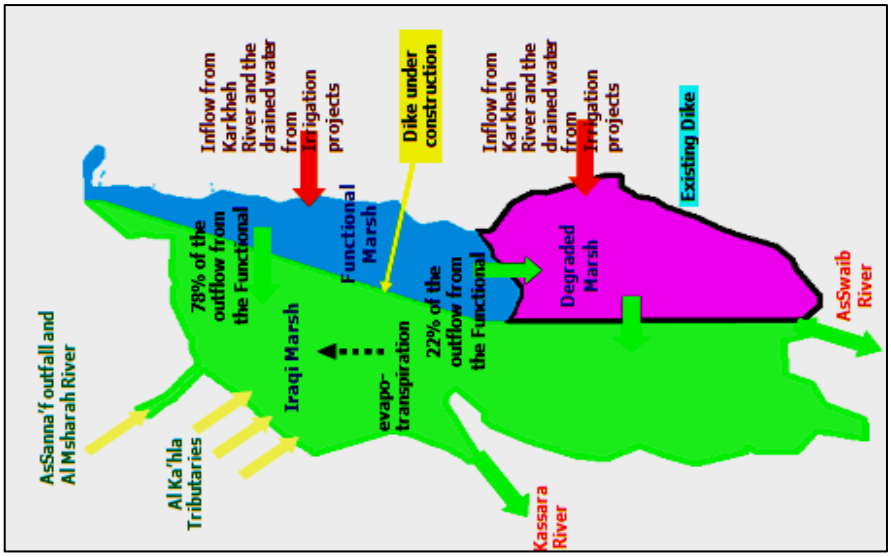

Fig. 3. Schematic diagram for the hydrological interference.

Fig. 4. Classification of the soils within the marsh area.

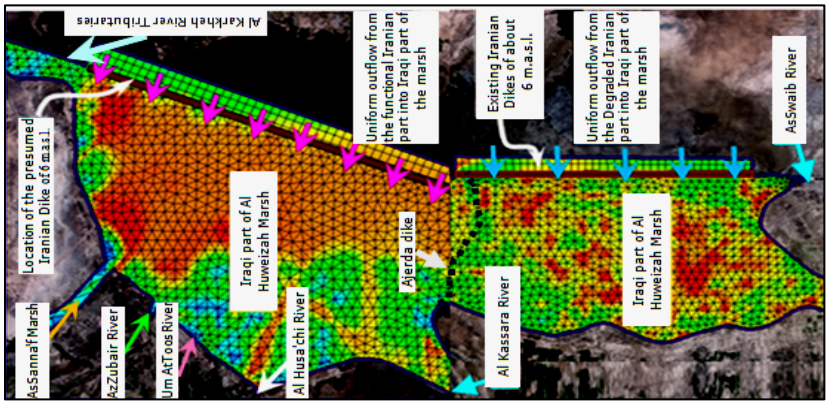

Fig. 5. The inflow from Iranian part into the Iraqi part of the marsh.

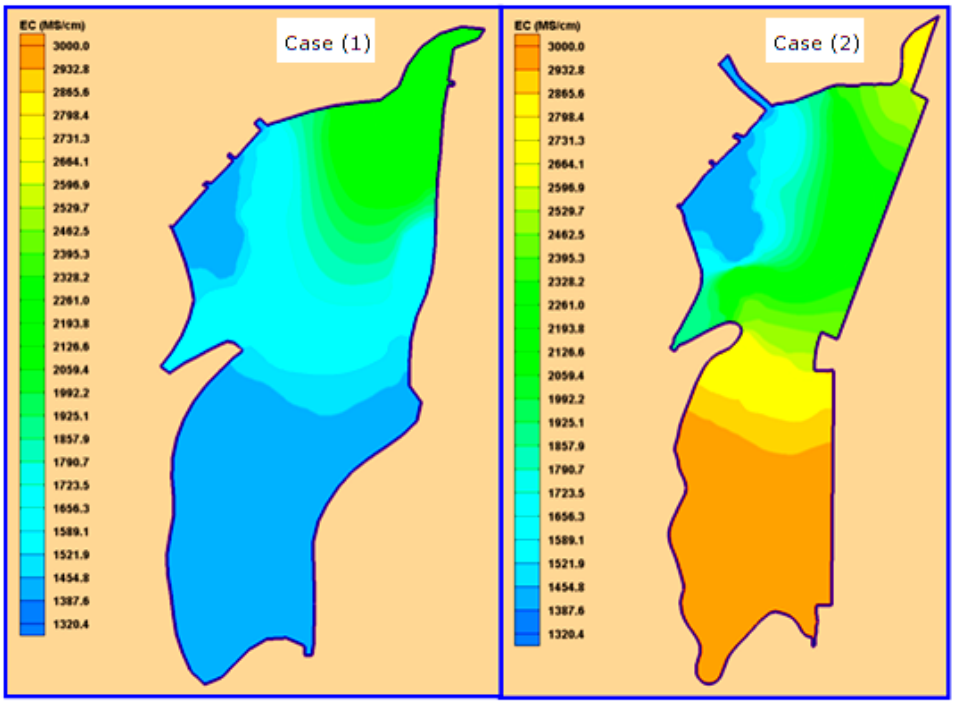

Fig. (6). Distribution of during autumn for wet year.

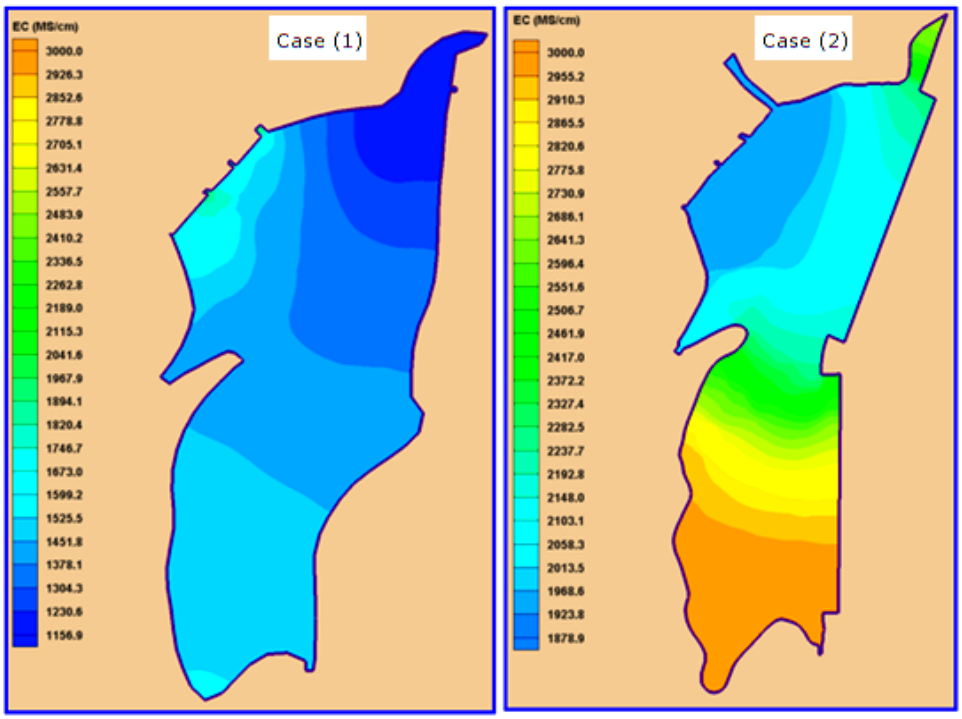

Fig. 7. Distribution of EC during winter for wet year.

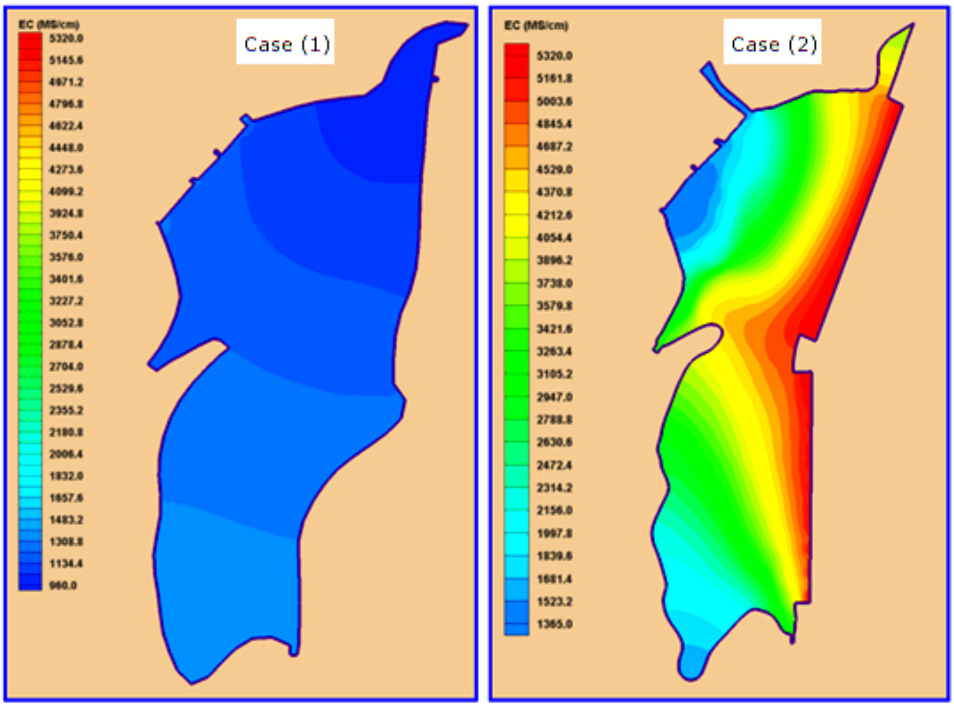

Fig. 8. Distribution of EC during spring for wet year.

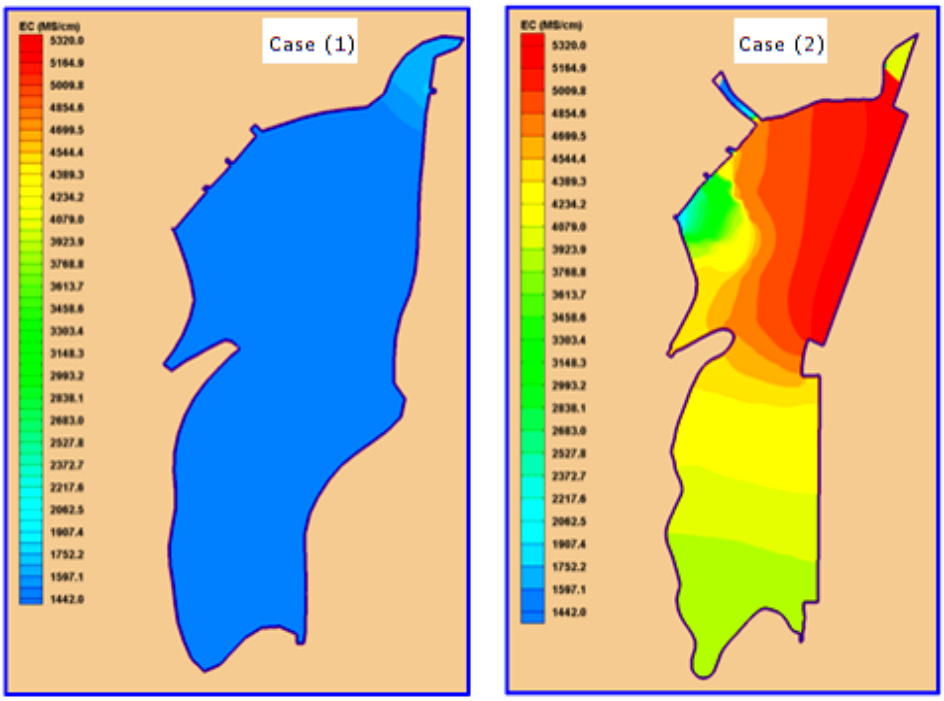

Fig. 9. Distribution of EC during summer for wet year.

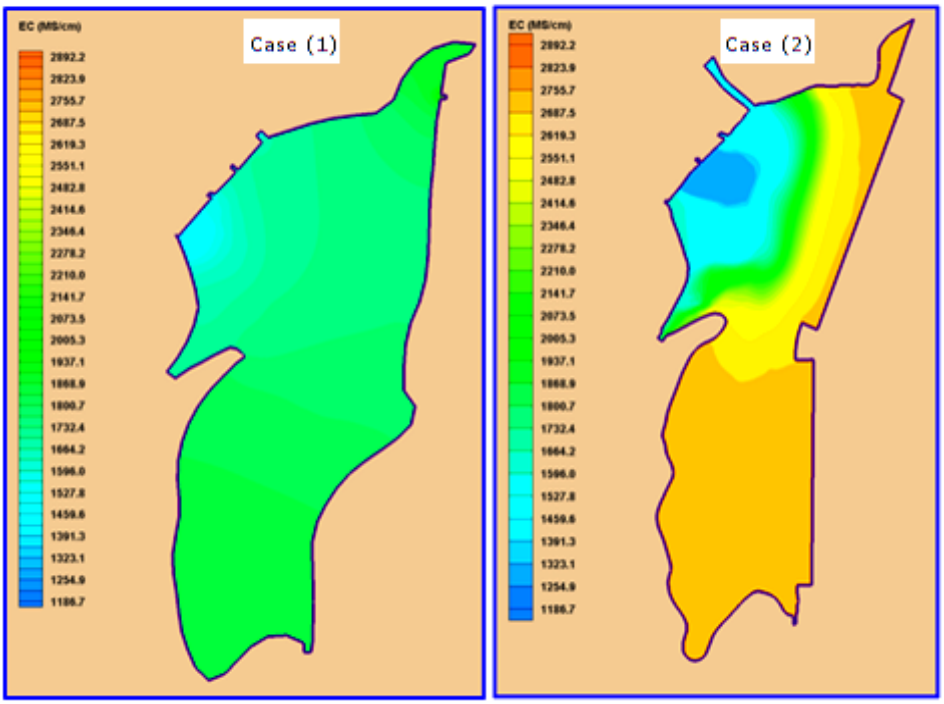

Fig. 10. Distribution of EC during autumn for moderate year.

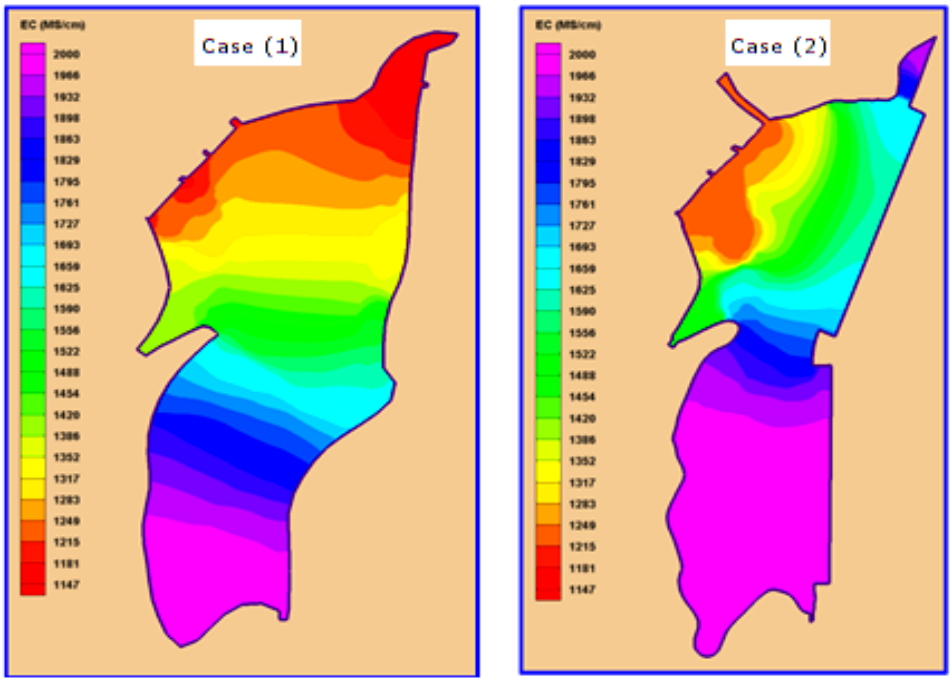

Fig. 11. Distribution of EC during winter for moderate year.

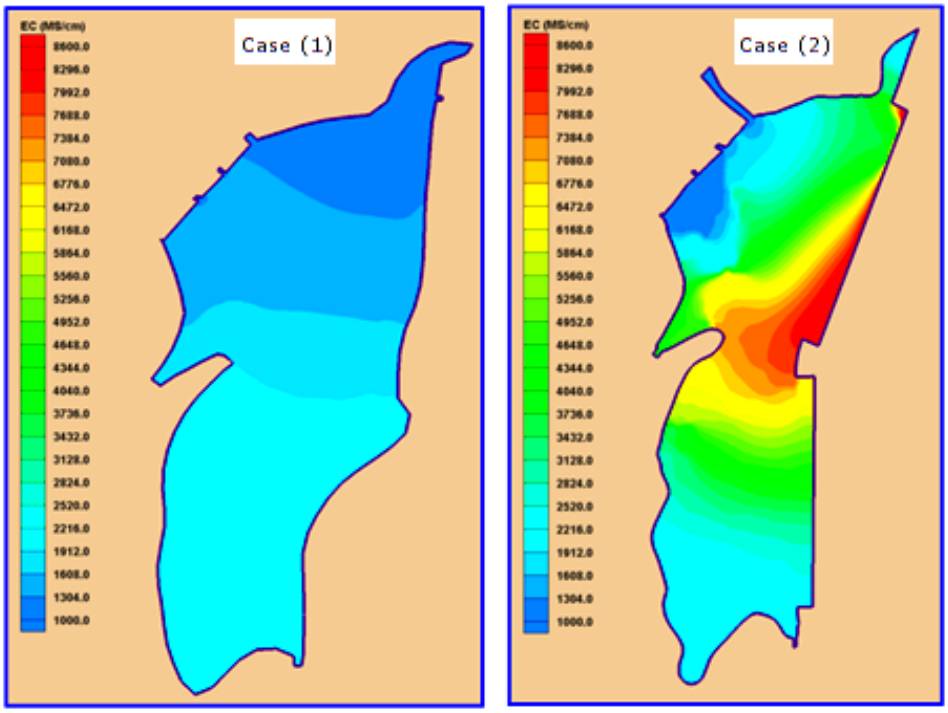

Fig. 12. Distribution of EC during spring for moderate year.

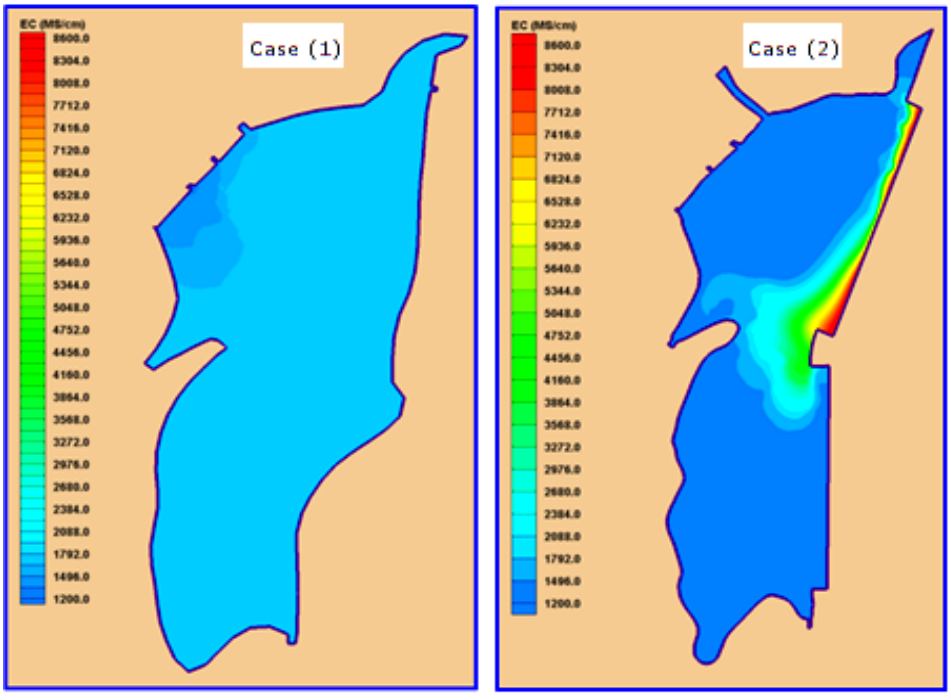

Fig. 13. Distribution of EC during summer for moderate year.

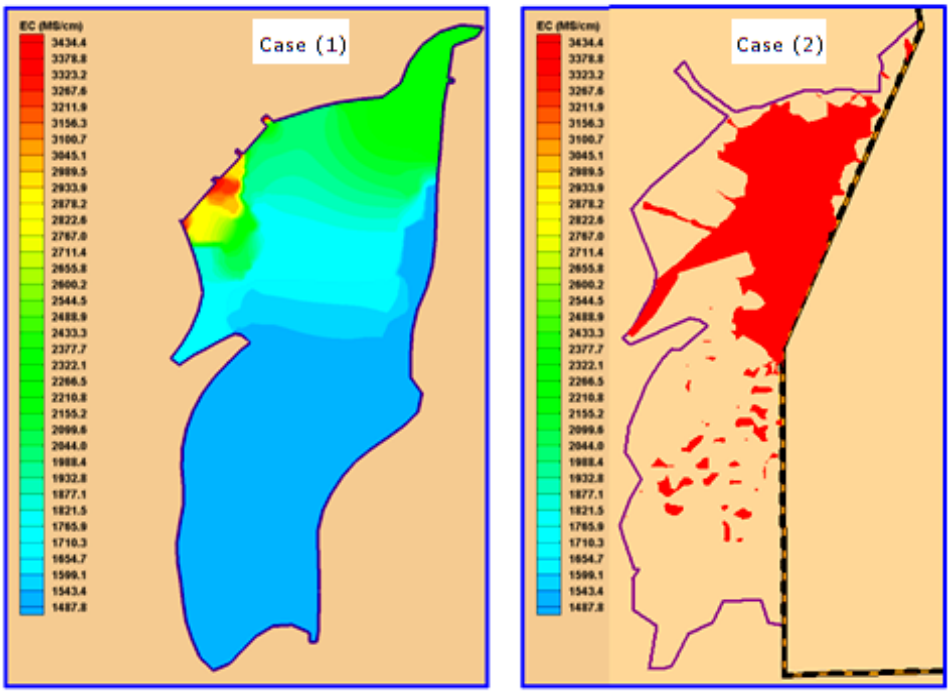

Fig. 14. Distribution of EC during autumn for dry year.

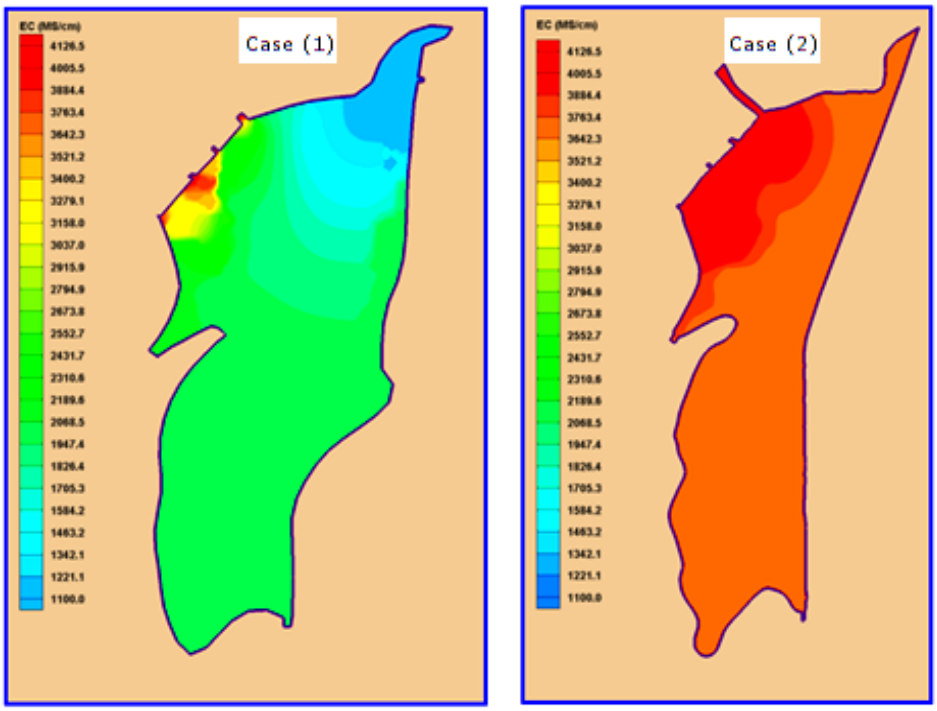

Fig.15. Distribution of EC during winter for dry year.

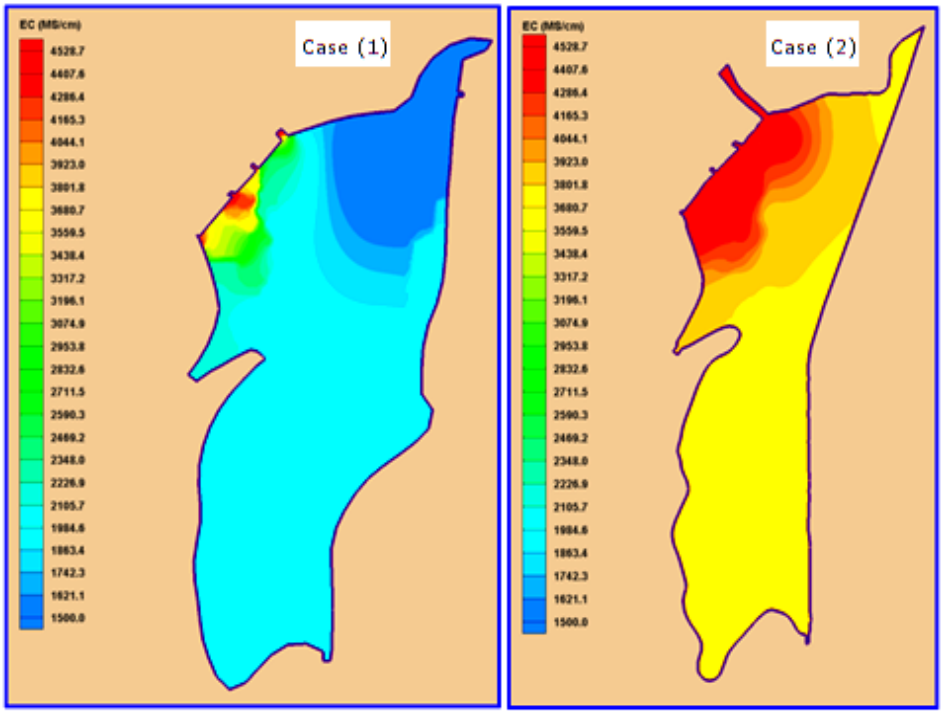

Fig. 16. Distribution of EC during spring for dry year.

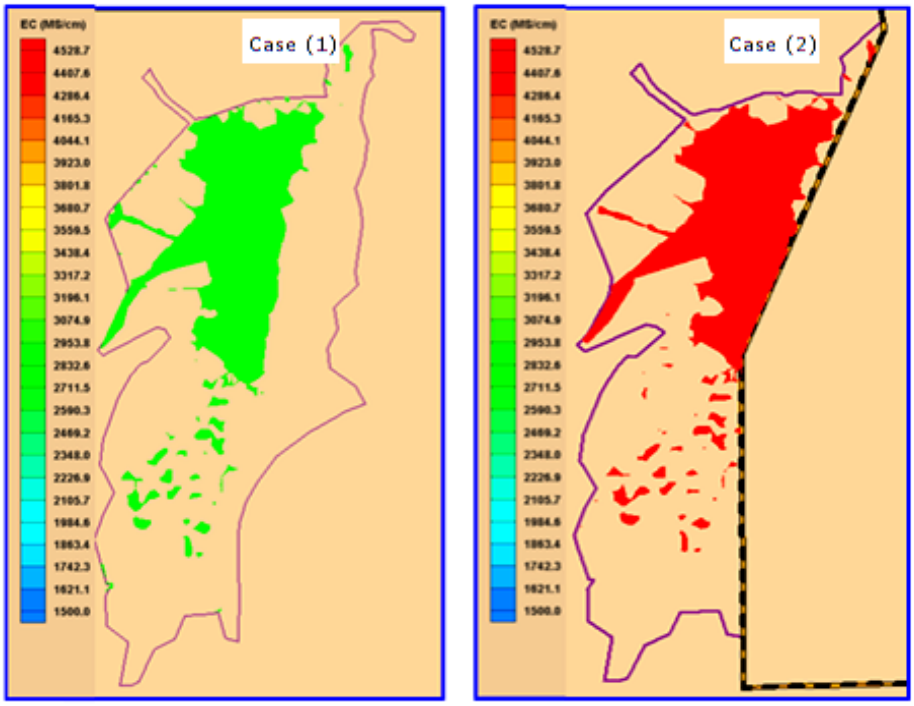

Fig. 17. Distribution of EC during summer for dry year.

SDPLL-Based Frequency Estimation of a Sinusoid in Colored Noise

Asst. Prof. Nuha Abdul Sahib Alwan

Department of Computer Engineering
College of Engineering
Baghdad University
Email: n.alwan@ieee.org

Asst. Lect. Zainab Hassan Fakhri

Department of Computer Engineering
College of Engineering
Baghdad University
Email: zainab.h.fakhri@gmail.com

ABSTRACT:

The problem of frequency estimation of a single sinusoid observed in colored noise is addressed. Our estimator is based on the operation of the sinusoidal digital phase-locked loop (SDPLL) which carries the frequency information in its phase error after the noisy sinusoid has been acquired by the SDPLL. We show by computer simulations that this frequency estimator beats the Cramer-Rao bound (CRB) on the frequency error variance for moderate and high SNRs when the colored noise has a general low-pass filtered (LPF) characteristic, thereby outperforming, in terms of frequency error variance, several existing techniques some of which are, in addition, computationally demanding. Moreover, the present approach generalizes on existing work that addresses different methods of sinusoid frequency estimation involving specific colored noise models such as the moving average (MA) noise model. An insightful theoretical analysis is presented to support the practical findings.

Keywords: Sinusoidal digital phase-locked loop (SDPLL); Cramer-Rao bound (CRB); colored noise; frequency error variance; signal-to-noise ratio (SNR).

تقدير التردد للموجة الجيبية في الضوضاء الملونة اعتماداً على حلقة اقفال الطورالرقمية الجيبية

أ.م. نهى عبد الصاحب العلوان

قسم هندسة الحاسبات
كلية الهندسة / جامعة بغداد

م.م. زينب حسن فخري

قسم هندسة الحاسبات
كلية الهندسة / جامعة بغداد

الخلاصة:

هذا البحث يتناول مشكلة تقدير التردد للموجة الجيبية المفردة في وجود الضوضاء الملونة. ان المقدر المتبع يرتكز على عمل حلقة اقفال الطور الرقمية الجيبية التي تحمل معلومات التردد داخل خطأ الطور بعد الحصول على الموجة الجيبية المشوبة بالضوضاء بواسطة حلقة اقفال الطور. وضحنا عن طريق برنامج محاكاة بالحاسبة ان مقدر التردد يتغلب على الحد الادنى لمحدد كريمر في خطأ التغير لنسب الاشارة-الى-الضوضاء المتوسطة والعالية عندما تكون خصائص الضوضاء الملونة تشبه الخصائص العامة لمرشح الترددات الوطئة ،وبذلك يتحسن الاداء، مقاسا بصيغة خطأ التغير بالتردد، عن عدة تقنيات موجودة والتي يتطلب قسم منها عبأ حسابيا عاليا. اضافة الى ذلك فان الطريقة الحالية يمكن اعتبارها تعميما للبحوث الحالية التي تتناول عدة طرق لتقدير التردد الجيبي تتضمن نماذج معينة للضوضاء الملونة مثل نموذج المعدل المتحرك للضوضاء. وتم تقديم تحليل نظري حدسي لدعم النتائج العملية.

الكلمات الرئيسية: حلقة اقفال الطور الجيبية الرقمية؛ محدد كريمر؛ الضوضاء الملونة؛ خطأ التغير بالتردد؛ نسبة الاشارة – الى –الضوضاء.

1. INTRODUCTION

Rapid frequency estimation of a sinusoid in the presence of noise is a problem that is frequently encountered in signal processing and communications with applications varying from radar, sonar, signal interception and detection, carrier synchronization and many others. Many methods of sinusoidal frequency estimation have been developed especially for the white noise case. The maximum likelihood (ML) estimator involving the location of the peak of the periodogram is well-known. The performance of the ML estimator in terms of estimator error variance achieves the CRB at high signal-to-noise ratios (SNR's), but at the expense of a large computational complexity, even when the fast Fourier transform (FFT) is used (Fu H. et al, 2007). The ML estimator is also a batch processing technique starting the processing only after all samples have been received (Richard Brown III D. et al, 2010). Subsequent to the introduction of the ML method, several fast and accurate sinusoidal frequency estimators in the presence of white noise have been reported (Kay S.,1989) attaining the CRB on variance for high enough SNR.

Frequency estimation techniques driven by a frequency tracking loop such as the PLL have also been reported in the literature in the context of operation in a white noise environment (Sithamparanathan K., 2008). The advantage of such an approach is that the PLL acts as a dynamic band-pass filter (BPF) to track the frequency, which improves the SNR due to reduced bandwidth (BW) once the signal is acquired. This improvement in SNR certainly leads to an improvement in the frequency error variance for a given system. Indeed, it has been shown that such a frequency estimator using an arc-tan DPLL (Sithamparanathan K., 2008) beats the CRB for low numbers of estimation samples. The appeal of DPLLs is also evident in that they offer low-complexity sample-by-sample operation suitable for real-time applications (Richard Brown III D. et al, 2010).

In this paper, we improve on the work in (Sithamparanathan K., 2008) to include the case where the accompanying noise is colored. This case occurs in many applications and is definitely more practically relevant (Stoica P. et al, 1997) In our work, however, we choose to investigate the SDPLL as a frequency estimator in colored noise. Among DPLL's, the uniform sampling SDPLL's are particularly popular, as they are simple to implement and suitable for relatively wide locking ranges (Hussain Z. M. et al, 2011). (Elasmi-Ksibi R. et al, 2010) have recently treated the case of frequency estimation of a sinusoid in colored noise exploiting high-order lags of the autocorrelation function (ACF) of the noisy sinusoid, and consequently restricting the investigation to MA noise models but achieving low computational complexity. The present SDPLL-based work compares favorably with (Elasmi-Ksibi R. et al, 2010) as regards computational complexity, the extension of the MA case to generally any LPF characteristic, in addition to attaining and even surpassing the CRB associated with the white noise case for a wide range of SNR values extending from moderate to high values. A high-pass filtered (HPF) characteristic of noise, however, is shown to render the system incapable of attaining the CRB. Obviously, however, long settling time and the presence of overshoot are drawbacks of PLL frequency estimation (Saber M. et al, 2011).

The rest of the paper is organized as follows: Section 2 summarizes the SDPLL analysis and explains the design methodology. Sections 3 and 4 focus on the SDPLL as a frequency estimator in white and colored noise respectively, analytically highlighting the improvement on the error variance that is achieved with a low-pass filtered noise characteristic. Section 5 presents simulation results of the proposed system. Finally, Section 6 concludes the paper.

2. ANALYSIS AND DESIGN OF THE NOISE-FREE SDPLL

SDPLLs are non-uniform sampling sinusoidal PLLs that have the advantage of being simple to implement and having relatively wide locking ranges. The block diagram of this system is shown in **Fig. 1**. The SDPLL consists of a sampler-ADC unit which serves as a phase detector, a digital LPF (DF), and a digital voltage-controlled oscillator (DCO). The latter provides constant-amplitude but variable-frequency output pulses that control the sampling instants of the sampler-ADC unit (Hussain Z. M. et al, 2011).

The DF output is input to the DCO to vary its phase and hence sampling instant of the input analog signal x(t). When the signal is absent, the DCO runs at its free-running frequency which we call f_o. When the sampler takes a sample of x(t) at the kth sampling instant, the ADC converts the analog value of the input into a digital value that the DF uses at its input to yield y(k) at its output. This digital y(k) is then input to the DCO. As the DCO input changes, so does the sampling period T(k) of the ADC. The sampling process is non-uniform, i.e. the sampling frequency is not constant. Under certain conditions, namely, the locking conditions, the convergence or locking occurs such that T(k) approaches the inverse of f_i, the input sinusoid frequency. **Fig. 2** shows the waveforms associated with the SDPLL.

For the dual purpose of clarity and symbols unification, we find it convenient to summarize the elementary analysis of the SDPLL already present in the literature such as in (Hussain Z. M. et al, 2011).

Assume the sinusoidal input is given by:

$$x(t) = A\sin(\omega_i t + \theta_o) \quad (1)$$

where A is the signal amplitude, $\omega_i = 2\pi f_i$ is the sinusoidal angular frequency, and θ_o is a constant phase. The locking range of the loop is the range of instantaneous frequencies that the loop can track. Since the locking range is dependent on the deviation of ω from the loop center frequency ω_o, we can then write eq. (1) as:

$$x(t) = A\sin[\omega_o t + \theta(t)] \quad (2)$$

$\theta(t)$ is the information-bearing phase given by:

$$\theta(t) = (\omega_i - \omega_o)t + \theta_o = \Delta\omega t + \theta_o$$

After sampling, the input signal at the kth sampling instant t(k) will take on the following form:

$$x(k) = A\sin[\omega_o t(k) + \theta(k)] \quad (3)$$

Now we can define the input phase at the kth sampling instant as:

$$\phi(k) = \omega_o t(k) + \theta(k)$$

The sampling interval of the DCO at the kth sampling instant is given by:

$$T(k) = To - y(k-1) \quad (4)$$

To is the DCO free-running period. This shows that the kth output sample of the DF, y(k), effectively determines the sampling period T(k+1). Eq. (4) reveals how the DCO operates; it decreases its period (increases its frequency) as the DF output increases.

From the above findings, the phase difference equation of the system is given by (Hussain Z. M. et al, 2011):

$$\phi(k+1) - \phi(k) = \theta(k+1) - \theta(k) + \omega_o y(k)$$

Let us assume that the digital filter transfer function is H(z)=G1 where G1 is a constant. This yields a first-order SDPLL. Then, the above equation is used to modify the difference equation to:

$$\phi(k+1) = \phi(k) - K_2 \sin[\phi(k)] + \Lambda_o$$

where $\Lambda_o = 2\pi(\omega_i - \omega_o)/\omega_o$ and $K_2 = \omega_i G_1 A$.

Defining K1 to be $K_1 = \omega_o G_1 A$ and W as the frequency ratio $W = \omega_o / \omega_i$, then:

$$K_2 = K_1(\omega_i / \omega_0) = K_1 / W .$$

The parameters K1 and W control the locking range. The locking conditions have been derived in (Hussain Z. M. et al, 2011). We state here the results of the derivation in (Hussain Z. M. et al, 2011) as these results are key attributes in SDPLL design.

$$K_1 > 2\pi|1-W|$$
$$K_1 < \sqrt{(4+4\pi^2)W^2 - 8\pi^2 W + 4\pi^2} \quad (5)$$

The above two equations specify a range of K1 that ensures that the input frequency is within the frequency locking range of the first-order SDPLL.

According to the above inequalities, we may design our first-order SDPLL. For example, if we choose a DCO with $f_o = 1Hz$ and the input frequency $f_i = 0.83Hz$, then clearly W=1.2. And from the locking conditions of eq. (5), K1 can be safely chosen as K1=1.7.

3. THE SDPLL AS A FREQUENCY ESTIMATOR OF A NOISY SINUSOID

The SDPLL can detect the input frequency in the presence of noise, even for low SNRs. Having designed the first-order SDPLL in Section II, we now explain the frequency estimator driven by the SDPLL when the input sinusoid is contaminated by additive white Gaussian noise (AWGN). The noisy input sinusoid may be written as:

$$x(k) = A\sin[\phi(k)] + n(k) \quad (6)$$

where n(k) is additive noise. We are interested in estimating the frequency of the noise-free input sinusoid which we call f_i. The SDPLL is a computationally efficient sample-by-sample method to extract f_i from noisy observations. The PLL acts as a dynamic BPF that tracks the input frequency improving the SNR by bandwidth reduction. The SNR improvement leads to an improvement in frequency error variance. Using the symbols in Section 2, the sequence t(k) can be used to generate a frequency sequence $f_n(k)$ by inverting the interval between each two consecutive samples of t(k) and assigning it to $f_n(k)$. The probability density function of the instantaneous frequency $pdf(f_n)$ has a maximum at approximately f≒ f_i. The variance of this frequency estimator is a function of the SNR; it decreases as the SNR increases. **Fig. 3** shows $pdf(f_n)$ for the design of Section 2 and for the white noise case.

4. THE SDPLL FREQUENCY ESTIMATOR OF A SINUSOID IN COLORED NOISE

In this paper, we wish to investigate the colored noise case. In (Elasmi-Ksibi R. et al, 2010), a novel method of frequency estimation of a sinusoid in colored noise using multiple autocorrelation lags is presented. However, the method is applicable only to environments where the colored noise is of finite memory, i.e. moving average (MA) noise models. The method features low computational complexity and compares favorably with its forerunners. We show that frequency estimation in colored noise is possible with different types of low-pass-filtered noise, including the MA noise model, whereas the method in (Elasmi-Ksibi R. et al, 2010) is applicable only to the MA model.

In particular, for the SDPLL, we find that low-pass-filtered colored noise, added to the input sinusoid whose frequency is to be estimated, significantly enhance the SNR when compared to the white noise case, whereas a high-pass-filtered noise has the adverse effect. We have also found that this is true for any kind of low-pass-filtered noise. We simulate the colored noise by passing AWGN through a first-order IIR LPF first, then a FIR LPF of a MA type. We can explain this favorable behavior of the SDPLL as follows: Since the output pulses from the DCO control the sampling of the sine-plus-colored-noise signal, the digital LPF sampling frequency has, on average, a value of f_i=0.83 Hz according to the design of Section 2. Therefore, the folding frequency (corresponding to the digital frequency of π radians) is f_i/2=0.415 Hz. The periodic frequency transfer function of this digital LPF has a typical form shown in **Fig. 4**. It is clear that this filter has high gain around 0.83 Hz. This means that LPF colored noise boosts the SNR thereby improving the frequency error variance for the SDPLL acting as a frequency estimator. On the other hand, a HPF for producing colored noise has the typical transfer function shown in **Fig 5**. The presence of a peak at half the input frequency, i.e. at 0.415 Hz, results in a degradation of the

performance of the SDPLL as a frequency estimator and the frequency error variance increases.

As in any estimation problem, the idea is to produce from a noisy observation vector f_n an unbiased estimate $\hat{f}_i$ of a deterministic parameter f_i. The estimation error variance is lower-bounded by the Cramer-Rao bound (CRB):

$$E[(\hat{f}_i - f_i)^2] \geq CRB \quad (7)$$

The CRB is given by:

$$CRB = E\left[\frac{d}{df_i}\ln(p(f_n; f_i))\right]^2 \quad (8)$$

The probability density function $p(f_n; f_i)$ of f_n, corresponding to a given value of f_i, is called the likelihood function of f_i, while $\ln(p(f_n; f_i))$ is the log-likelihood function of f_i. The expectation is with respect to $p(f_n; f_i)$.

The CRB in our work is the lower bound of the frequency error variance as in eq. (7). Analytical evaluation of the CRB (Vaseghi S.V., 2006) is usually extremely difficult, if not impossible; therefore we resort to computer simulation to find it (Noels N. et al, 2002).

5. SIMULATION RESULTS

The first-order SDPLL is simulated in MATLAB 7. The program for the white noise case is listed below in pseudo-code; the symbols are as presented in Section 2.

SDPLL algorithm for sinusoid frequency estimation

INPUT: Noise vector n, and parameters from which to compute sinusoid vector x, plus other loop parameters.
OUTPUT: Frequency error variance vector vs. SNR vector.
/*Loop parameters*/
Frequency ratio (W)=1.2
Design Constant Value (K1)=1.7
Input phase angle (θ_o)=1 rad

/*Other parameters*/
Sinusoid amplitude (A)=1
Center frequency (fo)=1 Hz
Center angular frequency (wo)=2*pi*fo rad/s
DCO period (To)=1/fo s
Input sinusoid frequency (fi)=fo/W Hz
Input sinusoid angular frequency (wi)=2*pi*fi rad/s
Constant (K2)=K1/W
Digital filter gain (G1)=K1/(wo*A)

/*Main loop*/

FOR Signal/Noise ratio (SNR)=0 to 30 step 10 **DO**

Standard deviation (sd)=sqrt(0.5/10^(SNR/10))

/*Initialization*/

First noisy sine sample (xo)=A*sin(θ_o)
+sd*n(1)
Filter output (yo)=G1*xo
First period T(1)=To-yo
First sampling instant t(1)=T(1)

/*For the rest of the samples*/

FOR k=1 to 999 **DO**
Noisy sine sample x(k)=A*sin(wi*t(k)+
θ_o)+sd*n(k+1)
Filter output y(k+1)=G1*x(k)
Sampling period T(k+1)=To-y(k)
Sampling instant t(k+1)=t(k)+T(k+1)
END FOR
Frequency vector fn=1/T
Frequency variance=variance(fn)

END FOR
RETURN dB-variance vs. SNR

The corresponding MATLAB code yields the frequency error variance versus SNR. For the colored noise case, we pass the AWGN through a LPF transfer function to produce colored noise. We demonstrate two cases:

Case I: IIR first-order LPF. The transfer function is given by:

$$H(z) = \frac{z}{z - a}$$

If we assume that σ_i^2 is the input noise power to the LPF, then it is straightforward to prove that:

$\sigma_o^2 = \dfrac{\sigma_i^2}{1-a^2}$ is the output noise power.

We assume that the input noise power (variance) is equal to unity. Therefore, to compare between white and colored noise effects, we have to equate the powers of the two. Thus, we multiply the colored noise sequence by $\sqrt{1-a^2}$ before adding it to the sine wave. If we take a=0.9, then we have to multiply by $\sqrt{0.19}$. After making the necessary modification to the above pseudo-code and the corresponding MATLAB code, we plot the variance versus SNR on the same graph as that for the white noise case as in **Fig. 6**. The variance versus SNR for the corresponding HPF filtered colored noise case is also shown in the figure.

Case II: We also test low-pass filtered noise using a MA process. We choose the FIR MA filter transfer function as:

$H(z) = 0.2(1 + z^{-1} + z^{-2} + z^{-3} + z^{-4})$.

The power relation is:

$\sigma_o^2 = \sigma_i^2 \sum_{l=0}^{4} b_l^2 = \sigma_i^2 / 5$.

The $b_l's$ are the impulse response values of the FIR MA filter.

Also assuming unity input noise power, we have to multiply the filter output by $\sqrt{5}$ for a meaningful comparison. The resulting curve is also included in **Fig. 6**, and is shown to coincide nearly with IIR filter case. The conclusion is that for LPFs, in general, the frequency error variance is improved (decreased).

The Cramer Rao bound (CRB) is a lower bound on the error variance of any unbiased estimator and serves as an important benchmark to compare practical estimators (Noels N. et al , 2002), (Vaseghi S.V., 2006). **Fig. 6** is extended to include high SNRs. The CRB is the asymptote to the curves as SNR increases. Therefore, we can find it practically as the figure shows. **Fig. 7** is a zoom-in to the moderate-to-high SNR region of **Fig. 6**. It can be seen from **Fig. 7** that when the additive noise is a low-pass-filtered one, we gain an improvement over the white noise case as regards the variance of the frequency estimate for moderate and high SNRs.

6. CONCLUSIONS

An SDPLL-based single-sinusoid frequency estimator in white and colored noise has been simulated and tested. It has been shown that when the additive noise to the sinusoid has a LPF characteristic we gain an improvement of the estimator performance in terms of reduced frequency error variance regardless of the type of LPF whether IIR or FIR. This work is an extension of related PLL-based methods reported in the literature for the white noise case, and of specifically MA-noise-model non-PLL-based frequency estimators. We have shown through simulation that our estimator beats the CRB of the white noise case for moderate and high SNRs.

REFERENCES

Elasmi-Ksibi R., Besbes H., Lopez-Valcarce R., Cherif S., "Frequency estimation of real-valued single-tone in colored noise using multiple autocorrelation lags", Signal Processing, vol. 90, 2010, pp. 2303-2307.

Fu H., Kam P. Y., "MAP/ML estimation of the frequency and phase of a single sinusoid in noise", IEEE Transactions on Signal Processing, vol. 55, no. 3, March, 2007, pp. 834-845.

Hussain Z. M., Sadik A. Z., O'Shea P., *Digital signal processing, an introduction with MATLAB and applications*, Springer Verlag, Berlin Heidelberg, 2011.

Kay S., "A fast and accurate single frequency estimator", IEEE Transactions on Acoustics, Speech and Signal Processing, vol. 37, no. 12, December 1989, pp. 1987-1990.

Noels N., Steendam H., Moeneclaey M., "The true Cramer-Rao bound for estimating the carrier phase of a convolutionally encoded signal", in Proc. IEEE SVCT 2002, Louvain-la-Neuve, Belgium, Oct. 2002, pp. 9-14.

Richard Brown III D., Liao Y., Fox N., "Low-complexity real-time single-tone phase and

frequency estimation", in 2010 Military Communication Conference, San Jose, CA, 31 Oct.- 3 Nov., 2010.

Saber M., Khan M. T. A., Jitsumatsu Y., "Frequency and power estimator for digital receivers in Doppler shift environments", Signal Processing: An International Journal, vol. 5, no. 5, 2011, pp. 185-202.

Sithamparanathan K., "Digital-PLL assisted frequency estimation with improved variance", IEEE Global Telecommunications Conference (GLOBECOM 2008), New Orleans, LA, USA, 30 Nov.- 4 Dec. 2008, pp. 1-5.

Stoica P., Jakobsson A., Li J., "Cisoid parameter estimation in the colored noise case: Asymptotic Cramer-Rao bound, maximum likelihood and nonlinear least-squares",IEEE Transactions on Signal Processing, vol. 45, no. 8, 1997, pp. 2048-2059.

Vaseghi S. V., *Advanced digital signal processing and noise reduction*, Wiley, West Sussex, England, 3rd edition, 2006.

SYMBOLS AND ACRONYMS

A	the signal amplitude
$b_l's$	impulse response values of the FIR MA filter
f_i	frequency of the noise-free input sinusoid
$\hat{f}_i$	unbiased estimate of f_i
f_n	noisy observation vector
To	DCO free-running period
T(k)	sampling period of the ADC
W	frequency ratio
x(t)	input analog signal
y(k)	input to the DCO
θ_o	constant phase
$\theta(t)$	information- bearing phase
σ_i^2	The input noise power to the LPF
$\phi(k)$	input phase at the kth sampling instant
ω_i	sinusoidal angular frequency
ω_o	loop center frequency
ACF	autocorrelation function
ADC	analog to digital converter
AWGN	additive white Gaussian noise
BPF	band-pass filter
BW	bandwidth
CRB	Cramer-Rao bound
DCO	digital voltage-controlled oscillator
DF	digital filter
DPLL	digital phase-locked loop
FFT	fast Fourier transform
FIR	finite impulse response
HPF	high-pass filter
IIR	infinite impulse response
LPF	low-pass filter
MA	moving average
ML	maximum likelihood
pdf	probability density function
PLL	phase-locked loop
SDPLL	sinusoidal digital phase locked loop
SNR	signal-to-noise ratio

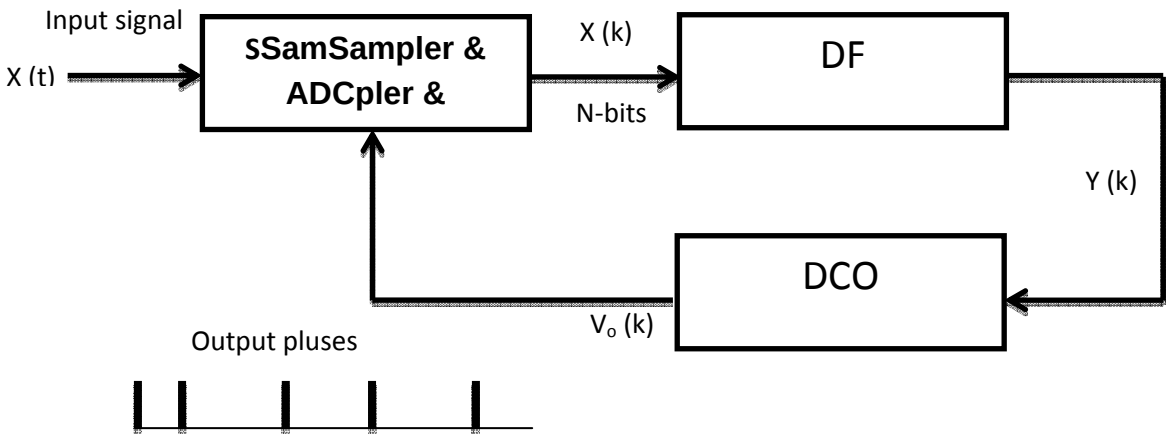

Fig. 1: A block diagram of SDPLL (Hussain Z. M. et al., 2011).

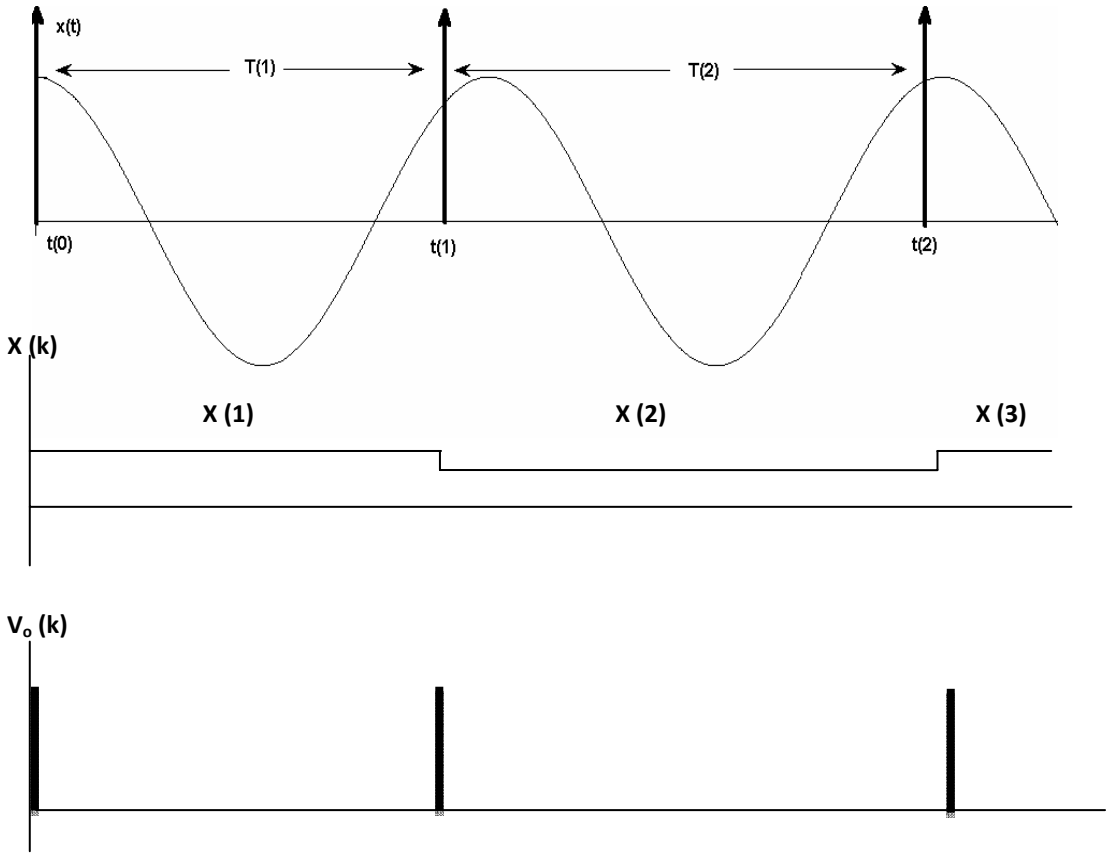

Fig. 2: Waveforms associated with SDPLL (Hussain Z. M. et al., 2011).

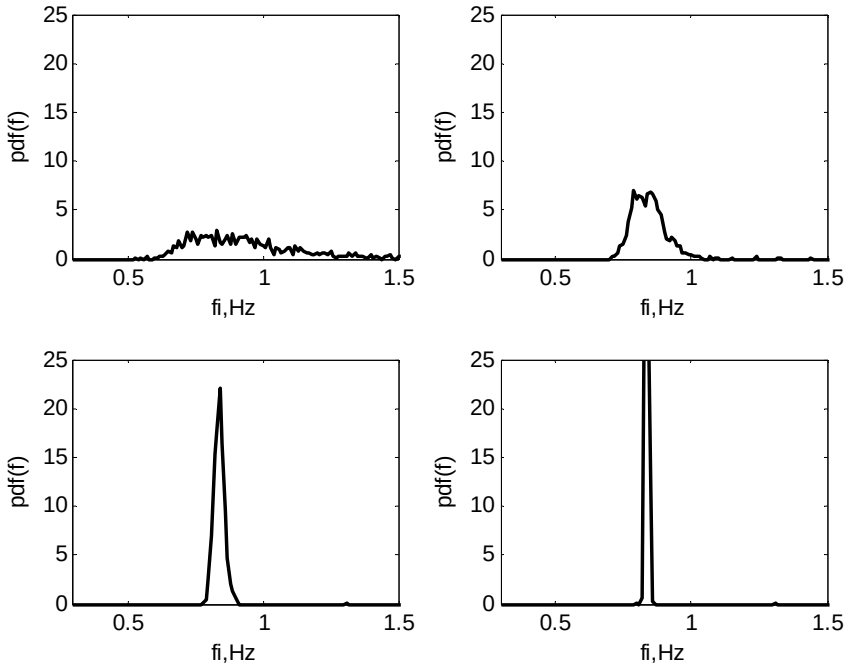

Fig. 3: Frequency tracking probability density function (PDF) for different SNRs in AWGN. From left to right, top to bottom: SNR=0, 10, 20, 30 dB.

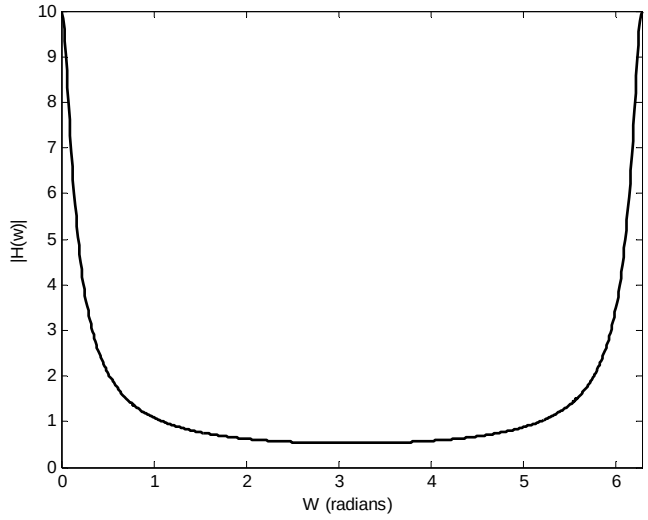

Fig. 4: 1st order IIR LPF magnitude transfer function [H(z)=z/(z-0.9)]. The digital frequency w= π (or 3.14 rad) corresponds to 0.415 Hz and 2π (or 6.28 rad) corresponds to 0.83 Hz. Notice the peak is at 0 and 2π corresponding to 0.83 Hz.

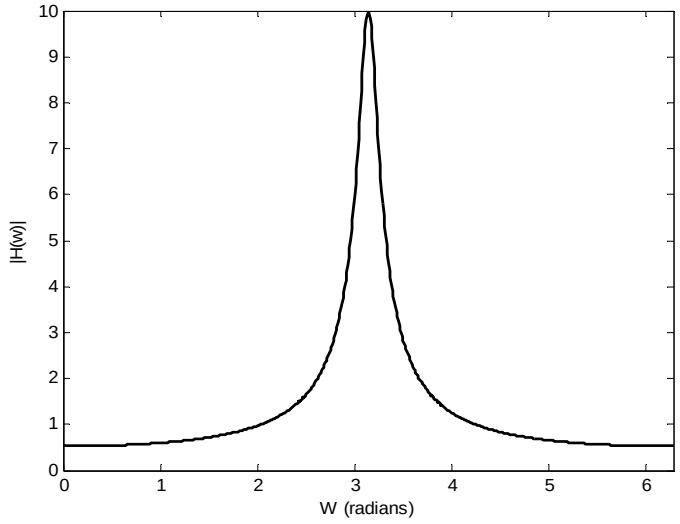

Fig. 5: **1st order IIR HPF magnitude transfer function [H(z)=z/z+0.9]. Notice the peak at π or 3.14 radians corresponding to 0.415 Hz.**

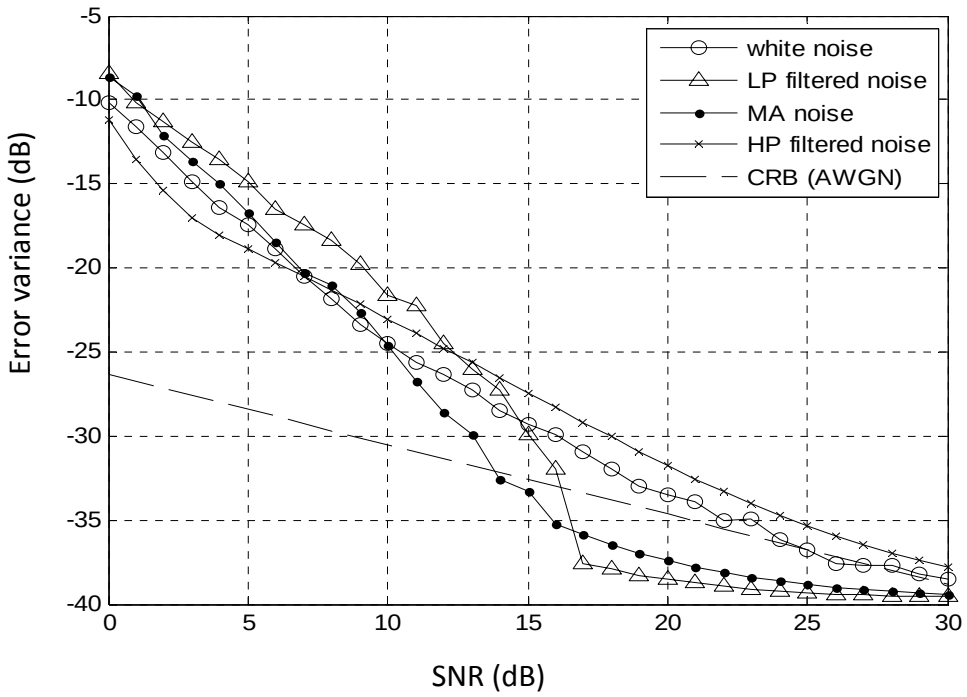

Fig. 6: **Frequency error variance (dB) versus SNR (dB) for SPDLL estimator and for different noise types. The CRB lower bound is shown for the white noise case.**

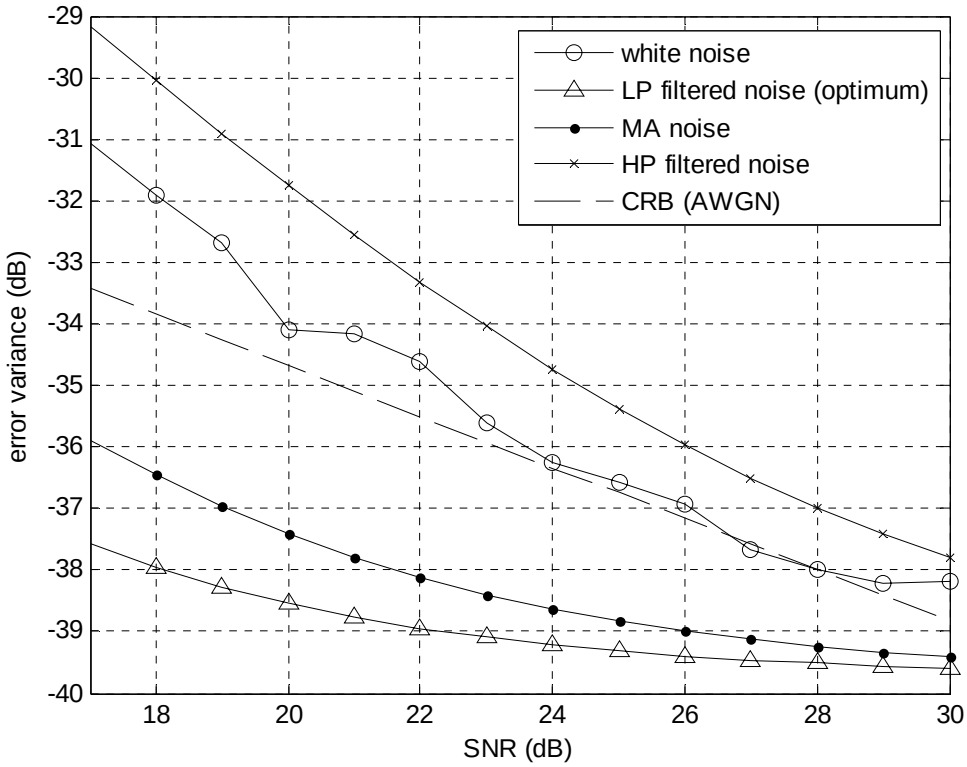

Fig. 7: Frequency error variance (dB) versus SNR (dB) for SDPLL estimator and for different noise types with emphasis on the moderate-to-high SNR region. The CRB lower bound is shown for the white noise case.

An Investigation into Heat Transfer Enhancement by Using Oscillating Fins

Prof. Dr. Ihsan Y. Hussain
Mechanical Engineering Department
University of Baghdad
drihsan@uobaghdad.edu.iq
dr.ihsanyahya1@yahoo.com

Asst.Prof. Dr.Karima E.Amori
Mechanical Engineering Department,
University of Baghdad
drkarimaa@yahoo.com

Asst.Lecturer. Dheya G. Mutasher
Mechanical Engineering Department,
University of Technology
dheya_ghanim@yahoo.com

ABSTRACT

The present work describes numerical and experimental investigation of the heat transfer characteristics in a plate-fin, having built-in piezoelectric actuator mounted on the base plate (substrate). The geometrical configuration considered in the present work is representative of a single element of the plate-fin and triple fins. Air is taken as the working fluid. A performance data for a single rectangular fin and triple fins are provided for different frequency levels (5, 30 and 50HZ) , different input power (5,10,20,30,40 and 50W) and different inlet velocity (0.5, 1, 2, 3, 4, 5 and 6m/s) for the single rectangular fin and triple fins with and without oscillation. The investigation was also performed with different geometrical fin heights (50mm and 35mm) and distance between the fins (3mm and 6mm). It is observed that the heat transfer increases with the increase in the frequency and Reynolds number. It is further observed that triple fins with (height=50mm and distance between the fins=3mm) gives better enhancement as compared to other cases, The study shows that the piezoelectric actuator when mounted on the rectangular fins gives great promise for enhancing the heat transfer rate.

Keywords: oscillating fins, forced convection, heat transfer enhancement, experimental and numerical study

دراسة لزيادة معدلات انتقال الحرارة باستخدام الزعانف المتذبذبة

أ.د.احسان يحيى حسين
قسم الهندسة الميكانيكية

أ.م.د. كريمة اسماعيل عموري
قسم الهندسة الميكانيكية

م.م. ضياء غانم مطشر
قسم الهندسة الميكانيكية

الملخص:

العمل الحالي يبحث عدديا وتجريبيا خصائص انتقال الحرارة في زعانف مدمجة مع (Piezoelectric Actuator) *ومثبتة على قاعدة الزعانف* (Substrate). واخذ بنظر الاعتبار الزعنفة المنفردة والزعانف الثلاثية. واستخدم الهواء كمائع عمل. اختبرت قيم الاداء للزعنفة المنفردة والزعانف الثلاثية لمستويات تردد مختلفة (5، 30، و50 هيرتز) ، قدرات ادخال مختلفة (5، 10، 20، 30، 40، و 50 واط) ، وسرع دخول مختلفة (0.5، 1، 2، 3، 4، 5 و 6 م/ثا) مع وبدون ذبذبة. وانجز البحث مع ارتفاعات زعانف مختلفة (35 ملم ، 50 ملم) ، ولمسافات بين الزعانف (3 ملم ، 6 ملم) . يلاحظ ان انتقال الحرارة يزداد مع زيادة التردد وعدد رينولد . كذلك يلاحظ ان الزعانف الثلاثية مع (الارتفاع=50 ملم والمسافة بين الزعانف=3 ملم) تعطي افضل

تحسن في انتقال الحرارة مقارنة مع الحالات الاخرى ، وتوضح الدراسة انه عند دمج ال (Piezoelectric Actuator) مع الزعانف المستطيلة يعطي تحسن كبير في معدل نقل الحرارة .

الكلمات الرئيسية: زعانف متذبذبة، حمل فسري، تحسين انتقال الحرارة، دراسة عددية وتجريبية

INTRODUCTION

Heat transfer enhancement has become popular recently in the development of high performance thermal systems. A wide variety of industrial processes involve the transfer of heat energy. These processes provide a source for energy recovery and process fluid heating or cooling. Enhanced heat transfer surfaces can be designed through a combination of factors that include increasing fluid turbulence, generating secondary fluid flow patterns, reducing the thermal boundary layer thickness and increasing heat transfer surface area (David 2010).Electronic portable devices, especially desktop PCs and CPUs, have become challenging and popular. Today's rapid IT development like the Internet PC is capable of processing more data at a tremendous speeds. This leads to higher heat density and increased heat dissipation, making the CPU temperature rise and causing a shortened life, malfunction, and failure of CPU, (R. Mohan 2011). Heat transfer under the influence of vibration and flow oscillation (also sound) has been the subject of many researches since the early 1950's. Enhancement of heat transfer for a circular cylinder by using oscillations was studied by (H.M.Blackburn 1993), (Chin 1997), (C.Gau 2001), (H.G.Park 2001), Fu [2002],(Tait 2006), (Yue-Tzu 2008), (Osama 2009) and (Jalal 2009). In addition to numerous methods have been proposed to enhance heat transfer rate by using block moving back and forth on a heated surface in a channel flow, this phenomena causes the heat transfer rate of the heat surface to be enhanced because it destroys and suppresses the velocity and thermal boundary layers on the heat surface periodically studied by (Wu-Shung 2000) , (Wu-Shung 2001),(Wu-Shung 2001) and (Wu-Shung2010).(Hiroshi 1971)studied analytically the time –mean heat transfer of the Incompressible laminar boundary layer on a flat plate under the influence of oscillation. The results show that, when the oscillation is of high frequency, the time –mean heat flux to the wall can be several times as large as that without oscillation.(Wu-Shung 2001) proposed a method for enhancing heat transfer of a

finned heat sink for electronic device cooling. They used extremely thin fins swinging back and forth in a flow. The Galerkin finite element method with moving meshes was used to solve the differential governing equations. They studied the effects of Reynolds number (ranged between 500 to 1500), swinging speed and amplitude of the fins. The results show that: as the fins swing with a small speed, the variations of the flow and thermal fields are slight and similar to the fluid flowing over a flat plate. (Subhrajit 2009) Carried out a numerical investigation using finite volume method for a 3D oscillating fin to disturb the thermal boundary layer to enhance forced convection heat transfer from conventional heat sink. The fin dimensions were (0.5" *1"*0.01") and substrate was (1"*1"). The power supplied to the substrate was 20W. It was found that such oscillations lead to tip-leakage vortices from the fins. Most of the reviewed literatures deal with flow oscillation and study the effect of this oscillation on heat transfer and fluid flow. Also they focus on study the effect of wall oscillation, body moving, heated surface and oscillation of the cylinder to destroy the thermal boundary layer developed on the heated surface. Up to our knowledge, very rare previous work focus on heat transfer rate from an oscillating fin (by using a piezoelectric actuator) attached to a hot substrate in a flowing fluid. The experimental and theoretical parts of the present work are concerned with the effect of fin height, fin spacing, power supplied to the hot substrate, fins number (single or triple), frequency of oscillations, and inlet velocity of the flowing fluid. The present study is involved with the

enhancement of convective heat transfer by utilizing fixed or oscillating fins from a hot plate to a longitudinal flowing fluid. The investigation is carried out for different parameters, namely; number of fins (single or triple), height of fins, distance between the fins, power supply to the hot plate, frequency of the oscillated fins and velocity of flowing fluid. In the present study a combine substrate and oscillated fins model is design and instrumented. Fig. (1) Shows isometric view of the model

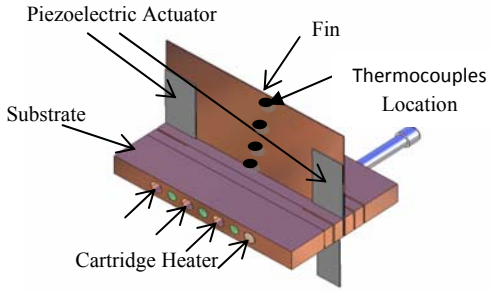

Fig. (1): The Structure of Oscillating Fin

NUMERICAL SIMULATION

In order to analyze the flow field over plate fin with and without oscillation, a solution of Navier-stokes equations is required. Conservation equations for continuity and momentum for laminar model of the plate fins are presented in FLUENT built-in solver. For air flows involving additional heat transfer (added or removed) an additional equation for energy conservation is solved. In the present work, the mathematical model of the fixed and oscillating fins are solved numerically using a CFD Code FLUENT 6.3.26 after describing the mesh model using the Gambit 2.2.30.

The model solved a finite volume formulation using an implicit solver approach. The Navier-Stokes momentum equations were discretized For time-dependent calculations, conservation equations are solved using an explicit time marching scheme. Pressure velocity coupling of the continuity equation was achieved using the SIMPLE algorithm that is valid for small time steps used in the simulation. The system geometry in the present work basically consists of a box (which represents the flow tunnel) and this box contains the substrate combined with fins (three fins).

The geometry was designed using basic five geometries (cuboids) for flow duct, substrate and three fins. Also it is good to say here that three regions are interconnected with split function so the analysis of the results are continuum and interchangeable in between of them.

MODELLING AND MESHING

The exact geometry and the corresponding mesh of the oscillating fin are shown in fig. (2). The computational region dimension is 600mm in length, 340 in width, 340mm in height. In the present work, a higher order element type tetrahedral / hybrid is used for mesh generation to approximate precisely the geometry interfaces. Grid refinement tests for residual coefficients indicated that a grid size of approximately (2 million cell) provide sufficient accuracy and resolution to be adopted as the standard for fin wall junction with upstream substrate and (400,000 cells) for fin wall junction only. In our case study the UDFs used here play the rules of substituting the effect of the sinusoidal behavior of the fins during the transient time change in dissipating of heat from substrate to the flow. A UDF is a function (programmed by the user) written in C language which can be dynamically linked with the FLUENT solver.

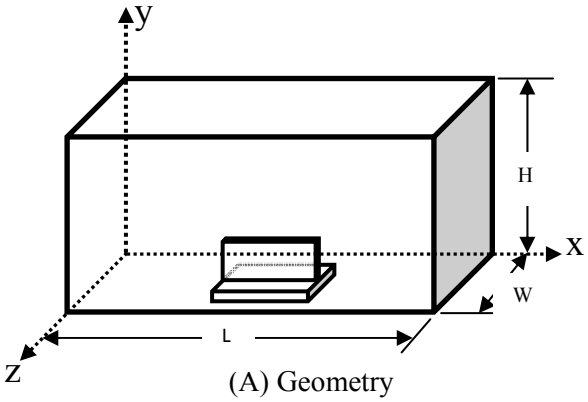

(A) Geometry

Fig. (2): (A)Geometry and (B)Model Mesheing

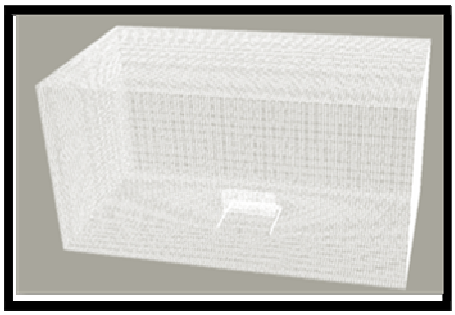

(B) Model Meshing

at the wall; u=v=w=0

at the inlet ; $T=T\infty$ and $u=u_{in.}$

at the outlet; p=patm.

Fig. (2): Continued

EXPERIMENTAL WORK

A schematic drawing of the experimental set-up is shown in Fig. (3). The experiments were carred out in the Energy lab at Cardiff University of School of Engineering U.K.The experimental set-up of the wind tunnel consists mainly of a filter, a nozzle with flow straighteners, the test section, a damping chamber, a diffuser, and an AC fan. The main duct which supplies air to the test section contains the impeller fan. a flow straightener (screen) at the air inlet side of the wind tunnel, honeycombs to reduce the swirl motion of the air stream and to break up occasional large eddies that may reach the working section. The air flow is induced by means of a fan driven by variable speed electric motor at the side of the tunnel. Air enters the base of the tunnel by way of a muslin strainer and is led through a contraction cone to the working section. The test section consists of rectangular duct (340mm ×340 mm and 600mm length). The tested model consists of square base plate, tested fins, and heating unit. The base plate is made from copper plate, of 100 mm long, 100 mm wide and 11 mm thickness. The tested fins are made from the pure copper plate of (t) thickness 0.075mm, (H) height 35 and 50mm and (L) long 100mm.

Four copper–constantan thermocouples were distributed uniformly along fin height at mid plane. During the experiments, the effect of the fin height (H), fins spacing (W) and the fins number (N) were investigated. The heating unit mainly consists of the four cartridge electric heater and the thermal insulation. The total heater output power is 1200 W at 250 V and current of 4.8A. The electrical power input to the heaters was controlled by a PID controller and power transformer variac to obtain constant heat flux along the base plate over the range of the tested conditions and measured by an in-line digital plug-in power and energy monitor. The cartridge heaters were isolated thermally by using Isofrax paper (k = 0.073W/m.K) also insulated from the bottom surface by Insulfrax Blanket (k = 0.07 W/m. K) with 80 mm thickness. The experiments of the fluid flow and heat transfer were carried out for each tested model for seven values of Reynolds number depend on hydraulic diameter of test section (10885.88 to 130630.61). Inside the test section, there is substrate with fins. The first fin is fixed at middle of the substrate and another two fins fixed on both sides of first fin. The finned substrate is fixed at bottom surface of test section.

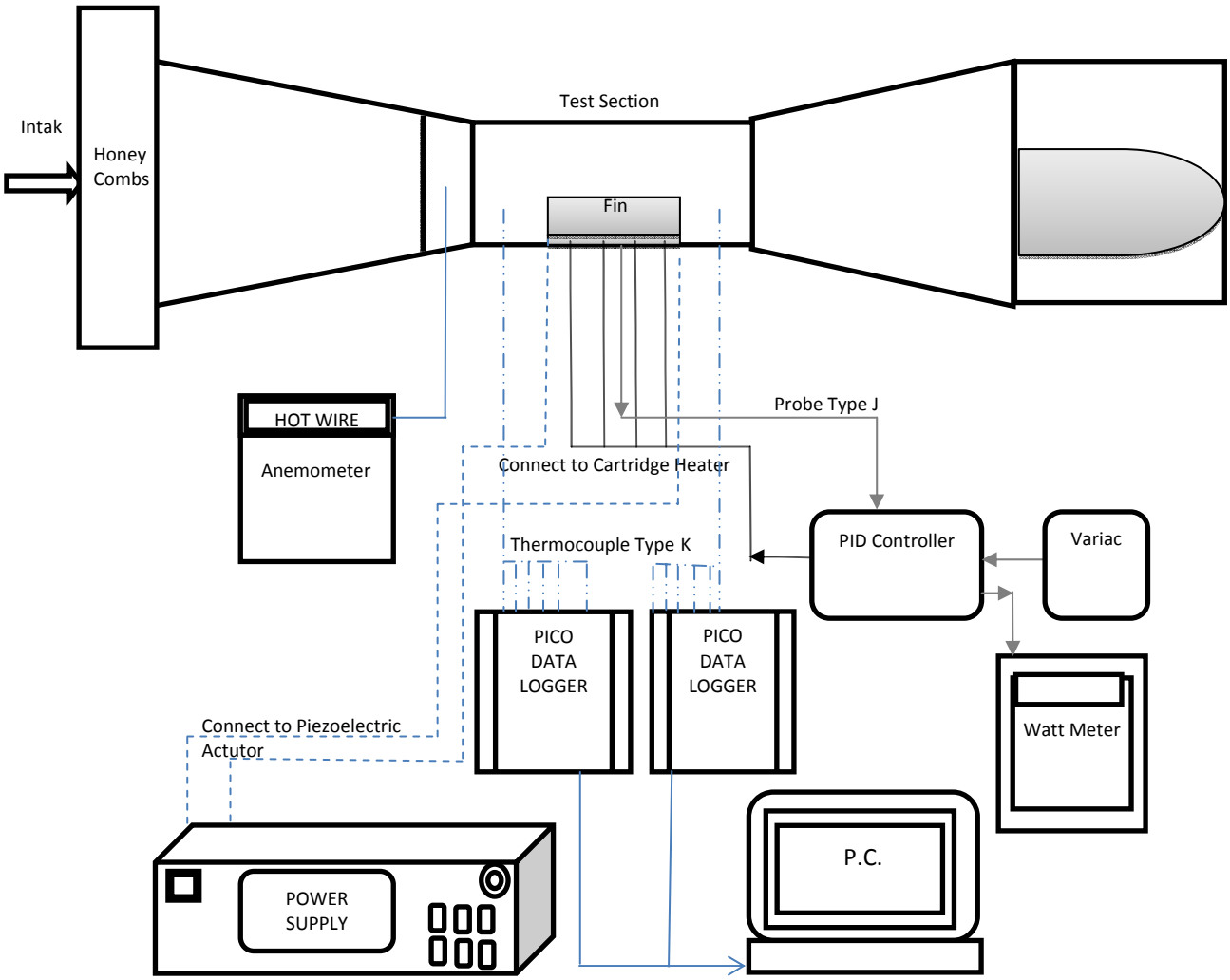

Fig.(3) A Schematic Drawing of the Experimental Set-Up

RESULTS AND DISCUSSION

1) Experimental results

Fig. (4) shows the steady state temperature distribution through the middle fin for case of fixed and oscillated fins with 50HZ. The temperature begins to drop with increase in the frequency. The cooling effect appears at the tip, that means the effect of oscillation increases with the height of fin and be more effective at tip of the fin. The top curve represents (T1) at root of the middle fin, and the lower curve is (T4) at the tip, the other two curves are between the root and tip. The best performance is with case of triple fins (height=50mm and the inter-fin space =3mm).

The temperature at the tip of the middle fin is decrease by (45 %) by using oscillating frequency of 50HZ w.r.t. case with fixed fins. For case (height =35mm and the inter-fin space =3mm), the influence of oscillation with this height is not effective. For case (height =50mm and the inter-fin space =6mm), where the cooling with this distance between the fins is good, the drop occurs in the temperature distribution from the root fin to the tip of the fin, but the effect of oscillation in this case is low. The temperature at the tip of the middle fin is decrease by (10 %) by using oscillating frequency of 50HZ w.r.t. case with fixed fins.

For the case (height =35mm and the inter-fin space =6mm), the cooling is good for substrate and fins with this height and distance between the fin, but the effect of oscillation is weak. For single fin case (height =50mm), where there is drop in the temperature distribution of the fin with increasing oscillation but with low effect. The temperature at the tip of the middle fin is decrease by (7 %) by using oscillating frequency of 50HZ w.r.t. case with fixed fins.

Fig. (5) shows the transient temperature distribution through the middle fixed and oscillated fin. The temperature is decreasing with increasing (Re) due to increasing the flow velocity around the fin and decreasing (B.L) thickness. The figure shows the change of temperature from the root of the fin (T1) to tip (T4), also the change with time until the steady state for all inlet velocity and input power. The temperature decreased with increasing the momentum of flow passes the fin. But, the high velocity affects the performance of oscillation or reduces the effect of oscillation, because the air works as damping to the oscillation. The result shows that the effect of oscillation on the tip of the fin is more than that in the root of the fin. So, the cooling of the fins with oscillation is better than the case without oscillation. The effect of frequency 50HZ on the temperature distribution through the middle fin indicates the best performance in transferring the heat from the substrate and dissipating through the fins, where the oscillation with this frequency helps the fin to deliver the heat quickly, this is especially observed at the tip of the fin.

Fig. (6) manifests the variation of the temperature at the tip of the middle fin with time for different inlet velocities and frequencies. The top curve case, no oscillations, displays higher temperature along the height of the fin until the near neighbourhood of the fin tip. There is a clear enhancement of the oscillations even for the moderate frequency of 5HZ, case (B). Then, the enhancement increases markedly along the fin height. With increasing frequency of oscillation, cases (C) and cases (D), even greater enhancements are attained. The temperature at the tip of the fin affects strongly with increasing the frequency, especially with 50HZ. This frequency produced a big drop in the temperature at the tip of the fin. This enhancement occurs for all inlet velocities in case (height=50mm and the inter-fin space =3mm). Also the best perform at low inlet velocity such as 0.5,1 and 2m/s.

Fig. (7) shows the variation of the temperature at the tip of the middle fin with time for different input powers. The improvement in the performance of enhancement of heat transfer with oscillation is observed, that is clear at high input power only from 20Watt to 50Watt and low velocity (0.5m/s, 1m/s and 2m/s). The temperature at the tip of the fin with oscillation begins in drop quickly from the first and uniformly after that.

Fig. (8) exhibits the effect of height of the fin (H) on the local Nusselt number for all inlet velocities and for fixed and oscillating fins at 50HZ, for case (height =50mm and the inter-fin space =3mm). The results display that local Nusselt number is higher at the tip of the fin, and it increases with increasing the inlet velocity, that means increasing the flow capacity for convective heat transfer. It is clear that (Nu) increases toward fins tip due to the convection of large heat from the tip of the fins. Local Nusselt number increases with frequency of 50HZ compare to fixed fins, and the relative improvement is better at lower Re than at higher values for fin oscillation. The local up wash on the lateral surfaces of the fin leads to an overall enhancement in heat transfer through the rest of the fin surface when compared with a conventional static fin. The variation in flow at the fin tip indicated strong flow fluctuations near the fin. At an oscillation frequency of 50HZ, the enhancement was large enough to give rise to surface heat transfer coefficients. Since the oscillation of the fins in the same direction and with large oscillation space, can generate larger airflow. for case (height =35mm and the inter-fin space =3mm or the inter-fin space =6mm), the increase of the frequency gave no significant effect on the local Nusselt number, because the height of piezoelectric is not suitable with this height of the fin; that means the height of the fin must be larger than height of the piezoelectric actuator. for case (height =50mm and the inter-fin space =6mm). The results show decrease in local Nusselt number compared to case (height=50mm and inter-fin space=3mm) especially at high velocity.

Fig. (9) illustrates the effect of height of the fin (H) on local heat transfer (Nusselt number) for all inlet velocities and for fixed and oscillated single fins with 50HZ, for case (height =50mm) and input power = 50Watt. The results display that (Nu) is higher at the tip of the fin also, the (Nu) increases with increasing inlet velocity, that means increasing the flow capacity for convective heat transfer. The comparison between the figures clarified the increase of the frequency with no significant effect on the local Nusselt number.

Fig. (10) present four cases which are respectively correspond to the four investigated cases: (A) no oscillation, (B) 5HZ oscillations, (C) 30HZ oscillations and (D) 50HZ oscillations. All cases are with input power 50Watt. The heat transfer is high and increases with increasing (y/h) until (y/h=1) due to the convection of large heat from the tip of the fins.

The results show that the best case is with frequency 50HZ, where a higher local Nusselt number determined, especially at the tip of the fin. Also the best performance is for oscillation with a range of velocity from 0.5m/s to 2m/s. After that, the increase of the velocity of the air gives no good performance, because the air at high velocity works as damping for oscillation.

Fig. (11) reveals the effect of height of the fin (H) on local heat transfer (Nusselt number) with a triple oscillated fin for frequency 50HZ. This case is with input power 10, 30 and 50Watt. The heat transfer is high and increases with increasing (y/h) until (y/h=1) due to the convection of large heat from the tip of the fin.

2) numerical results and comparison

Figure (12 to 15) present the numerical results of the present work compared to the experimental ones. Good agreement can be observed from the figures with maximum deviation of 5% for all investigated cases. The maximum deviation occurred at the tip of the fin.

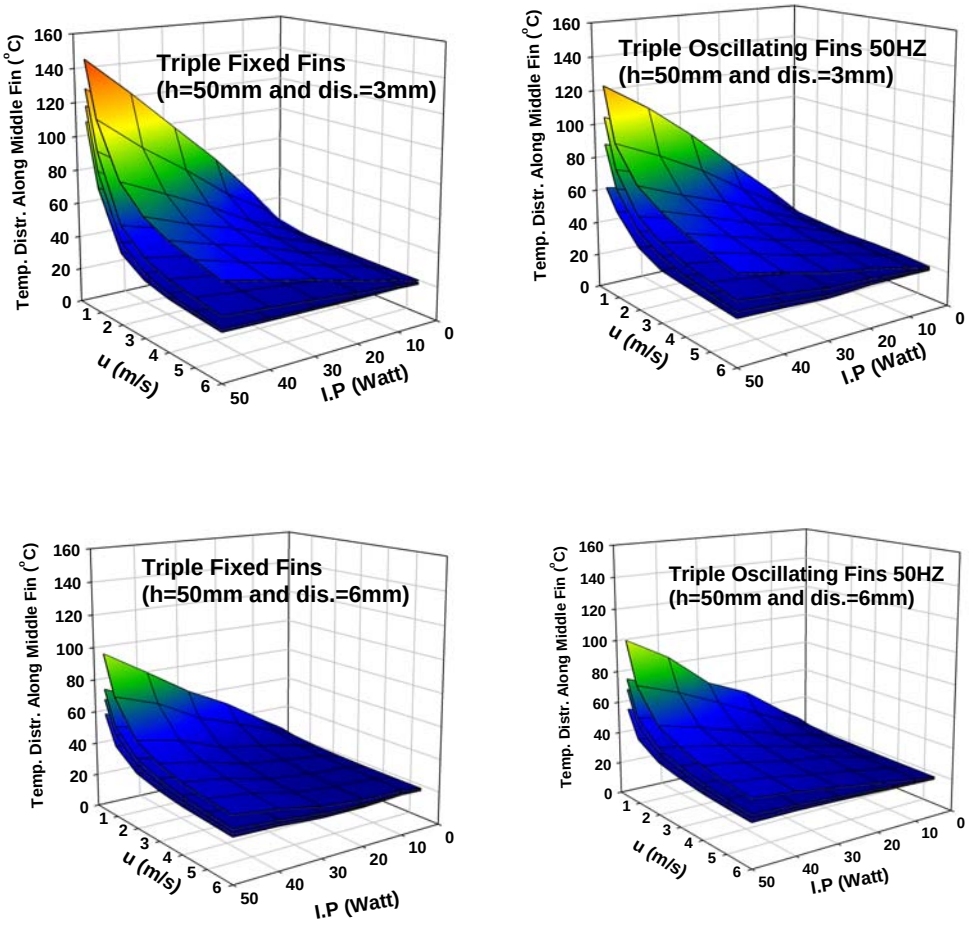

Fig. (4): Variations of the Temperature Distribution along the Height of Middle Fin with Inlet Velocity and Input Power. Single and Triple Fins

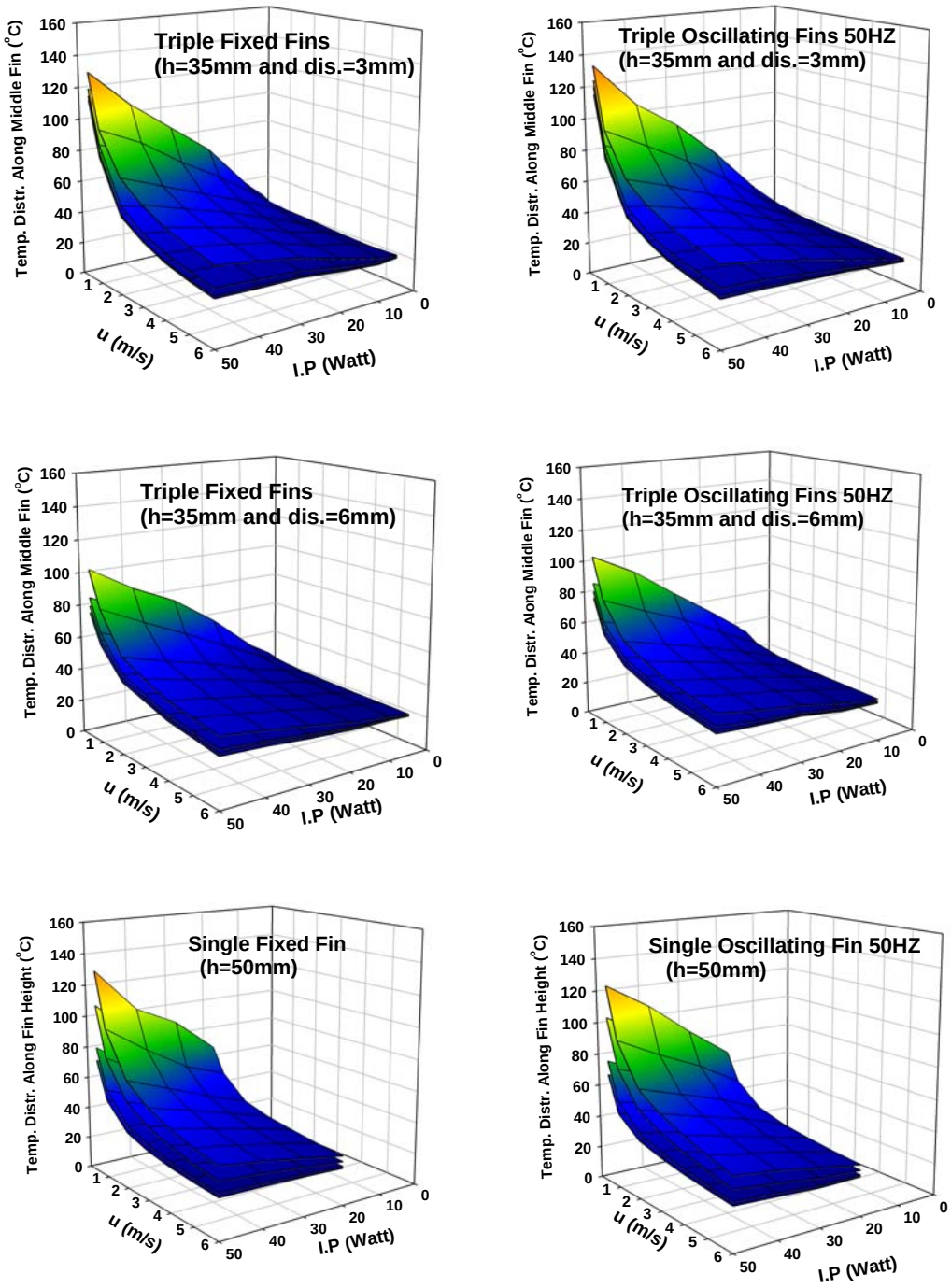

Fig. (4): Continued

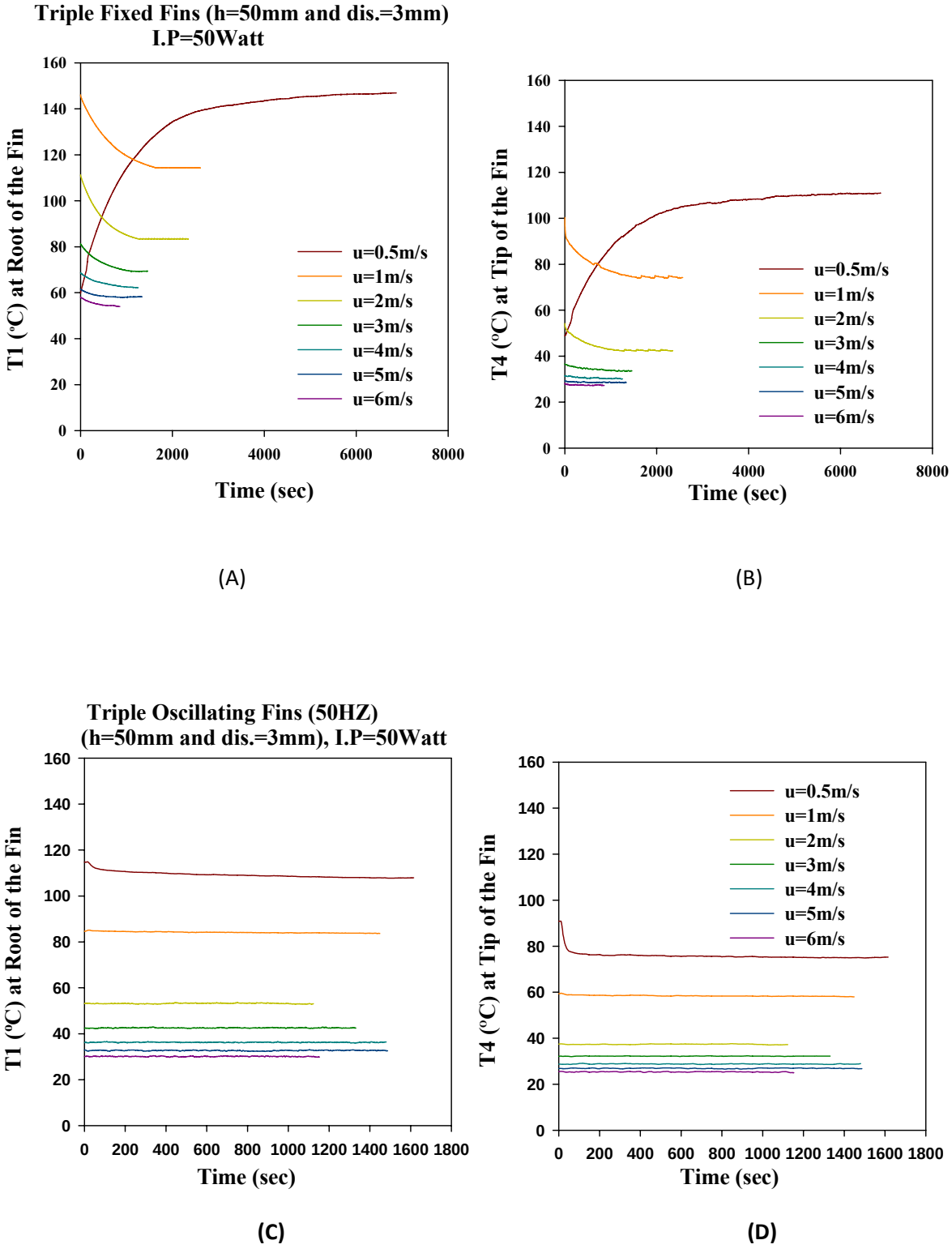

Fig. (5): Variations of the Temperature Distribution along the Middle Fin with Time for Various Inlet Velocities. (A, B); Triple Fixed Fins, (C, D) Triple Oscillating Fins Of (H=50mm and dis. =3mm).

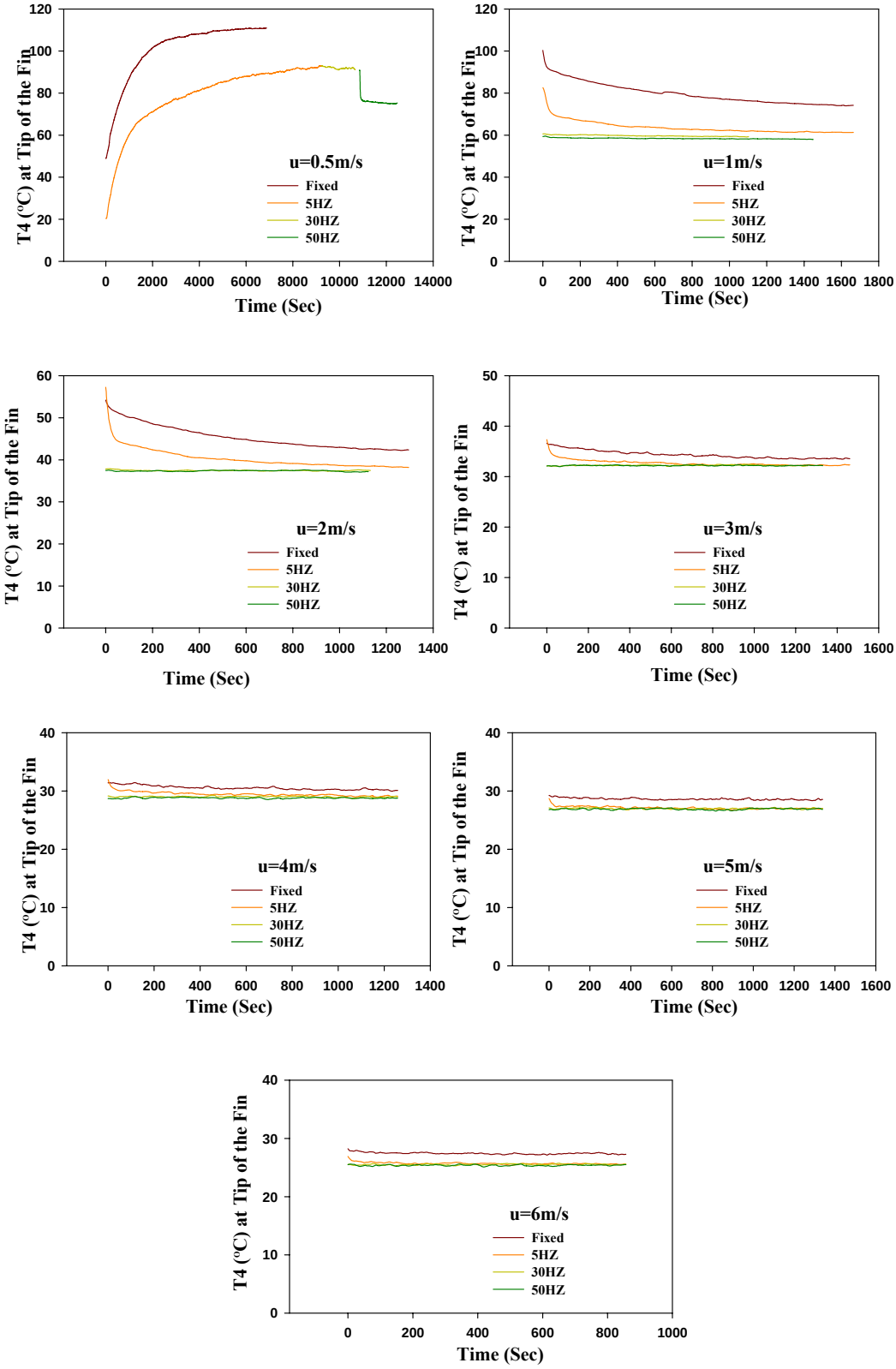

Fig. (6): Variations of the Temperature at the Tip of the Middle Fin with Time for Various Frequency and Inlet Velocity. Triple Fins Of (H=50mm and dis. =3mm), I.P=50Watt.

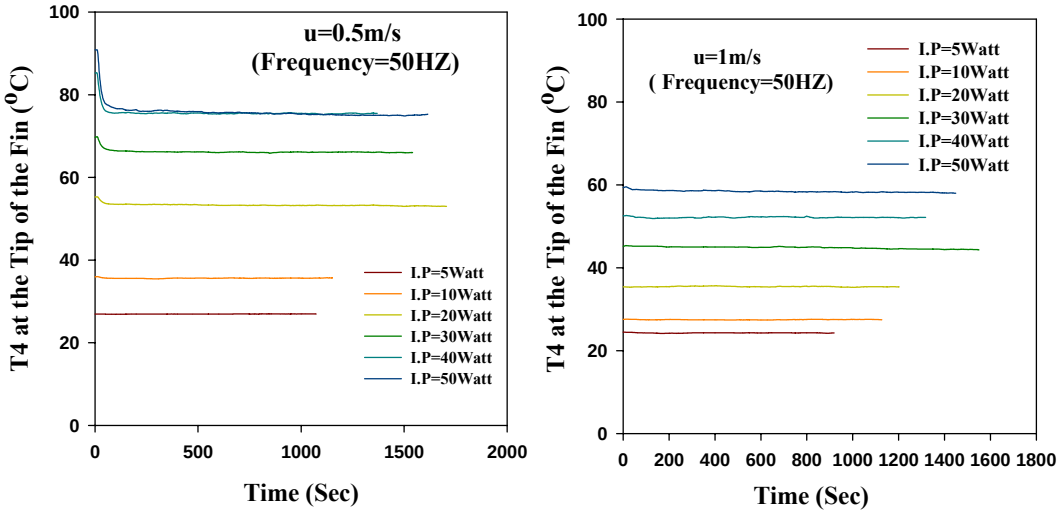

Fig.(7): Variation of the Temperature at the Tip of the Middle Fin with Time for Various Input Power and Inlet Velocity, Triple Fins of (H=50mm and dis.=3mm)

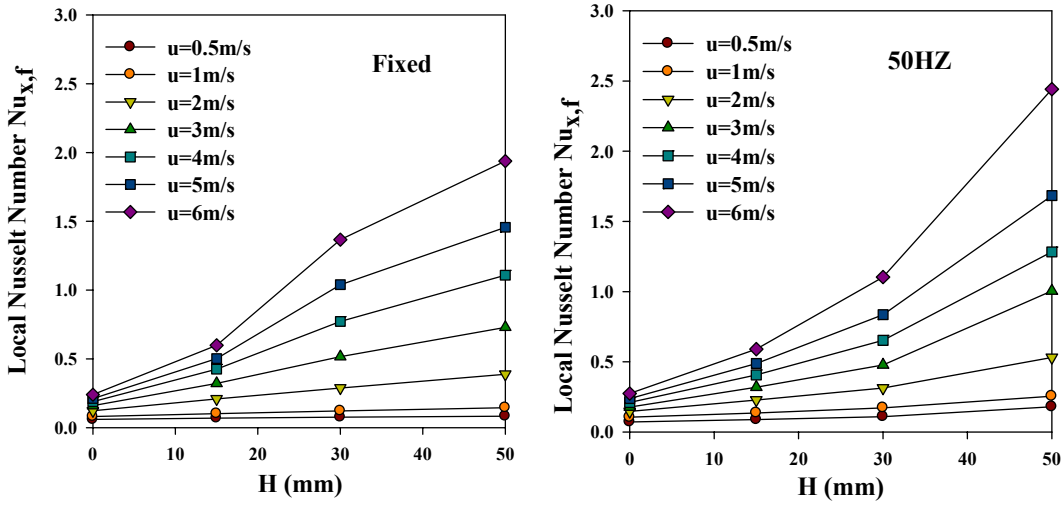

Fig. (8): Variation of the Local Nusselt Number along the Height of the Middle Fin For Different Inlet Velocity. Triple Fins of (H=50mm and dis. =3mm), I.P=50Watt.

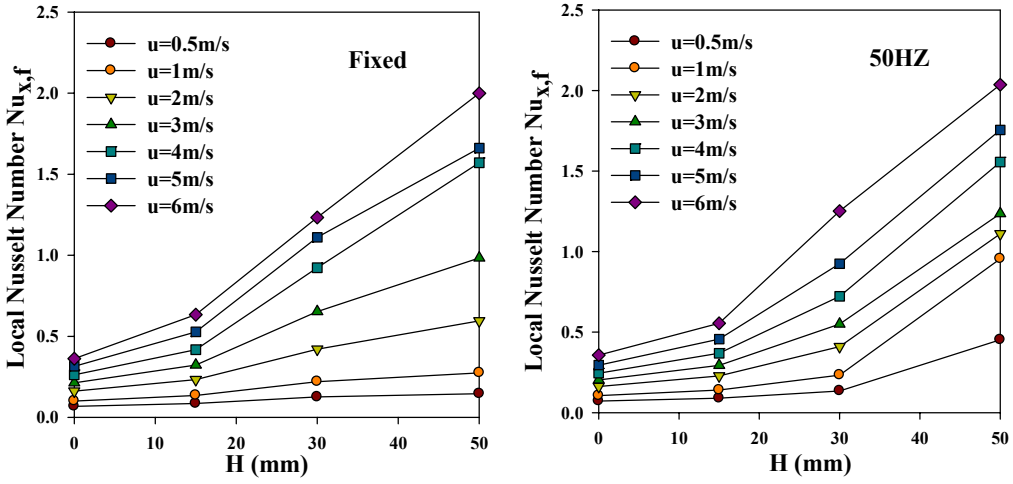

Fig. (9): Variation of the Local Nusselt Number along the Height of the Fin for Different Inlet Velocity. Single Fin (H=50mm), I.P=50Watt.

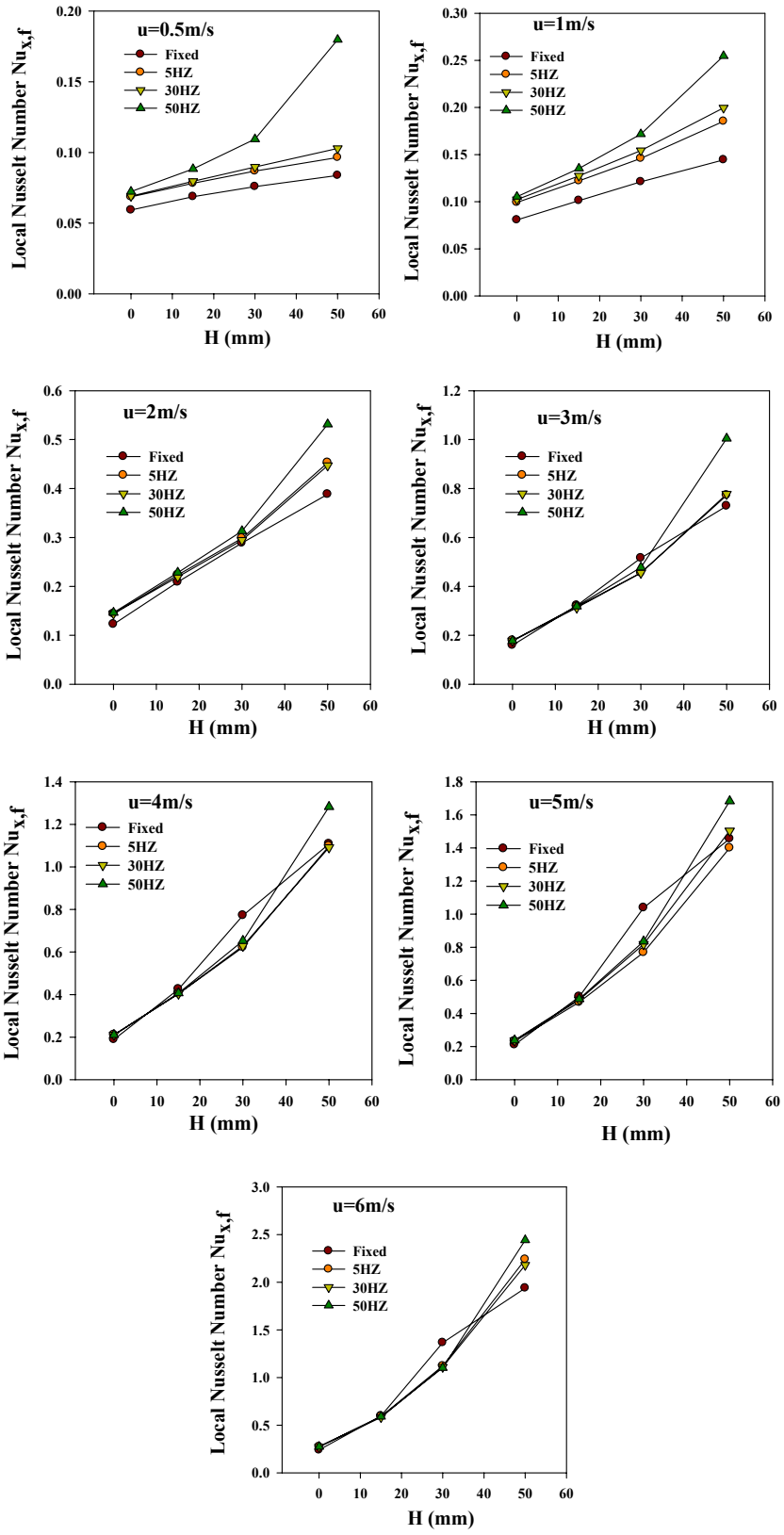

Fig. (10): Variation of the Local Nusselt Number along the Middle Fin with Height for Different Frequency. Triple Fin (H=50mm and dis. =3mm), I.P=50Watt.

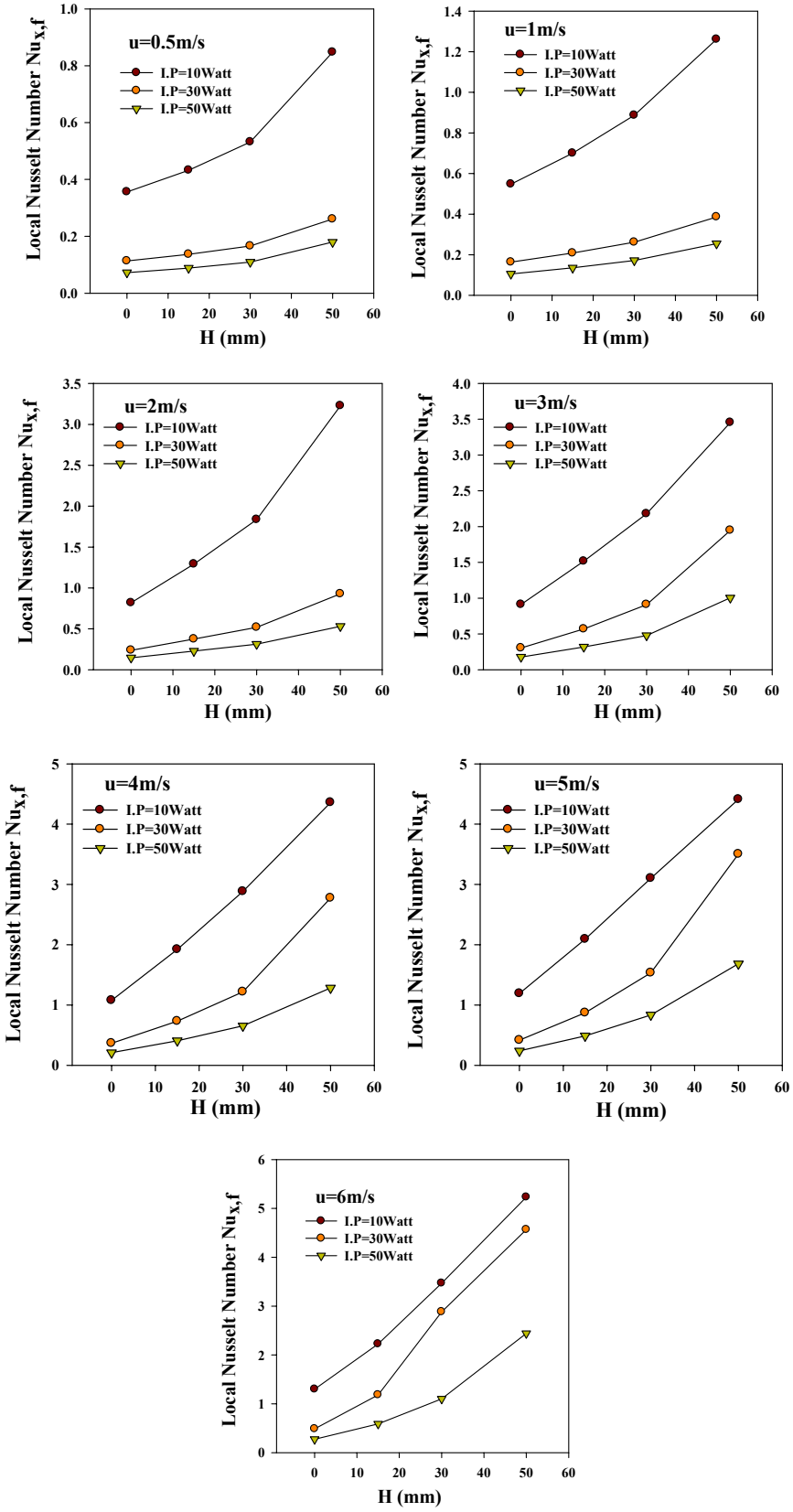

Fig. (11): Variation of the Local Nusselt Number along the Middle Fin with Height for Different Input Power. Triple Fin (H=50mm and dis.=3mm), Frequency=50HZ.

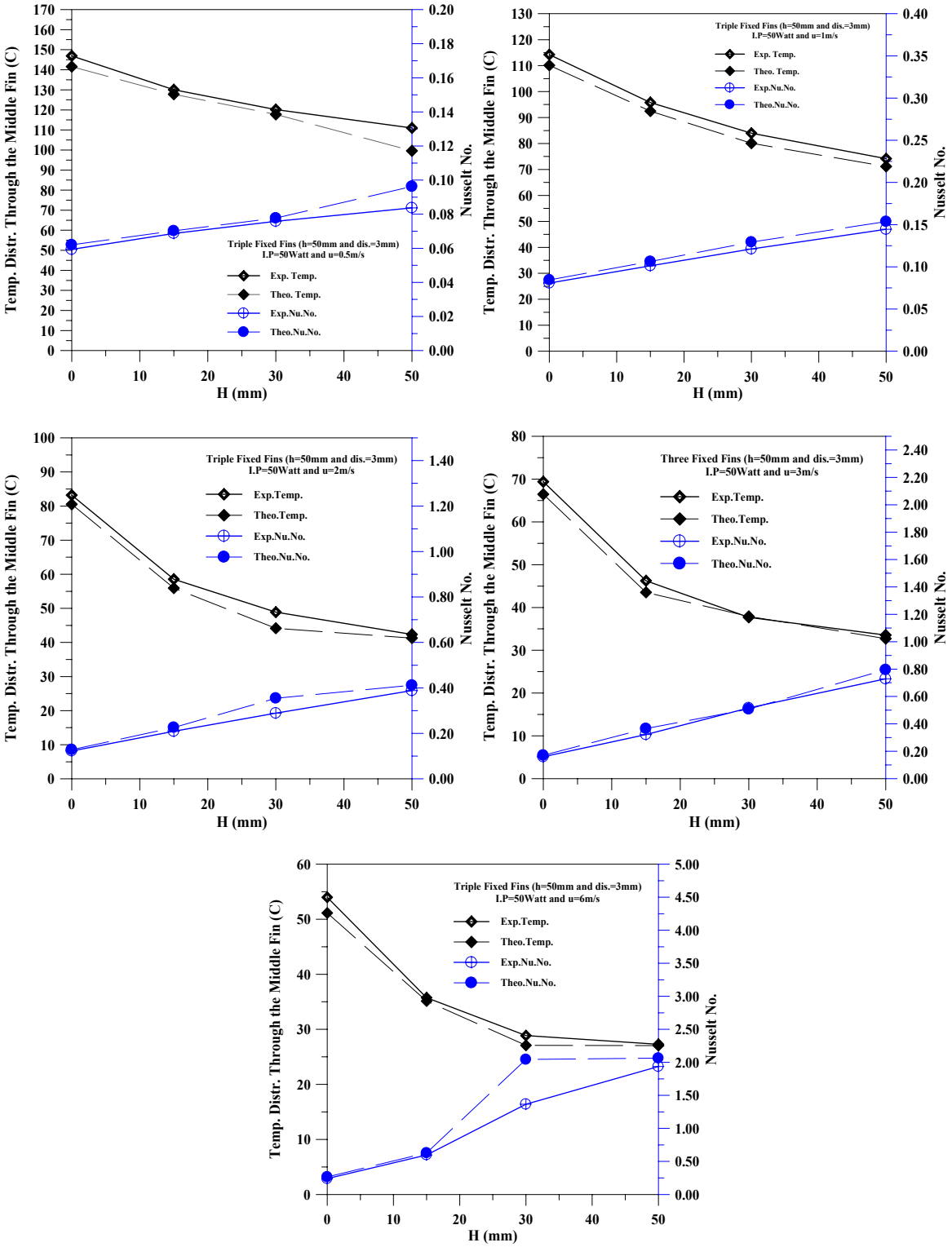

Fig. (12): Comparison between Experimental and Theoretical Temperature Distribution and Local Nusselt No. through the Height of the Middle Fin. (Triple Fixed Fins)

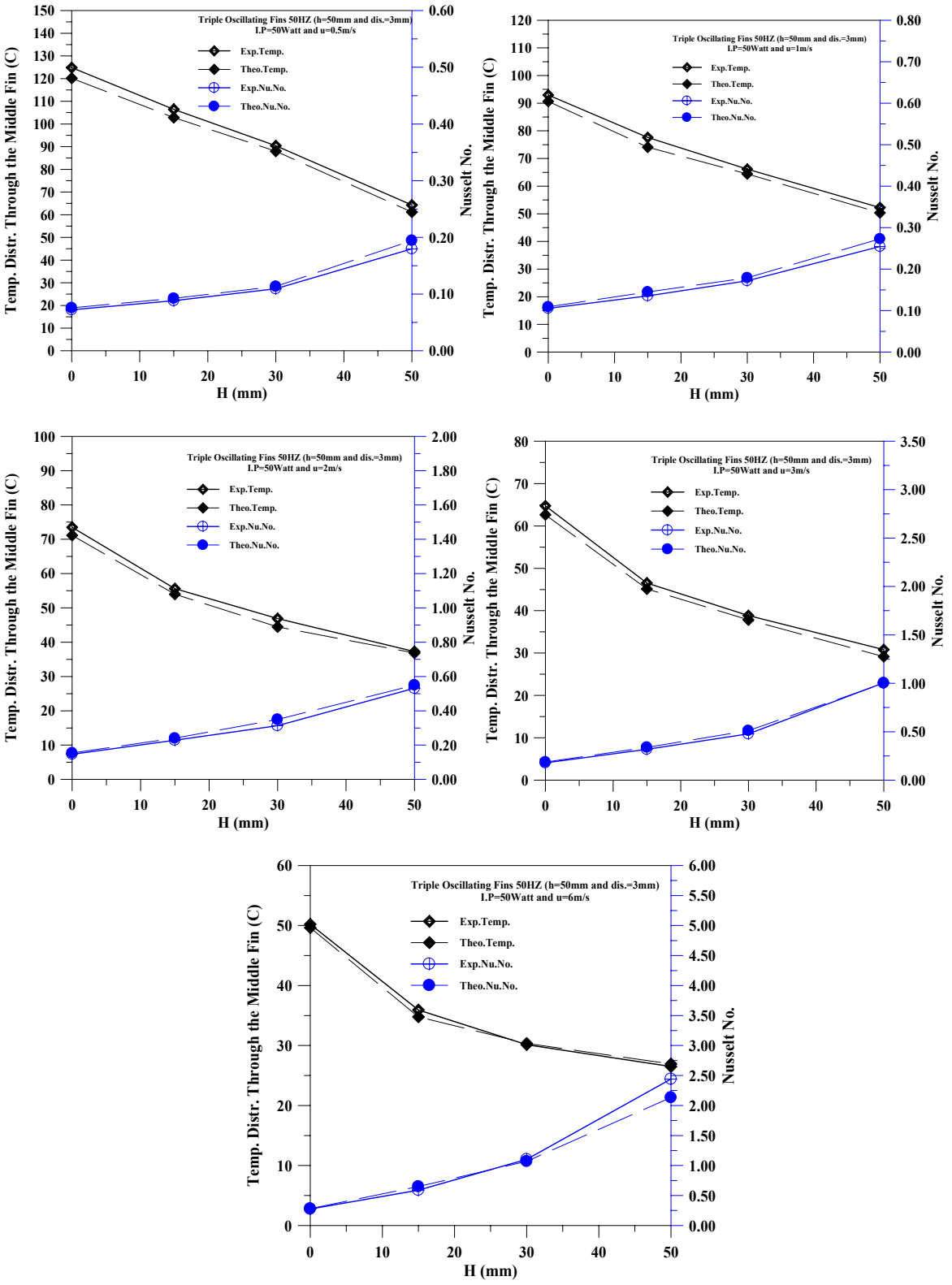

Fig. (13): Comparison between Experimental and Theoretical Temperature Distribution and Local Nusselt No. through the Height of the Middle Fin. (Triple Oscillating Fins)

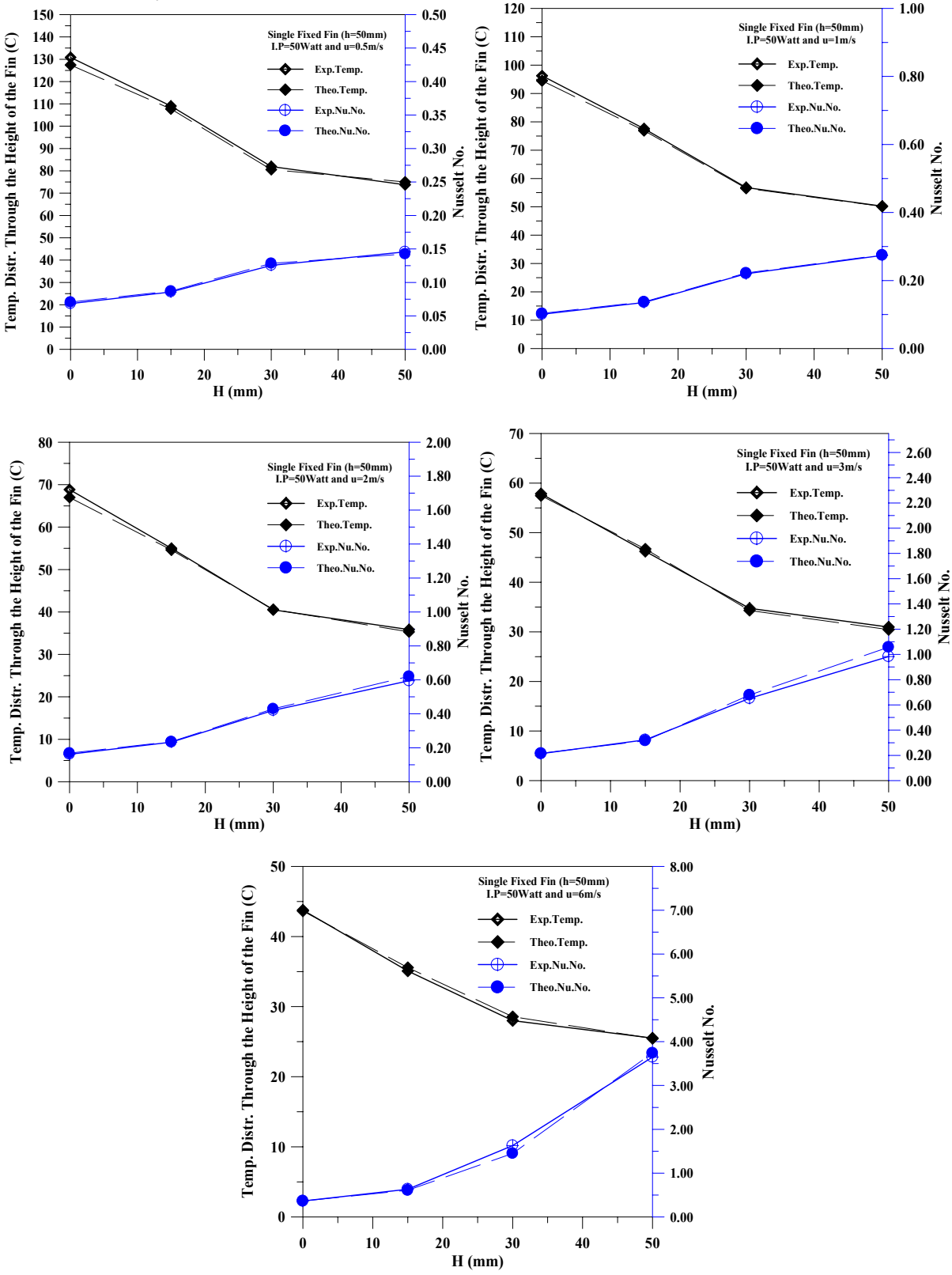

Fig. (14): Comparison between Experimental and Theoretical Temperature Distribution and Local Nusselt No. through the Height of the Middle Fin. (Single Fixed Fin)

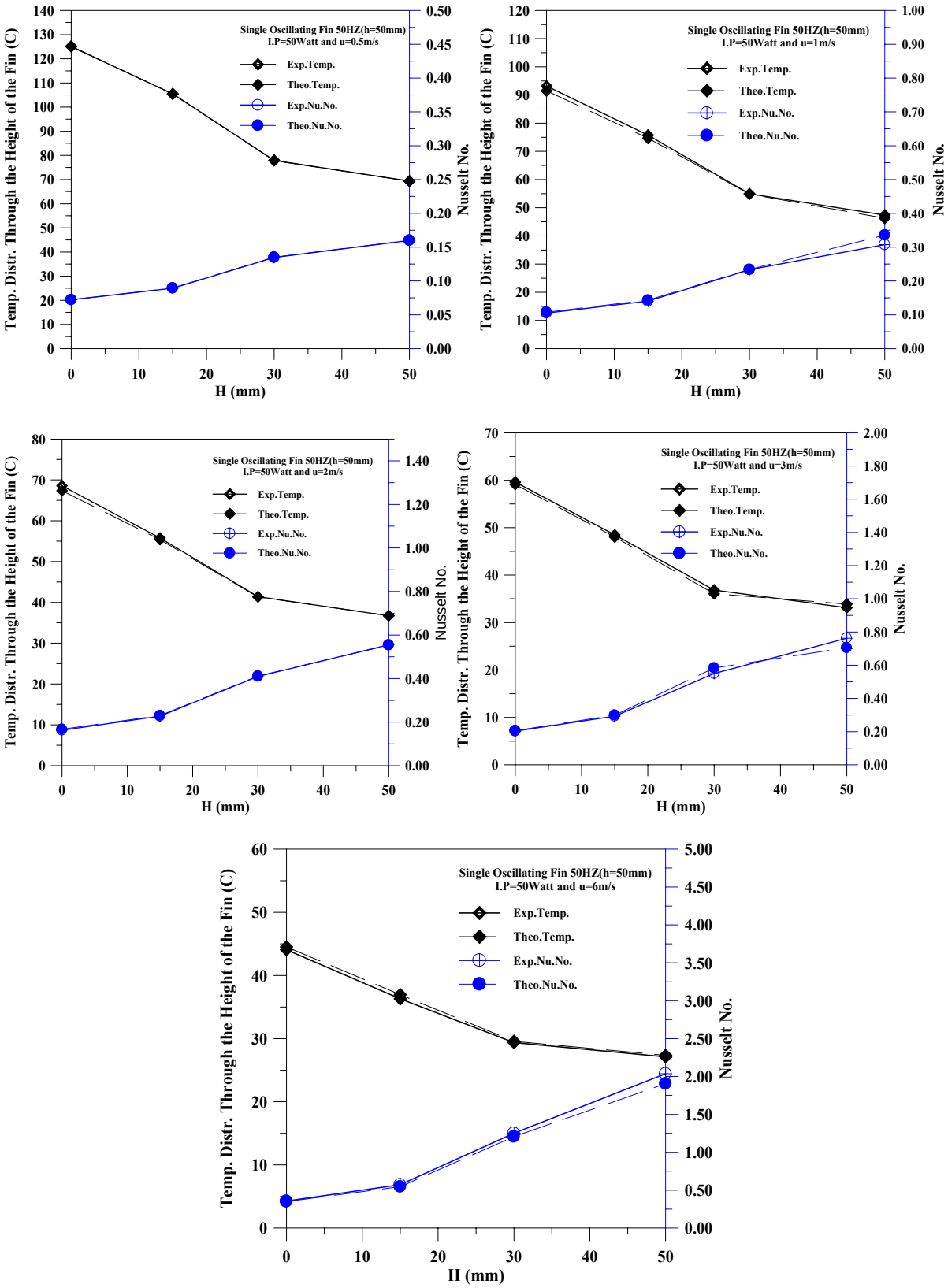

Fig. (15): Comparison between Experimental and Theoretical Temperature Distribution and Local Nusselt No. through the Height of the Middle Fin. (Single Oscillating Fin)

CONCLUDING REMARKS

It was concluded that:

1- Triple fins (h=50mm and dis.=3mm) is the best case for enhancing heat transfer and the triple fins (h=35mm and dis.=3mm) gives minimum heat transfer with respect to the other height.

2- The maximum enhancement of heat transfer occurs at the tip of the fins.

3- With low velocity and high input power, The temperature at the tip of the middle fin is decrease by (45 %) by using oscillating frequency of 50HZ for the case (h=50mm and dis.=3mm) w.r.t. case with fixed fins. While 10% for the case (h=50mm and dis.=6mm) and 7% for single fin.

4- The optimal height for the fins is 35mm. so the better cooling with triple fixed fins for the case (h=35mm and dis.=3mm or dis.=6mm). While this height is not effective with oscillating.

5- The enhancement of heat transfer with oscillating well with low velocity from 0.5m/s to 2m/s and high input power.

6- The high velocity effect reduce the effect of oscillation because the air work as damping to the oscillating.

ACKNOWLEDGEMENT

The authors thank Prof.Dr.Tim O'Doherty , BEng PhD CEng FIMechE MEI and Dr.Daphne M O'Doherty, BEng PhD CEng MIMechE MEInst for their contributions to current work. We Also thank Mr. Paul Malpus and Mr.Steev from the Workshop in School of Engineering in Cardiff University, Institute of Energy.

REFERENCES

Chin-Hsiang Cheng, Jing-Lia Hong, (1997): "Numerical Prediction of Lock-on Effect on Convective Heat Transfer from a Transversely Oscillating Circular Cylinder" Int.J. Heat Mass Transfer. Vol. 40, No.8, pp. 1825-1834.

C.Gau , S.X.Wu and H.S.Su, (2001): "Synchronization of Vortex Shedding and Heat Transfer Enhancement Over a Heated Cylinder Oscillating with Small Amplitude in Streamwise Direction" J. Heat Transfer , vol/123, December by ASME, pp.1139-1148.

David J.Kukulka, Kevin G. Fuller, (2010): "Development of an Enhanced Heat Transfer Surface" 20th European Symposium on Computer Aided Process Engineering-ESCAPE20, Elsevier B.V.

H.G.Park and Morteza Gharib, (2001): "Experimental Study of Heat Convection From Stationary and Oscillating Circular Cylinder in Cross Flow" J. Heat Transfer , vol/123, December by ASME, pp.51-62.

H.M.Blackburn and G.E.Karniadakis, (1993): "Two- and Three-Dimensional Simulations of Vortex-Induced Vibration of a Circular Cylinder" Presented at the 3RD Int. Offshore &Polar Engng Conf., Singapore, 3, 715-720.

Hiroshi Ishigaki, (1971): "The Effect of Oscillation on Flat Plate Heat Transfer" J.Fluid Mec. National Aerospace Laboratory, Kakuda Branch, Miyagi, Japan, Vol. 47, part 3, pp. 537-546.

Jalal M. Jalil, Adil A.H.Al-Moosawy, Mohsen G.Hamza, (2009): "Heat transfer Enhancement Due to Oscillating Heated Cylinder in a Cross Flow at Low Reynolds Numbers" J. of Enhanced Heat Transfer, Vol. 16, No.1, pp. 1-17.

Osama A.Marzouk , (2009): "Direct Numerical Simulations of the Flow Past a Cylinder Moving with Sinusoidal and Nonsinusoidal Profiles" J. Fluid Engineering, Vol. 131, ASME , pp. 1-8.

R. Mohan and Dr. P. Govindarajan , (2011): " Thermal Analysis of CPU with CCC and Copper Base Plate Heat Sinks Using CFD". Heat Transfer-Asian Research, 40(3).

Subhrajit Dey and Debapriya Chakrbrty, (2009): "Enhancement of Convective Cooling Using Oscillating Fins" Int. Communications in Heat and Mass Transfer 36 pp. 508-512.

Tait Sherman Pottebaum and Mory Gharib, (2006): "Using Oscillations to Enhance Heat Transfer for a Circular Cylinder" Int. J. Heat and Mass Transfer 49 , pp.3190-3210.

Wu-Shung Fu, Bao-Hong Tong, (2002): "Numerical Investigation of Heat Transfer From a Heated Oscillating Cylinder in a Cross Flow" Int. J. Heat and Mass Transfer 45 , pp.3033-3043.

W.-S. Fu, S.-J.Yang, "Numerical Simulation of Heat Transfer Induced by a Body Moving in the Same Direction as Flowing Fluids" Int. J. heat mass transfer, 36, pp.257-264, 2000.

Wu-Shung Fu and Suh-Jenq Yang, (2001): "Heat transfer Induced by a Body Moving in Opposition to a Flowing Fluid" Int. J. heat mass transfer, 44, pp.89-98.

Wu-Shung Fu, Shih-Fa Chen and Ke-Nan Wang, (2001): "Effect of Moving Distance of a Moving Block on Heat Transfer in a Channel Flow" Int. J. heat mass transfer, Vol. 28, No.3, pp. 411-426.

Wu-Shung Fu, Jieh-Chau Huang, Chung-Gang Li (2010): "Enhancement of Forced Convection Heat Transfer in a Three-Dimensional Laminar Channel Flow with Insertion of a Moving Block" Int. J. heat mass transfer, 53, pp. 3887-3897.

W.-S.Fu, S-J. Yang, (2001): "A numerical Study of Effects of the Swinging Amplitude of Fins on Heat Transfer Characteristics in a Flow" Int. J. heat mass transfer, 38, pp. 55-63, 2001.

Yue-Tzu Yang and Cheng-Hua Chen, (2008): "Numerical Simulation of Turbulent Fluid Flow and Heat Transfer Characteristics of Heated Blocks in the Channel with an Oscillating Cylinder" Int. J. heat mass transfer, 51, pp.1603-1612.

NOMENCLATURE

CPU	Central Processing Unit
dis.	Distance Between the Fin (mm)
D_h	Hydraulic Diameter (mm)
h	Local Heat Transfer Coefficient ($W/m^2.^oC$)
H	Height of the Duct (mm)
I.P.	Input Power (Watt)
K	Thermal Conductivity ($W/m.^oC$)
Lc	Characteristic Length of the Fin
L	Length of the Duct (mm)
N	Number of Fins
$Nu_{x,f}$	Local Nusselt Number = h Lc/Ka
PID	Proportional Integral and Derivative
Re	Reynolds Number = $\rho V D_h / \mu$
t	Thickness of the Fin (mm)
T	Temperature (^oC)
T1	Temperature at the Root of the Fin (^oC)
T4	Temperature at the Tip of the Fin (^oC)
u	Inlet Velocity (m/s)
u	x-Direction Velocity (m/s)
UDF	User Defined Function
v	y-Direction Velocity (m/s)
w	Z-Direction Velocity (m/s)
W	Width of the Duct (mm)
X, Y, Z	Rectangular Coordinates

Vibration Control Analysis of a Smart Flexible Cantilever Beam Using Smart Material

Dr. Wedad Ibraheem Majeed
University of Baghdad
Eng. Coll. Mech. Dep.

Dr. Shibly Ahmed Al-Samarraie
University of Technology
Mechatronic Dep.

Mohanad Mufaq AL-SAIOR
University of Baghdad
Eng. Coll. Mech. Dep.

ABSTRACT

This paper features the modeling and design of a pole placement and output Feedback control technique for the Active Vibration Control (AVC) of a smart flexible cantilever beam for a Single Input Single Output (SISO) case. Measurements and actuation actions done by using patches of piezoelectric layer, it is bonded to the master structure as sensor/actuator at a certain position of the cantilever beam.

The smart structure is modeled based on the concept of piezoelectric theory, Bernoulli -Euler beam theory, using Finite Element Method (FEM) and the state space techniques. The number of modes is reduced using the controllability and observability grammians retaining the first three dominant vibratory modes, and for the reduced system, a control law is designed using pole placement and output feedback techniques.

The analyzed case studies concern the vibration reduction of a cantilever beam with a collocated symmetric piezoelectric sensor/actuator pair bonded on the surface. The transverse displacement time history, for an initial displacement field at the free end, is evaluated. Results are compared with other works, and the control design shows that Pole Placement method is an effective method for vibration suppression of the beam and settling time reduction.

Keywords: vibration, active vibration control, smart material, cantilever beam.

الخلاصة:

هذا البحث يصف التمثيل الرياضي والتصميم لطريقة السيطرة الخاصة بتغيير موقع الجذور واستخدام الارجاع للمتغيرات الناتجة وذلك لاستخدام السيطرة الفاعلة على الاهتزازات لعتبة ذكية وباستخدام حالة ادخال واخراج مفردة. عمليات التوجيه و التحسس لازاحة العتبة تتم بواسطة موجهات و متحسسات مصنوعة من المواد الذكية على شكل ملصقات باحجام محددة تكون ملصوقة على سطح العتبة الرئيسية و بمواقع محددة.

تمت نمذجة العتبة الذكية باستخدام نظرية المواد الكهربية الذكية، نظرية برنولي – اويلر للعتبات و نظرية العناصر المحددة و حل المعادلات باستخدام نظرية الحالة المخمنة. عدد الاطوار الكلي للنموذج تمت تقليصها الى الثلاث اطوار الاساسية و المسيطرة باستخدام نظرية محددات معاملات السيطرة و التخمين. تم تصميم قانون للسيطرة للنموذج المقلص الجديد حيث استخدمت نظرية ابدال الجذور للنموذج الرياضي و السيطرة باستخدام ارجاع المخرجات.

درست الحالة في هذا البحث تقليص الاهتزاز لعتبة مصنوعة من الالمينوم باستخدام زوج واحد من المواد الذكية ملصوق بشكل متناظر على سطحي العتبة. الاهتزاز في العتبة منتج بواسطة ازاحة راس العتبة من الجهة السائبة بمسافة 1 سم. و تم تسجيل هذا الاهتزاز بالنسبة للزمن اضافة الى ذلك تمت مقارنة النتائج باعمال اخرى. اظهرت الدراسة ان نظرية السيطرة الفاعلة للاهتزاز فعالة لاخماد الاهتزازات في هكذا هياكل.

INTRODUCTION

It is desired to design lighter mechanical systems carrying out higher workloads at higher speeds. However, the vibration may become prominent factor in this case. Smart materials and active control methods can be used to eliminate the undesired vibration. This combination of smart material and active vibration control paid considerable attention in the last decade especially in the space structures application.

Since the middle of the 19th century and due to the importance of providing a lighter, strong and vibration resisting structures specially in aero-structure and space application, the smart materials and active vibration control methods considered important for these application [Anna-Maria R. McGowan, 1998].

1.1. Piezoelectric Materials (Smart Materials)

In the year 1880, the brothers Pierre and Jacques Curie discovered the direct piezoelectric effect at tourmaline crystals. The inverse piezoelectric effect was predicted in 1881 by M. G. Lippmann based on thermodynamic considerations and afterwards confirmed experimentally by the brothers Curie [R.G. Ballas, 2007].

T.C. Manjunath and B. Bandyopadhyay (2007) [T.C. Manjunath, 2007] presented the modeling and design of a (FOS) Feedback control technique for the Active Vibration Control of a smart flexible aluminium Cantilever beam for a (SISO) case. The entire structure modeled in state space form using the concept of piezoelectric theory, Euler-Bernoulli beam theory and FEM techniques. The conclusions drawn for the best performance and for smallest magnitude of the control input required to control the vibrations of the beam. The MATLAB program used in results simulations.

Tamara Nestorović and Miroslav Trajkov (2010) [Tamara Nestorović, 2010] studied the piezoelectric applications in active vibration and noise attenuation in mechanical and civil engineering involving subsequent steps of modeling, control, simulation, experimental verification and implementation.

Deepak Chhabra, Pankaj Chandna , Gian Bhushan (2011) [Deepak Chhabra, 2011] designed the state/output feedback control by Pole placement technique and LQR optimal control approach achieve the desired control for the same smart cantilever beam in [T.C. Manjunath, 2007]. Sufficient vibrations attenuation was achieved. Pole placement technique is used to obtain the desired Eigen values of controlled system.

Meysam Chegini, Milad Chegini and Hadi Mohammadi (2011) [Meysam Chegini, 2011] used the PID control technique in their paper instead of (FOS) Feedback controller in (T.C. Manjunath and B. Bandyopadhyay (2007)) for the same smart cantilever beam, concluding that it is possible to implement classical controllers, such as PID and PI to control the amplitude and time of the vibration.

The analysis performed by **Gergely Takács (2011)** [Gergely Takács, 2011] presents the smart cantilever beam but with digital feedback control loops inside ANSYS transient simulations using the proprietary macro language of the software package. The close agreement of the closed-loop simulation results and laboratory measurements indicates the potential to use ANSYS for the preliminary prototyping of active vibration control systems (AVC).

1.2. Smart Structures

Piezoelectric materials could be divided, from structural viewpoint, into ceramic and polymeric forms. The most popular piezoelectric ceramics (or in short, piezoceramics) are compounds of lead zirconate titanate (PZT), the properties of which can be optimized to suit specific applications by appropriate adjustment of the zirconate–titanate ratio.

The polymeric form of the piezoelectric materials as polyvinylidene fluoride (PDVF) having low stiffness and electromechanical coupling coefficients (when compared to ceramics like PZT, for instance) [Nader Jalili, 2010].

Structures with added functionality over and above the conventional purpose of providing strength by reinforcement or stiffness may be regarded as smart. Smart or adaptive structures, based on using a small change in the structure geometry at critical locations induced by internally generated control signals, can result in a non-linear amplification of the shape, stiffness or strength, and so the structure will adapt to a functional need. In practice, smart structures may be classified depending on their functionality and adaptation to the changing situation:

1. *Passive smart*
2. *Active smart*
3. *Intelligent*.

2. MODELING OF SMART CANTILEVER BEAM

The smart structure is modeled based on the concept of piezoelectric theory, Bernoulli - Euler beam theory, using Finite Element Method (FEM).

2.1. Displacement Functions

A beam element is considered with two nodes at its end. Each node is having two degree of freedom (DOF). The shape functions of the element are derived by considering an approximate solution and by applying boundary conditions. The mass and stiffness matrix is derived using shape functions for the beam element. Mass and stiffness matrix of piezoelectric (sensor/actuator) element are similar to the beam element. To obtain the mass and stiffness matrix of smart beam element that consists of two piezoelectric materials and a beam element, all the three matrices added.

FEM assembly of beam element and smart beam element models the cantilever beam. The last two row's two elements of first matrix are added with first two row's two element of next matrix. The global mass and stiffness matrix is formed. The boundary conditions are applied on the global matrices for the cantilever

beam. The first two rows and two columns should be deleted as one end of the beam is fixed. The actual response of the system, i.e., the tip displacement u (x,t) is obtained for all the various models of the cantilever beam with and without the controllers[Deepak Chhabra, 2011].

A beam element of length L_b with two DOFs at each node i.e. translation and rotation is considered[T.C. Manjunath, 2007].

$$W(x) = a_1 + a_2 x + a_3 x^2 + a_4 x^3, \quad (1)$$

Application of the boundary condition of the cantilever beam yields:

$$\begin{bmatrix} a_1 \\ a_2 \\ a_3 \\ a_4 \end{bmatrix} = \frac{1}{l_b^3} \begin{bmatrix} l_b^3 & 0 & 0 & 0 \\ 0 & l_b^3 & 0 & 0 \\ -3l_b & -2l_b^2 & 3l_b & -l_b^2 \\ 2 & l_b^3 & -2 & l_b^3 \end{bmatrix} \begin{bmatrix} w_1 \\ \theta_1 \\ w_2 \\ \theta_2 \end{bmatrix}, \quad (2)$$

Substituting the constants obtained from (2) into (1) and by rearranging the terms, the final form for W(x) is obtained as:

$$w(x) = [n]^T [q], \quad (3)$$

where $[n]$ gives the shape function as, [Ranjan Vepa, 2010]:

$$[n] = \begin{bmatrix} 1 - 3\frac{(x-x_i)^2}{l_b^2} + 2\frac{(x-x_i)^3}{l_b^3} \\ (x-x_i) - 2\frac{(x-x_i)^2}{l_b} + 2\frac{(x-x_i)^3}{l_b^2} \\ 3\frac{(x-x_i)^2}{l_b^2} - 2\frac{(x-x_i)^3}{l_b^3} \\ -\frac{(x-x_i)^2}{l_b} + 2\frac{(x-x_i)^3}{l_b^2} \end{bmatrix}, \quad (4)$$

and $[q]$ is the vector of displacements and slopes (nodal displacement vector) and is given by:

$$[q] = \begin{bmatrix} w_1 \\ \theta_1 \\ w_2 \\ \theta_2 \end{bmatrix}, \quad (5)$$

2.2. DYNAMIC EQUATION OF THE BEAM ELEMENT

The equation of motion of the regular beam element is obtained by the lagrangian equation:

$$\frac{d}{dt}\left[\frac{\partial T}{\partial \dot{q}_i}\right] + \left[\frac{\partial U}{\partial q_i}\right] = [F_i], \quad (6)$$

As:

$$M^b \ddot{q} + K^b q = f^b(t), \quad (7)$$

The strain energy U and the kinetic energy T for the beam element with uniform cross section in bending is obtained as:

$$U = \frac{E_b I_b}{2} \int_{l_b} \left[\frac{\partial^2 w}{\partial x^2}\right] dx, = \frac{E_b I_b}{2} \int_{l_b} [w''(x,t)]^T [w''(x,t)] dx, \quad (8)$$

$$T = \frac{\rho_b A_b}{2} \int_{l_b} \left[\frac{\partial w}{\partial t}\right]^2 dx, = \frac{\rho_b A_b}{2} \int_{l_b} [\dot{w}(x,t)]^T [\dot{w}(x,t)] dx, \quad (9)$$

Element in its explicit form is obtained as:

$$\frac{\rho_b A_b}{420} \begin{bmatrix} 156 & 22l_b & 54 & -13l_b \\ 22l_b & 4l_b^2 & 13l_b & -3l_b^2 \\ 54 & 13l_b & 156 & -22l_b \\ -13l_b & -3l_b^2 & -22l_b & 4l_b^2 \end{bmatrix} \begin{bmatrix} \ddot{w}_1 \\ \ddot{\theta}_1 \\ \ddot{w}_2 \\ \ddot{\theta}_2 \end{bmatrix} + \frac{E_b I_b}{l_b} \begin{bmatrix} \frac{12}{l_b^2} & \frac{6}{l_b} & -\frac{12}{l_b^2} & \frac{6}{l_b} \\ \frac{6}{l_b} & 4 & -\frac{6}{l_b} & 4 \\ -\frac{12}{l_b^2} & -\frac{6}{l_b} & \frac{12}{l_b^2} & -\frac{6}{l_b} \\ \frac{6}{l_b} & 4 & -\frac{6}{l_b} & 4 \end{bmatrix} \begin{bmatrix} w_1 \\ \theta_1 \\ w_2 \\ \theta_2 \end{bmatrix} = \begin{bmatrix} F_1 \\ M_1 \\ F_2 \\ M_2 \end{bmatrix}, \quad (10)$$

where F_1 and $F_2$are the forces at the nodes 1 and 2, M_1 and M_2 are the bending moments acting at the nodes 1 and 2 respectively.

The piezoelectric beam element shown in Figure (1) is obtained by sandwiching the regular beam element between two piezoelectric thin layers of thickness t_a or t_s.

The bottom layer acts as a sensor and the upper layer acts as an actuator. Similar to the equation (10) obtained for a regular beam

element, the Lagrangian equation of motion of the piezoelectric beam element is obtained as,

$$M^p\ddot{q} + K^p q = f^p(t), \qquad (11)$$

where $M^p$and K^p are the mass and stiffness matrices of the piezoelectric element and is obtained as, [Daniel J. Inman, 2006]:

$$[M^p] = \frac{\rho A}{420}\begin{bmatrix} 156 & 22l_b & 54 & -13l_b \\ 22l_b & 4l_b^2 & 13l_b & -3l_b^2 \\ 54 & 13l_b & 156 & -22l_b \\ -13l_b & -3l_b^2 & -22l_b & 4l_b^2 \end{bmatrix}, \qquad (12)$$

and

$$[K^p] = \frac{EI}{l_b}\begin{bmatrix} \frac{12}{l_b^2} & \frac{6}{l_b} & -\frac{12}{l_b^2} & \frac{6}{l_b} \\ \frac{6}{l_b} & 4 & -\frac{6}{l_b} & 4 \\ -\frac{12}{l_b^2} & -\frac{6}{l_b} & \frac{12}{l_b^2} & -\frac{6}{l_b} \\ \frac{6}{l_b} & 4 & -\frac{6}{l_b} & 4 \end{bmatrix}, \qquad (13)$$

where :

$$EI = E_b I_b + 2E_p I_p, \qquad (14)$$

$$I_p = \frac{1}{12} b t_a^3 + b t_a \left(\frac{t_a + t_b}{2}\right)^2, \qquad (15)$$

$$\rho A = b(\rho_b t_b + 2\rho_p t_p), \qquad (16)$$

2.3. Piezoelectric strain rate sensors and actuators

The sensor equation is derived from the direct piezoelectric equation. The electric displacement developed on the sensor surface is directly proportional to the stress acting on the sensor. If the poling is done along the thickness direction of the sensors with the electrodes on the upper and the lower surfaces, the electric displacement D is given by, [Michael R. Hatch, 2001]:

$$D_z = d_{31} E_p \varepsilon_x = e_{31} \varepsilon_x, \qquad (17)$$

where d_{31} is the piezoelectric constant, e_{31} is the piezoelectric stress / charge constant, E_p is the young's modulus and ε_x is the strain that is produced.

2.3.1. Sensor equation

The total charge $Q(t)$ developed on the sensor surface is the spatial summation of all the point charges developed on the sensor layer. Thus, the expression for the current generated is obtained as, [Ranjan Vepa, 2010]:

$$i(t) = \frac{d\,Q(t)}{dt} = \frac{d}{dt}\int_A e_{31}\,\varepsilon_x\,dA = z e_{31} b \int_{x_i}^{x_i+l_p} n_1^T \dot{q}\,dx, \qquad (18)$$

where, $z = \frac{t_b}{2} + t_a$, and n_1 is the second spatial derivative of the shape function given in (Appendix 1) [T.C. Manjunath, 2007].

After converting the current i using signal conditioning device with gain G_c into voltageV_s, thus the sensor output voltage is obtained as,:

$$V_s(t) = G_c\, e_{31}\, z\, b \int_{x_i}^{x_i+l_p} n_1^T\, \dot{q}\,dx, \qquad (19)$$

Substituting for n_1 and $\dot{q}$ in equation (19) and simplifying, we get the sensor voltage for a 2-nodes finite element as:

$$V_s(t) = [G_c e_{31} z b \;\; 0 \;\; -G_c e_{31} z b \;\; 0]\begin{bmatrix} \dot{w}_1 \\ \dot{\theta}_1 \\ \dot{w}_2 \\ \dot{\theta}_2 \end{bmatrix}, \qquad (20)$$

$$V_s(t) = P^T \dot{q}, \qquad (21)$$

where $\dot{q}$ is the time derivative of the modal coordinate vector q , P is a constant vector which

depends on the type of sensor, its characteristics and its location on the beam.

2.3.2. Actuator equation

The actuator strain is derived from the converse piezoelectric equation. The strain developed a ε_a on the actuator layer is given by

$$\varepsilon_a = d_{31} E_f, \qquad (22)$$

where d_{31} and E_f are the piezoelectric strain constant and the electric field respectively. When the input to the piezoelectric actuator $V_a(t)$, is applied in the thickness direction t_a, the electric field, E_f which is the voltage applied $V_a(t)$ divided by the thickness of the actuator t_a ; and the stress, σ_a which is the actuator strain multiplied by the young's modulus E_p of the piezoelectric actuator layer are given by

$$E_f = \frac{V_a(t)}{t_a}, \qquad (23)$$

$$\sigma_a = E_p\, d_{31}\, \frac{V_a(t)}{t_a}, \qquad (24)$$

The strain developed on the actuator layer is directly proportional to the electric field E_f, The resultant moment M_a acting on the beam is thus determined by integrating the stress through the structural thickness as, [T.C. Manjunath, 2007]:

$$M_a = E_p\, d_{31}\, \bar{z}\, V_a(t), \qquad (25)$$

where $\bar{z} = \frac{t_a + t_b}{2}$ is the distance between the neutral axis of the beam and the piezoelectric layer [T.C. Manjunath, 2007]. Finally, the control force applied by the actuator is obtained as:

$$f_{ctrl} = E_p\, d_{31} b\, \bar{z} \int_{x_i}^{x_i + l_p} n_2\, dx\, V_a(t), \qquad (26)$$

$$V_s(t) = \begin{bmatrix} 0 & 0 & 0 & -E_p\, d_{31} b\, \bar{z} \end{bmatrix} \begin{bmatrix} \dot{w}_1 \\ \dot{\theta}_1 \\ \dot{w}_2 \\ \dot{\theta}_2 \end{bmatrix}, \qquad (27)$$

$$f_{ctrl} = h\, V_a(t) = h\, u(t), \qquad (28)$$

2.4. Formulation

The dynamic equation of the smart structure is obtained by using both the regular and piezoelectric beam elements given by equations (10, 12 and 13), the mass and stiffness of the bonding or the adhesive between the master structure and the sensor / actuator pair is neglected.

After assembling the general mass and stiffness matrices and including the generalized structural damping matrix $[C] = \alpha * [M] + \beta * [K]$, where α and β are the frictional damping constant and the structural damping constant, and applying the cantilever beam boundary condition, the system equation of motion for the 4-element cantilever beam is:

$$[M]_{8\times 8}\, \ddot{q}(t) + [C]_{8\times 8}\, \dot{q}(t) + [K]_{8\times 8}\, q(t) = f, \qquad (29)$$

and

$$f = f_{ext} + f_{ctrl}, \qquad (30)$$

for free vibration condition f_{ext} equal to zero, so the remaining applied force on the

system is the controlling force exerted by the controller.

2.5. State Space model of the smart cantilever beam

The equation (29) could be written in state space form as follows, Let the states of the system be defined as,

$$q = x, \quad (31)$$

$$q = \begin{bmatrix} q_1 \\ q_2 \end{bmatrix} = \begin{bmatrix} x_1 \\ x_2 \end{bmatrix} = x, \quad (32)$$

$$\dot{q} = \dot{x} = \begin{bmatrix} \dot{x}_1 \\ \dot{x}_2 \end{bmatrix} = \begin{bmatrix} x_3 \\ x_4 \end{bmatrix}, \quad (33)$$

$$\ddot{q} = \begin{bmatrix} \dot{x}_3 \\ \dot{x}_4 \end{bmatrix}, \quad (34)$$

Substituting equations (31 – 34) in (29), we get,:

$$[M]\begin{bmatrix} \dot{x}_3 \\ \dot{x}_4 \end{bmatrix} + [C]\begin{bmatrix} x_3 \\ x_4 \end{bmatrix} + [K]\begin{bmatrix} x_1 \\ x_2 \end{bmatrix} = f_{ctrl}, \quad (35)$$

$$\begin{bmatrix} \dot{x}_3 \\ \dot{x}_4 \end{bmatrix} = -[M]^{-1}[C]\begin{bmatrix} x_3 \\ x_4 \end{bmatrix} - [M]^{-1}[K]\begin{bmatrix} x_1 \\ x_2 \end{bmatrix} + [M]^{-1} f_{ctrl}, \quad (36)$$

and finally written in state equation form as:

$$\begin{bmatrix} \dot{x}_1 \\ \dot{x}_2 \\ \dot{x}_3 \\ \dot{x}_4 \end{bmatrix} = \begin{bmatrix} 0 & I \\ -M^{-1}K & -M^{-1}C \end{bmatrix}\begin{bmatrix} x_1 \\ x_2 \\ x_3 \\ x_4 \end{bmatrix} + \begin{bmatrix} 0 \\ M^{-1}h \end{bmatrix} u(t), \quad (37)$$

$$\dot{x} = A\,x(t) + B\,u(t), \quad (38)$$

The output equation (sensor equation) for a SISO case is given by:

$$y(t) = V_s(t) = P^T \dot{q} = P^T \begin{bmatrix} x_3 \\ x_4 \end{bmatrix}, \quad (39)$$

$$y(t) = \begin{bmatrix} 0 & P^T \end{bmatrix}\begin{bmatrix} x_1 \\ x_2 \\ x_3 \\ x_4 \end{bmatrix}, \quad (40)$$

$$y(t) = C\,x(t) + D\,u(t), \quad (41)$$

The SISO state space model (state equation and output equation (41)) of the smart cantilever beam finally is given by equations (38) and (41), with,

$$A = \begin{bmatrix} 0 & I \\ -M^{-1}K & -M^{-1}C \end{bmatrix}_{16\times16}, \quad (42)$$

$$B = \begin{bmatrix} 0 \\ M^{-1}h \end{bmatrix}_{16\times1}, \quad (43)$$

$$C = \begin{bmatrix} 0 & P^T \end{bmatrix}_{1\times16}, \quad (44)$$

$$D = 0, \quad (45)$$

3. ACTIVE VIBRATION CONTROL

Active vibration control (AVC) is an important problem in structures. One of the ways to tackle this problem is to make the structure smart, intelligent, adaptive and self-controlling by making use of the smart material.

3.1 Output Feedback Control

The vibrations of many structures and devices are controlled by sophisticated control methods. Examples of the use of feedback control to remove vibrations range from machine tools to tall buildings and large spacecraft. This method considered, as one of most popular way to control the vibrations of a structure by measuring the position and velocity vectors of the structure and to use that information to drive the system in direct proportion to its positions and velocities [Daniel J. Inman, 2006].

Consider the following dynamical system form,

$$M\ddot{q}(t) + (C + G)\dot{q}(t) + Kq(t) = f(t), \quad (46)$$

Where, q represent a generalized coordinate that may not be an actual physical coordinate or position but is related, $M = M^T$is the mass, or inertia, matrix, $C = C^T$is the viscous damping matrix, $G = G^T$is gyroscopic matrix, $K = K^T$is stiffness matrix, and The n vector $f = f(t)$ represents applied external forces and is also time varying.

A condition to ensure stability, $\mathbf{M}$, $\mathbf{C}$ and $\mathbf{K}$ is positive definite, such that $(x^T A\, x < 0)$ for all nonzero real vectors x, and $(x^T A\, x = 0)$ if and only if x is zero.

When Output Feedback Control done for the above system, Equation (46) becomes

$$M\ddot{q}(t) + (C + G)\dot{q}(t) + Kq(t) = -K_p q(t) - K_v \dot{q}(t) - f(t), \quad (47)$$

Here, K_p and K_v are called feedback gain matrices [Daniel J. Inman, 2006].

3.2 Model Order Reduction

It is necessary to reduce the order of a model before performing a control analysis and designing.

The approach taken for reduction the order of a given model based on deleting the coordinates, or modes, that are the least controllable and observable. The idea here is that controllability and observability of a state (coordinate) are indications of the contribution of that state (coordinate) to the response of the structure, as well as the ability of that coordinate to be excited by an external disturbance[Daniel J. Inman, 2006].

A useful measure is provided for asymptotically stable system of the form given by Equations (38) and (41) by defining the controllability grammian, denoted by W_C, as

$$W_C^2 = \int_0^\infty e^{At} BB^T e^{A^T t} dt, \quad (48)$$

and the observability grammian, denoted by W_O, as:

$$W_O^2 = \int_0^\infty e^{A^T t} C^T C e^{At} dt, \quad (49)$$

If the system is controllable (or observable), the matrix W_C (or W_O) is nonsingular. These grammians characterize the degree of controllability and observability by quantifying just how far away from being singular the matrices W_C and W_O are. This is equivalent to quantifying rank deficiency. The most reliable way to quantify the rank of a matrix is to examine the singular values of the matrix. [Daniel J. Inman, 2006]

Let the matrix $\mathbf{P}$ denote a linear similarity transformation, which when applied to Equations (38) and (41) yields the equivalent system

$$\dot{x}' = A'\, x' + B'\, u, \quad (50)$$

$$y = C'\, x', \quad (51)$$

These two equivalent systems are related by

$$x' = \mathbf{P}\, x, \quad (52)$$

$$A' = \mathbf{P^{-1}}\, A\, \mathbf{P}, \quad (53)$$

$$B' = \mathbf{P^{-1}}\, B, \quad (54)$$

$$C' = C\,\mathbf{P}, \qquad (55)$$

Here, matrix $\mathbf{P}$ can be chosen such that the new grammians defined by

$$W_C' = \mathbf{P}^{-1} W_C\ \mathbf{P}, \qquad (56)$$

and,

$$W_O' = \mathbf{P}^{-1} W_O\ \mathbf{P}, \qquad (57)$$

are equal and diagonal. That is,

$$W_C' = W_O' = \Lambda_W = \mathrm{diag}[\sigma_1\ \sigma_2 \cdots \sigma_{2n}]$$

where the numbers σ_i are the singular values of the grammians and are ordered such that

$$\sigma_i > \sigma_{i+1}, \qquad i = 1,2,\ldots,2n-1$$

The MATLAB program offer a good algorathems for the system order reduction using the controllability and observability gramians called Control System Toolbox. The command (balreal) used to perform the balanced relization based on controllability and observability gramians, where the command (modred) used for system order reduction [Michael R. Hatch, 2001].

3.3 Controller Design using Pole Placement and output feedback techniques

Stability of a system are closely related to the location of poles or eigenvalues of the system. Pole placement can be achieved by feedback control. The poles of this system are eigenvalues of A.

Using the state feedback

$$u = -\mathbf{K}_{ctrl}\, x, \qquad (58)$$

Where $(\mathbf{K}_{ctrl}\, x)$ is linear state feedback.

Under this feedback control, the controlled closed loop system is given by[Deepak Chhabra, 2011]:

$$\dot{x} = A_{ctrl}\, x(t) + Er(t), \qquad (59)$$

Where:

$$A_{ctrl} = (A - B\mathbf{K}_{ctrl}), \qquad (60)$$

To find out the value of feedback gain matrix $\mathbf{K}_{ctrl}$, A characteristic equation of the system is considered as:

$$\varphi(s) = s^n + a_{n-1}s^{n-1} + a_{n-2}s^{n-2} + \cdots + a_1 s + a_0, \qquad (61)$$

The poles of the controlled system is in the desired locations represented by the desired characteristic equation as:

$$\varphi(s) = s^n + a'_{n-1}s^{n-1} + a'_{n-2}s^{n-2} + \cdots + a'_1 s + a'_0, \qquad (62)$$

This can be achieved by letting the feedback matrix be:

$$\mathbf{K}_{ctrl} = [k_0 \quad k_1 \quad \ldots \quad k_{n-1}]$$
$$= [a_0 - a'_0 \quad a_1 - a'_1 \quad \ldots \quad a_{n-1} - a'_{n-1}], \qquad (63)$$

The MATLAB command (place) in Control System Toolbox could be used to

computes the feedback gain matrix $\mathbf{K}_{ctrl}$ that achieves the desired closed-loop pole locations. The algorathem used in this command uses the extra degrees of freedom to find a solution that minimizes the sensitivity of the closed-loop poles to perturbations in A or B matrices, and it optimizes the choice of eigenvectors for a robust solution.

4. NUMERICAL SIMULATION AND RESULTS

Figure (2) illusterate the smart canteliver beam with the embaded sensor and actuator layers, showing the devisions considered in the FEM solution.

The dimensions of the piezoelectric patch are given in Table (1) and Table (2).

The bode plot of the original system and the balanced reduced system is shown if figure(3)

The resulted natural frequencies (N.F) from the numerical simulation is matching the reference N.F, also A complete match was found between the original system model and the reduced system model for the first three modes.

The tip response of smart cantilever beam for free vibration case with initial tip displacement of (1 cm) is shown in figure (4) for the case at which the sensor/actuator patches placed onto position of element 2. In addition, the free vibration tip response for the case at

which the patches placed onto element 4 is shown in figure(5).

After applying the control law the new closed loop system bode plot is shown in figure(6) for the case of the patches onto element 2, also the effect of the control action on the cantilever response for the case of the patches onto element 2 is represented in figure(7). Moreover, for the case of the patches onto element 4 is represented in figure (8).

The patches position affects the free response of the beam as shown in figures (4) and (5). In addition, the case in which the piezoelectric patches placed onto the position of element (2) is better than the position of element (4) in vibration suppression using the proposed control law.

5. Conclusions

In conclusion, it could be said that the vibration suppressed successfully for the cantilever beam using 2 piezoelectric patches of piezoelectric material as sensor and actuator.

It is found out that, the Pole Placement method is an applicable way for the active vibration control vibration

The reduction method used was very effective.

On the other hand, it is possible to implement optimal control techniques to control the amplitude and time of the vibration.

REFERENCES

- Anna-Maria R. McGowan, et. al., NASA Langley Sesearch Center, Aeroelasticity and Structural Dynamics branches, “Aeroservoelatic and structural dynamics research on smart structruras conducted at NASA Langley Research Center”, Hampton, Virginia, May, 1998.
- B. Bandyopadhyay, T.C. Manjunath, M. Umapathy “Modeling, Control and Implementation of Smart Structures, A FEM - State Space Approach”, Springer

Berlin Heidelberg, New York, USA, 2007.

- Daniel J. Inman, "Vibration with Control", John Wiley & Sons Ltd, England, 2006.
- Deepak Chhabra, Pankaj Chandna and Gian Bhushan," Design and Analysis of Smart Structures for Active Vibration Control using Piezo-Crystals", International Journal of Engineering and Technology Volume-1 No.3, December, 2011.
- Gergely Takács, "Experimental Verification Of The Closed-Loop Response Of An Active Vibration Control System Modeled In ANSYS", The 4th International conference - Modeling Of Mechanical And Mechatronic Systems, Faculty of Mechanical engineering, Technical university of Košice, Slovak, 2011.
- Meysam Chegini, Milad Chegini and Hadi Mohammadi," Vibration Suppression of a Beam of Structures", IACSIT International Journal of Engineering and Technology, Vol.3, No.2, 2011.
- Michael R. Hatch, "Vibration simulation using MATLAB and ANSYS", Chapman & Hall/CRC, 2001.
- Nader Jalili, "Piezoelectric-Based Vibration Control, From Macro to Micro/Nano Scale Systems", Springer Berlin Heidelberg, New York, USA, 2010.
- R.G. Ballas, "Piezoelectric Multilayer Beam Bending Actuators: Static and Dynamic Behavior and Aspects of Sensor Integration", Springer-Verlag Berlin Heidelberg, 2007.
- Ranjan Vepa, "Dynamics of Smart Structures", John Wiley and Sons Ltd. Publication, UK, 2010.
- Scott M. Newman, Thesis Titled "Active Damping Control of a Flexible Space Structure Using Piezoelectric Sensors and Actuators", NAVAL Postgraduate School, Monterey, California, 1992.
- T.C. Manjunath and B. Bandyopadhyay, "Control of Vibrations in Flexible Smart Structures using Fast Output Sampling Feedback Technique", International Journal of Information and Mathematical Sciences 3:2, 2007.
- Tamara Nestorović, Miroslav Trajkov, "Active Control of Smart Structures an Overall Approach", FACTA Universitatis, Architecture and Civil Engineering, Vol. 8, No 1, pp. 35 – 44, 2010.

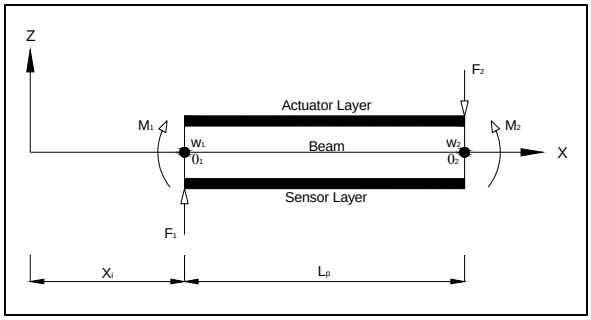

Figure 1 Smart beam element

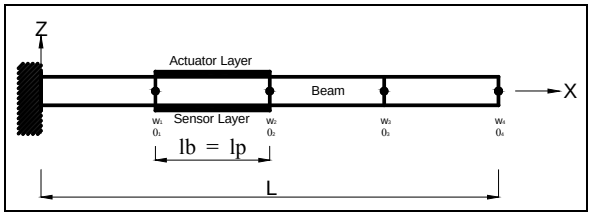

Figure2 smart cantilever beam

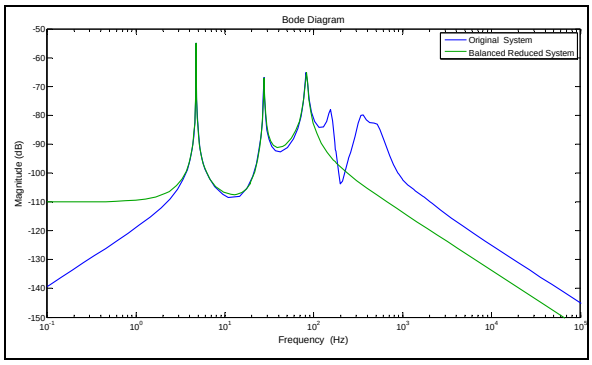

Figure 2 Bode plot of the original system and the balanced reduced system

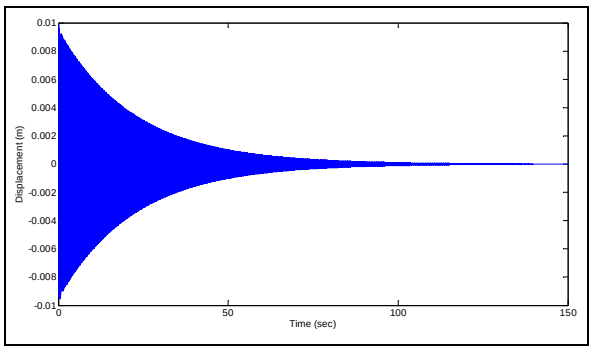

Figure 3 Free Vibration tip response for sensor/actuator patches on to element 2

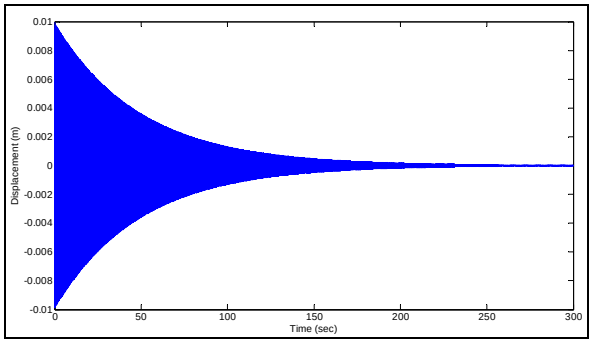

Figure 4 Free Vibration tip response for sensor/actuator patches on to element 4

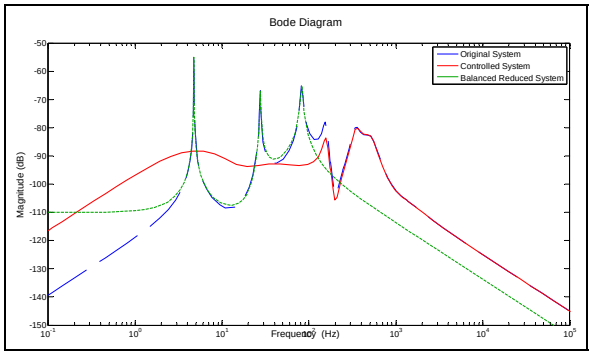

Figure 5 Bode plot of the original system, the balanced reduced system and the new closed loop controlled system

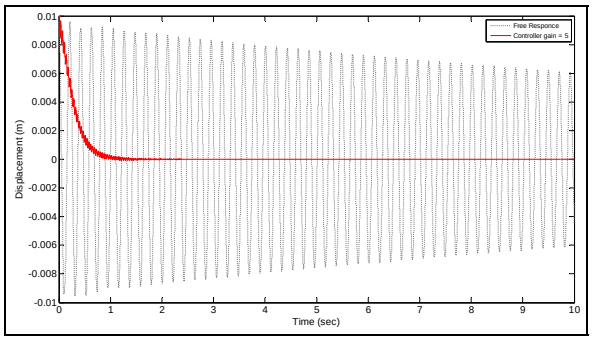

Figure 6 AVC for beam with patch on element(2)

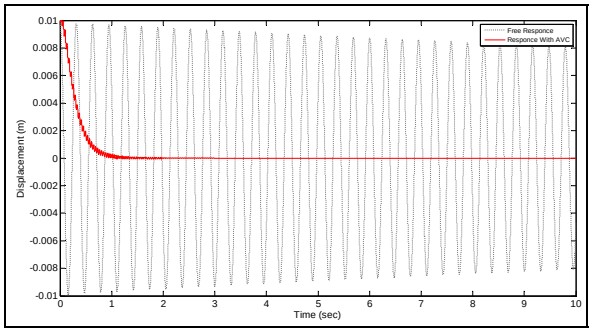

Figure 7 AVC for beam with patch on element(4)

Table (1) properties of the flexible cantilever beam when the beam is divided into 4 elements [B.Bandyopadhyay, 2007]

Parameter	Symbol	Numerical Value
Length (m)	l_b	0.03
Width (m)	b	0.03
Thickness (mm)	t_b	0.5
Young's Modulus (Gpa)	E_b	193.06
Density (kg/m3)	ρ_b	8030
Damping constant used in (C)	α , β	0.001, 0.0001

T able (2) properties of the piezoelectric element when the beam is divided into 4 elements [B. Bandyopadhyay, 2007].

Parameter	Symbol	Numerical Value
Length (m)	l_p	0.075
Width (m)	b	0.03
Thickness (mm)	t_p	0.35
Young's Modulus (Gpa)	E_p	68
Density (kg/m3)	ρ_p	7700
Piezoelectric Stain constant (m/V)	d_{31}	125×10^{-12}
Piezoelectric Stress constant (V.m/N)	e_{31}	10.5×10^{-3}

Table (3) shows the natural frequency in (Hz) and verification with the reference paper

N.F.	Numerical result by MATLAB	N.F. Ref. [B. Bandyopadhyay, 2007]	Error (%)
ω_1	4.738	4.73	0.00
ω_2	27.429	27.43	0.00
ω_3	81.868	--	--

Table(4) Symbols Description

Syb.	Description	Unit
α	Fractional damping constant	
β	Structural damping constant	
ϵ	Strain	
ϵ_x	Mechanical normal strain	
υ	Poisson's ratio	
ρ_b	Density of the beam	Kg/m^3
ρ_p	Density of the piezoelectric patch	Kg/m^3
ρA	Mass / unit length	
σ_a	Stress in the actuator	
σ	Stress	N/m^2
ω	Natural frequency	Hz
ξ	Damping ratio	

Appendix - 1 -

Spatial Derivative of The Shape Function of Bernoulli-Euler Beam,

$$[n] = \begin{bmatrix} 1 - 3\frac{(x-x_i)^2}{l_b^2} + 2\frac{(x-x_i)^3}{l_b^3} \\ (x-x_i) - 2\frac{(x-x_i)^2}{l_b} + 2\frac{(x-x_i)^3}{l_b^2} \\ 3\frac{(x-x_i)^2}{l_b^2} - 2\frac{(x-x_i)^3}{l_b^3} \\ -\frac{(x-x_i)^2}{l_b} + 2\frac{(x-x_i)^3}{l_b^2} \end{bmatrix} = [n_2]$$

$$[n_2] = [n_3'] = \begin{bmatrix} -6\frac{(x-x_i)}{l_b^2} + 6\frac{(x-x_i)^2}{l_b^3} \\ 1 - 4\frac{(x-x_i)}{l_b} + 6\frac{(x-x_i)^2}{l_b^2} \\ 6\frac{(x-x_i)}{l_b^2} - 6\frac{(x-x_i)^2}{l_b^3} \\ -2\frac{(x-x_i)}{l_b} + 3\frac{(x-x_i)^2}{l_b^2} \end{bmatrix}$$

$$[n_1] = [n_2'] = \begin{bmatrix} -\frac{6}{l_b^2} + 12\frac{(x-x_i)}{l_b^3} \\ -\frac{4}{l_b} + 12\frac{(x-x_i)}{l_b^2} \\ \frac{6}{l_b^2} - 12\frac{(x-x_i)}{l_b^3} \\ -\frac{2}{l_b} + 6\frac{(x-x_i)}{l_b^2} \end{bmatrix}$$

Irrigation Scheduling Effect on Water Requirements

Amer Hassan Al-Haddad

Assist Professor

Water Resources Engineering Dept.

ameralhaddad1950@yahoo.com

Tamara Sideeq Bakr

M.Sc. Water Resources Engineering

tamarasideeq@yahoo.com

ABSTRACT:

Irrigation scheduling techniques is one of the suggested solutions for water scarcity problem. The study aims to show the possibility of using practical and applicable irrigation scheduling program which was designed by Water Resources Department at the University of Baghdad by using Spreadsheet Formulas for Microsoft Excel program, version 2007, with some modification to generalize it and made it applicable to various climatic zone and different soil types, as a salvation for the shortage of irrigation water inside the irrigation projects. Irrigation projects which incidence of Tigris River basin will be taken as an applicable example. This program was based on water budgeting and programmed depending on scientific concepts which facilitate irrigation structures operation and ease the use by farmers. By using the abilities of this program, the monthly and annually water requirements and drainage water were estimated. Finally a comparison is made between the calculated discharges with the designers suggested ones. This comparisons showed that the use of this type of irrigation scheduling (i.e. predicted irrigation scheduling) with its applicable constrains require high attention when choosing the cropping pattern for each climate zone. Also it found that this irrigation program is a useful tool for saving water if cropping pattern has been chosen carefully.

Keywords:Irrigation scheduling, percentage of maximum root depth, water resources dept. program, water budget, Nahr Sa'd irrigation project.

اثر الجدولة الاروائية على الاحتياجات المائية

الخلاصة:

تقنيات الجدولة الاروائية هي احدى الحلول المقترحة لمشكلة شحة المياه. تهدف الدراسة الى معرفة امكانية استخدام برنامج جدولة اروائية قابل للتطبيق العملي تم اعداده في قسم هندسة الموارد المائية في جامعة بغداد باستخدام برنامج مايكروسوفت اكسل نسخة 2007، مع اجراء بعض التعديلات عليه لجعله قابلا للتطبيق في المناطق المناخية المختلفة ولأنواع مختلفة من الترب، كحل لمواجهه النقصان في مياه الري داخل المشاريع الاروائية. تم اخذ المشاريع الواقعة على حوض نهر دجلة كمثال تطبيقي. بني هذا البرنامج بالاعتماد على الموازنة المائية وعلى مفاهيم و أسس علمية تسهل تشغيل منشاءات الري وتسهل تطبيقها من قبل المزارعين. باستخدام امكانيات هذا البرنامج امكن تخمين متطلبات مياه الري الشهرية والسنوية وضائعات المياه، قورنت التصاريف المحسوبة باستخدام البرنامج مع ما اقر من قبل دوائر الدولة المعنية. اظهرت نتائج هذه المقارنة ان استخدام هكذا نوع من الجدولة الاروائية (جدولة الري المتوقع) بخصائصه التي تجعله قابلا للتطبيق يتطلب عناية شديدة عند اختيار نمط توزيع النباتات والمساحات المزروعة بهذه النباتات لكل منطقة مناخية. كما ووجد ان هذا البرنامج يمثل اداه مفيدة للحفاظ على المياه اذا ما احسن اختيار نمط توزيع النباتات.

الكلمات الرئيسيه :الجدولة الاروائية، النسبة المئوية لاطول جذر، البرنامج الخاص بقسم هندسة الموارد المائية، الموازنة المائية، مشروع نهر سعد الاروائي.

INTRODUCTION

Irrigation scheduling means how much water should be applied and when to irrigate. To make this decision, there is some steps should be followed to make right decision. First of all crop pattern and information of each crop should be known, such as growing season, growing and harvesting date, root depth, and allowable depletion, soil physical properties, climate, availability of water resources, and field water losses also should be known. Three main schedules are known, these are: constant depth; constant interval; and practical irrigation schedule.

A range of irrigation scheduling methods have been developed to assist farmers and irrigators to apply water more efficiently taking into account crop evaporation and rainfall. Irrigation scheduling includes the following methods:

First - traditional method which unfortunately is the method adopted many farmers. This method is based on individuals decision and depends on previous observations without taking into account the need of plant to water. This method consumes a large amount of water without scientific justification, and it may cause Lack of soil aeration, Washing nutrients from the soil, and Lack of productivity.

Therefore, this method must be disposed of.

Second - modern methods which are methods based on scientific base to take into account several factors affecting water consumption, and these methods depend on climatic factors, soil factors, plant type, or depending on all these factors.

The use of computer programs to help scheduling irrigation was introduced in the 1970's. However, only recently with the introduction of fast, personal computers have they begun to gain wider acceptance (Martin, 2009). Irrigation scheduling is based on three methods and tools; they are plant stress measurement, predictive models, and soil moisture measurement (Antosch, 2007).

Nevertheless, since 1990's there has been a wide range of proposed novel approaches to irrigation scheduling which have not yet been widely adopted; many of these are based on sensing the plant response to water deficits rather than sensing the soil moisture status directly (Jones, 1990a). Infrared sensors have been used to determine canopy temperature and scheduling irrigations (Stockle and Dugas, 1992; Alves and Pereira, 2000)

Alternative approach to irrigation scheduling has been opened up, this approach based on measurements of sap-flow rates, because sap-flow rates are expected to be sensitive to water deficits and especially to stomatal closure. Sap-flow measurement used by many workers for irrigation scheduling and control in a diverse range of crops, including grapevine (Eastham and Gray, 1998; Ginestar *et al*., 1998 a, b), fruit and olive trees (Giorio and Giorio, 2003; Remorini and Massai, 2003; and Moriana, 2007) and even greenhouse crops (Ehret *et al*., 2001).

Hamad (1996) developed a practical and easy procedure for preparing seasonal or annual irrigation programs for an irrigation project. The developed procedure is based upon some practical criteria among them are the:

- Supplied discharge would be constant in all irrigations;
- Time of application would be also be constant throughout the season;
- Starting day of all irrigation in the season or the year would be the same day in the weak in order to make the farmers and irrigators accustomed to the days of irrigation; and
- Irrigation intervals are selected in such a way to avoid crop stress due to insufficient soil moisture.

Al-Hadaad (1997) developed a model to pre-schedule irrigations in large irrigation projects based upon average physical soil properties and crop water requirements. This model also includes estimating expected annual crop production of the project for a given cropping pattern.

Riffat (1999) developed an optimization process to maximize total crop production from a given cropping pattern in an irrigation project by using pre-scheduled irrigations and pre-specified constraints on the volumes of applied water and cropping intensity.

Irrigation scheduling using pan evaporation (CPE), relies on measuring the amount of water evaporated from the container

based on cumulative depth in millimeter. It is an easy way and does not require high-tech. The idea of this method depends on the farms crops lose water during the irrigation process by evapotranspiration; this quantity is a large missing depends on climatic factors, so the method give the irrigator indication when to irrigate. Several experiments have been carried out using this method in Saudi Arabia, where it became clear that this method has provided a quantity of irrigation water and up to 25% compared to traditional methods, which rely only on the period between irrigations without taking into account the climatic factors (Alderfasi, 2000).

Al-Hadaad (2001) evaluated the effect of using weighted average root depths and a certain level of depletion in building an irrigation scheduling program for large projects containing different crops on water stress of wheat crop during the growing season.

Irrigation scheduling by using the guide of the crop water stress (CWSI), takes into account the climatic factors like air temperature and relative humidity and temperature of the plant as well as the water situation of the soil and crop. This guide is divided into ten equal parts where each part refers to the situation of water for each soil, plants, and sets time limit for irrigation manner. This method is a modern and requires sophisticated technology based on the theory of remote sensing to measure the temperature of vegetation and its relation to the situation of water for soil and plants. Irrigation scheduling using this method has given good results in the case study of water plants and irrigation scheduling and is recommended for use in most agricultural crops, since they rely mainly on climatic factors, which account for most of the water consumption of plants (Alderfasi and Nielsen, 2001).

Al-Mesh'hedany (2002) investigated the effect of using a practical irrigation scheduling procedure (based upon average information about plants consumptive use rate and effective root zones) on the production and growth of each plant, for a given cropping pattern grown in a large irrigation project. The research included executing a water budgeting procedure on a daily basis considering the amounts of water moving into and out of the root zone for each plant grown in the project during its growing season. This research showed that there is a certain irrigation scheduling program, which minimize water losses, prevents water stress for all plants grown in the project, maximizes project outcomes, minimizes project requirements such as applied irrigation volume throughout the whole year, and maximizes effective irrigation water stored in the root zone.

Al-Azba *et al*. (2004) developed a computerized program by using GIS for estimating irrigation water requirements in KSA. He took into consideration easiness in use. The methodology which was provided by (Allen *et al*., 1998) for calculating crop water requirements was followed. Noting that they considered that crop coefficient (k_c) value during development and maturity stages are constant like initial and mid-season stages. The value of (k_c) for development stage was taken as an average of (k_c) during initial and mid-season stage, and maturity stages are calculated as an average of (k_c) during mid-season and (k_c) at the end of growing season.

Fortes *et al*. (2004) presented the GISAREG scheduling model which is a Geographical Information System (GIS) based application integrating both ISAREG. It is a conceptual non-distributed water balance model for simulating crop irrigation schedules at field level and computes irrigation requirements under optimal and/or water stressed conditions, and KCISA. It was developed to create the appropriate crop data inputs for ISAREG. The model operation for different water management scenarios and the production of crop irrigation maps and time dependent irrigation depths at selected aggregation modes.

Al-Talib *et al*. (2005) proposed a computerized model with (Microsoft QuickBasic version 1.1) for simulating the effect of deficit irrigation for maize crop during spring and autumn seasons in Mosul region. The simulation was based on climatological data which is used to calculate daily reference evapotranspiration with Penman-Monteith equation. The model predicts yield reduction by changing irrigation depth for three different irrigation methods.

Vellidis *et al*. (2008) described a prototype real-time, smart sensor array for measuring soil moisture and soil temperature that uses off-the-shelf components was developed and evaluated for scheduling irrigation in cotton. The array consists of a centrally located receiver connected to a laptop computer and multiple sensor nodes installed in the field. Integration of the sensors with precision irrigation technologies

provided a closed loop irrigation system where inputs from the smart sensor array determined timing and amounts for real-time site-specific irrigation applications.

Irrigation Industry Association of British Columbia's (IIABC) (2009) developed a new agriculture irrigation scheduling calculator. This calculator determines an irrigation schedule for all type of agricultural irrigation systems and a crop types, and use real time climate data. Also Harrison (2009) review the various methods available for irrigation scheduling.

The scheduling procedure adopted in this research is that developed by Hamad (1996) and Al-Haddad (1997). It is a practical and applicable procedure that can be adopted in large irrigation projects since it is simple to use and easy to understand by project manager and farmers. It was based on the following constrains:

1. Applied discharge at the project head gate is constant throughout the whole year, such application would facilitate the operation of controlling and distribution structures of irrigation network.

2. Irrigation time is held constant during the year or at least during the growing season, in order to habituate the worker and farmer on irrigation time in the project.

3. Irrigation time must be chosen in a way that facilitates water distribution and project operation and should be full-days and avoiding parts of the day.

4. Irrigation interval must be selected in a way that crops will not be stressed due to decreasing soil moisture content and will not cause over-irrigation.

5. Starting date of each irrigation during the year is the same day of the week and the day of starting of irrigation scheduling. Such a practice would habituate the farmer to irrigation date, and the date of water distribution between farmers.

These constrains can be useful for a single large project. Since this program is intended to be applied along the Tigris River basin which is different in soil properties, climate, and types of planted crops; such variation should be taken in account when building a scheduling program. Some modifications on these constrains are required to make it more comprehensive, so the third and fifth constrains are modified as follows:

1. For heavy soils, the starting day of each irrigation during the year is the same day of the week as the day of starting the irrigation schedule or irrigation year. For light soils, there are two possible irrigation days in the week, first day has the same interiority of heavy soils irrigation day and the second is in the middle of week of the day of starting irrigation year.

2. In winter season, time of irrigation will be chosen in a way that does not affect crop growth, while in summer season there is a continuous irrigation except in rainy zones.

Additional constrains shall be used and these are:

1. Soil is homogenous and isotropic;

2. Initial soil water content at the beginning of irrigation scheduling is known; and

3. Soil water content at field capacity and wilting point are constant throughout the root zone of the whole project.

DESCRIPTION OF THE STUDY AREA

Soil-physical properties of Iraqi soils vary from one site to another. The General Scheme of Water Resource and Land Development in Iraq divided Iraqi territory to four zones (General scheme of water resources and land development in Iraq, 1982) they are: mountain-valley soil, Jazeera desert (its northern part), piedmont gently sloping–undulating plain, and lower Mesopotamian plain.

The climate of Iraqi is subtropical, continental, summer is long, hot and dry, and winter is short with mean monthly temperatures above zero, intensive cyclonic activity in the atmosphere provoking rainfall. The mean annual amount of precipitation in the country tends to decrease from north to south and from east to west. In summer no rainfall occurs in the country. Temperature, air humidity, and evaporation increase from north to south (General scheme of water resources and land development in Iraq, 1982). The general scheme of water resource and land development in Iraq divided Iraqi territory into zones according to the natural humidity, which characterizes identity of crops irrigation regimes. Three natural-climatic zone and four

subzones where singled out within the territory of the country (see: Appendix (1)). From the measurement of these climatic descriptions, reference evapotranspiration was calculated by using modified Penman-Monteith equation, and a rainfall rate was measured. In this research, these values are adopted.

CONCEPTUAL FORMULATION

The first step in irrigation scheduling is to determine crop water requirements. Actual monthly crop water requirements can be estimated from reference evapotranspiration and crop coefficient as follows:

$$ET_{cij} = K_{cij} * ET_{oi} \quad \text{..... (1)}$$

where:

$ET_{c\,ij}$: Actual monthly evapotranspiration rate of the j^{th} crop during the i^{th} month (mm/month),

K_{cij}: Monthly crop coefficient of the j^{th} crop during the i^{th} month (dimensionless),

ET_{oi}: Monthly reference crop evapotranspiration rate (potential evapotranspiration rate) during the i^{th} month (mm/month),

i : Month index, and

j : Crop index.

Since a cropping pattern contains many crops, the weighted average of crop evapotranspiration rate ought to be used to estimate irrigation water requirements. The monthly weighted average of actual crop evapotranspiration for certain crop pattern can be calculated from:

$$WET_{ci} = \frac{\sum_{j=1}^{n}(ET_{cij} * NA_j)}{\sum_{j=1}^{n} NA_j} \quad \text{.....(2)}$$

where:

WET_{ci} : Monthly weighted average actual crop evapotranspiration for certain cropping pattern during the i^{th} month (mm/month),

n: Number of planted crops in adopted crop pattern, and

NAj: Net area planted with the j^{th} crop, it is equal to NA * PAj (don.),

don.: 2500 (m^2),

PAj: Percentage of area planted with the j^{th} crop, and

NA: Net irrigated project area (don.).

Net monthly volume of irrigation water requirements can be calculated from subtracting average monthly effective rainfall from monthly crop consumptive use rate and multiplying by the area as follows:

$$NIi\ req. = \sum_{j=1}^{n} C * NAj * (WETci - ERi) \quad \text{..... (3)}$$

where:

NI i req.: Net volume of water required during the i^{th} month (m^3),

ERi: Monthly effective rainfall during the i^{th} month (mm/month), and

C: Conversion for units (dimensionless).

So, the net continuous irrigation discharge required during the i^{th} month would be:

$$NQ\ i\ req. = C * \frac{NI.i\,req}{NDi} \quad \text{.....(4)}$$

where:

$NQ_{i\ req.}$: Net continuous discharge required during the i^{th} month (m^3/sec), and

ND_i: Number of days in i^{th} month.

The gross continuous irrigation discharge required during the i^{th} month can be calculated by:

$$GQ\ i\ req. = \frac{NQ\ i\ req}{IEi} \quad \text{.....(5)}$$

where:

$GQ_{i\ req.}$: Gross continuous discharge required during the i^{th} month (m^3/sec), and

IE: Expected irrigation efficiency in the project expressed as a percentage.

The water duty which represents the irrigation capacity of unit irrigation water can be calculated from:

$$WDi = C * \frac{NQi}{NAi} \quad \text{.....(6)}$$

where:

WD i: Water duty during the i^{th} month ((l/sec)/ha), and

NA_i: Net irrigated project area during the i^{th} month (don.).

One of the main and important parameters that affects irrigation scheduling is soil water content. First step to estimate soil water content is to know the root zone depth. Adopting maximum root depth means occurrence of water losses on areas planted with crops having shallow root zones, while adopting minimum root depth means water shortage and/or water stress on areas planted with crops having deep root depth zone. Thus, in this research a percentage of maximum root depth shall represent root zone depth for a certain cropping pattern, it can be calculated from:

$$URDi = \max RDij * \% RD \quad \text{..... (7)}$$

where:

URDi: Used root depth during the i^{th} month (mm),

RDij: Root depth of the the j^{th} crop during the i^{th} month (mm), and

% RD: Percentage of the root depth.

The total available water is calculated as:

$$TAWi = (FC - PWP) * URDi \quad \text{..... (8)}$$

where:

TAW_i: Total available water (mm),

FC: Soil water content at field capacity expressed as a percentage by volume, and

PWP: Soil water content at permanent wilting point expressed as a percentage by volume.

The readily available water is expressed as a percentage of the total available water, or:

$$RAWi = TAWi * AD \quad \text{..... (9)}$$

where:

RAW_i: Readily available water in the root zone during the i^{th} month (mm), and

AD: Allowable depletion expressed as a percentage.

The allowable depletion differs from one crop to another and it is a function of evaporation power of the atmosphere. Allen *et al*. (1998) gave an allowable depletion for ET_c=5 mm/day. Therefore, an adjustment is required for different evapotranspiration rates and they suggested, an adjustment formula. In this research, the fraction of allowable depletion and adjustment formula for each crop presented by Allen *et al*. (1998) will be adopted. The adjustment formula is:

$$ADj = \text{Allen } et\ al.\ (1998)\ AD + 0.04 * (5 - ETc)$$

..... (10)

where:

AD_j: Allowable depletion of the the j^{th} crop expressed as a percentage, and

Allen *et al*. (1998) AD: Soil water depletion fraction for no stress for crops.

As allowable depletion is different from one crop to another as was mentioned above, the weighted average allowable depletion for an project irrigation will be adopted, and is calculated as follows:

$$AD = \frac{\sum_{j=1}^{n} ADj * PAj}{\sum_{j=1}^{n} PAj} \quad \text{..... (11)}$$

The initial soil water deficit at the first day of irrigation scheduling may either be measured or assumed. Therefore, the soil water deficit at the second day of schedule can be calculated as:

$$SWDB_{k\,i} = SWDA_{(k-1)\,i} + WET_{cki} - ER_{ki} \quad \text{..... (12)}$$

where:

$SWDB_{ki}$: Soil water deficit on the k^{th} day before irrigation during the i^{th} month (mm),

$SWDA_{(k-1)i}$: Soil water deficit after irrigation on the $(k-1)^{st}$ day during the i^{th} month (mm), and

k: Day index.

When a new month begins, root zone depth increases due to a plant growth if the soil

water at the end of the previous month is greater than the soil water at the beginning of the new month, then the increase in root depth requires additional quantity of water to raise its water content. This additional quantity of water is calculated as follows:

$$SWDL_i = \frac{SWDAL_i}{URD_i} \quad \text{..... (13)}$$

where:

$SWDL_i$: Soil water deficit after irrigation (if there is any) at the last day in the i^{th} month measured as a percentage, and

$SWDAL_i$: Soil water deficit after irrigation (if there is any) at the last day in the i^{th} month expressed as a depth of water (mm).

The additional soil water required to raise the soil water content due to the additional root depth calculated as follows:

$$ASWD_{(i+1)} = (FC - ISWC - SWDL_i) * ARD_{(i+1)} \quad \text{.....(14)}$$

where:

$ASWD_{(i+1)}$: Additional soil water deficit in the $(i+1)^{th}$ month (mm),

ISWC: Initial soil water content (mm), and

$ARD_{(i+1)}$: Additional used root depth and is equal as $URD_{(i+1)} - URD_i$ (mm).

This additional water is added to the soil water deficit on the first day of the $(i+1)^{th}$ month and it is equal to zero when root depth at i^{th} month is equal or greater than root depth at $(i+1)^{th}$ month or when the soil water content at the last day of the month is less than the initial soil water.

The soil water deficit after irrigation during the i^{th} month can be calculated from:

$$SWDA_{ki} = SWDB_{ki} - I_{ki} \quad \text{..... (15)}$$

where:

I_{ki}: Applied net irrigation depth infiltrated in the soil on the k^{th} day during the i^{th} month (mm).

Irrigation water must be applied whenever soil water content reaches a pre-specified value expressed as a percentage of RAWi or difference between $SMDB_i$ and RAW_i. To avoid crop water stress, irrigations should be applied before or on the day when the used readily available water is depleted (i.e., $SWDB_{ki} \leq RAW_i$).

The net applied irrigation depth can be calculated from:

$$Ii = C * \frac{IRR_{time\ i} * Q_{max} * IE}{NAi} \quad \text{..... (16)}$$

where:

$IRR_{time\ i}$: Irrigation time (days), and

Q_{max}: Gross maximum or design project discharge (m^3/sec).

For practical purposes, the irrigation time would be held constant during winter season (from November until the end of April) and during first month of irrigation scheduling. Since the net depth of irrigation water required during

first month of irrigation scheduling is not only to meet crop water requirements during that month, but adding to that the amount required to raise the initial soil water content in the root zone depth. In the summer season, continuous irrigation will be adopted.

For practical purposes, the irrigation time would be held constant during winter season (from November till the end of April) and during first month of irrigation scheduling. Since the net depth of irrigation water required during first month of irrigation scheduling not only to meet crop water requirements during that month, but adding on that amount required to raise the initial soil water content in the root zone depth. At the summer season, continues irrigation will be adopted. Figure (1) illustrates flowchart showed the main steps of irrigation scheduling model.

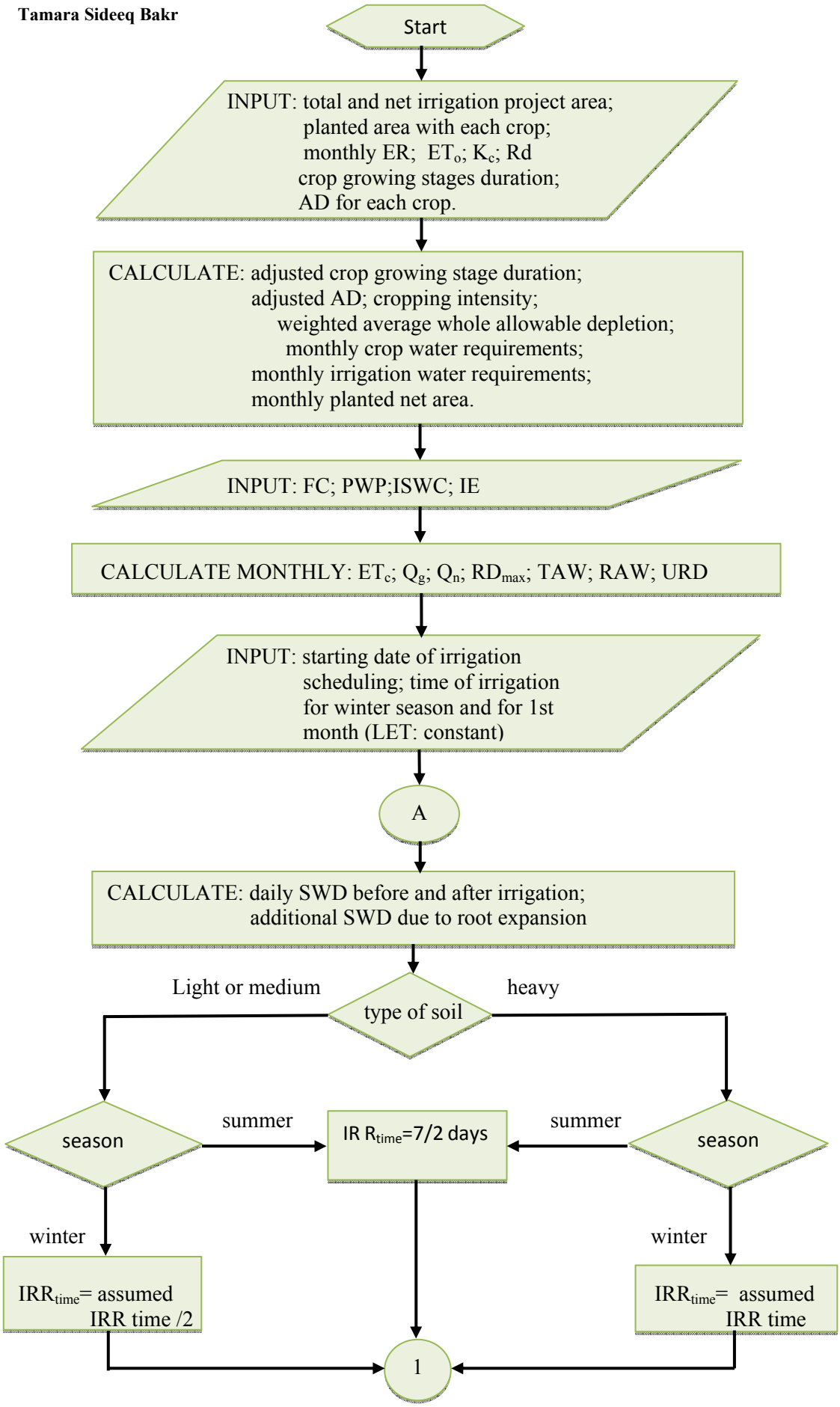

Figure (1). Flowchart illustrates the main steps of irrigation scheduling model.

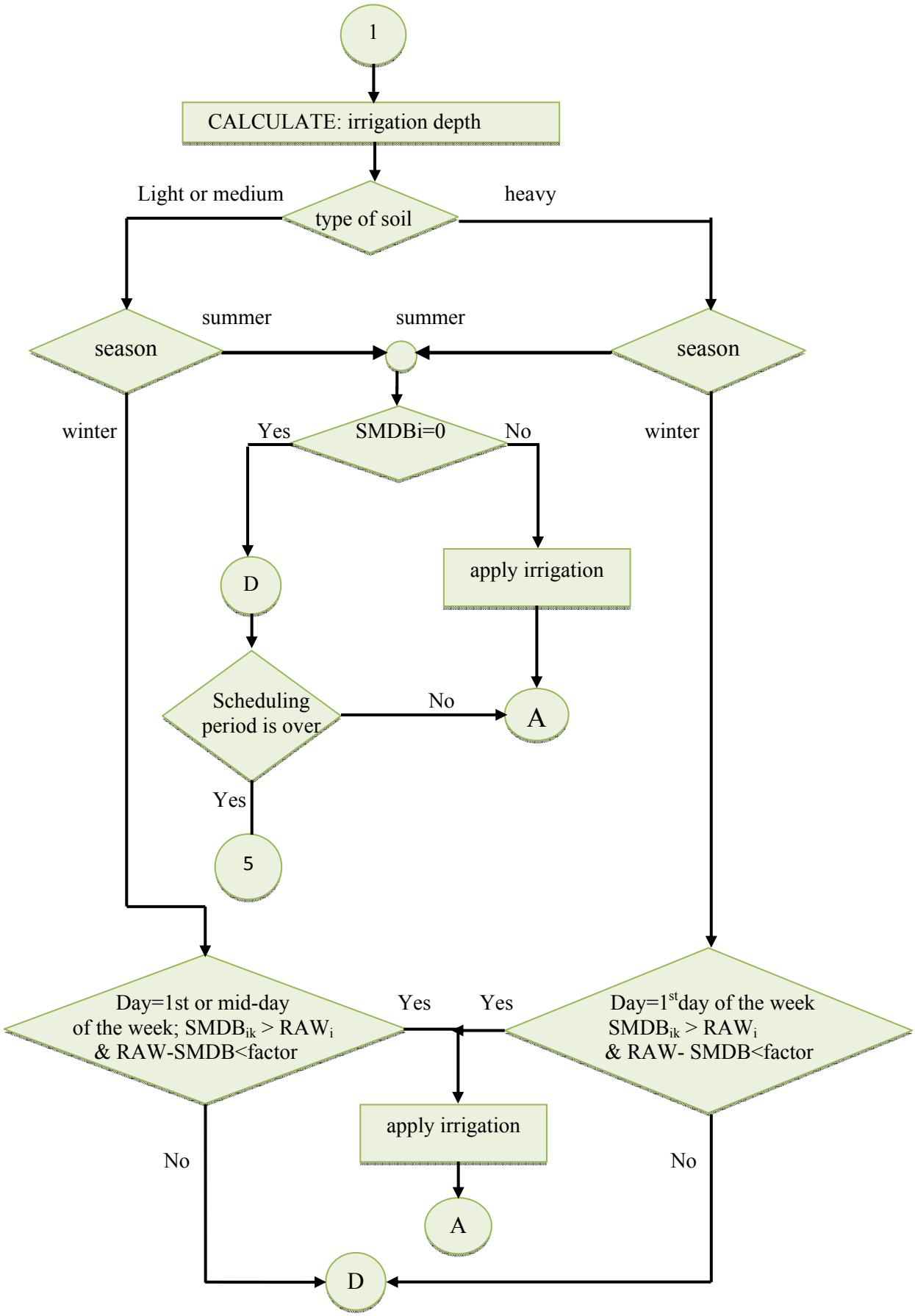

Figure (1). continued

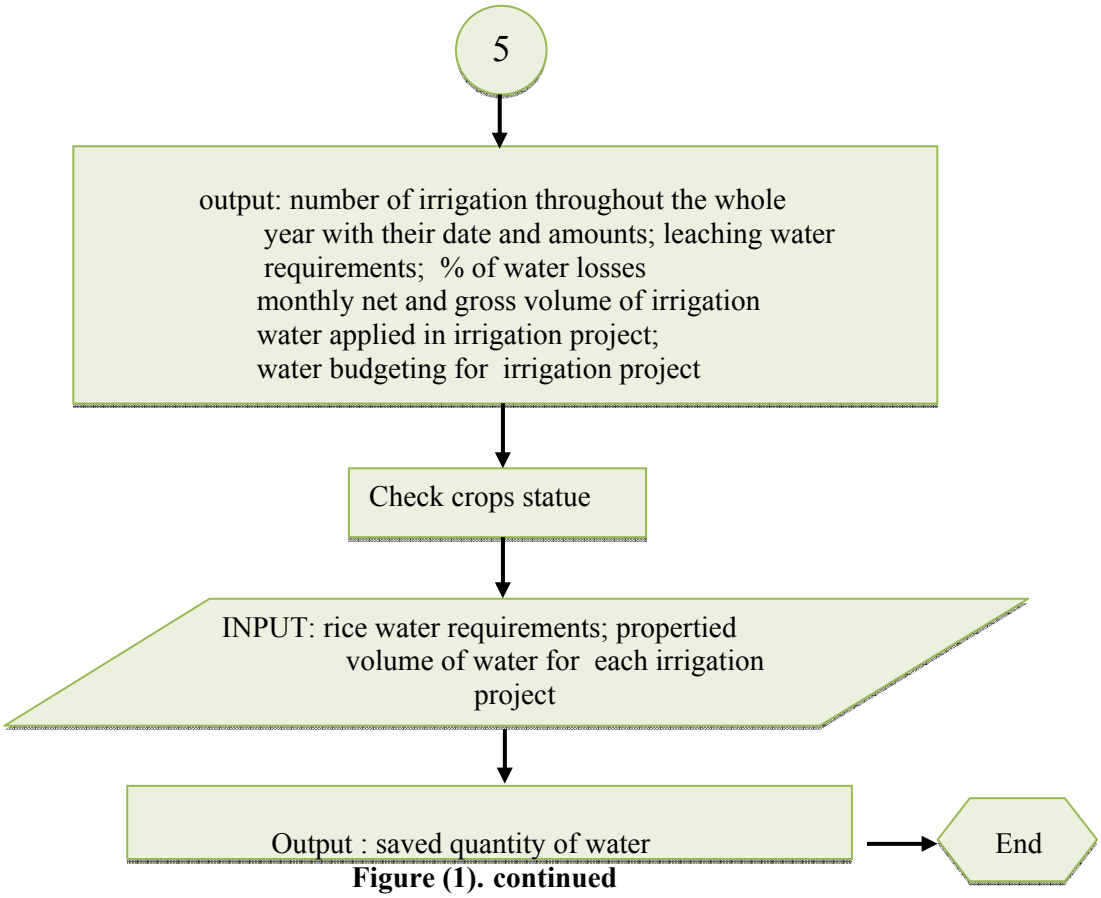

Figure (1). continued

RESULTS AND DISCUSSION

To simplify discussion, Nahr Sa'd irrigation project in Maysan Governorate was taken as an example. Nahr Sa'd irrigation project is located within the southern zone. This zone has a different textured soil refers to the ancient irrigation zone. At present, this zone has a saline soil to a variable degree, average additional leaching water requirements for southern Iraq were taken as 19-19.5% (General Scheme of Water Resource and Land Development of Iraq, 1982). In winter season and during the first month of irrigation scheduling calendar (October), irrigation depth was applied twice a week if it is required, with a chosen time of irrigation, taking in account the irrigation interval. In summer season, continuous irrigation is used since there is no rainfall during the summer season period and crop water requirements become large during this season. To minimize water losses and avoid plant water stress in summer season, irrigation depth was applied twice a week with an irrigation interval equals irrigation time and equal 3.5 (days). In this zone, the effective rainfall is not sufficient to supply crops water requirements. In other words, irrigation water is required even in winter season to supply crop water requirements. Figure (2) shows monthly applied irrigation volumes distribution by using irrigation scheduling and by designers suggestions.

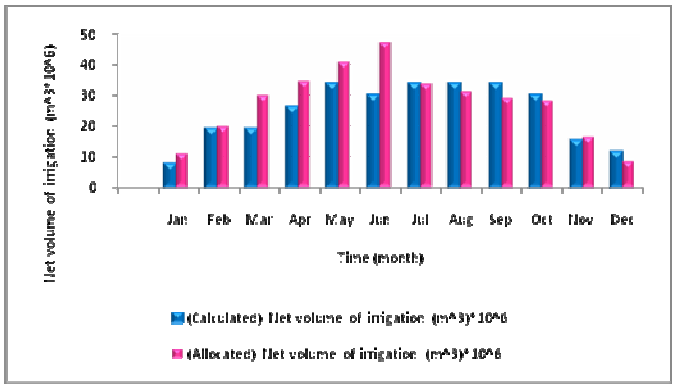

Figure (2). Variation of monthly applied irrigation volumes distribution between scheduled irrigation case (calculated) and designers suggestion case (allocated) for Nahr Sa'd irrigation project.

The monthly and annual net and gross amounts of water due to applying irrigation scheduling procedure on Nahr Sa'd irrigation project is illustrated in table (1).

Table (1). Monthly and annual net and gross amounts of water for Nahr Sa'd irrigation project.

Month	From Calculation		From General Scheme
	(Calculated) Net Volume of Irrigation 10^6 m^3	Gross Volume of Irrigation 10^6 m^3	(Allocated) Net Volume of Irrigation 10^6 m^3
1	7.51	11.92	10.95
2	18.78	29.81	19.77
3	18.78	29.81	29.93
4	26.29	41.73	34.36
5	33.80	53.65	40.59
6	30.04	47.69	47.00
7	33.80	53.65	33.60
8	33.80	53.65	31.16
9	33.80	53.65	29.06
10	30.04	47.69	28.01
11	15.02	23.85	16.50
12	11.27	17.88	8.60
Sum	292.936	464.98	329.53
Percentage of drainage water		7	
Saved volume of water 10^6 m^3		36.59	
Percentage of leaching requirements		19.5	
Percentage of water losses		…	

Figure (2) and table (1) show the difference in applied water distribution between applying irrigation scheduling procedure (calculated) case and designer suggestion (allocated) case. Applied irrigation volumes in scheduled case are less than those allocated to the project, and there is 7% of water lost as drainage water. It is known that the southern zone requires 19-19.5% of water to leach salts, so the 7% of applied water which is lost as a drainage water, is used to leach salts, therefore it can be said that there are no water losses. Table (1) also shows that 36.59 million m^3 of water were saved. This is a good result if the plants are not suffering stress. After checking plant statue by using a water budgeting program it was found that:

All winter crops are suffering from stress and soil moisture content is below wilting point at the beginning of growing season. The maximum plant root depth under soil moisture content below the wilting point is approximately 5 (cm) long. It was supposed that this case is an acceptable, since in spite of the plant initially requires high frequent and little quantities of water, "shallow root depth can absorbs required water when it logged to full the soil water reservoir". Since planted crops root depths are between 600–2000 (mm), So 50-60 (mm) root depth "which represents 10% of minimum plant root depth" was considered as little root depth, and under this depth, the plants will not be lost even the soil moisture content is under the wilting point level. Winter plants statue is illustrated in the figure (3).

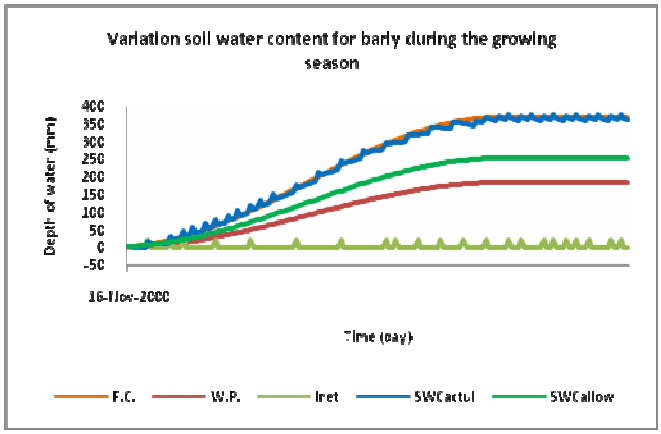

Figure (3). Variation of soil water content for barley during the growing season for Nahr Sa'd irrigation project.

Figure (3) shows a good plant statue since soil water content curve approximately conforms to field capacity curve. At the beginning of growing season, the soil water content curve overreaches wilting point curve, this is done with root depth not exceeds 60 mm, so it is acceptable as mentioned previously.

Summer crops have two behaviors: the first one is soil water content exceeds wilting point at the beginning of the growing season with root depth not exceeding 60 (mm). The second one is soil water content exceeds wilting point at the beginning of the growing season with root depth exceed 60 (mm), which means losing the crops. Figure (4), and (5) show these two behaviors, respectively.

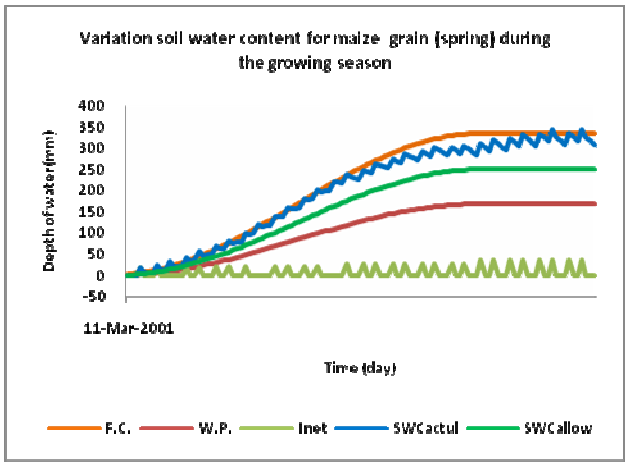

Figure (4). Variation of soil water content for maize grain (spring) during the growing season for Nahr Sa'd irrigation project.

Figure (5) shows summer crop with good statue since the soil water content curve is between field capacity curve and readily available water curve except at the beginning of growing season. At the beginning of growing season, the soil water content curve overreaches wilting point curve, this is done with root depth not exceeds 60 mm.

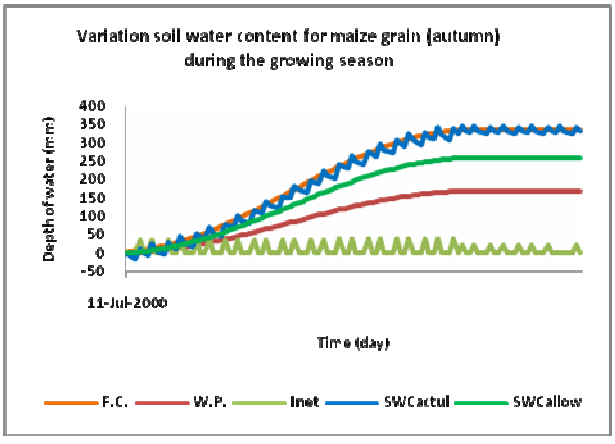

Figure(5). Variation of soil water content for maize grain (autumn) during the growing season for Nahr Sa'd irrigation project.

Figure (5) shows stressed summers crop with the soil water content exceeds wilting point with root depth not exceeding 60 mm.

Perennial crops have no overreaching of wilting point and showing good plant statue as shown in the figure (6).

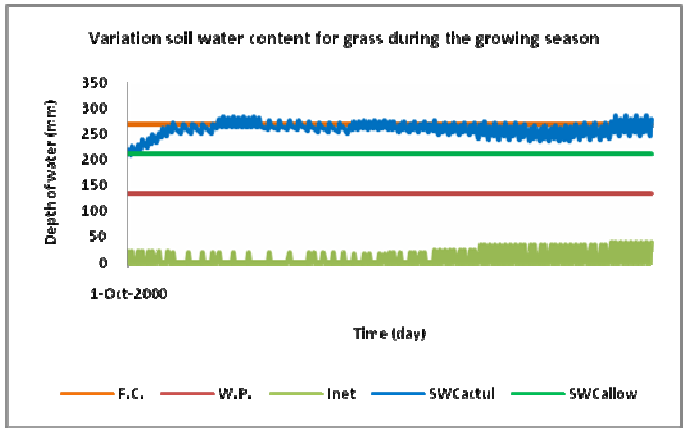

Figure (6). Variation of soil water content for palms during the growing season for Nahr Sa'd irrigation project.

During summer months, time of irrigation is at its maximum possible value and applied irrigation depth is maximum possible. In spite of that, the plants such as maize grain (autumn) do not receive enough depths to prevent stress. To know the reasons that lead to lose maize grain (autumn), several possibilities were considered, these possibilities are reviewed below and examine their impacts on the output of irrigation scheduling procedure. It should be noted that these possibilities vary in success between one irrigation project and another.

First possibility is applied discharge is not sufficient to supply crops water requirements. To study the discharge effects, assumed annual discharges are fed to irrigation scheduling program and the results are shown in table (2).

Table (2) shows that the increment in applied discharge shows no responding of Maize grain (autumn) plant statue, beside the increment in water losses and reduction in water saving. The increment in applied discharge causes increment in applied irrigation depth per irrigation. This increments in applied depth caused changing in applied irrigation frequency, but this change in frequency does not affect Maize grain (autumn) statue. This indicates that the applied discharge is enough for satisfying crops water requirements, other parameters are require some management.

Table (2). A comparison among four used annual net discharges for Nahr Sa'd irrigation project.

Second possibility is soil water reservoir not sufficient to supply crops water requirements. Many researches used weighted average of plants root depths as a guide to choose the right depth of soil water reservoir, which minimize applied irrigation water depth without stressed plants, when more than one crop are planted. In this research, the weighted average of plants root depths was replaced by using a percentage of the longest monthly planted crops root depth as a proposed solution for stressed plant in crop pattern. By using a percentage of maximum root depth, the balance between water losses, plant statue, and applied irrigation depths be possible and be more flexible by controlling the frequency of applied irrigation depth.

		Q (m^3/sec)			
		12.42 *	13	14	15
Applied irrigation volume (10^6 m^3)		292.94	306.63	317.52	335.66
Percentage of drainage water		7	12	16	21
Saved water (10^6 m^3)		36.59	22.9	12.01	-6.13
Percentage of water losses		...	…	…	1.5
No. of lost plants	winter	…	…	…	…
	summer	Maize grain (autumn)	Maize grain (autumn)	Maize grain (autumn)	Maize grain (autumn)
	perennial	…	…	…	…

To study whether used soil water reservoir depth is sufficient for storing enough water for crops, a comparison among ten used percentages of maximum root depth is shown in table (3):

It is clear from table (3) that when reservoir depth increases, water losses decreases due to the increase in reservoir capacity. Saved volume of water also increased. This is because when reservoir depth is small, it can store little quantity of water with more frequent irrigations and the rest is lost as drainage water. With the increase in soil water reservoir depth, irrigation frequency will be less, stored water volume increases and lost water decreases. Table (3) shows reduction in saved volume of water and increase in applied irrigation volume at last two percentages, this is due to the change in irrigation frequency . As shown in table (3), maize grain (autumn) does not respond due to changing the soil water reservoir depth. This indicates that the used soil water reservoir depth is enough to satisfy crops water requirements, other parameters require some management.

Third possibility is using inefficient percentage of planted area to study the effect of the percentage of planted area, assumed percentages of planted area are fed to irrigation scheduling program. In Nahr Sa'd irrigation project, same planted crops were used but with an assumed area for these crops. With many trials, the right percentages of plant area which improve water saving without losing crops could not be found.

Last possibility that used cropping pattern inefficient for applying used irrigation scheduling procedure, to improve that the used procedure is useful for saving water without harmful stress if cropping pattern are chosen carefully, Nahr Sa'd irrigation project with assumed cropping pattern will be discussed. In assumed crop pattern, 5 winter season crops, 11 summer season crops, and 6 perennial crops are planted with cropping intensity equals 137%.

The results are shown in the table (4). The table shows an acceptable percentage of water losses with more than 59 million m^3 of water saving. After checking crops statue it was found that all planted crops have no harmful stress. This result proves that if cropping pattern is chosen carefully, used program is useful for water saving.

Table (3). A comparison among ten used percentages of maximum root depth for Nahr Sa'd irrigation project.

		% RD_{max}									
		10	20	30	40	50	60	70	80	90	100
Applied irrigation volume (10^6 m^3)		394.34	360.54	338.00	307.96	300.45	300.45	296.69	292.94	296.69	300.45
Percentage of drainage water		31	26	21	14	12	12	9	7	7	7
Saved water (10^6 m^3)		-64.81	-31.01	-8.47	21.57	29.08	29.08	32.84	36.59	32.84	29.08
No. of lost plants	winter	…	…	…	…	…	…	…	…	…	…
	summer	Maize grain (autumn)	Maize grain (autumn)	Maize grain (autumn)	Maize grain (autumn)	Maize grain (autumn)	Maize grain (autumn)	Maize grain (autumn)	Maize grain (autumn)	Maize grain (autumn)	Maize grain (autumn)
	perennial	…	…	…	…	…	…	…	…	…	…

Table (4). Monthly and annual net and gross amount of water for an assumed cropping pattern/Nahr Sa'd irrigation project.

month	From Calculation		From General Scheme
	(Calculated) Net Volume of Irrigation 10^6 m^3	Gross Volume of Irrigation 10^6 m^3	(Allocated) Net Volume of Irrigation10^6 m^3
1	3.55	5.63	10.95
2	21.29	33.80	19.77
3	24.84	39.43	29.93
4	28.39	45.06	34.36
5	31.94	50.69	40.59
6	28.39	45.06	47.00
7	31.94	50.69	33.60
8	31.94	50.69	31.16
99	31.94	50.69	29.06
10	14.19	22.53	28.01
11	10.65	16.90	16.50
12	10.65	16.90	8.60
Sum	269.687	428.07	329.53
Percentage of drainage water		19	
Saved volume of water 10^6 m^3		59.84	
Percentage of leaching requirements		19.5	
Percentage of water losses		…	

Winter, summer, and perennial plants statue are illustrated in figures (7), (8), and (9), respectively.

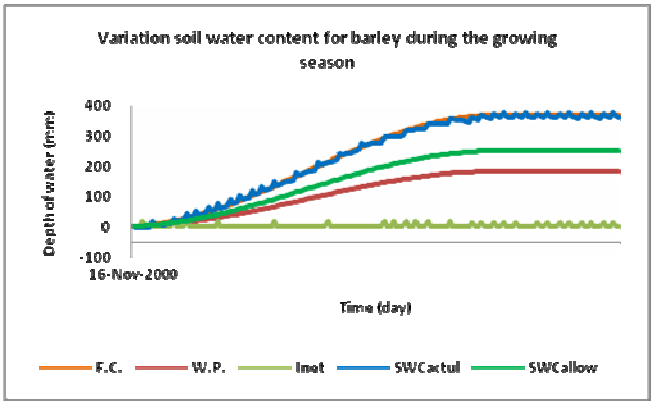

Figure (7). Variation of soil water content for barley during the growing season for assumed cropping pattern/ Nahr Sa'd irrigation project.

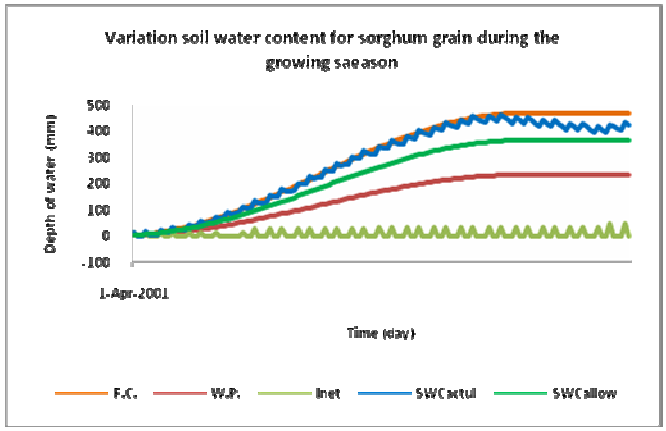

Figure (8). Variation of soil water content for sorghum during the growing season for assumed cropping pattern/ Nahr Sa'd irrigation project.

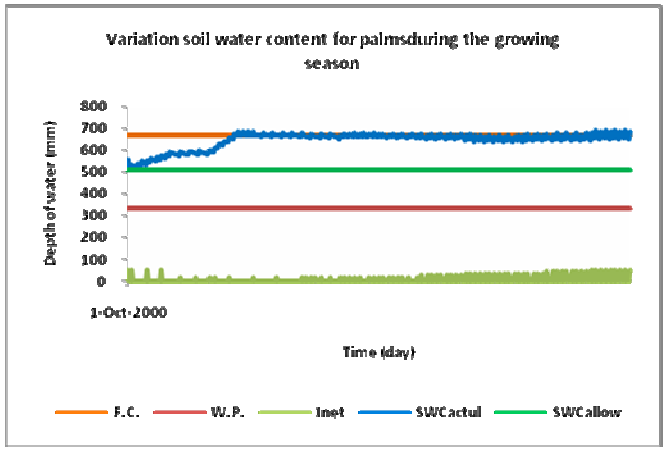

Figure (9). Variation of soil water content for palms during the growing season for assumed cropping pattern/ Nahr Sa'd irrigation project.

CONCLUSIONS

1. The comparison between applied discharges by using irrigation scheduling procedure and designers suggested discharges for the most of studied irrigation projects are impossible, because in these projects some planted crops are lost.

2. Irrigation scheduling procedure is useful if cropping patterns are chosen carefully. Some of studied irrigation projects are requires selecting more suitable cropping pattern;

others required only changing the percentage of planted area with each crop.

3. Using percentage of monthly maximum planted crop root depth giving flexibility to have a balance between applied irrigation, saved water, drainage losses, total available water, readily available water, and plant statue by control applied irrigation frequency.

4. The distribution of monthly applied irrigation volumes by irrigation scheduling procedure is unlike suggested one by designers.

5. Irrigation frequency plays an important role in saving plants, applying same quantities of water with less frequency that should be applied may suffers young plants from water shortage as their roots are not able to take up water from the lower layers of the root zone.

REFERENCES

Alderfasi, Ali Abdullah. (2000). "Response of four Genotypes of Wheat to Irrigation Schedules." Saudi J. Bio.Sci. 7 (2): 171-178.

Alderfasi, Ali A. and D. Nielsen. (2001). "Use of Crop Water Stress Index for Monitoring Water Status and Scheduling Irrigation in Wheat." Agricultural Water Management. 47 (1): 71-77.

Al-Haddad, A. H. (1997). "Irrigation Scheduling in Large Irrigation Project." PhD. Dissertation submitted to the College of Engineering, University of Baghdad.

Al-Haddad, A. H. (2001). "Effect of Prescheduled Irrigation on Wheat Growth." First National Conference in Civil Engineering, College of Engineering, University of Al-Anbar.

Allen R.; L. Pereira; D. Raes; M. Smith. (1998). "Crop Evapotranspiration: Guidelines for Computing Crop Water Requirements." Irrig. and Drain. Paper No. 56, Food and Agricultural Organization of United Nations (FAO), Rome, Italy.

Al-Mesh'hedany, U. N. K. (2002). "The Role of Irrigation Scheduling in Crop Production." M. Sc. Thesis submitted to the College of Engineering, University of Baghdad.

Alves, I and L. S. Pereira. (2000). "Non-water-stressed Baselines for Irrigation Scheduling with Infrared Thermometers: A New Approach." Irrig Sci 19(2): 101-106.

Antosch, Larry M. (2007). "Irrigation water management for Ohaio. Procedure guide for the development and implementation of a systematic water management program".

Eastham, J.; S. A. Gray. (1998). "A Preliminary Evaluation of the Suitability of Sap Flow Sensors for Use in Scheduling VineyardIrrigation." American Journal of Enology and Viticulture 49: 171–176.

Ehret, D. L.; A. Lau; S. Bittman; W. Lin; T. Shelford. (2001). "Automated Monitoring of Greenhouse Crops." Agronomie 21: 403–414.

Fortes , P. S.; Lu´ıs S. Pereira; Ant´onio A. Campos. (2004). "GISAREG – A GIS Based Irrigation Scheduling Simulation Model." Projet INCO-WADEMED Actes du S´eminaire Modernisation de l'Agriculture Irrigu´ee Rabat, du 19 au 23 avril 2004.

General scheme of water resource and land development of Iraq. (1982). Ministry of water irrigation, Iraq.

Ginestar, C.; J. Eastham; S. Gray; P. Iland. (1998a). "Use of Sap-flow Sensors to Schedule Vineyard Irrigation." I. Effects of Post-veraison Water Deficits on Water Relations, Vine Growth, and Yield of Shiraz Grapevines. American Journal of Enology and Viticulture. 49: 413–420.

Ginestar, C.; J. Eastham; S. Gray; P. Iland. (1998b). "Use of Sap-flow Sensors to Schedule Vineyard Irrigation. II. Effects of Post-veraison Water Deficits on Composition of Shiraz Grapes." American Journal of Enology and Viticulture. 49: 421–428.

Giorio, P.; G. Giorio. (2003). "Sap Flow of Several Olive Trees Estimated with the Heat-pulse Technique by Continuous Monitoring of a Single Gauge." Environmental and Experimental Botany. 49: 9–20.

Harrison, k. (2009). "Irrigation Scheduling Methods." The University of Georgia Cooperative Extension.

Irrigation Industry Association of British Columbia's IIABC. (2009). "Landscape Calculator." website www.irrigationbc.com.

Jones, HG. (1990a). "Plant Water Relations and Implications for Irrigation Scheduling." Acta Horticulturae. 278: 67–76.

Maher, M.; and others. (2005). "Computer-Aided Mapping Irrigation Scheduling for Arab Republic of Egypt."

Martin, Edward C. (2009). "Methods of Measuring for Irrigation Scheduling-WHEN." The University of Arizona Cooperative Extension.

Moriana , Alfonso; David Pérez-López; Aurora Gómez-Rico; María de los Desamparados Salvador; Nicolás Olmedilla; Francisco Ribas and Giuseppe Fregapane. (2007). "Agricultural Water Management." 87(2).171-179.

Remorini, D.; R. Massai. (2003). "Comparison of Water Status Indicators for Young Peach Trees." Irrigation Science. 22: 39–46.

Riffat, R. U. N. (1999). "Variation of Water Use Efficiency with the Cropping Pattern." M. Sc. Thesis submitted to the College of Engineering, University of Baghdad.

Stockle, O. C.; William A. Dugas. (1992). "Evaluating Canopy Temperature- Based Indices for Irrigation Scheduling." Irrig Sci. 13: 31-37.

Vellidis, G.; M. Tucker; C. Perry; C. Kvien; and C. Bednarz. (2008). "A Real-time Wireless Smart Sensor Array for Scheduling Irrigation." Journal of Computers and Electronics in Agriculture. 61(1): 44-50.

انمار عبد العزيز الطالب، عبد الستار يونس الدباغ، حمد أزهر ذنون ألنعيمي. 2005." نمذجة احتياجات الري الناقص لمحصول الذرة الصفراء في منطقة الموصل." مجلة هندسة الرافدين، جامعة الموصل، الموصل.

صفاء نوري حمد. (1996). "برمجة الإرواء في مشاريع الري." مجلة هندسة الرافدين، جامعة الموصل، الموصل.

ABBREVIATIONS

Symbol	Description	Unit
% RD	Percentage of maximum root depth	%
%RAW	Percentage of depletion from readily available water	%
AD	Percentage of Allowable depletion	%
ARD	Additional used root depth	mm
ASWD	Additional soil water deficit	mm
C	Conversion for units	…
D_{wet}	Depth of wetted soil	mm
Dm	Number of days to reach maturity	day
Dp	Number of days after planting	day
DP	Deep percolation losses	mm
ER	Monthly effective rainfall	mm/month
ET_c	Actual monthly crop evapotranspiration	mm/month
ET_o	Monthly reference crop evapotranspiration	mm/month
F.C.	Soil moisture content at field capacity	mm
FC	Field capacity	%
$GQ_{req.}$	Gross continuous discharge required	m^3/sec
i	Index for time in month	month
I_{net}	Applied net irrigation depth	mm
IE	Expected irrigation efficiency	%
IRR_{time}	Irrigation time	day
ISWC	Initial soil water content	mm
j	Index for crop grown in the project	…
k	Index for time in days	day
K_c	Crop coefficient	%
Kc max	Maximum crop coefficient	%
Kco	Initial crop coefficient	%
n	Number of crops grown in the project	…
NA	Net irrigated project area	don.
NA_i	Net area in the project planted during the i^{th} month	don.
NA_j	Net area planted with the j^{th} crop	don.
ND	Number of days in month	day
NI req.	Net volume of water required	m^3
$NQ_{req.}$	Net continuous discharge required	m^3/sec
PA	Percentage of area planted with each crop	%
PWP	Permanent Wilting point	%
Q_{max}	Maximum discharge	m^3/sec
RAW	Readily available water in the root zone	mm
RD	Root depth at any time	mm
RDo	Initial root depth.	mm
SWC	Soil water content in the root zone	mm
$SWC_{(actual)}$	Actual soil moisture content	mm
$SWC_{(allow)}$	Allowable soil water content	mm
SWD	Soil water deficit	mm
SWDA	Soil water deficit after irrigation.	mm
SWDAL	Soil water deficit after irrigation at the last day in the month	mm
SWDB	Soil water deficit before irrigation	mm
SWDL	Percentage of Soil water deficit after irrigation at the last day in the month	%
TAW	Total available water	mm
URD	Used root depth	mm

WD	Water duty	$l/sec/ha$
WL	Water losses	mm
W.P.	Soil moisture content at wilting point	mm

Appendix (1).

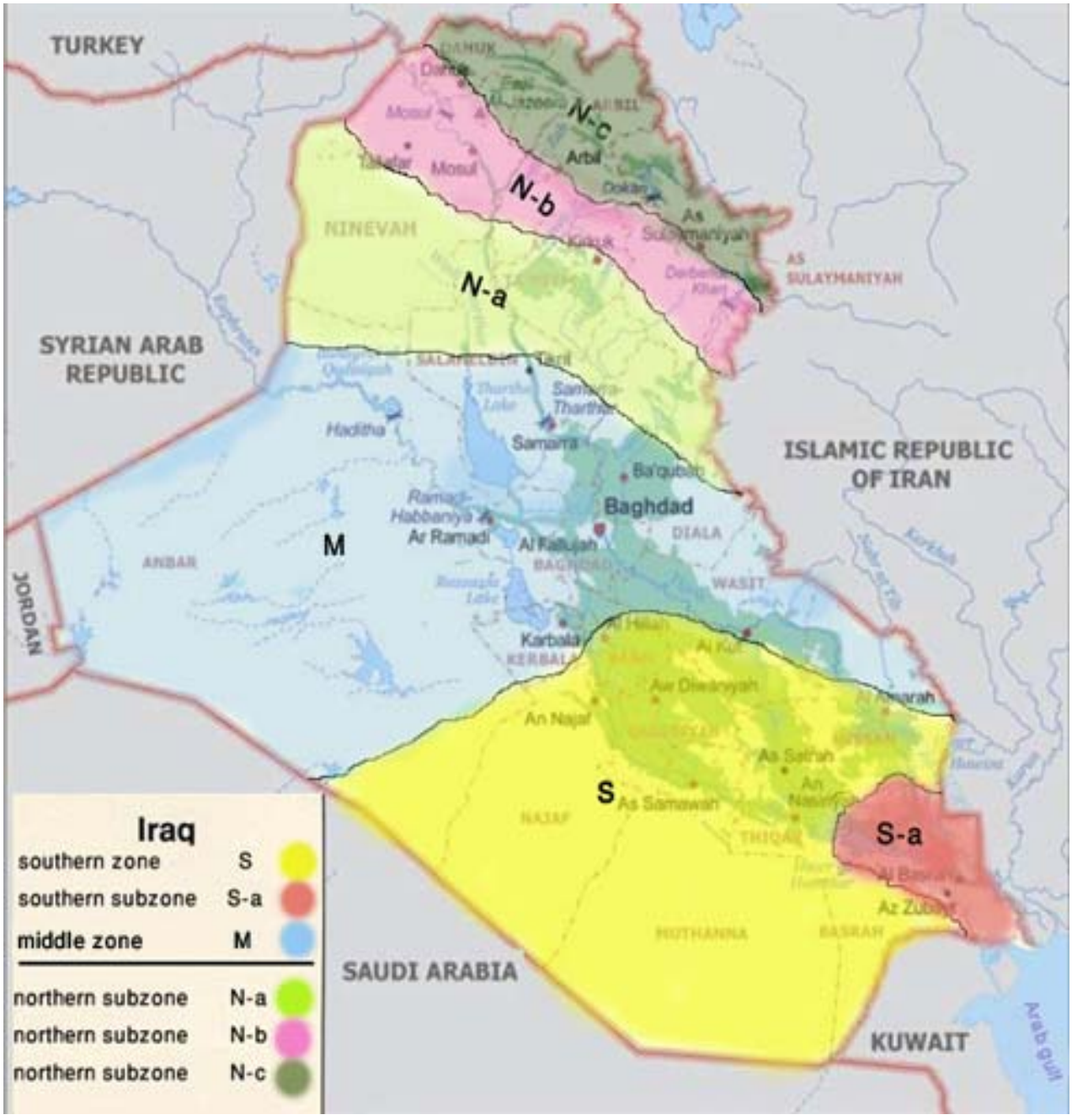

Climate zones of Iraq (General Scheme of Water Resource and Land Development in Iraq, 1982).

Free Head Shear Test on Decomposed Granite Soil

Dr.Haider Mohammed Mekkiyah
Lecturer
College of Engineering
University of Baghdad
E-mail:hydmekk@yahoo.com

Abbas Malik Khallawi
Asst. Lecturer
Management of Dormitories
University of Baghdad
E-mail:amkhfar@yahoo.com

ABSTRACT

The study presents the test results of Completely Decomposed Granite (CDG) soil tested under drained triaxial compression, direct shear and simple shear tests. Special attention was focused on the modification of the upper halve of conventional Direct Shear Test (DST) to behave as free head in movement along with vertical strain control during shear stage by using Geotechnical Digital System (GDS). The results show that Free Direct Shear Test (FDST) has clear effect on the measured shear stress and vertical strain during the test. It has been found that shear strength parameters measured from FDST were closer to those measured from simple shear and drained triaxial compression test. This study also provides an independent check on the consistency of the data by providing an interpretation for angle of dilation together with shearing resistance by using flow rule analysis.

Keywords: decomposed granite soil, free direct shear test, simple shear, triaxial test, angle of internal friction

فحص القص الحر لتربة الكرانيت المتفككة

الخلاصة

الدراسة تقدم نتائج الفحوص على تربة الكرانيت المتعرية التي تم فحصها من خلال الفحوص التالية(triaxial compression،direct shear،simple shear). تم التركيز على تحوير صندوق القص المباشر لجزئه العلوي ليسمح له بالحركة بشكل حر مع سيطرة على الانفعال الراسي باستخدام جهاز (GDS). اظهرت نتائج الفحص التاثير المباشرللقص الحرعلى نتائج اجهاد القص عند الفشل ومقدار الانفعال خلال الفحص. كذلك لوحظ معاملات المقاومة المحسوبة من خلال القص الحر هي اقرب من مثيلاتها في فحص القص البسيط والثلاثي(triaxial compression،simple shear). الدراسة ايضا اعطت تدقيق غير مباشر لتوافق النتائج من خلال دراسة زاوية التمدد(angle of dilation) ومقاومة القص باستخدام مبدأ تحليل الانسياب (flow rule).

الكلمات الرئيسيه: تربة الكرانيت المتفككة،فحص القص الحر،القص البسيط، الفحص الثلاثي،زاوية الاحتكاك الداخلي

1- INTRODUCTION

The conventional Direct Shear Test (DST) has been used to determine the residual strength parameters, since the direction of defined failure planes, the magnitude and direction and/or rotation of the principle stresses and pore pressure measures are not determined in DST. The DST analysis can open the results to various interpretations (Hill, 1990) and this test is rarely used to determine the undrained or peak effective strength parameters. Simple shear and/or triaxial compression test may be performed more conveniently with better control and finally provide best understanding for shear strength parameters and stress-strain behavior. The direct shear box is only suitable for measuring the shear strength parameters because of non-uniformity of stress and strain on the central plane of soil (Hvorslev, 1960 and Sowers, 1964) and also may be due to the restraints of box ends that can create an even more markedly non uniform shear surface as shown in Figure (1). Nevertheless the DST remains popular in practice due its simplicity and different sample preparation procedure. This test can be used per standards in order to minimize or even eliminate the influence of the upper shear box-soil sample friction. This can be achieved by adding lubrication or smooth material such Teflon plate at the points where the upper shear box is in contact with the bearing ring that measure the shear surface (Nithiaraj et al., 1996).

The Completely Decomposed Granite (CDG) soil is the product of in-situ for measuring the shear strength parameters because of non-uniformity of stress and strain weathering of rocks due to the warm and wet climate in South East Asia. In peninsular of Malaysia for example this type of soil has covered a large area of (Matsuoko and Liu, 1998).

The soil used in this study was CDG soil, the conventional DST has been modified to minimize the friction of the upper shear box and to investigate the stress-strain behavior with FDST. The results obtained from FDST are compared with those measured from DST [ASTM D3080/3080M-11], simple shear test [ASTM D6528-07] and triaxial compression test [ASTM D 7181-11].

2- DATA ANALYSIS

Two angles were interpreted from conventional DST and/or FDST test. Firstly is friction angle of direct shear by using Mohr Coulomb failure criteria as follows:

$$\tau = c + \sigma \tan\phi_{DST} \qquad (1)$$

where τ and σ are the shear and normal stress at failure plane; c is the soil cohesion and ϕ_{DST} the direct shear angle of friction which refers to the shearing resistance on the planes along where there is no extension (i.e. no linear increment strain). Secondly the plain strain angle of friction is ϕ_{PS} of soil. The two angles can be written as:

$$\sin\phi_{PS} = \frac{\tan\phi_{DST}}{\cos\varphi + \sin\varphi \tan\phi_{DST}} \qquad (2)$$

where φ is the dilation angle of soil.

The analysis through the critical state can support the data consistency by using flow rule expressed in terms of shearing resistance and the incremental strain on a plane along where there is no linear incremental strain can occur by using Taylors flow rule (1948) as:

$$\tan\phi_{PS} - \tan\varphi = \sin\phi_{CV} \qquad (3)$$

where ϕ_{CV} is the critical friction angle of soil. Another flow rule was used proposed by Bolton (1986) as:

$$\phi_{PS} - 0.8\varphi = \phi_{CV} \quad (4)$$

In case of simple shear apparatus the test should mobilize the ϕ_{DST} in the soil on the central plane similar to DST test.

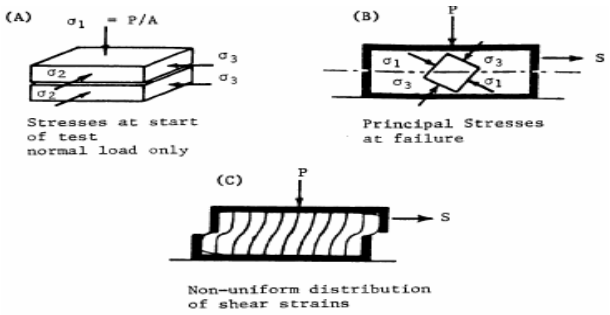

Figure (1): Rotational of Principal Stresses and Non Uniform Shear Stresses on Horizontal Surfaces at Failure in DST (Sowers, 1964)

3-MATERIAL USED

The soil used in this study was obtained from Serdang area, Kuala Lumpur, Malaysia. The CDG soils consist mainly of sand-silt mixture. The physical properties of CDG soil are listed in Table (1).

Table (1): Physical Geotechnical Properties of CDG soil.

Soil Parameter	Symbol	Value
Specific Gravity	G_s	2.68
Liquid Limit, (%)	L.L	52
Plastic Limit, (%)	P.L	22
Plasticity Index, (%)	P.I	30
Max. Dry Unit Weight, (kPa)	γ_d	15.4
Optimum Water Content, (%)	w_c	21.4
pH	pH	4.8
Compression Index	c_c	0.087
Swelling Index	c_s	0.027

4- SYSTEM DESCRIPTION

The schematic diagram for the FDST is shown in Figure (2). The upper shear box was modified using a metal rod with a flexible head connected with the proving ring. The free rod movement is not restricted and can rotate freely in any direction from the center line with a maximum angle of 35 degree. The flexible connection of the rod allows the upper shear box to move vertically and horizontally without restriction during shear stage while the lower shear box is fixed in both directions.

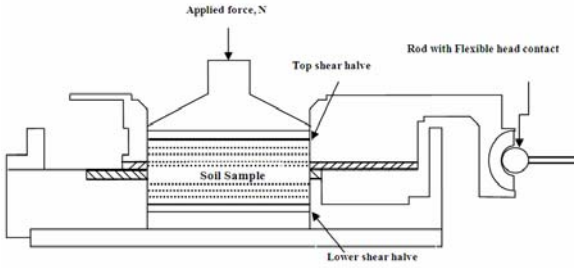

Figure (2): Schematic Diagram of Free Direct Shear Test

5- DIRECT SHEAR TEST

In this series of test the soil samples were tested under direct shear test setup that was fully computerized by using Geotechnical Digital System (GDS), the detailed description of the system elements were given by GDS laboratory manual (GDS Instruments Ltd, 2002).The GDSLAB control and acquisition software was highly developed, flexible software platform to run different types of modules. The CDG soil was tested under conventional DST and FDST with applied normal stress of 85 kPa, 165 kPa and 250 kPa. The saturated soil samples of 60 mm (i.e. square box) were tested under drained conditions with a unit weight of 17.6 kPa prepared by using moist tamping method. Figure (3) shows the Shear stress versus horizontal strain relationship under DST and FDST with different normal stresses. As expected, higher shear stress developed under higher normal stress. The results

obtained from FDST had lower shear stresses compared to those obtained from DST, and this may be due to the free head modification that allows the movement without any restraints at the end of the box. Without this modification higher measured shear stresses can be developed at box ends. Figure (4) shows the relationship between the vertical and horizontal strains (85 kPa, 165 kPa and 250 kPa) the vertical strains measured by FDST were lower than those measured by DST. It further indicates that the vertical soil movement in DST was restricted to one direction while the soil was allowed to move freely in FDST within the flexibility of upper shear box. The free-interface soil movement in FDST may be similar to the movement of soil sample in simple shear test where the soil movement of soil sample was not restricted to one direction. Figure (4) also shows the contractive soil behavior during shear stage.

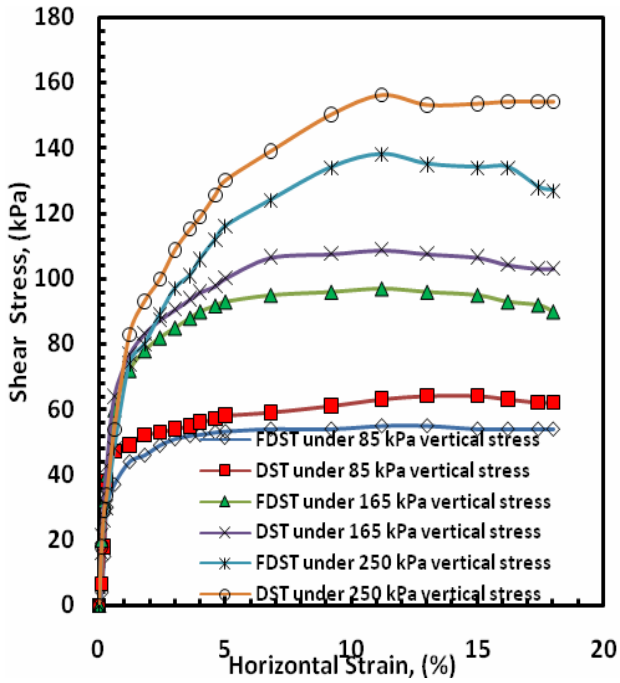

Figure (3): Shear Stress vs. Horizontal Strain for both DST and FDST.

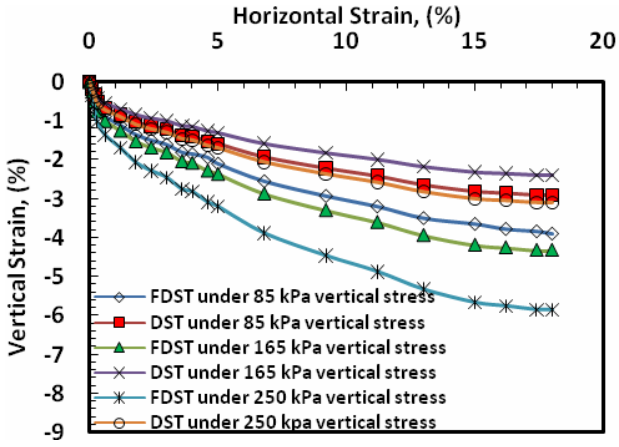

Figure (4): Vertical Strain vs. Horizontal Strain for both DST and FDST under 85 kPa, 165 kPa and 250 kPa.

6- SIMPLE SHEAR TEST

In this series of test the soil samples were tested under Simple Shear (SS) test setup that was fully computerized by using GDS-system under 92 kPa, 170 kPa and 265 kPa. The saturated soil samples of 70 mm diameter were tested under drained conditions with a unit weight of 17.6 kPa prepared by using moist tamping method. Figure (5) shows shear stress versus horizontal strain relationship of CDG soil under simple shearing. Figure (6) shows the contractive behavior of CDG soil especially at low horizontal strains, which were similar to the soil in FDST and DST.

7- TRIAXIAL COMPRESSION TEST

In this series of tests the triaxial setup was fully computerized by using GDS-system. Specimens of 50 mm in diameter and 100 mm in height with a unit weight of 17.6 kPa were prepared by using the moist-tamping technique tested under triaxial Compression (TC) with a confining stress of 100 kPa, 200 kPa and 300 kPa. Figure (7) indicates the relationship between the deviator stress and axial strain. The results illustrate that hardening soil behavior of weathered granite. Figure (8) shows the contractive tendency of CDG soil

under low axial strain similar to the behavior of soil under simple shear test.

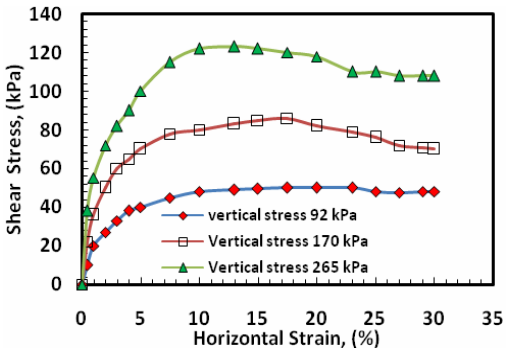

Figure (5) Shear Stress vs. Horizontal Strain for Simple Shear Test.

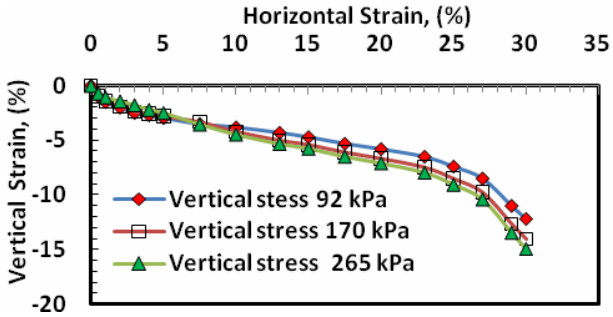

Figure (6): Vertical Strain vs. Horizontal Strain for Simple Shear Test

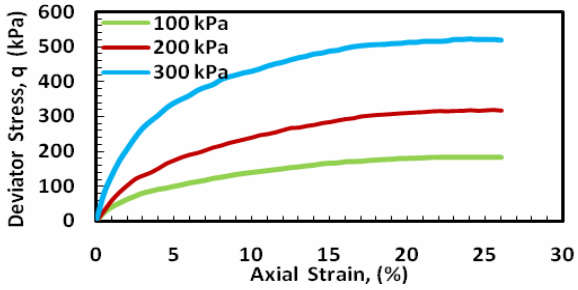

Figure (7): Deviator Stress vs. Axial Strain for Triaxial Compression Test.

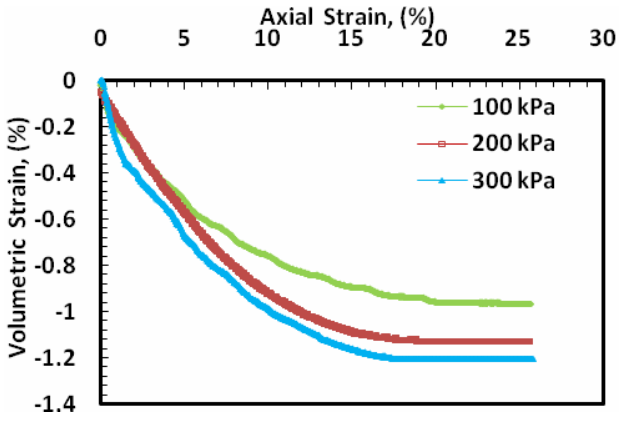

Figure (8): Volumetric Strain vs. Axial Strain for Triaxial Compression Test

8- DISCUSSION

From the above presented results the shear strength parameters of CDG soil were calculated and shown in Table 2. The shear strength parameters obtained from DST were higher than those obtained from FDST, simple shear and triaxial compression tests. It appears from Table (2) that FDST results were closer to those measured by simple shear and triaxial compression tests. In general the shear strength parameters measured by the DST does not agree completely with those measured by triaxial compression test, due to predetermined failure plane in DST (Liu and Mastuok, 2005). This is also may be due to restraints at the ends of box that create zone of complex and higher principal stress ratio at failure (σ'_1/σ'_3) compared with FDST, simple shear or triaxial test and as shown inTable(3).

Table (2): Comparison of Shear Strength Parameters of CDG soil measured from Different tests.

Test Type	C′ (kPa)	ϕ'_{DST} (Degree)
DST	26.5	27.1
FDST	23.1	24.0
SS	18.5	20.1
TC	17.2	23.8

Table (3): Principal Stress Ratio at Failure of CDG soil for all Tests.

Test Type	σ'_1/σ'_3
DST 1	4.02
DST 2	3.07
DST 3	2.89
FDST 1	3.67
FDST 2	2.88
FDST 3	2.66
SS1	2.67
SS2	2.16
SS3	2.03
TC 1	2.86
TC2	2.62
TC3	2.61

The soil friction angle from FDST were found to be lower than the results obtained from DST, similar observation were reported on Toyoura sand as shown in Table (4).

Table (4): Soil Friction Angle for Toyoura Sand from DST and improved DST (Liu et al., 2005)

Test type	ϕ'_{DST} (Degree)
DST	44.8
Improved DST (I)	41.1
Improved DST (II)	41.8
Triaxial Test (Matsuoka and Liu, 1998)	40.0

The trend behavior of vertical strains was found to be affected by test type as shown in Figures (4), (6) and (8). Both DST and FDST show the same trend but with different vertical strains level, while these vertical strains are less in case of simple shear test and found to be varied under different normal stress with high dilation angle as measured and shown in Table (5). The vertical strain levels in FDST were found to be closer to those measured in triaxial compression test. Figure (9) indicates the relationship between shear stiffness (K_s) and normal stress for (DST and FDST)/or confining stress for TC. The K_s value increased as the normal and/or confining stress increased. Shear stiffness K_s in DST shows higher response compared with those from FDST and simple shear test. Shear stiffness from simple shear shows similar level value obtained from triaxial test as shown in Figure (9b). Table (5) illustrates the shear resistance analysis for 165 kPa and 170 kPa normal stress were carried for (DST, FDST) and SS tests respectively; the analysis show also that dilation angle was high in SS test while it was less in case of DST or FDST. These reflected by the measured direct shear angle and/or plain angle of friction. Low variations were observed between critical flow rule analysis and conventional analysis, which provided support for the data accuracy to the measured stresses and strain during the shearing stage.

Table (5): Analysis for Peak Shearing Resistance of CDG Soil Measured from DST, FDST and SS.

Note: the range of critical friction angle assumed in flow rule analysis ϕ_{cv}=(24.0°- 28.0°)

Criteria	DST	FDST	SS
Vertical Stress, kPa	165	165	170
$(\tau'/\sigma')_{max}$	0.57	0.66	0.5
$(dy/dx)_{max}$	0.0133	0.008	0.36
$\varphi=\tan^{-1}(dy/dx)_{max}$, (Deg)	0.76°	0.45°	19.8°
Direct Shear Angle of Friction ϕ_{DST}			
Measured in Simple Shear			20.1°
Conventional Analysis (Eq.1)	24.0°	27.1°	
Flow Rule Analysis (Eq.3)	(22.8°-25.7°)	(22.5°-25.5°)	
Plain Strain Angle of Friction ϕ_{ps}			
Measured in Simple Shear			(39.8°-43.84°)
Conventional Analysis (Eq.2)	26.3°	30.6°	
Flow Rule Analysis (Eq.4)	(24.6°-28.6°)	(24.4°-28.4°)	

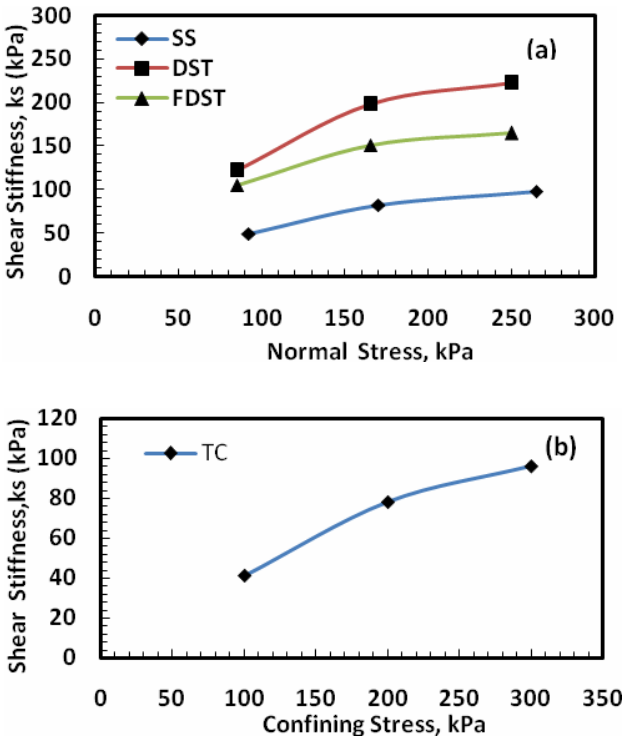

Figure (9): (a) Shear Stiffness vs. Normal Stress for DST and FDST, (b) Shear Stiffness vs. Normal Stress for TC Test.

Figures (10 and 11) indicate the shear displacement corresponding maximum stress increased with normal stress, in terms of rate of dilation, the soil exhibits moderate Dilation Ratio (DR) at the beginning of shear stage then a lower dilation ratio observed at the end of shearing stage and gradually increases as the normal stress increases. Contraction soil behavior was more pronounced.

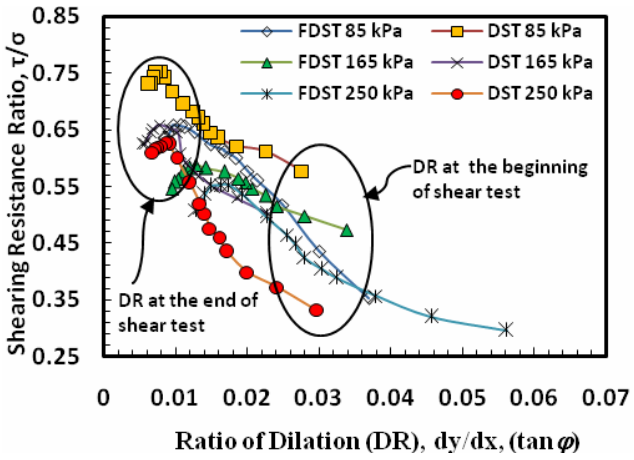

Figure (10): Direst Shear Test on CDG Soil showing the Influence of Boundary Condition in DST and FDST

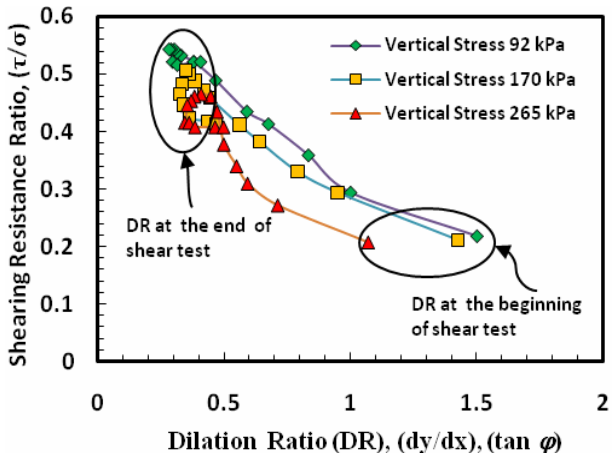

Figure (11): Direst Shear Test on CDG Soil showing the Influence of Boundary Condition in SS Test

9-CONCLUSIONS

From the series of tests carried on CDG soil using DST, FDST, SS and TC, the shear strength parameters were found in FDST to be closer to those obtained from triaxial and simple shear test.

In general the defined failure planes in DST along with end restraints in the upper box halve cause increase in shear strength parameters and shear stiffness when compared with other tests values. The free movement of the upper box half had similar behavior of soil sample in simple shear test.

The vertical shear strains in DST were closer to those measured in triaxial test while these values were less in case of SS and FDST tests. Rate of dilation at failure increased with increasing normal stress. The soil showed contractive behavior for DST, FDST, SS and TC tests. Both friction angles ϕ_{DST} and ϕ_{ps} showed in conventional DST test more conservative values compared with FDST, similar behavior in flow rule analysis. The test results of SS showed underestimation of friction angles in conventional analysis ϕ_{DST} while overestimation ofϕ_{ps} it was in plain strain analysis. The lower limit of friction angles from conventional analysis and /or plain strain analysis can be estimated from DST test, while the upper respective limit of friction angles can be estimated from FDST test since the direction of failure planes are not defined**.**

10- REFERENCES

- ASTM D3080 / D3080M – 11,"Standard Test Method for Direct Shear Test of Soils Under Consolidated Drained Conditions".
- ASTM D6528 – 07,"Standard Test Method for Consolidated Undrained Direct Simple Shear Testing of Cohesive Soils".
- ASTM D7181–11, "Method for Consolidated Drained Triaxial Compression Test for Soils".
- Bolton, M. D. (1986). "The Strength and Dilatancy of Sands". *Geotechnique*, 36(1), pp (65-78).
- GDS Instruments Limited (2002). GDS Laboratory Manual.

- Hill, R. (1950). "The Mathematical Theory of Plasticity". Oxford University Press, Oxford.
- Hvorslev, M. J., (1960). "Physical Components of Shear Strength of Saturated Clay". ASCE Research Conf. on Shear Strength of Cohesive Soil, Boulder, Colorado, pp (169-273).
- Matsuoka, H., Liu, SH. (1998). "Simplified Direct Shear Box Test on Granular materials. Soils and Foundation": 38(4), pp (275-284).
- Nithiaraj, R., Ting, W. H., and Balasubramaniam, A. S. (1996). "Strength Parameters of Residual Soils and Application to Stability Analysis of Anchored Slopes". Geotehnical Engg. Journal: 27(2), pp (55-82).
- Liu, SH., De′an Sun, and Matsuoka, H., (2005). "On the Interface Friction in Direct Shear Test"". Computer and Geotechnics: 32, pp (317-325).
- Sowers, G. F. (1964). "Strength Testing of Soils, Laboratory Shear Testing of Soils"; ASTM Special Technical Publication No. 361, pp (9-l4).
- Taylor, D. W. (1948). "Fundamental of Soil Mechanics", Wiley, New York.

A Proposal Algorithm to Solve Delay Constraint Least Cost Optimization Problem

Waleed A. Mahmoud **Dheyaa J. Kadhim**
Electrical Engineering Department
College of Engineering / University of Baghdad
Email: deya_naw@yahoo.com

ABSTRACT

Traditionally, path selection within routing is formulated as a shortest path optimization problem. The objective function for optimization could be any one variety of parameters such as number of hops, delay, cost...etc. The problem of least cost delay constraint routing is studied in this paper since delay constraint is very common requirement of many multimedia applications and cost minimization captures the need to distribute the network. So an iterative algorithm is proposed in this paper to solve this problem. It is appeared from the results of applying this algorithm that it gave the optimal path (optimal solution) from among multiple feasible paths (feasible solutions).

Keywords: Routing, Routing Algorithms, QoS, Optimization and Feasible Problem.

الخلاصة

بشكل عام أختيار المسار خلال عملية تحديد المسار يمكن معاملتها كمشكلة أقصر مسار أمثل. أن الدالة الموضوعية للامثلية ممكن ان تكون اي متغير من المتغيرات الاتية: عدد القفزات، زمن التاخير، الكلفة... الخ. مشكلة تحديد المسار باقل كلفة بزمن تاخير محدد درست في هذا البحث لان تحديد زمن التاخير هو متطلب مهم من متطلبات تطبيقات وسائط النقل وتقليل الكلفة لتسهيل النقل وتوزيع البيانات في الشبكة. لذلك تم اقتراح خوارزمية تكرارية في هذا البحث لحل هذه المشكلة. وقد ظهر من نتائج التطبيق هذه الخوارزمية انها تعطي المسار الافضل (الحل الامثل) من بين عدة مسارات ملائمة (حلول ملائمة).

1. INTRODUCTION:

The Delay-Constrained Least-Cost (DCLC) path problem is searching for a path that has the minimum cost and a delay not exceeding a given upper bound [G.Feng2001].

The single mixed weight idea proposed in this paper can be briefly described as follows; "Given a network with a delay and a cost associated with each link, it can first obtain a single mixed weight for each link by combining its delay and cost in terms of one parameter, and then use Dijkstra's Algorithm to find the corresponding shortest path". It can be theoretically proved that as long as the parameter is appropriately chosen the obtained shortest path must be a feasible solution with a cost no greater than that of the least delay (LD) path. Based on this result, a heuristic algorithm is used that can produce good solutions by executing Dijkstra's shortest path algorithm at most three times. To further improve the quality of the solution, then two iterative algorithms are proposed that can generate a series of parameters gradually improving the corresponding solutions. A large number of numerical experiments are carried out and the results of them are compared [R.Sriram1998].

2. THE DCLC PATH PROBLEM [G.FENG]:

Any network can be represented by a directed graph G (V, E), where V is the set of nodes, and E is the set of links. Assume that N= [V], and M= [E].

A weight w define a nonnegative real number w(e) associated with each link, i.e., W: E→R_0^+. In particular, weight d: E→R_0^+ is called delay, while c: E→ R_0^+ is called cost. A path is a finite sequence of non –repeated nodes p=(v_1 ,v_2,....., v_k) such that for 0≤i<k, there exists a link from v_1 to $v_i + 1$, i.e.. (v_i ,$v_i + 1$) ∈ E. A link e ∈ p means that p passes through link e. A weight w, like delay or cost, additive if the weight of a path p is equal to the summation of the weights of all links along that path,

$$w(\rho) = \sum_{e \in p} w(e) \quad (1)$$

In particular, the delay and cost of a path p are given by two equations below:

$$d(\rho) = \sum_{e \in p} d(e) \quad (2)$$

$$c(\rho) = \sum_{e \in p} c(e) \quad (3)$$

In general sense, the delay of a link is the average transmission time on that link, while the cost of a link may be the fee charged to transmitting a message on that link. However, delay and cost may be redefined as other metrics such as jitter, loss etc., as long as they are additive.

Now a formal definition for the DCLC (Delay Constraint Least Cost) problem using the above notation is illustrated below.

Definition 1:

Given a network G (V, E), a source s ∈ V and a destination node d ∈V, a delay and a cost for each link, and a delay constraintC_d, the delay – constrained least-cost (DCLC) path problem is to find a path p from s to d, such that .

(i) d (p) ≤ C_d,

(ii) c (p) ≤ c(q) for any path q from s to d that satisfies d (p) ≤ C_d,

(iii) There doesn't exit a path q from s to d, for which c(p)=c(q),

While d (p)> d (q).

It should be noted though that the third requirement is not included in a standard definition for the DCLC problem; it is introduced here to reflect our preference for a path resulting in better performance if there exist more than one solution for the standard problem. For convenience, a path that at least satisfies the first requirement in the above definition is called a ***feasible solution*** (or feasible path); a path that satisfies all the three requirements is called an ***optimal solution*** (or optimal path).

The following definition and notations are needed to describe the algorithms to be proposed in this chapter.

Definition 2:

Given two additive weights $w_1$and w_2, a mixed weight w= $w_1 + \alpha\, w_2$ means that for any link e,

$$w(e) = w_1(e) + \alpha\, w_2(e) \quad (4)$$

Where ∈ R_0^-. Apparently, a mixed weight of two additive weights is also additive.

Definition 3:

Given a source node s , a destination node d and an additive weight w. It defines a function (or procedure) Dijk (w) that returns the shortest path w from s to d found using Dijkstra's algorithm. In particular it is equivalent to let p_d=Dijk (d) be the least delay (LD) path, and p_c=Dijk (c) the least cost (LC) path between s and d. Note that that relations d (p_d) ≤ d (p_c) and c (p_d) ≥ c (p_c) always hold.

Another function to be used in our algorithms is ModiDijk (c,d). If there exist multiple LC paths with different delays from s to t, function ModiDijk (c,d) will return the one that the minimum delay. This can be done using a modified Dijkstra's algorithm.

3. THE SINGLE MIXED WEIGHT IDEA:

The basic idea of the algorithms proposed in the next section is to solve the DCLC problem by first combining the delay and cost into a single mixed weight, and then using Dijkstra"s algorithm to find a feasible path. In this section, the basic idea is illustrated through a simple network model.

Consider the problem defined in Fig.1 (a), in which we need to find a DCLC path from s to t with a delay bound of 8. Now, solving this problem manually required checking all four paths between s and t. even though this network model is very simple. However, it is easy to find that the LC path is s-u-t, which has a delay of 9 and is infeasible. The LD path is s-v-t, which has a delay of 5 and a cost of 24. Although the LD path is feasible, it is not the optimal solution.

Now let us construct a mixed weight w=d+αc. If we let α=0.5.then the weight w associated with each link is shown in Fig.1 (b).by using Dijkstra"s algorithm, the shortest path from s to t, s-u-v-t, can be easily found. This path has a delay of 8 and a cost of 16, and it turns out to be the optimal path.

This example indicates that selecting an appropriate parameter to construct a mixed weight, reducing the DCLC problem to the shortest path problem, this can be readily solved using Dijkstra"s algorithm.

The key issue for this idea is how to choose the parameter for constructing the mixed weight. A randomly selected value for α may result in a disappointing solution. For instance, in Fig.1 (c) let α=0.2 hence the shortest path w becomes the LD path. While in Fig.1 (d), let α=2 hence the shortest path becomes the LC path.

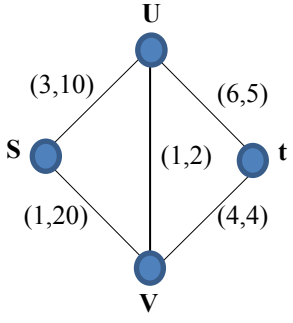

Path from s to t with delay bound=8
Figure 1 (a) A DCLC Problem

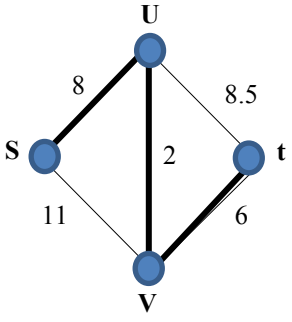

Shortest Path s-u-v-t :delay=8, cost=16
Figure 1 (b) Mixed weights when α=0.5

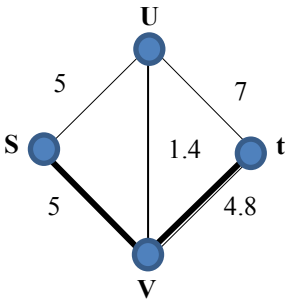

Shortest Path s-v-t :delay=5, cost=24
Figure 1 (c) Mixed weights when α=0.2

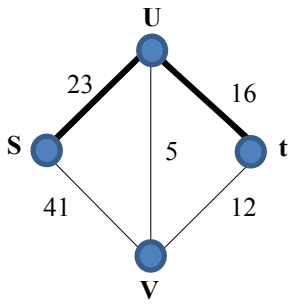

Shortest Path s-u-t :delay=9, cost=15
Figure 1 (d) Mixed weights when α=2

4. HEURISTIC ALGORITHMS FOR THE DCLC PROBLEM:

In the DCLC problem, the attention will be focused on finding good feasible solutions. This section will describe a basic algorithm which the other two proposed iterative algorithms based on it.

As indicated in the previous section of paramount importance in the single- mixed – weight idea is how to choose the4 parameter. the following observation shows the basic relationship between the parameter and the cost and delay of the resulting shortest path .

Theory [S.Chen and K.Nahrstedt 1998]:

If p=Dijk (d+αc) , q =Dijk (d+βc), α≥β, α∈R_0^+,β∈R_0^+ ,then;

c(p)≤ c(p), d(p)≥d(q).

Proof :

Since p is the shortest path weight d+ αc found by Dijkstra's algorithms, then:

$$d(p)+\alpha c(p)\le d(q)+\alpha c(q) \quad (5)$$

Similarly the following inequality holds:

$$d(q)+\beta c(q)\le d(q)+\beta c(p) \quad (6)$$

By combining the two inequalities, result in

$$\alpha c(p)\le d(q)+\alpha c(q)-d(p)$$

$$= d(q)+\beta c(q)-\beta c(q)+ \alpha c(q)-d(p)$$

$$\le d(p)+\beta c(p)-\beta c(q)+ \alpha c(q)-d(p)$$

$$=\beta c(p)+ (\alpha- \beta)\, c(q). \quad (7)$$

By moving the first term in the right – hand side to the left – hand side in equation (4.7), result in

the relation c(p) ≤ c(q). Furthermore, from inequality (4.2) .it can founded that

d(p)≥ d(q) +β {c(q) – c(p)}≥d (q) (8)

The following conclusions can be obtained from the above theory:

1) Given α ∈ R_0^+ ,if p= Dijk (d+αc) is feasible , then for any nonnegative real number β<α , q=Dijk (d+βc) is feasible.

2) Given α ∈ R_0^+, if p=Dijk (d+ αc) is infeasible , then for any nonnegative real number β>α, q=Dijk(d+βc) is infeasible .

3) if p =Dijk (d+αc) , where 0<α<+∞ , then

c(pd) ≥ c(p) ≥ c(pc), d(pd) ≤ d(p) ≤d(pc) .

Previous theory implies that the larger the parameter, the smaller the cost of the resulting shortest path, while the larger the delay of the path .as long as the delay constraint is not violated , a larger parameter will absolutely result in a better solution . Therefore, our remaining work is to find this goal is achieved by (Lagrange relaxation technique) that calculates lower bounds and finds good solutions for DCLC problem. This technique produces the following equation to get the value
of α that is given by:

$$\alpha \leftarrow \frac{C_d - D(p)}{C(p) - C(q)} \qquad (9)$$

The above description for solving DCLC problem is programmed here in (Visual Basic) language, the procedure of this algorithm (DCLC) is shown below:

Algorithm DCLC (G,s,t,c,d,Cd)

Step 0: Start.

Step 1: if there is more than one path with minimum cost, find the least cost path between s and d with minimum delay, and let this path named q.

q← ModiDijk(c,d)

Step 2: check the delay of the selected path in (step1) is less than or equal the delay constrained.

If (d(q)≤Cd) then

Step 3: if the result of (step) is true then the suitable path is q.

Return q

Step 4: if the result of step2 is false then the let p be the shortest path in corresponding to delay (i.e. the path that has minimum delay).

p← Dijk(d)

Step 5: check if the delay of the path p if greater than delay constrained

If (d(p)>Cd)then

Step 6: if the result of (step5) is true then there is no feasible path.

Return NULL

Step 7: if the result of step5 is false then calculate the parameter of constructing the mixed weight (α), where:

$$\alpha = \frac{delay\ constrained - delay\ of\ path(p)}{cost\ of\ path(p) - cost\ of\ path(q)}$$

$$\alpha \leftarrow \frac{Cd - d(p)}{c(p) - c(q)}$$

Step 8: Convert each path to one parameter (w), where:

w=delay+α*cost for each path

Then let p is the minimum path corresponding to (w) value.

p←Dijk(d+αc)

Step 9: p is the algorithm choice of most suitable path.

Return p

Step 10: END

5. THE PROPOSED ITERATIVE ALGORITHM:

Algorithm DCLC is very simple and fast-it only need to execute Dijkstra's algorithm at most three times.in the following section ,a proposed iterative algorithm will be described than can improve the quality of solution.

After obtaining a feasible path which is better than LD path, another parameter can be computed through the equation

$$\alpha = \frac{Cd - d(pd)}{c(pd) - c(Pc}$$

By replacing c(pd)and d(pd),respectively.as long as the new parameter is longer than the previous one, a better solution possibly can be found.

The above description for the proposed iterative algorithm named as (DCLC-A) is programmed here in (Visual Basic) language; the procedure of this algorithm is shown below:

Algorithm DCLC (G,s,t,c,d,Cd)

Step 0: Start.

Step 1: if there is more than one path with minimum cost, find the least cost path between s and d with minimum delay, and let this path named q.

q← ModiDijk(c,d)

Step 2: check the delay of the selected path in (step1) is less than or equal the delay constrained.

If (d(q)≤Cd) then

Step 3: if the result of (step) is true then the suitable path is q.

Return q

Step 4: if the result of step2 is false then the let p be the shortest path in corresponding to delay (i.e. the path that has minimum delay).

p← Dijk(d)

Step 5: check if the delay of the path p if greater than delay constrained

If (d(p)>Cd)then

Step 6: if the result of (step5) is true then there is no feasible path.

Return NULL

Step 7: Create a flag variable named continue with Boolean type having initial value= True

Continue=TURE

Step 8: Building a close loop with a condition continue=true and exit the loop just when continue=false

While continue do

Step 9: if the result of step5 is false then calculate the parameter of constructing the mixed weight (α), where:

$$\alpha=\frac{delay\ constrained-delay\ of\ path(p)}{cost\ of\ path(p)-cost\ of\ path(q)}$$

$$\alpha\leftarrow\frac{Cd-d(p)}{c(p)-c(q)}$$

Step 10: Convert each path to one parameter (w), where:

w=delay+α*cost for each path

Then let r is the minimum path corresponding to (w) value.

r←Dijk(d+αc)

Step 11: Check: If cost of the path(r) equal the cost of path(q) or the cost of the path P.

If (c(r) = c(q) or c(r) = c(p) then

Step 12: If the result of the condition in (step 11) is true then let continue =false to exit loop (step 15)

Continue=False

Step 13: If the result of the condition in (step 11) is false then (step 14)

Else

Step 14: Let P=the minimum path(r)

p←r

Step 15: p is the algorithm choice of most suitable path.

Return p

Step 16: END

6. DEMONSTRATION EXAMPLE:

In the following sections, demonstration examples are submitted to describe the DCLC algorithm and the proposed iterative algorithm DCLC-A and how these algorithms proceed to find a solution.

6.1 Procedure of DCLC Algorithm:

Fig. 2 shows a DCLC problem, in which it is required to find a DCLC path from node 1 to node 6 with a delay upper bound of 12. It is easy to find that the LD path is Pd=[1-3-6], while the LC path is Pc=[1-4-6]. Thus it have d(Pd)=2, c(Pd)=28, d(Pc)=18 and c(Pc)=2. Using an exact algorithm, the optimal solution to this problem is 1-4-5-6, it has a delay of 10 and a cost of 6.

When the basic algorithm DCLC is used to find a solution, it first finds the LC path and plus it in q. Since the LC path is infeasible, it continues to find the LD path and puts it in P. Since the LD path is feasible, it proceeds to compute the parameter α from equation (9), hence α=5/13. This obtains a mixed weight for each link, as shown in Fig. 3. The shortest path from node 1 to node 6, which is also the final solution of algorithm DCLC. Hence the path is 1-3-5-6. This solution, which has a delay of 3 and a cost of 16, is not optimal; however it is better than the LD path.

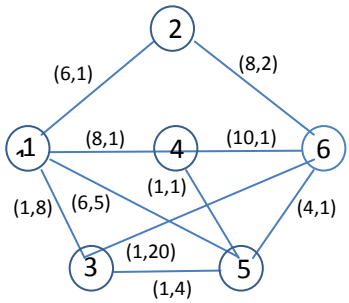

Figure 2: Optimal path from node 1 to node 6 with delay bound=12

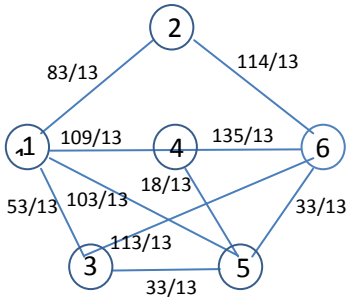

Figure 3: Shortest Path 1-3-5-6 found by DCLC and the same it can obtain by DCLC-A; after 1st iteration

6.2 Procedure of DCLC-A Algorithm:

The first iterative algorithm DCLC-A is based on algorithm DCLC. After finding the LC path q and the LD path p, the algorithm enters the iterative procedure.

In each iteration, a parameter α is first computed by equation (10) for constructing the mixed weight, and then the corresponding shortest path r is found. If r has a lower cost than p, then p is replaced by r. in the first iteration, the parameter is the same as the one used in DCLC, and correspondingly path r=[1-3-5-6] is returned. Since r is better than p, p is replaced by r. in the second iteration, the parameter is reevaluated by α=(12-3)/(16-2)=9/14.

The corresponding mixed weight is shown in Fig. 4(a), and the shortest path r=[1-5-6] is returned. Again, p is replaced by r. in the third iteration, the parameter becomes α=(12/7)/(9-2)=(5/7), and the corresponding mixed weight is shown in Fig. 4(b).

Since the retuned shortest path is the same as the one obtained in the previous iteration, this algorithm stops. The final solution is 1-5-6, which has a delay of 7 and a cost of 9. It is better than the solution of algorithm DCLC, but it is still not optimal.

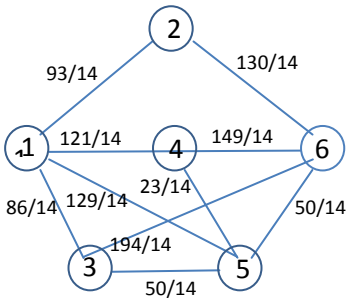

Figure 4(a): Shortest Path 1-5-6: Delay=7: Cost=9
Solution obtained after 2nd iteration

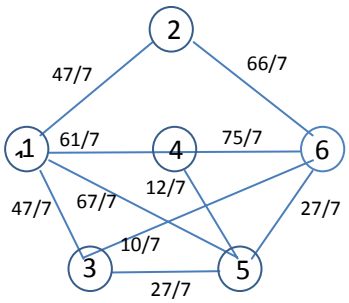

Figure 4(b): Shortest Path 1-5-6: Delay=7: Cost=9
Solution obtained after 3rd iteration

7. CONCLUSIONS:

The path selection algorithm of a routing protocol in high-speed networks must be very responsive in order to achieve a low set-up time. It must also be capable of finding solutions of high quality to ensure the most efficient utilization of network resources.

A single-mixed weight idea was proposed to solve QoS unicast routing problems was successfully used to develop heuristic algorithms for the DCLC problems. The proposed heuristics algorithm was demonstrated to be able to find solutions of high quality yet practically have very low time complexities.

8. REFERENCES:

G.Feng, "Neural network and algorithmic methods for solving routing problems in high speed network", PHD Thesis, University of Miami, Department of Electronics and Communications, 2001.

R.Sriram, "Delay Constrainted Routing in Connection-Oriented Network", Project Report, Department of Computer Science and Engineering, Indian Institute of Technology, Madras, May 1998.

S.Chen and K.Nahrstedt, "On Finding Multi-Constrained Paths", ICC'98, pp. 874-879, Atlanta, Georgia, June 1998.

Cross Dipole Antennas Solution for Angle of Arrival Estimation

Noori Hussein Noori
University of Baghdad
Noori_AlNoori@yahoo.com

Dr.Bassim Sayed Mohammed
University of Technology
Bassim_sayed@yahoo.com

Dr. Jafar Wadi Abdul-Sadah
University of Baghdad
jafarwadi@yahoo.com

ABSTRACT:

The Multiple Signal Classification (MUSIC) algorithm is the most popular algorithm to estimate the Angle of Arrival (AOA) of the received signals. The analysis of this algorithm (MUSIC) with typical array antenna element ($\lambda/2$ *dipole*) shows that there are two false direction indication in the plan aligned with the axis of the array.

In this paper a suggested modification on array system is proposed by using two perpendiculars crossed dipole array antenna in spite of one array antenna. The suggested modification does not affect the AOA estimation algorithm. The simulation and results shows that the proposed solution overcomes the MUSIC problem without any effect on the performance of the system.

Keywords: component; Angle of Arrival Estimation; MUSIC; Adaptive Array Antenna System.

نوري حسين نوري د. باسم سعيد محمد ا.د. جعفر وادي عبد السادة

الخلاصة:

ان خوارزمية تصنيف الاشارات المتعددة (MUSIC) من الخوارزميات الاكثر شعبية لتقدير زاوية وصول الاشارة الراديوية (AOA) . ان التحليلات العملية لخوارزمية الـ(MUSIC) مع مجموعة الهوائيات ثنائية القطب ($\lambda/2$) تظهر وجود دلاله لاتجاهين خاطئين مع المحور المستلقي عليه مجموعة الهوائيات.

في هذا البحث قد تم اقتراح تعديل على مجموعة الهوائيات ويتم ذلك عن طريق استخدام هوائيين متعامدين من الهوائيات ثنائية القطب بدلاً من الهوائي الواحد. وان الحل المقترح لا يؤثر في خوارزمية اكتشاف زاوية وصول الاشارة الراديوية. حيث ان النتائج تظهر ان الحل المقترح يتغلب على مشكلة خوارزمية الـ(MUSIC) من دون اى تأثير فى اداء النظام

INTRODUCTION

Over the last decade, the smart antenna system was taken a great interest in the wireless communication industry which helps to improve the wireless communication system performance by increasing the channel capacity and spectrum efficiency, extending range coverage, steering the multiple beams to track any object (M. Chryssomaillis, 2000).

The Angle of Arrival (AOA) estimator is one of the basic blocks that construct the smart antenna system, because, if there are several operating transmitters, it is important to estimate the (AOA) of all received signals in order to decide which transmitter are present and what are their angular directions.

The MUSIC algorithm is the most important and accurate algorithm which is used for estimating the (AOA) of received signals (F. Taga, 1997).

The adaptive antenna system shown in Fig. (1) is considering a smart antenna system.

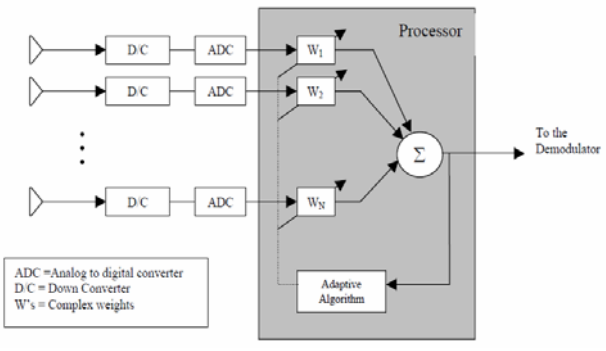

Figure (1) N weighted received signals

The covariance matrix of the received signals contains all the needed information to estimate the AOA of the received signals. To construct $N \times N$ covariance matrix N elements array antenna is needed followed by N adapted weight vector as shown in Fig. (1).

The received signals vector $\boldsymbol{X(k)}$, where k is the number of received snapshot, is given by.

$$\boldsymbol{X(k) = X_d(k) + X_i(k) + X_n(k)} \quad (1)$$

Where: $\boldsymbol{X_d(k),\ X_i(k)\ and\ X_n(k)}$ are desired, interference and thermal noise $(N \times 1)$vectors, respectively.

The adaptive array output signal can be written as

$$y(k) = \sum_{j=1}^{N} w_j x_j(k) \quad (2)$$

The vector form of Eq. (2) is

$$y(k) = \boldsymbol{W^T X = X^T W} \quad (3)$$

Where the weight vector $(\boldsymbol{W})$ and the received signals vector $\boldsymbol{X}$ are given by

$$\boldsymbol{W} = [w_1, w_2, \ldots, w_N]^T \quad (4)$$

$$\boldsymbol{X} = [x_1, x_2, \ldots, x_N]^T \quad (5)$$

The covariance matrix of received signal vector of array antenna is defined as

$$\boldsymbol{Cov[XX] = E([X - E(X)]^*[X - E(X)]^T)} \quad (6)$$

Since $\boldsymbol{X(t)}$ is zero mean stationary process, then

$$\boldsymbol{Cov[XX] = E[X^* X^T] = R_{xx}} \quad (7)$$

Where $\boldsymbol{R_{xx}}$ is $(N \times N)$ autocorrelation matrix of a received signal vector $\boldsymbol{X(t)}$ and for *N*-element array antenna it may be written in the following form

$$\boldsymbol{R_{xx} = E[X^* X^T] = [X^* X^T]} \quad (8)$$

The autocorrelation matrix $\boldsymbol{R_{xx}}$ is Hermitian (i.e. $\boldsymbol{R_{xx} = R_{xx}^{*T}}$) (L.C. Godora, 1997).

Eigen VECTOR DECOMPOSITION

From theory of matrices, a positive definite Hermitian matrix $\boldsymbol{R_{xx}}$ can be diagonalized by a nonsingular orthonormal transformation matrix $\boldsymbol{Q}$ which is formed by eigenvectors of $\boldsymbol{R_{xx}}$ as follows:

$$\boldsymbol{Q^* R_{xx} Q^T = \Lambda} \quad (9)$$

Where: $\boldsymbol{\Lambda}$ Is $(N \times N)$ diagonal matrix, its diagonal elements are a real eigenvalues $\lambda_1, \lambda_2, \ldots \ldots, \lambda_N$, and the corresponding eigenvectors is

$$\boldsymbol{Q} = [\boldsymbol{e}_1, \boldsymbol{e}_2, \ldots \ldots \ldots, \boldsymbol{e}_N] \quad (10)$$

Where $\boldsymbol{e_i}$ is $(N \times 1)$ eigenvector corresponds to eigenvalue λ_i.

The eigenvalues of $\boldsymbol{R_{xx}}$ are given by the solutions of the equation

$$|\boldsymbol{R_{xx}} - \lambda_i \boldsymbol{I}| = 0 \quad for \quad i = 1,2, \ldots, N \quad (11)$$

Where $\boldsymbol{I}$ is $(N \times N)$ an identity matrix.

Corresponding to each eigenvalue there is an associated Eigenvector $\boldsymbol{e_i}$ that satisfies

$$\boldsymbol{R_{xx}\, e_i} = \lambda_i \boldsymbol{e_i} \quad (12)$$

Since, $\boldsymbol{R_{xx} = E\{X^* X^T\}}$, it follows that Eq.(8) may be written as

$$\boldsymbol{[Q^*\, R_{xx}\ Q^T] = [Q^* X^* X^T Q^T] = [X^{*\sim} . X^{T\sim}]} \quad (13)$$

then $\boldsymbol{x_i^{*\sim} = e_i^{\dagger} . X^*}$ $\boldsymbol{for}\ i = 1,2, \ldots, N$ (14)

where † is dagger notation (i.e. tranjugate).

The array correlation matrix has N eigenvalues $(\lambda_1, \lambda_2, \ldots, \lambda_N)$ along with N associated eigenvectors $\boldsymbol{Q} = [\boldsymbol{e}_1, \boldsymbol{e}_2, \ldots, \boldsymbol{e}_N]$ where N is the number of sensors.

If the eigenvalues are sorted from smallest to largest, matrix $\boldsymbol{Q}$ can be divided into two sub space such that $\boldsymbol{Q} = [\boldsymbol{Q}_n, \boldsymbol{Q}_s]$.

The first subspace $\boldsymbol{Q_n}$ is called the noise subspace and is composed of $(N - D)$ eigenvectors associated with the noise, the eigenvalues are given as $\lambda_1 = \lambda_2 = \ldots = \lambda_{N-D} = \sigma_n^2$ where D is the number of received signals.

The second subspace $\boldsymbol{Q_s}$ is called the signal subspace and is composed of D Eigen vectors associated with the received signals (Md. Bakhar 2009).

MUSIC ALGORITHM

The MUSIC algorithm is a simple, popular, high resolution and efficient Eigen structure method (Md. Bakhar 2009). The MUSIC spatial spectrum for the MUSIC algorithm can be expressed as follows

$$DF(\theta) = \frac{1}{\boldsymbol{C^T(\theta)\, Q_n Q_n^{\dagger} C^*(\theta)}} \quad (15)$$

Where $C(\theta)$ is a spatial vector given by

$$C(\theta) = \left[g_z(\theta)\, e^{-j\varphi\beta d\cos(\theta)} \right]^T \quad z = 0,1,\ldots N-1 \qquad (16)$$

So $g_z(\theta)$ is the element pattern for the array and θ is a spatial angle from 0 to 2π

The MUSIC technique flow graph is illustrated in Fig (2)

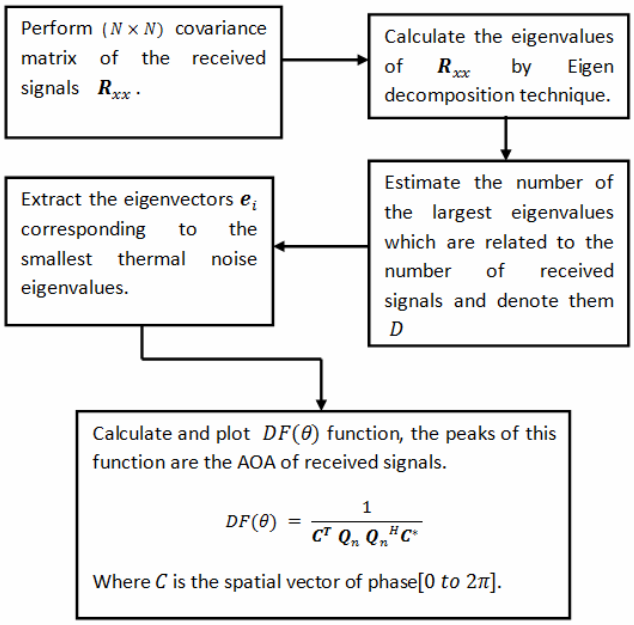

Figure (2) the flow graph of MUSIC technique.

Cross Dipole Array Elements

In order to make the resultant array antenna pattern approximates the isotropic array pattern (i.e. spherical pattern) two perpendicular crossed dipoles in the same plane are proposed as shown in Fig.(3) and Fig(4).

The pattern for a single $\lambda/2$ dipole in the (z-y) plane laying along z axis is given by (Stutzman, 1981).

$$g_1(\theta) = \frac{\cos\left[\frac{\pi}{2}*\cos\theta\right]}{\sin\theta} * \sin\varphi \qquad (17)$$

Since the elevation angle $\varphi = 90^\circ$ for the received signal and that leads to $\sin\varphi = 1$.

And for a dipole in the same (z-y) plane laying along y axis is given by

$$g_2(\theta) = \frac{\cos\left[\frac{\pi}{2}*\cos(\theta-\frac{\pi}{2})\right]}{\sin(\theta-\frac{\pi}{2})} * \sin\varphi \qquad (18)$$

The resultant pattern of cross dipole $g(\theta)$ is given by

$$g(\theta) = g_1(\theta) + g_2(\theta)$$

$$= \frac{\cos[\frac{\pi}{2}*\cos\theta]}{\sin\theta} + \frac{\cos[\frac{\pi}{2}*\cos(\theta-\frac{\pi}{2})]}{\sin(\theta-\frac{\pi}{2})} \qquad (19)$$

The array factor for circular isotropic array elements given by (Liu Jin, 2008)

$$AF_c(\theta,\varphi) = \sum_{i=0}^{N-1} e^{-j(\beta r\cos(\theta-\varphi_i)} \qquad (20)$$

Where φ_i is the array antenna distribution angle as shown in Fig.(4) and it is given by

$$\varphi_i = \frac{2\pi(i-1)}{N} \quad for\ i = 1,2,\ldots N \qquad (21)$$

and r is array circle radius with respect to wavelength λ and given by

$$r = N * d * \lambda/2\pi \qquad (22)$$

Then the total circular array pattern array with cross dipole element can be written as

$$G_c(\theta) = g(\theta) * AF_c(\theta,\varphi) \qquad (23)$$

Where $g(\theta)$ is the array element pattern of the crossed dipole. The array pattern in Eq.(23) is considered as a basic block for generating the covariance matrix of the received signals which in turn used in the calculating the eigenvectors of noise channel in the DF function of the MUSIC see Fig(2). The effects of using crossed dipole will reflect directly on the performance of MUSIC technique when a $\lambda/2$ dipole element is used in the antenna system.

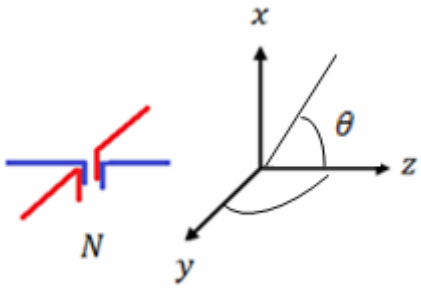

Figure (3) cross dipole element

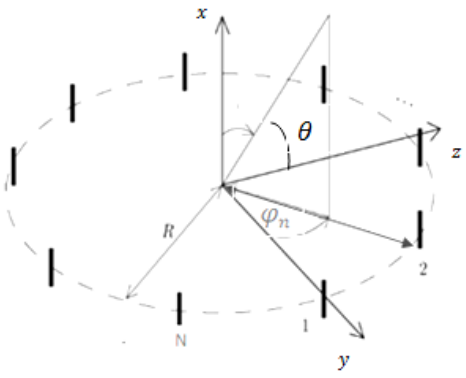

Figure (4) cross dipole circular array

Simulation Results

All the simulation programs were written by MATLAB 7.1 and the following assumption are used

a) The array number of elements is six (N=6) which they are distributed on the circumference of a circle.
b) The inter element spacing equal to 0.5 λ
c) The input $SNR = 0dB$
d) The radius of the circle r according to the E.(30) equal to 0.4774 λ.

Three type of antenna element were tested in this simulation.

A. Isotropic elements:

Six isotropic elements with 0.5λ inter element spacing distributed on a circle with radius 0.4774 λ .

Figs.(5) shows the final MUSIC DF plot for one received signal from broadside ($\theta = 90^o$) and Fig.(6) shows four received signals from ($0^o, 30^o, 120^o, 180^o$) it can be shown that the system does not suffer any problem to track a multiple sources at the same time.

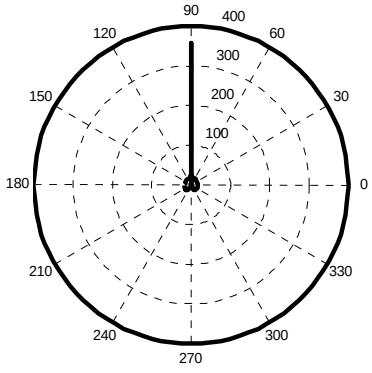

Figure (5) DF function plots for MUSIC Technique with six isotropic elements array for incoming signal from 90°

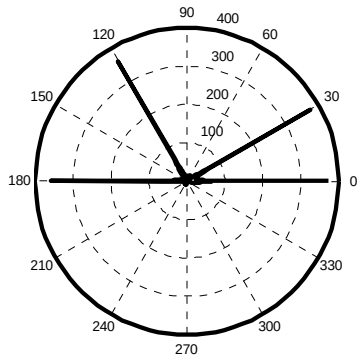

Figure (6) DF function plots for MUSIC Technique with six isotropic elements array for incoming signals from ($0^o, 30^o, 120^o, 180^o$)

B- $\lambda/2$ Dipole Elements:

Six $\lambda/2$ dipoles array elements with 0.5λ inter element spacing distributed on a circle with radius 0.4774 λ.

Fig.(7) shows that there are three sources from angles $0^\circ, 90^\circ, 180^\circ$, while there is only one actual source from 90° which means that the MUSIC DF function gives a false indication from angles $0^\circ, 180^\circ$ in additional to the real source. These two false DF direction are due to the existence of nulls in the element pattern from these direction as shown in Fig.(8). According to the mathematical form of the MUSIC DF function these nulls will be interpreted as a real source from these directions.

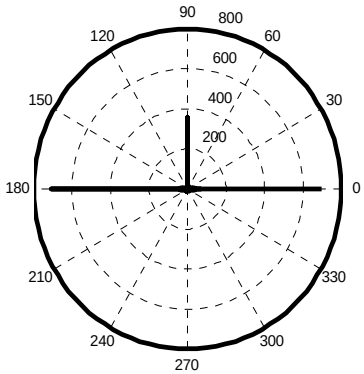

Figure (7) DF function plots for MUSIC Technique with six $\lambda/2$dipole elements array for incoming signal from 90°

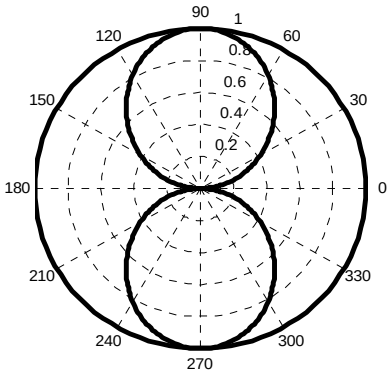

Figure (8) Element pattern for $\lambda/2$ dipole

C- Perpendicular Crossed Dipole Elements:

For the same assumption of case B the crossed $\lambda/2$ dipole antenna are used in spite of a single $\lambda/2$ dipole antenna as elements of the array antenna.

Fig.(9) shows that the resultant pattern of the crossed dipole is approximate the isotropic pattern which leads to the cancellation of nulls appears in single dipole .

Fig.(10) shows that the final DF pattern shows only the single source from $\theta = 90^{\circ}$ and nothing from $(0^{\circ}, 180^{\circ})$.

To insure that the suggested solution does not affect the performance of the system four signals coming from $(0^{\circ}, 30^{\circ} 120^{\circ}, 180^{\circ})$ is considered, Fig.(11) shows that there are a clear indication from these directions and the suggested solution doesn't cancel the reading for the incoming signal from $(0^{\circ}, 180^{\circ})$

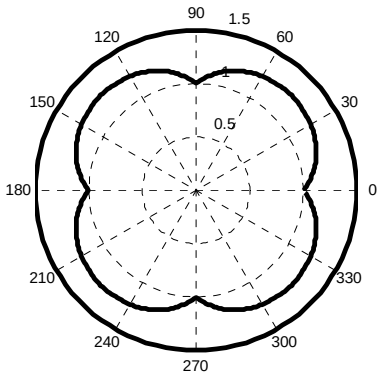

Figure (9) Element pattern for cross $\lambda/2$ dipole

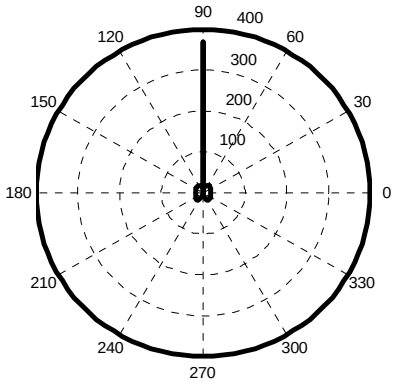

Figure (10) DF function plots for MUSIC Technique with six crossed dipole elements array for incoming signal from 90°

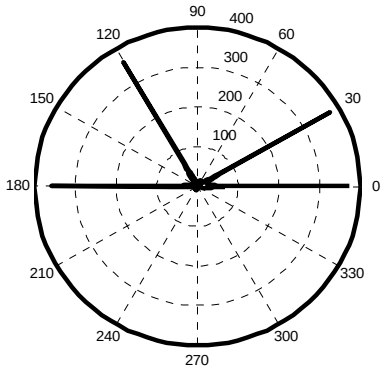

Figure (11) DF function plots for MUSIC Technique with six crossed dipole elements array for incoming signal from $(0^{o}, 30^{o}, 120^{o}, 180^{o})$.

Conclusions

Angle of arrival (AOA) estimation based on MUSIC algorithm with isotropic, $\lambda/2$ dipole and crossed $\lambda/2$ dipole is investigated.

The MUSIC AOA estimation results show the following:-

1- With isotropic array elements the MUSIC DF can simultaneously read the direction to the multiple source even from the sources placed at 0°or180°.

2- When $\lambda/2$ dipole is used as an array element, it has been found that the MUSIC DF system gives a false direction from angles $0^{\circ}, 180^{\circ}$ which coincides with the nulls in the element pattern.

3- The suggested perpendicular crossed $\lambda/2$ dipole gives a satisfied solution for the false direction referred in (2), without degradation in the performance of the system when dealing with real source placed at angles $0^{\circ}, 180^{\circ}$

4- Finally the suggested solution will increase the complexity of the antenna system by increasing the number of the elements.

REFERENCES

F. Taga "Smart MUSIC Algorithm for DOA Estimation" ELECTRONIC LETTERS Vol.33 No.3 30th January 1997.

L.C. Godora “Application of Antenna Arrays to Mobile Communications, Part II: Beam-Forming and Direction-of-Arrival Considerations” proceeding of IEEE, VOL. 85, NO. 8 , pages 1195-1245, AUGUST 1997.

Liu Jin, Li li, Huazhi Wang “Investigation of Different Types of Array Structures for Smart Antennas” IEEE. ICMMT Proceedings. 2008.

M. Chryssomaillis “Smart Antennas” IEEE antenna and propagation magazine, volume 42, No.3, June 2000, pages 129-136.

Md. Bakhar, Dr. Vani. R.M and Dr. P.V. Hunagund “Eigen Structure Based Direction of Arrival Estimation Algorithms for Smart Antenna Systems” IJCSNS International Journal of Computer Science and Network Security, VOL.9 No.11, November 2009.

Stutzman “Antenna Theory and Design” ISBN 0-471-04458-x, year 1981.